

REFERENCE ONLY



UNIVERSITY OF LONDON THESIS

Degree PhD Year 2007 Name of Author CRISTIANA
ARCIDIACONO

COPYRIGHT

This is a thesis accepted for a Higher Degree of the University of London. It is an unpublished typescript and the copyright is held by the author. All persons consulting the thesis must read and abide by the Copyright Declaration below.

COPYRIGHT DECLARATION

I recognise that the copyright of the above-described thesis rests with the author and that no quotation from it or information derived from it may be published without the prior written consent of the author.

LOAN

Theses may not be lent to individuals, but the University Library may lend a copy to approved libraries within the United Kingdom, for consultation solely on the premises of those libraries. Application should be made to: The Theses Section, University of London Library, Senate House, Malet Street, London WC1E 7HU.

REPRODUCTION

University of London theses may not be reproduced without explicit written permission from the University of London Library. Enquiries should be addressed to the Theses Section of the Library. Regulations concerning reproduction vary according to the date of acceptance of the thesis and are listed below as guidelines.

- A. Before 1962. Permission granted only upon the prior written consent of the author. (The University Library will provide addresses where possible).
- B. 1962 - 1974. In many cases the author has agreed to permit copying upon completion of a Copyright Declaration.
- C. 1975 - 1988. Most theses may be copied upon completion of a Copyright Declaration.
- D. 1989 onwards. Most theses may be copied.

This thesis comes within category D.

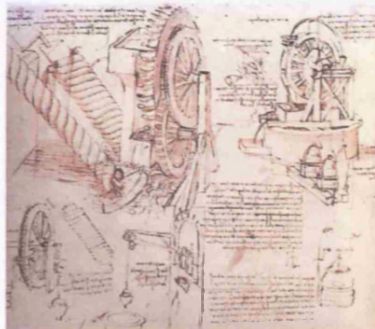
This copy has been deposited in the Library of UCL

This copy has been deposited in the University of London Library, Senate House, Malet Street, London WC1E 7HU.

Ionisation Studies by Positron Impact

A thesis submitted to the University College London for the degree of
Doctor of Philosophy

Cristiana Arcidiacono



Department of Physics and Astronomy
University College London

December 2006

UMI Number: U592588

All rights reserved

INFORMATION TO ALL USERS

The quality of this reproduction is dependent upon the quality of the copy submitted.

In the unlikely event that the author did not send a complete manuscript and there are missing pages, these will be noted. Also, if material had to be removed, a note will indicate the deletion.



UMI U592588

Published by ProQuest LLC 2013. Copyright in the Dissertation held by the Author.
Microform Edition © ProQuest LLC.

All rights reserved. This work is protected against
unauthorized copying under Title 17, United States Code.



ProQuest LLC
789 East Eisenhower Parkway
P.O. Box 1346
Ann Arbor, MI 48106-1346

*Papamnak es
Nagypapamnak*

Acknowledgments

I would like to thank a number of people who have helped and accompanied me during my PhD years. Firstly, I would like to mention my supervisor Prof. Nella Laricchia for her endless support and guidance. Thanks also to Dr Akos Kover for his assistance, enthusiasm and inspiring conversation. Special thanks, to my best friend Zoran, who taught me so much, both in and outside the laboratory and for always being there. Thanks to all I have shared the office with Josie, Dan and Simon. In particular, thanks to Dan for having proofread this thesis, having provided me with some amusing distractions during difficult moments. Thanks to Rafid and Ted for their technical help. Also thanks to my family and all friends abroad. Last but not least thanks to Anemone, Anna Lea, Anna, Clara, Zsuzsa and Simone for their ongoing help and friendship. Thanks also to John and Simon A for their prompt proofreading.

Abstract

Differential studies of positron impact ionisation have been performed to understand the energy shift (Kövéér *et al.*, 2001) of $\sim 1.6\text{eV}$ between the theoretical and measured energy spectrum of the ejected electron in the triply-differential cross-section, $d^3\sigma_i^+ / dE_- d\Omega_- d\Omega_+$, at 50eV incident energy on H_2 . Firstly, an absolute energy calibration has been carried out to check for possible contact potential effects in the determination of Kövéér *et al.* (2001). Secondly, D_2 and He have been investigated at the same residual kinetic energy as in Kövéér *et al.* (2001) to probe the occurrence of molecular dissociation or excitation. Finally, the distribution of kinetic energies of scattered positrons from the same collision system ($e^+ - \text{H}_2$) has been measured for the first time. This work shows an unexpected asymmetry in the energy sharing between electron and positron. Possible reasons for this finding are discussed.

An extensive study has been carried out also on water vapour ionisation upon positron collision for the first time. Besides their intrinsic interest, ionisation data are essential to provide a measure of the energy released in living matter during radiobiological applications. Preliminary results for the total, σ_i^+ , and direct, σ_i^+ , ionisation cross-sections of water have been obtained for collision energies from the threshold to $\sim 1\text{keV}$. σ_i^+ is higher, by up to a factor of 2, than that for electron impact, whereas the dissociative ionisation cross-section, σ_D^+ , for H^+ production is similar to that for electron impact. Under the assumption that the difference between σ_i^+ and σ_i^+ is primarily due to positronium formation, σ_{ps} has been extracted. This amounts to a significant fraction contribution of σ_i^+ , contrary to the work of Sueoka *et al.* (1987). Finally, to probe in more detail ionisation in $e^+ - \text{H}_2\text{O}$ scattering, the doubly differential cross-section, $d^2\sigma_i^+ / dE_+ d\Omega_+$, at $\sim 0^\circ$, for 100eV positrons colliding with water has been measured. The differential cross-section appears more forward scattered than in Ar . Fragmentation channels are also identified.

Contents

	Page
Abstract	2
Contents	3
Figure Captions	7
Table Captions	20
Chapter 1: Introduction	21
1.1 Historical Background	21
1.2 Fundamental Properties of Positron and Positronium Formation	22
1.2.1 Positrons	22
1.2.2 Positronium Formation	24
1.3 Development of Positron Beams	26
1.4 Positron Interaction with Atoms and Molecules	29
1.4.1 Total Scattering Cross-Sections	30
1.4.2 Annihilation	34
1.4.3 Bound States	37
1.4.4 Elastic Scattering	38
1.4.5 Molecular Vibrational and Electronic Excitation	40
1.4.6 Ps Formation Cross-Sections	42
1.4.7 Integral and Differential Ionisation Cross-Sections	47
1.5 Positronium Interaction with Atoms and Molecules	59
1.6 Motivation of the Present Work	63
Chapter 2: Experimental Apparatus for Differential Studies of Positron Impact Ionisation	65
2.1 Overview	65

2.2 The Vacuum System	67
2.3 Positron Beam Production	68
2.3.1 β^+ Source and Moderator	68
2.4 Positron Beam Transport	70
2.5 Tandem Parallel Plate Analyser and Detection System	71
2.5.1 Analyser	71
2.5.2 Multichannel Plate Detector	74
2.5.3 Channeltron (CEM1)	75
2.5.4 Energy Resolution of Parallel Plate Analyser	75
2.5.5 A Computer Simulation of $e^- - e^+$ Flight Times	77
2.6 Ion Extractor and Gas Inlet	79
2.7 Summary	81
Chapter 3: Triply Differential Studies of Positron Impact	82
Ionisation: Results and Discussion	
3.1 Overview	82
3.2 Absolute Energy Calibration	83
3.3 TDCS(e^-) for Deuterium	88
3.4 TDCS(e^-) for Helium and TDCS(e^+) for Molecular Hydrogen	93
3.4.1 The Electronics	93
3.4.2 Experimental Method	94
3.4.3 TDCS(e^-) for Helium	96
3.4.4 Positron Energy Spectrum for H_2 : TDCS(e^+)	97
3.5 Summary	100
Chapter 4: Experimental Apparatus for Measuring	101
Integral Cross-Section for Positron Impact Ionisation of H_2O	
4.1 Overview	101
4.2 The Vacuum System	103
4.3 Positron Beam Production	103
4.3.1 β^+ Source and Moderator	103
4.3.2 Retarding Field Analysis	105
4.4 Positron Beam Transport and Detection System	106

4.4.1	Magnetic Guidance	106
4.4.2	Components	106
4.5	Interaction Region	110
4.6	System for Purification of Water and Target Gas Jet	111
4.7	Ion Extractor	113
4.7.1	Design	113
4.7.2	Simulated Performance of the Ion Extractor	113
4.7.3	Extraction Efficiency	118
4.8	Energy Dependence of Positron Detection Efficiency	120
4.9	Summary	121
 Chapter 5: Positron Impact Ionisation of Water Molecules		123
5.1	Overview	123
5.2	Integral Ionisation Cross-Sections	125
5.2.1	Direct Ionisation Cross-Section: Methods	125
5.2.2	Total Ionisation Cross-Section: Experimental Methods	131
5.2.3	Normalisation	135
5.2.4	Test of the System with Argon	137
5.2.5	Direct and Total Ionisation Cross-Sections of Water: Preliminary Results	138
5.2.6	Positronium Formation	142
5.3	Doubly Differential Ionisation Cross-Sections	145
5.3.1	Experimental Method	145
5.3.2	Results and Discussion	147
5.4	Summary	151
 Chapter 6 Conclusion and Future Work		153
 Appendix I		156
 Appendix II		160
 Appendix III		161

Appendix IV	162
Appendix V	164
References	165
Appendix VI <i>Published Works</i>	178

Figure	Caption	Page
Chapter 1		
1.1.	One of the cloud chamber photographs which proved the existence of the positron (Anderson, 1933).	22
1.2.	Feynman diagrams of (a) one, (b) two, (c) three and (d) four photon decay modes.	23
1.3.	Energy level diagram for Ps.	26
1.4.	Energy distribution of positrons emitted from a ^{58}Co source and after moderation by a W(100) moderator	27
1.5.	Simplified illustration of the interaction of positrons at a metal surface (from Mills, 1983a).	27
1.6.	Top: buffer-gas trap structure; bottom: typical pressure and voltage profile as a function of distance z . (Figure taken from Sullivan <i>et al.</i> , 2002).	28
1.7.	Total cross-section for e^{\pm} - noble gases scattering (from Stein and Kauppila, 1982). The arrows indicate thresholds for Ps formation, excitation and ionisation in order of increasing energy.	31
1.8.	Total cross-sections for positron scattering on molecular hydrogen. <ul style="list-style-type: none"> • Karwasz <i>et al.</i> (2006); □ Hoffman <i>et al.</i> (1982); + Charlton <i>et al.</i> (1983a) Δ Deuring <i>et al.</i> (1983) ♦ Zhou <i>et al.</i> (1994); --- Varella <i>et al.</i> (2002); — Gianturco <i>et al.</i> (1996). 	32
1.9.	Total cross-section for e^{\pm} - H_2O scattering. The arrows indicate the Ps formation and ionisation thresholds. The inset shows in detail the structure observed by Zecca <i>et al.</i> (2006) around 3.5eV.	33

- 1.10. The variation of Z_{eff} with temperature for H_2O : 35
 • the experimental value of Iwata *et al.* (2000) multiplied by 0.5;
 line, the theory of Gianturco *et al.* (2001).
- 1.11. Positron annihilation rate, Z_{eff} , for (a) butane, (b) propane and 36
 (c) ethane, as a function of positron energy (from Gilbert *et al.*, 2002).
 The vibrational modes are indicated by vertical lines along the abscissa.
- 1.12. Ratios of $S(3\gamma)$ to $S(2\gamma)$ signals (with statistical uncertainties) 37
 versus ΔE (positron energy minus the energy of the initial Ps formation
 threshold) for Ar, N_2 , CO and N_2O .
- 1.13. Positron-He scattering: • $\sigma_{\text{el}} + \sigma_{\text{ex}} + \sigma_{\text{i}}$ (Coleman *et al.*, 1992) ; full curve, 38
 σ_{i} (Stein *et al.*, 1978); broken curve, $\sigma_{\text{el}} + \sigma_{\text{ex}}$ deduced by Campeanu *et al.*
 (1987); dotted curve, $0.224 \pi a_0^2 + \sigma_{\text{ex}} + \sigma_{\text{i}}$ (Varracchio, 1990; Knudsen *et al.*,
 1990). (Figure taken from Coleman *et al.*, 1992).
- 1.14. Total (tot) and elastic (el) scattering cross-sections for e^+ + (noble gas atom) 39
 collision near the Ps –formation threshold (Ps) as a function of the positron
 energy E . The broken curves represent σ^0 , which is the part of the total (or
 elastic) cross-section at the threshold that is uncoupled from the non elastic
 channel . The solid curves give the prediction for σ_{tot} and σ_{el} . Below threshold
 $\sigma_{\text{tot}} = \sigma_{\text{el}}$. (Figure taken from Moxom *et al.*, 1994).
- 1.15. Elastic differential cross-section for e^+ - Xe scattering at an 40
 incident energy of 2eV: (•) Marler *et al.* (2006); (- -) the theoretical
 prediction from the calculations carried out within the framework of
 the Dirac equation with no fitted parameters (see Marler *et al.*, 2006);
 (-) the theoretical prediction folded about 90° ; (□) electron data
 (Register *et al.*, 1986). (Figure taken from Marler *et al.*, 2006).

- 1.16. Integral electron/positron-impact vibrational excitation of the ν_3 vibrational mode of CF_4 : (●) the positron-impact results (○) the electron-impact results. (From Marler and Surko, 2005a) 40
- 1.17. Absolute integral cross-sections for the excitation of the $3p^5(^2P_{3/2})4s$ and $3p^5(^2P_{1/2})4s$ atomic states of Ar from the threshold to 30eV. Cross-sections by positron impact: (●) Sullivan *et al.* (2001b). (□) Coleman *et al.* (1982). (◇) Mori and Sueoka (1994) scaled by 0.6. (--) Parcell *et al.* (2000). (Figure taken from Sullivan *et al.*, 2001b). 41
- 1.18. On the left, integral cross sections in N_2 for the excitation of the $a^1\Pi$ state by (●) positrons (Marler and Surko, 2005b) and (○, □) electrons (Campbell *et al.*, 2001; Mason and Newell, 1987). The theoretical predictions for positron impact are from Chaudhuri *et al.* (2004) On the right, integral cross sections for the excitation of the $A^1\Pi$ state in CO by (●) positron and (○) electron impact (Ajello, 1971). Also shown is the theoretical calculation of the $A^1\Pi$ state in CO by electrons (Lee *et al.*, 1996). 42
- 1.19. Positronium formation cross-sections for He, Ne, Ar, Kr and Xe as a function of incident positron energy. 43
- 1.20. Measurements of Marler and Surko (2005b) of the integral cross-sections for O_2 : (●) positronium formation and (■) total ionisation cross-section. Also shown for comparison are the experimental results for (□) the total ionisation cross-section from Laricchia *et al.* (1993), and (○) the positronium formation from Griffith (1983). Vertical bars mark the positions of the Ps formation and direct ionisation thresholds. The experimental cross-section for the excitation to the Schumann-Runge continuum from Katayama *et al.* (1987) is also shown as the dashed line. 45
- 1.21. Estimation of the Ps formation cross-section in the case of C_3H_8 . An illustration of the method used by Makochekanwa *et al.* (2006). 46

- 1.22. Single ionisation cross-section with equivelocity (e^{\pm}, p^{\pm}) projectiles on He. 47
 Positron impact: (—) σ_{tot}^+ by Moxom *et al.* (1995), (- - -) σ_i^+ by Jacobsen *et al.* (1995) and Moxom *et al.* (1996). Electron impact: (—) σ_i^+ by Krishnakumar and Srivastava (1988). Proton impact: (- · -) σ_{tot}^+ and (- · ·) σ_i^+ by Shah and Gilbody (1985) and Shah *et al.* (1989). Antiproton impact: (·····) σ_i^+ by Andersen *et al.* (1990) and Hvelplund *et al.* (1994). (Figure taken from Knudsen and Reading, 1992).
- 1.23. Direct ionisation cross-sections as a function of positron energy 48
 for Ne, Ar, Kr, and Xe. (●) Marler *et al.* (2005). These data are compared with two other determinations of these cross-sections: (□) the direct ionisation measurements from Moxom *et al.* (1996) and Kara *et al.* (1997); and (—) using the total ionisation from Laricchia *et al.* (2002) minus the measurements for the positronium formation of Marler *et al.* (2005). Also shown for comparison in Ar are (Δ) the experimental data from Jacobsen *et al.* (1995). (Figure taken from Marler *et al.*, 2005).
- 1.24. The triply differential cross-section for the ejection of electrons in the 51
 beam direction ($\theta_a = \theta_b = 0^\circ$) from the ionisation of atomic hydrogen by 1keV positron impact as a function of the electron ejection energy E_b . The broken curve is for an electron-positron plane wave as the final state; the full curve is for a Coulomb wave as the final state. (Figure taken from Brauner and Briggs, 1986).
- 1.25. Comparison of the DDCS of ejected electrons from 100eV e^+ -H collision 52
 determined by (-) a quantum mechanical (Bandyopadhyay *et al.*, 1994) and (- -) a CTMC calculation (Schultz and Reinhold, 1990). The curves marked I to XII represent all angles from 0° to 180° . (Figure taken from Bandyopadhyay *et al.*, 1994).
- 1.26. Ejected e^- energy spectra deduced from time-of-flights at various e^+ impact 53

- energies. (Figure taken from Moxom *et al.*, 1992).
- 1.27. Energy distribution for electrons (o) and positrons (●) scattered close to 0° at impact energies of a) 100, b) 150 and c) 250eV (Kövéř *et al.*, 1993). The line represents the results of CTMC calculations (Sparrow and Olson, 1994). 54
- 1.28. Doubly differential cross-sections (DDCS) for the single ionisation cross-section of Ar gas by impact of 100eV electrons. The solid circles on the eye-guide line are from Dubois and Rudd (1978), whilst the open circles are Kövéř *et al.* (1994) a) 30° , b) 45° . 55
- 1.29. Doubly differential cross-sections (DDCS) for the single ionisation cross-section of Ar gas by impact of 100eV positrons. (\diamond) Scattered positrons; (Δ, ∇) ejected electrons (Kövéř *et al.*, 1994); solid line, calculation of Sparrow and Olson (1994) a) 30° , b) 45° . 56
- 1.30. The triply-differential electron spectrum in $e^+(100\text{eV}) + \text{H}_2 \rightarrow e^+(\theta \sim 0^\circ) + e^-(\theta \sim 0^\circ, E.) + \text{H}_2^+$; ● the experimental work of Kövéř and Laricchia (1998); the pink curve and red curve, theory of Berakdar (1998) and Fiol *et al.* (2001) folded with the experimental resolutions, respectively. The green curve is the CTMC by Fiol and Olson (2002). Dashed curve in blue is the First Born Approximation. 57
- 1.31. The triply differential ionisation cross-section for 50eV positrons incident on H_2 (Kövéř *et al.*, 2001). Full line: theory (Fiol *et al.*, 2001). Dashed Line: theory shifted backwards by 1.6eV. Dashed dot-dot: CTMC (Fiol and Olson, 2002). 58
- 1.32. Experimentally and theoretically determined cross-section 60

for the fragmentation of Ps in collision with He atoms.

- | | | |
|-------|--|----|
| 1.33. | Cross-sections, differential in longitudinal energy, for Ps(1s)+He(1 ¹ S) collisions for E_{Ps} =13, 18, 25, and 33 eV. . The experimental data (full circles) of Armitage <i>et al.</i> (2002) are shown alongside the blue theoretical curves calculated by Starrett <i>et al.</i> (2005). The vertical dotted line shows the expected peak position $E_r/2$. The cyan curves are the CTMC computations by Sarkadi (2003). | 61 |
| 1.34. | Calculations of the longitudinal energy distributions of e^+ (solid line) and e^- (dashed line) ejected in Ps-He collisions for 18eV (left) and 33eV (right) Ps scattering from He atoms by Sarkadi (2003) and Starrett <i>et al.</i> (2005). | 62 |

Chapter 2

- | | | |
|------|---|----|
| 2.1. | Schematic of the experimental arrangement. | 66 |
| 2.2. | Top view of the interior of the chamber. | 67 |
| 2.3. | The decay scheme and branching ratio of ²² Na. | 68 |
| 2.4. | Schematic of the source and moderator arrangement. | 69 |
| 2.5. | Schematic diagram of the cross-section of the Parallel Plate Analyser, to scale (Kövéér and Laricchia, 2001). | 72 |
| 2.6. | Distribution of the calculated time-of-flight as a function of the entrance angle for the PPA (Kövéér and Laricchia, 2001). | 74 |
| 2.7. | A section of the MCPs arrangement. | 75 |

2.8.	Measured beam energy profiles for 20, 33, 50, 62, 74, 86 eV impact energies.	76
2.9.	The total parallel plate analyser resolution, $(\Delta E_T)^2$, measured as a function of the positron beam energy, E_0^2 .	77
2.10.	Simulation of the 15eV e^+ trajectories through the PPA after ionisation from 50eV e^+ impact on H_2 . The voltages to the guard electrodes decrease in step of 1V.	78
2.11.	• Calculated and • measured position of the ionising signal on the MCA spectrum for $e^+ (50\text{eV}) + H_2 \rightarrow e^- (\theta \sim 0^\circ) + e^+ (\theta \sim 0^\circ, E_+) + H_2^+$.	79
2.12.	Schematic of the extraction and ion detection systems, not to scale.	80
2.13.	Simulation of 0.03eV H_2O^+ trajectories through the ion extractor.	81

Chapter 3

3.1.	A schematic diagram of the electronics and data collection system employed for the absolute energy calibration.	84
3.2.	A raw ion spectrum obtained for the absolute energy calibration of the positron beam. It was obtained with He for incident e^+ of 19.54eV (run-time ~ 3 days).	86
3.3.	a) Positronium formation cross-section, σ_{Ps} , near the threshold (Moxom <i>et al.</i> , 1994) and a least square fit to the square cross-section. b) Measurements of the ion yield close to the threshold for positronium formation in helium (Arcidiacono <i>et al.</i> , 2005a). The solid line corresponds to the fit to the results of Moxom <i>et al.</i> (1994).	87

- 3.4. A schematic diagram of the ion detection sequence and timing electronics employed for the study of the TDCS(e^-) from positron impact ionisation upon D_2 :
 e^+ (50eV) + $D_2 \rightarrow e^+$ ($\theta=0^\circ$) + e^- ($\theta=0^\circ$, E.) + D_2^+ or
 e^+ (50eV) + $D_2 \rightarrow e^+ + e^- + (D_2^+)^* \rightarrow e^+$ ($\theta=0^\circ$) + e^- ($\theta=0^\circ$, E.) + $D^+ + D^+$. 89
- 3.5. A coincidence spectrum between $e^- - D_2^+$ as obtained with the PPA set to detect 24.4eV electron (run time =325,641). 90
- 3.6. The triply differential ionisation cross-section for 50eV positrons incident on • D_2 (Arcidiacono *et al.*, 2005a)
• H_2 (Kövéér *et al.*, 2001). Full line: theory (Fiol *et al.*, 2001), 3C. Dashed Line: theory shifted backwards by 1.6eV. Dashed dot-dot: CTMC (Fiol and Olson, 2002). Blue line: eye guide representing a polynomial fit. 92
- 3.7. A schematic illustration of the delayed coincidence timing circuit used to measure the $e^+ - e^-$ coincidences from the following reactions:
 e^+ (59.1eV) + He $\rightarrow e^+$ ($\theta \sim 0^\circ$) + e^- ($\theta \sim 0^\circ$, E.) + He $^+$
and e^+ (50eV) + $H_2 \rightarrow e^-$ ($\theta \sim 0^\circ$) + e^+ ($\theta \sim 0^\circ$, E $_+$) + H_2^+ . 93
- 3.8. Examples of $e^+ - e^-$ coincidences obtained with the PPA set to detect 20.8eV positrons. (a) Raw spectrum acquired in 2 days in vacuum. (b) Sum of raw spectra with gas, H_2 , for a total run-time of 5 days. 94
- 3.9. The triply differential ionisation cross-section for
• 50eV positron incident on H_2 (Kövéér *et al.*, 2001);
• 50eV positrons incident on D_2 (Arcidiacono *et al.*, 2005a);
∇ 59.1eV positrons incident on He (Arcidiacono *et al.*, 2005a).
Full line: theory (Fiol *et al.*, 2001), 3C. Dashed Line: theory shifted backwards by 1.6eV. Dashed dot-dot: CTMC (Fiol and Olson, 2002). 96

Blue line: eye guide.

- 3.10. Experimental and theoretical results for the triply-differential ionisation cross-sections for ● the scattered positron spectrum for H₂ for 50eV incident positrons (Arcidiacono *et al.*, 2005a); ● the ejected electron spectrum for H₂ for 50eV incident positrons (Kövér *et al.*, 2001); ● the ejected electron spectrum for D₂⁺ (Arcidiacono *et al.*, 2005a); ▽ the electron spectrum for 59.1eV positrons incident on He (Arcidiacono *et al.*, 2005a). Dashed line is the theory folded with the experimental resolutions (Fiol *et al.*, 2001). Dash-dot-dot line is the CTMC calculation (Fiol and Olson, 2002). The blue and red solid lines are guides to the eye only. 98

Chapter 4

- 4.1. Schematic overview of the experimental set-up. 102
- 4.2. a) Picture of the moderator holder and Pb plug. 104
b) Section through the source-moderator arrangement (not to scale).
- 4.3. a) A retarding field profile with $V_m=10V$ and 105
b) the corresponding e^+ beam energy distribution.
- 4.4. Top-view of the repeller into the vacuum chamber. 107
- 4.5. Schematic of a Wien Filter. 107
- 4.6. Schematic diagram of the cylindrical retarding field analyser (Ashley, 1996). 108
- 4.7. Pictures during different stages of the MCPs assembly. 109

4.8.	Top-view of the scattering region before coating with graphite.	110
4.9.	Aperture on a linear manipulator employed during the beam alignment.	110
4.10.	System employed for the water purification.	112
4.11.	Simulation of the ion trajectories of H_2O^+ through the ion extractor (Setting IV). The dimensions on the x and y axes are expressed in mm.	114
4.12.	a) TOF dependence along x, b) TOF dependence along y, c) TOF dependence along z, d) TOF Histogram for thermal H^+ relative to voltage setting IV.	116
4.13.	Probability of extracting fragments, H^+ , of a certain kinetic energy, K, with the present ion extractor and working potentials (Setting IV).	119
4.14.	Kinetic energy distribution for proton dissociation from water (Cordaro <i>et al.</i> , 1986).	119
4.15.	Probability of extracting ions of a certain kinetic energy, K.	120
4.16.	The energy dependence of the positron detection efficiency.	121

Chapter 5

5.1.	Schematic diagram illustrating the timing electronics for the direct ionisation cross-section measurements.	126
5.2.	Time-of-flight spectrum of ions produced in water due to impact of 98.3eV positrons.	128

- 5.3. Energy dependence of the e^+ beam intensity during a gas run. 130
- 5.4. Schematic illustration of the random ion extraction circuit employed for the measurement of the total ionisation cross-section of water vapour. 132
- 5.5. Timing schematic of the pulses applied to the ion extractor and Wien filter. 133
- 5.6. A schematic illustration of the continuous ion extraction circuit employed for the measurement of the total ionisation cross-section of water vapour. 134
- 5.7. Direct ionisation cross-section for e^+ - Ar collision: • Present results; • Moxom *et al.* (1996). 137
- 5.8. Total ionisation cross-section for e^+ - Ar collision: • Present results; • Laricchia *et al.* (2002). 137
- 5.9. Direct ionisation cross-section of water for e^+ impact, $\sigma_i^+(e^+)$: 138
 a) using • pulsed and • DC extraction; b) • weighted mean of the values obtained using the two methods. The solid curve is $\sigma_i^+(e^-)$ by Champion *et al.* (2002). Partial ionisation cross-sections for e^- impact (Itikawa and Mason, 2005): • $\sigma_i^+(e^-)$ inclusive of H_2O^+ and OH^+ ; • H_2O^+ ; • OH^+ ; • H^+ . The arrow indicates the ionisation threshold.
- 5.10. a) Partial ionisation cross-section for H^+ in the dissociation of water: 140
 • present results, $\sigma_D^+(e^+)$; • electron impact, $\sigma_D^+(e^-)$ (Itikawa and Mason, 2005); b) the branching ratio $H^+/(H_2O^++OH^+)$ for • electron and • positron impact. Other branching ratios in the e^- case are shown (see label).
- 5.11. • Total single ionisation cross-section for e^+ - H_2O collisions; 141

- direct ionisation cross-section for e^+ - H_2O collisions;
 direct ionisation cross-section for e^- - H_2O collisions
 (Itikawa and Mason, 2005). The arrow shows the Ps formation threshold.
- 5.12. Positronium formation cross-section for e^+ - H_2O collisions: 143
- present results; ○ $\sigma_{Ps}(E_{Ps}+2eV)$ by Sueoka *et al.* (1987);
 dash-dot pink curve is the CDW-FS theory for $\sigma_{Ps(1s+2s)}$ formation
 (Hervieux *et al.*, 2006). • $\sigma_i^+(e^+)$; • $\sigma_i'(e^+)$; direct ionisation
 cross-section for $H_2O - e^-$ collision (Itikawa and Mason, 2005).
- 5.13. Ratio between the Ps formation and total cross-section, σ_{Ps}/σ_t , 144
 versus excess energy ($E_+ - E_{th}$) • water (σ_{Ps} by Arcidiacono *et al.*,
 2005b, 2007) and σ_t by Sueoka *et al.*, 1987); • water (σ_{Ps} by
 Arcidiacono *et al.*, 2005b, 2007) and σ_t by Kimura *et al.*, 2000);
 for the noble gases see legend..
- 5.14. A schematic diagram of the electronics and data collection employed 145
 for the doubly differential cross-section.
- 5.15. Time-of-flight spectrum of charged water ions 146
 for a scattered positron energy of 37.4eV.
- 5.16. Doubly differential ionisation cross-sections at 0° for 148
 $e^+(100eV) - H_2O$ collisions resulting in the production of
 the following ions: • H_2O^+ ; • OH^+ ; • H^+ . The curves represent
 the theory (Champion, 2006). The arrows indicate the corresponding
 ionisation limit ($E_+ - E_{th}$).
- 5.17. Comparison of the doubly differential ionisation cross-section for 149
 positrons scattered at $\sim 0^\circ$ after the collision between 100eV positrons
 and • H_2O (this work) and • Argon (Kövéér *et al.*, 1993), respectively.
 The arrows are as in the previous figure.

- 5.18. The branching ratio for $\text{OH}^+/\text{H}_2\text{O}^+$: • present data. The horizontal line represents the average value of the branching ratio for electron impact. The arrow indicates the ionisation limit ($E_+ - E_{\text{th}}$). 150
- 5.19 The branching ratio for $\text{H}^+/\text{H}_2\text{O}^+$: • present data corrected and • uncorrected values for the extraction efficiency. The horizontal line and the arrow as in the previous figure. 151

Appendix I

1. a) A double element cylindrical lens; b) a triple element cylindrical lens. 156
2. The modified Soa Gun (Canter, 1986). 157
3. Schematic of the transport lens. 157
4. Schematic of the deflector. 158
5. Schematic of the exit lens. 158

Appendix IV

1. Section through the source holder designed for the experiment. 163
The dimensions are indicated in mm (not drawn to scale).

Appendix V

1. The circuit employed to measure the beam intensity as a function of time. 164
2. The beam intensity as a function of time. 164

Table	Caption	Page
Chapter 1		
1.1.	Positronium properties: ^a Vallery <i>et al.</i> (2003), ^b Adkins <i>et al.</i> (1992), Milstein and Khriplovich (1994) and Adkins (2005), ^c Al-Ramadhan and Gidley (1994); ^d Khriplovic and Yelkhovskey (1990) and Adkins <i>et al.</i> (2003).	25
1.2.	Status on experimental collision studies with positrons.	29
1.3.	Status on experimental collision studies with Ps.	59
Chapter 4		
4.1.	Voltage settings employed for the ion extractor. The units are in Volts.	115
4.2.	The maximum variation of TOF along each axis ($\Delta\text{TOF}/\text{TOF}_{\text{MAXc}}$, with $c=x, y$ or z), the mean TOF value ($\langle\text{TOF}\rangle$) and extraction efficiencies (ϵ) for H_2O^+ and H^+ . All ions have been considered at thermal energies	117

Chapter 1

Introduction

1.1 Historical Background

The existence of the positron, the antimatter counterpart of the electron, is among the conclusions of Dirac's theory, in which, in 1928, he formulated a relativistic wave equation describing the motion of free electrons in the presence of an electromagnetic field. Possible solutions of this equation correspond to negative, as well as positive, total relativistic energies and led Dirac (1930a) to propose his "hole theory". This remarkable model assumes that the vacuum consists of negative energy levels (from $-m_0c^2$ to $-\infty$), which are normally fully occupied by electrons. The Pauli exclusion principle would then prevent transitions from positive to negative energy states. Dirac's theory allows electrons in negative energy states to be excited to vacant positive levels, leaving behind resultant "holes" which, in the distribution of negative energy electrons, would behave as electrons but with a positive charge. Dirac at first considered such holes as protons until later Weil (1931) showed that these holes necessarily had to have the same mass as electrons.

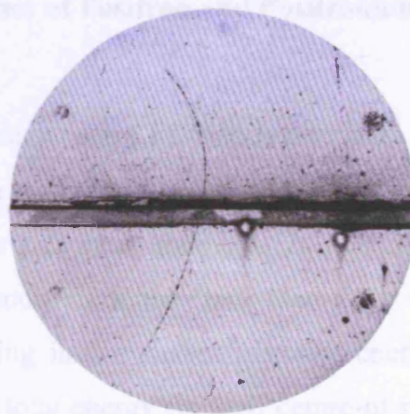


Figure 1.1. One of the cloud chamber photographs which proved the existence of the positron (Anderson, 1933).

The positron or “positively charged electron” was first observed by Anderson via the tracks left in cloud chamber photographs (Fig. 1.1) during cosmic shower studies (Anderson 1932a, b, and 1933). The confirmation of the discovery of a new particle came a year later by Blackett and Occhialini (1933), who showed that a positron has the same charge-to-mass-ratio as an electron.

Since then, positron (e^+) and positronium (Ps) (see §1.2.2) physics has advanced rapidly and played an important role in many fields. In atomic physics, following the advent of monoenergetic positron beams, extensive comparative studies of positrons with electron, proton and anti-proton scattering from various targets have yielded key information on the effect of mass, charge, electron exchange, polarisation and electron capture processes (see e.g. Knudsen and Reading, 1992, for a review). In astrophysics, the characteristic annihilation radiation of positrons has been observed from solar flares and from the centre of our galaxy (Brown and Leventhal, 1987; Teegarden *et al.*, 2005). In condensed matter, positrons have been used as a non-destructive bulk and surface probe of materials (Coleman, 2006). In medicine, positron emission tomography (PET) is now a well-established medical imaging technique (e.g. Phelps *et al.*, 1975; Czernin and Phelps, 2002; Muehllehner and Karp, 2006).

In the following sections of this chapter, fundamental properties of positrons and Ps are discussed. Finally, recent positron/Ps-atom (molecule) scattering experiments are discussed and results presented.

1.2 Fundamental Properties of Positron and Positronium Formation

1.2.1 Positrons

The positron is stable in vacuum with a lifetime greater than $2 \cdot 10^{22}$ years (Bellotti *et al.*, 1983). Its mass and spin are the same as those of an electron, e^- , but it has an opposite charge and hence opposite magnetic moment. A positron can annihilate with an electron, an event, which, according to the “hole theory”, is equivalent to an electron in a positive energy state falling into a vacant negative energy state. The result is the emission of photons, whose total energy (in their centre-of-mass frame), is equal to the total rest mass energy of the annihilating positron-electron pair, i.e. 1.022MeV. The number of photons emitted is governed by the charge parity, P_c , of the initial system, which must be conserved in the annihilation process. Since the charge parity of a photon is negative, a system of n photons has $P_c = (-1)^n$. Yang (1950) has shown that for

the positron-electron system P_c is given by $P_c = (-1)^{L+S}$, where L is the total orbital angular momentum and S the total spin of the positron-electron system. An odd or even number of photons is therefore released as a result of annihilation, depending on the total angular momentum of the positron-electron pair.

In figure 1.2, the lowest-order Feynman diagrams for positron-electron annihilation into one, two, three and four gamma rays are shown. The probability of any given number of emitted photons is directly proportional to α^m , where α is the fine structure constant ($=e^2/2\epsilon_0hc \sim 1/137$, where e , ϵ_0 , h and c are the elementary charge, the vacuum permittivity, the Planck constant and the speed of light respectively) and m is the number of vertices in the relevant Feynman diagram, corresponding to the number of photon emission/absorption events.

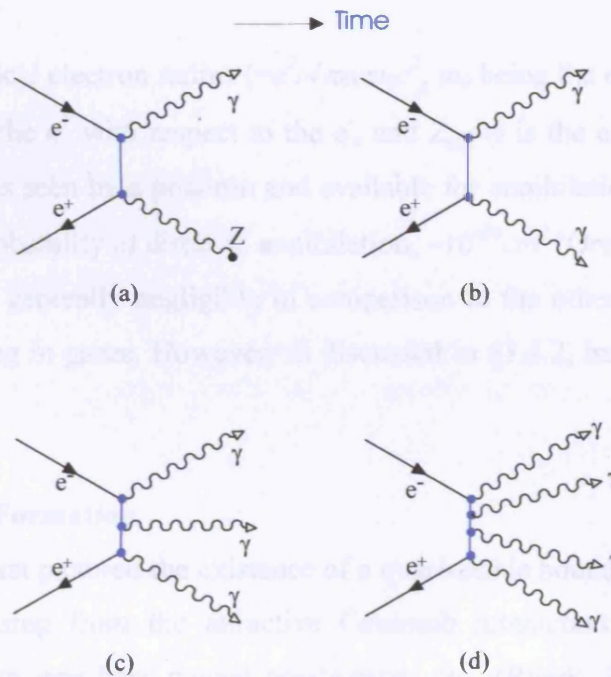


Figure 1.2. Feynman diagrams of (a) one, (b) two, (c) three and (d) four photon decay modes.

In the case of only two vertices, two-photon annihilation (if allowed) is the most probable decay mode. Although both one and three photon decay modes have $m=3$, the former process requires the presence of a third body (for energy and momentum conservation) suppressing its probability with respect to the latter process, by a factor of the order of α^3 . All these decay modes have now been observed by a) Palathingal *et*

al. (1991), b) Klemperer (1934), c) Chang *et al.* (1982, 1985) and d) Adachi *et al.* (1990).

The non-relativistic limit of the cross-section for two-photon annihilation of a positron with a free electron derived by Dirac (1930b) is:

$$\sigma_{2\gamma}^e(v) = \frac{\pi r_0^2 c}{v}. \quad (1.1)$$

This has been adapted for annihilation from an atom or molecule as follows:

$$\sigma_{2\gamma}^A(v) = \frac{\pi r_0^2 c Z_{eff}(v)}{v}, \quad (1.2)$$

where r_0 is the classical electron radius ($=e^2/4\pi\epsilon_0 m_0 c^2$, m_0 being the electron rest mass), v is the velocity of the e^+ with respect to the e^- , and $Z_{eff}(v)$ is the effective number of electrons per atom as seen by a positron and available for annihilation (e.g. Van Reeth *et al.*, 2005). The probability of direct e^+ annihilation, $\sim 10^{-26} \text{cm}^2$ (Ore and Powell, 1949; Bransden, 1969), is generally negligible in comparison to the other reaction channels found in e^+ scattering in gases. However, as discussed in §1.4.2, important exceptions exist.

1.2.2 Positronium Formation

Mohorovic (1934) first pictured the existence of a quasi-stable bound state of a positron and an electron arising from the attractive Coulomb interaction between the two particles. This system was later named positronium, Ps (Ruark, 1945) and the first experimental verification of its existence occurred during measurements of e^+ lifetimes in gases by Deutsch (1951). Ps is the lightest known atomic bound state, structurally equivalent to H but with half the reduced mass, twice the Bohr radius (1.05Å) and half the binding energy (6.8eV). Depending on the relative spin orientation of its constituent particles, Ps is formed in one of two ground states. These states and some of their characteristics are summarised in table 1.1. As ortho-Ps is a triplet state, its formation is statistically three times more likely than that of the singlet state.

	<i>Ortho - Ps</i>	<i>Para - Ps</i>
Ground state, spectroscopic terms Sub-states	1^3S_1 $m=0, \pm 1$	1^1S_0 $m=0$
Ground state decay rates (μs^{-1})	Exp: 7.0404(10)(8) (140ppm) ^a Theory: 7.0420 ^b	Exp: 7990.9 \pm 1.7 ^c Theory: 7989.5 ^d
Annihilation mode and details	3 coplanar γ -rays Plus 2 γ "pick off" mode in matter	2 γ -rays Exactly collinear for p-Ps at rest
Mean vacuum lifetime	142ns	0.125ns

Table 1.1. Positronium properties: ^a Vallery et al. (2003); ^b Adkins et al. (1992), Milstein and Khriplovich (1994) and Adkins (2005); ^c Al-Ramadhan and Gidley (1994); ^d Khriplovich and Yelkhovskiy (1990) and Adkins et al. (2003).

Figure 1.3 shows the energy levels for Ps as calculated by Fulton and Martin (1954).

1.3 Development of Positron Sources

For the first part of this project we started from the nuclear decay of radioactive isotopes from pure production to particle accelerators. In both cases, the positrons obtained are distinguished by a broad spectrum of energies. Early experiments consisted of measuring a positron-emitting isotope in solids, liquids and gases and detecting the photons produced through positronium annihilation. Variable low-energy positron beams (kilo-eV) were developed by compressing the entire β^+ energy distribution to a few eV, at the expense of intensity, using a so-called narrow peak filter (such as ^90Sr called Ni-modulator) (e.g. Carter et al., 1972). For instance, Fig. 1.4 compares the typical energy distributions of positrons emitted from a ^{60}Co source with that obtained in conjunction with a W-modulator.

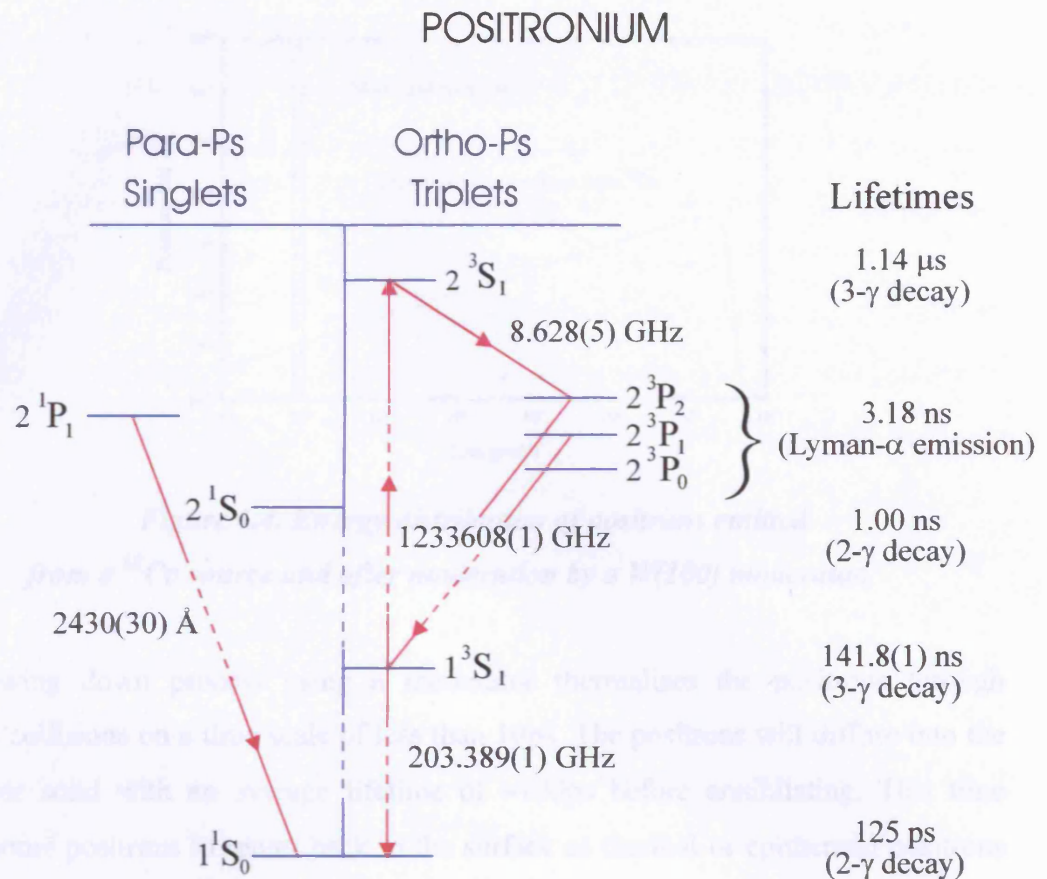


Figure 1.3. Energy level diagram for Ps.

1.3 Development of Positron Beams

For research purposes, positrons are obtained from the nuclear decay of radioactive isotopes or from pair production in particle accelerators. In both cases, the positrons obtained are characterised by a broad spectrum of energies. Early experiments consisted of immersing a positron-emitting isotope in solids, liquids and gases and detecting the photons produced through positron annihilation. Variable low-energy positron beams ($\leq 1\text{keV}$) were developed by compressing the entire β^+ energy distribution to a few eV, at the expense of intensity, using a so-called positron moderator (such as W or solid Ne-moderator) (e.g. Canter *et al.*, 1972). For instance, figure 1.4 compares the typical energy distribution of positrons emitted from a ^{58}Co source with that obtained in conjunction with a W moderator.

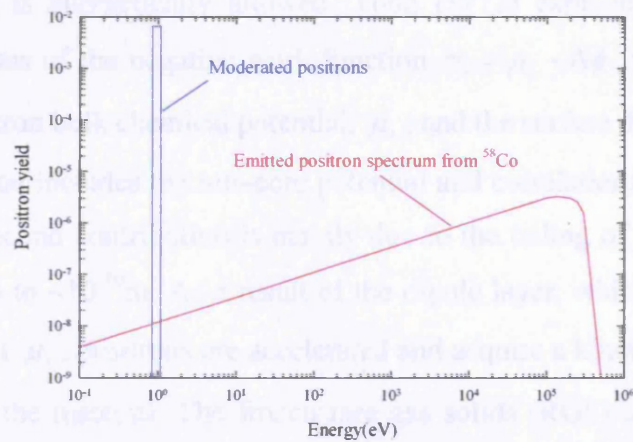


Figure 1.4. Energy distribution of positrons emitted from a ^{58}Co source and after moderation by a $\text{W}(100)$ moderator.

The slowing down process using a moderator thermalises the positrons through inelastic collisions on a time scale of less than 10ps. The positrons will diffuse into the moderator solid with an average lifetime of $\sim 100\text{ps}$ before annihilating. This time allows some positrons to return back to the surface as thermal or epithermal positrons (Madansky and Rasetti, 1950). In figure 1.5, the possible interactions of positrons at a metal surface are shown (Mills, 1983a).

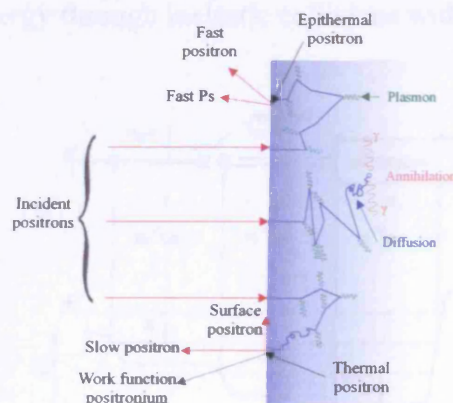


Figure 1.5. Simplified illustration of the interaction of positrons at a metal surface (from Mills, 1983a).

Positron moderators may be distinguished between negative work function materials ($\phi_+ < 0$) and wide band-gap materials. The first are clean crystalline or polycrystalline metals, such as W, in which the emission of a thermal positron from the

solid into vacuum is energetically allowed. Tong (1972) explained the reemission phenomenon in terms of the negative work function $\phi_+ = \mu_+ - \Delta\phi$, which arises from the sum of the positron bulk chemical potential, μ_+ , and the surface dipole layer, $-\Delta\phi$. The first contribution includes the ion–core potential and correlations with the electron gas, whereas the second contribution is mainly due to the tailing of the e^- distribution into the vacuum up to $\sim 10^{-10}$ m. As a result of the dipole layer, which counterbalances the binding effect of μ_+ , positrons are accelerated and acquire a kinetic energy equal to $e\phi_+$ as they leave the material. The frozen rare gas solids (RGS) are wide band-gap materials and are very effective β^+ particle moderators despite having a positive ϕ_+ (Gullikson and Mills, 1986). Here, the only mechanism for positron energy loss below the large band gap is via phonon excitation, which removes only a few meV per collision. Hence, epithermal positrons (~ 5 – 10 eV) travel at least an order of magnitude further in the RGS crystal than thermal ones in negative work function materials. This process leads to a considerable number of epithermal positrons reaching the moderator surface from where they may escape into the vacuum, over the smaller (positive) barrier, with kinetic energies extending up to several eV.

Recently, cold-trap–based positron beams have been developed (Gilbert *et al.*, 1997). Figure 1.6 shows positrons entering a Penning trap in the presence of a magnetic field. Positrons losing energy through inelastic collisions with a buffer gas (N_2) fall

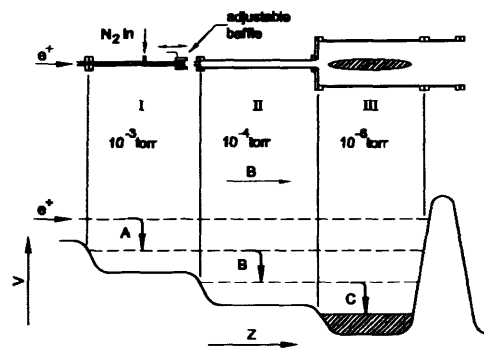


Figure 1.6. Top: buffer-gas trap structure; bottom: typical pressure and voltage profile as a function of distance z . (Figure taken from Sullivan *et al.*, 2002).

deeper into the stepped potential reaching room temperature. At the same time, this process allows new positrons to be accumulated. The slow rise and drop of the confining potential in stage III determines the release of positrons from the accumulator

in pulses of few ms containing around $2 \cdot 10^4$ positrons per pulse. Released positrons have a well-defined energy and energy spread ($\Delta E \leq 25 \text{ meV}$). The new device in conjunction with a magnetic scattering beamline has enabled scattering experiments at low energies with significantly improved state selectivity e.g. for excitation experiments (Sullivan *et al.*, 2001a, b).

1.4 Positron Interaction with Atoms and Molecules

Interaction	Experimental Status
Total Scattering Cross-Section $e^+ + A \rightarrow \text{all}$	σ_t for many atomic and molecular targets, including H, He, alkali and Mg
Elastic Scattering $e^+ + A \rightarrow e^+ + A$	Some σ_{el} and $d\sigma_{el}/d\Omega$
Electron Capture $e^+ + A \rightarrow Ps + (z-1)e^- + A^{z+}$	σ_{Ps} between 1 and 100eV, including alkali, Mg; some $d\sigma_{Ps}/d\Omega$
Target Excitation $e^+ + A \rightarrow e^+ + A^*$	First state-resolved σ_{ex} for electronic and vibrational excitations
Direct Ionisation $e^+ + A \rightarrow e^+ + n e^- + A^{n+}$	σ_i^{z+} from 1 to 1000eV; including H, some $d\sigma_i^+/d\Omega$, $d^2\sigma_i^+/d\Omega dE$ and $d^3\sigma_i^+/d\Omega_+ d\Omega_- dE$
Annihilation $e^+ + A \rightarrow 2\gamma + A^+$	Energy resolved measurements for Ar, Xe and a variety of molecular targets
Positronic Bound States $e^+ + A \rightarrow (PsC) + D^+$ $e^+ + M \rightarrow (e^+M)^* \rightarrow M^+ + 2\gamma$	Psh observed Evidence from annihilation experiment

Table 1.2. Status on experimental collision studies with positrons.

Work on positron interactions with atoms and molecules is reviewed in the following subsections. Particular attention is given to topics relevant to the subject of this thesis and to recent developments in the field of positron physics. More extensive reviews may be found in Laricchia and Charlton (1999), Charlton and Humberston (2001), Laricchia (2002) and Laricchia *et al.* (2003) and, more recently, Surko *et al.* (2005).

Table 1.2 summarises the current status on experimental studies for positron collisions with atoms and molecules. When the experiments do not distinguish between the processes of capture and direct ionisation, an important observable, not listed in Tab.1.2, is the total (single) ionisation cross-section $\sigma_i^+ = \sigma_{ps} + \sigma_i^+$ (Paludan *et al.*, 1997).

1.4.1 Total Scattering Cross-Sections

The experimental method to measure σ_i relies on determining the transmitted intensity, I , of a beam of incident intensity, I_0 , travelling a distance, l , through a scattering cell filled with a target of number density, n , according to the Beer-Lambert law expressed as:

$$\sigma_i = \frac{1}{nl} \ln\left(\frac{I_0}{I}\right). \quad (1.3)$$

Initially, the noble gases were investigated since these are in atomic form at room temperature. In particular, the total cross-section for helium was the first to be measured for positron impact (Costello *et al.*, 1972).

In figure 1.7, the total scattering cross-section by positron- and electron- impact on the noble gases (Stein and Kauppila, 1982) are shown. A common tendency for each noble gas target at low energies is that $\sigma_i(e^-)$ exceeds $\sigma_i(e^+)$, as both the static and polarisation interactions are attractive and sum up for e^- , whilst they are repulsive and attractive, respectively, and partially cancel each other for e^+ . However, as polarisation and exchange effects become negligible at high energies, the static interaction becomes increasingly dominant for both projectiles and, consequently, their cross-sections merge with the values dictated by the first Born approximation.

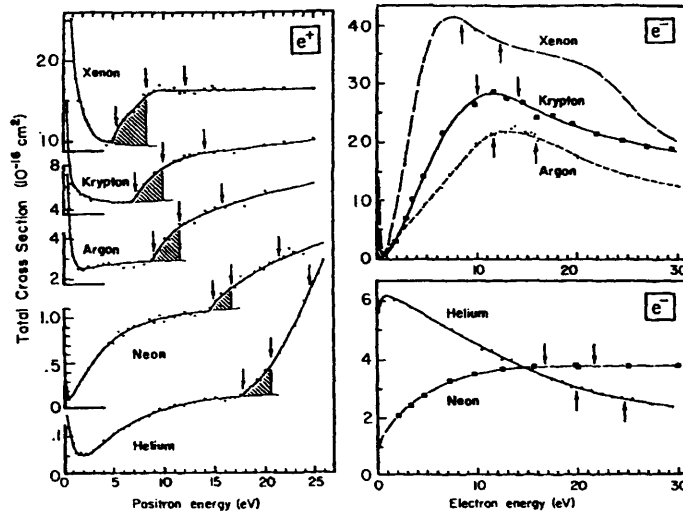


Figure 1.7. Total cross-section for e^\pm - noble gases scattering (from Stein and Kauppila, 1982). The arrows indicate thresholds for Ps formation, excitation and ionisation in order of increasing energy.

As can be discerned in figure 1.7, the significant role of Ps formation in low energy e^+ scattering is demonstrated by a pronounced increase in $\sigma_t(e^+)$ after the opening of this channel. The other phenomenon that takes place only for e^+ scattering is free annihilation (in general appreciable only for energies much less than 1eV). Although various inelastic channels also open for e^- impact, $\sigma_t(e^-)$ generally varies smoothly with energy for the noble gases. Narrow deep minima, called Ramsauer-Townsend minima, appear in $\sigma_t(e^-)$ for Ar, Kr and Xe at energies below 1eV (e.g. Ramsauer, 1921, 1923; Townsend and Bailey, 1922; Ramsauer and Kollath, 1929). These arise from a quantum mechanical effect linked to polarisation occurring whenever the s-wave function of the incident e^- experiences a phase shift equal to π or a multiple of π . In the case of e^+ scattering, minima are evident in $\sigma_t(e^+)$ for He and Ne at around 2eV and 0.6eV, respectively. These Ramsauer-Townsend minima are due to an s-wave shift going through zero value at low energies. However, for the heavier inert atoms, the appearance of minima is calculated to occur at higher energies, where significant partial wave cross-sections mask them (Raith, 1998).

Total cross-section measurements have included a variety of atomic and molecular targets. For example, $\sigma_t(e^+)$ was measured by Zhou *et al.* (1997) for H and a good agreement has been found with theory at all energies except in the lowest range. For many polyatomic molecules, the distinctive increase of the total cross-section curve

does not necessarily appear after the Ps threshold because this feature is weakened or washed out by the presence of additional reactions. In molecules such as H₂, CO₂ and CH₄, $\sigma_T(e^+)$ displays, generally, a shape similar to that observed for the noble gases (for a review see Kaupilla and Stein, 1990). Figure 1.8 displays the total cross-section for e⁺ scattering on H₂. The Trento group have been able to investigate the sub-eV energy range thanks to the good angular resolution of their apparatus (Karwasz *et al.*, 2006). They observed an increase towards zero energy in the $\sigma_T(e^+)$ for H₂, N₂ and Ar. As the impact energy increases, flat regions have also been seen in these targets from a few eV up to their respective Ps-formation thresholds.

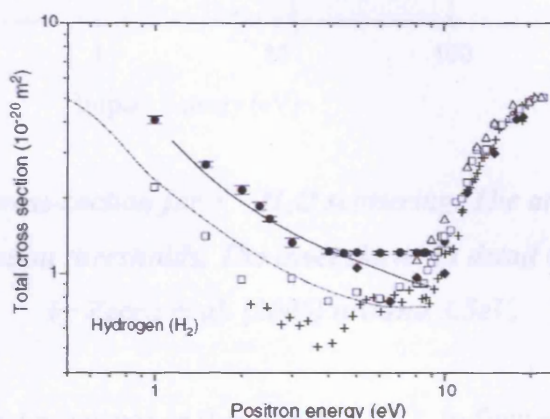


Figure 1.8. Total cross-sections for positron scattering on molecular hydrogen.

• Karwasz *et al.* (2006); □ Hoffman *et al.* (1982); + Charlton *et al.* (1983a);
 △ Deuring *et al.* (1983); ◆ Zhou *et al.* (1994); --- Varella *et al.* (2002);
 — Gianturco *et al.* (1996).

In the case of H₂, the best agreement of the data of Karwasz *et al.* (2006) is with the theory by Gianturco *et al.* (1996), whereas the calculations by Varella *et al.* (2002) have the same trend as the earlier data of Hoffman *et al.* (1982).

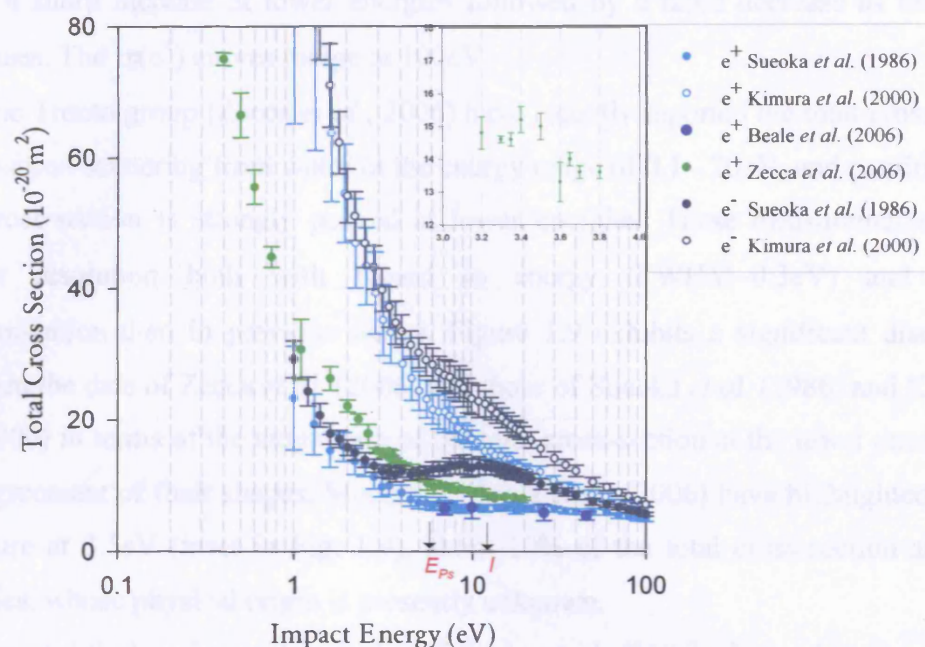


Figure 1.9. Total cross-section for e^{\pm} - H_2O scattering. The arrows indicate the P_s formation and ionisation thresholds. The inset shows in detail the structure observed by Zecca *et al.* (2006) around 3.5eV.

A molecule of great relevance in this thesis is H_2O . In figure 1.9, the data for $\sigma_t(e^+)$ of water measured in the energy range 1-400eV by Sueoka *et al.* (1986) is shown. They employed a retarding potential method to discriminate against particles with large energy loss due to inelastic scattering and to decrease forward-scattered contributions. Comparing $\sigma_t(e^{\pm})$ curves, they noted that these are characterised by a similar energy dependence and intensity: nearly merging at the highest and also the lowest energies. This similarity could be due to the dominance of a long-range dipole interaction in these energy ranges. Furthermore, the total cross-section for electrons is larger at the intermediate energies. Overall there is a lack of structure for both projectiles: no appreciable change at the P_s formation threshold for positrons, no shape resonances for electrons and in both cases no increase of σ_t due to the opening of ionisation channel. In the case of strongly polar molecules like water (dipole moment=0.72965a.u), the differential elastic cross-section (DCS) increases rapidly with decreasing scattering angles, so that forward-scattering corrections are very significant (e.g. Linder, 1977). Hence, Kimura *et al.* (2000) corrected the positron data of Sueoka *et al.* (1986) using the DCS for electron impact. As can be observed in figure 1.9, the corrected results

show a sharp increase at lower energies followed by a rapid decrease as the energy increases. The $\sigma_t(e^+)$ curves merge at 100eV.

The Trento group (Zecca *et al.*, 2006) have recently reported the total cross-section for positron scattering from water in the energy range of 0.1 - 20eV, and confirmed that the cross-section is strongly peaked at lower energies. These measurements have a higher resolution both with regard to energy (FWHM~0.3eV) and angular discrimination than in previous works. Figure 1.9 exhibits a significant discrepancy between the data of Zecca *et al.* (2006) and those of Sueoka *et al.* (1986) and Kimura *et al.* (2000) in terms of the magnitude of the total cross-section at the lower energy but a fair agreement of their shapes. Moreover, Zecca *et al.* (2006) have highlighted a small structure at 3.5eV (inset in Fig. 1.9), about 10% of the total cross-section at nearby energies, whose physical origin is presently unknown.

Figure 1.9 also shows the results of Beale *et al.* (2006) obtained in the range of impact energies 7 - 417eV. The findings are presented raw, that is, not corrected for the forward scattering effect. A retarding potential method has also been applied in this work to discriminate against forward-scattered particles. The $\sigma_t(e^+)$ agrees with the data of Sueoka *et al.* (1986) prior to the correction of Kimura *et al.* (2000).

The availability of differential cross-sections for elastic scattering of positrons from water would aid the resolution of these discrepancies.

1.4.2 Annihilation

Prior to the advent of trap-based magnetic beams, annihilation studies had been performed using lifetime techniques over the temperature range of 77-500K (e.g. a review by Heyland *et al.*, 1982; Charlton, 1990).

Iwata *et al.* (1995) measured the annihilation rate (see 1.2.1) of positrons in various substances using trapped clouds of room-temperature positrons (e.g. Surko *et al.*, 2005). For water, they found $Z_{eff}/Z=32$ (where Z is the atomic number), which is a large value compared to that found for most inorganic molecules. Gianturco *et al.* (2001) explored the Z_{eff} values for this target using an *ab initio* quantum dynamics treatment, which does not depend on empirical parameters. The calculated value was smaller by a factor of two than the experimental result (Iwata *et al.*, 1995). In figure 1.10, the experimental result multiplied by 0.5 is shown alongside the theoretical results of Gianturco *et al.* (2001).

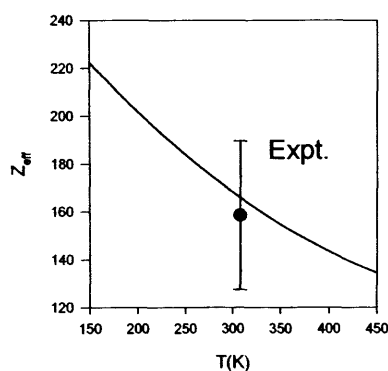


Figure 1.10. The variation of Z_{eff} with temperature for H_2O : • the experimental value of Iwata *et al.* (2000) multiplied by 0.5; line, the theory of Gianturco *et al.* (2001).

Much attention has been devoted to interpreting the anomalously high values for the room temperature annihilation rate ($Z_{eff} > 10^3$) from large organic molecules (Iwata *et al.*, 1995). Several mechanisms (e.g. virtual processes, bound states) have been proposed to explain these large Z_{eff} values, also in correlation to the appearance of structures in the energy dependence of Z_{eff} . These structures have now been observed theoretically in the proximity of various inelastic thresholds (see Van Reeth *et al.*, 2005 for a review). A semi-empirical model developed by Laricchia and Wilkin (1997) predicted a pronounced enhancement of the annihilation probability in the vicinity of inelastic collision energy thresholds due to the increasing significance of virtual processes, which leave the e^+ quasi-stationary near the target and thereby in a region of higher than average e^- density. Structures near molecular vibrational excitation thresholds were first observed by Gilbert *et al.* (2002) in energy-resolved measurements of the annihilation rate with a tunable trap-based-positron beam. Figure 1.11 shows that the positron annihilation rate, Z_{eff} , for butane, propane and ethane as a function of positron energy has a large annihilation signal somewhat below the threshold of the molecular vibrational modes. This provides support that the mechanism responsible for large Z_{eff} values is the formation of long-lived vibrational resonances of the positron-molecule complex as proposed by Gribakin (2000), the downshift of the resonance peak that occurs for butane and propane being the most direct evidence to date that the positron binds to molecules (e.g. Gribakin and Gill, 2004).

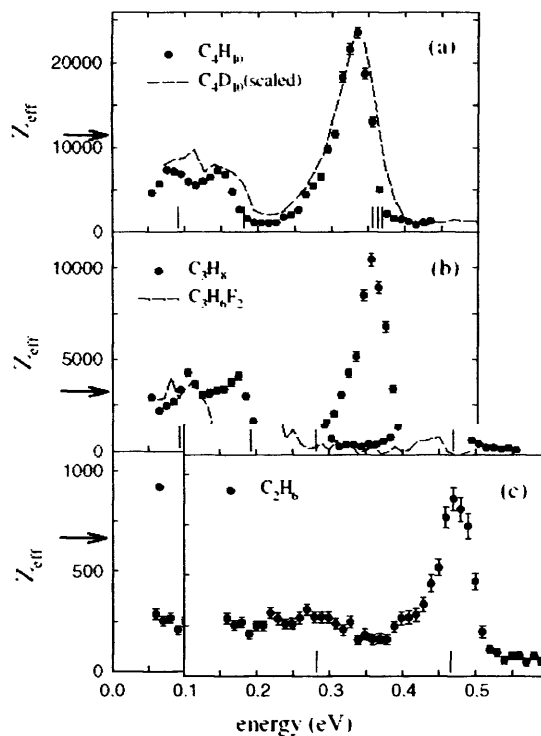


Figure 1.11. Positron annihilation rate, Z_{eff} for (a) butane, (b) propane and (c) ethane, as a function of positron energy (from Gilbert *et al.*, 2002). The vibrational modes are indicated by vertical lines along the abscissa.

Since then, suggestion of a second bound state through vibrational Feshback resonances of positrons in large alkane molecules ($C_{12}H_{26}$ and $C_{14}H_{30}$) was found by Barnes *et al.* (2006). This was inferred by the appearance of a second annihilation peak in the vicinity of the C-H stretch mode.

Recently, evidence of enhanced annihilation near an electronic excitation has been observed in N_2 . Kauppila *et al.* (2004) have developed a spectroscopic method for studying Ps in gases and its interaction with surfaces. This method consists in determining the ratio, R , of signals of 2γ rays in coincidence emerging from 1) 3γ annihilation of ortho-Ps and 2) 2γ annihilation from para-Ps decay and destruction of ortho-Ps at a scattering surface. In the most recent measurements of R for N_2 by Kauppila *et al.* (2006), a drop just before the opening of Ps formation channel can be observed in figure 1.12. This drop was not observed for other targets such as Ar, CO and N_2O also reported in figure 1.12. They thus suggested that it might be related to the proximity of the electronic excitation of the $a^1\Pi$ and $a^1\Sigma$ states of N_2 (starting near 8.5eV).

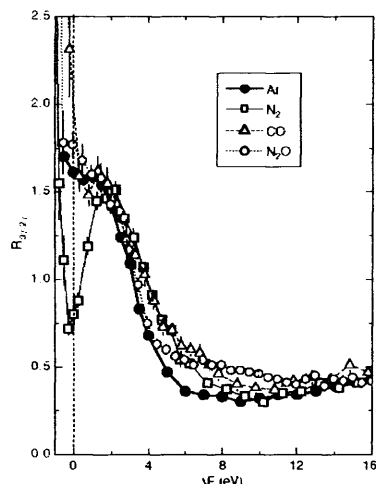


Figure. 1.12. Ratios of $S(3\gamma)$ to $S(2\gamma)$ signals (with statistical uncertainties) versus ΔE (positron energy minus the energy of the initial Ps formation threshold) for Ar, N_2 , CO and N_2O .

1.4.3 Positron Bound States

As well as Ps, e^+ may be bound as a negative ion, Ps^- (Mills *et al.* 1981, 1983b) or, in the presence of many e^+ -many e^- interaction forms Ps_2 (Cassidy *et al.*, 2005). Recently, Fleischer *et al.* (2006) determined the decay rate of Ps^- ($\Gamma=2.089(15) \text{ ns}^{-1}$) with higher accuracy than that obtained by Mills *et al.* (1983b).

Additionally, much theoretical and experimental effort has been devoted to studying new bound states, which originate from the attachment of Ps or e^+ to an atom/molecule. Theoretically more than 50 positronic bound states have been shown to be chemically stable (Mitroy *et al.*, 2002) including e^+Li , e^+Be , e^+Na , e^+Mg , e^+Ca , e^+Ag , e^+Cd , Ps^- , Ps_2 , PsH , PsF , $PsCl$, $PsBr$ and $PsOH$. Within the Born-Oppenheimer approximation, an infinite number of stable bound states are created around polar molecules with large dipole moments (Garrett, 1980), such as H_2O . The stability of the complex e^+H_2O has been investigated by using a diffusion Monte Carlo technique (Bressanini *et al.*, 1998). This work suggested that the complex might not be stable against dissociation. However, the estimated ionisation potential for the complex, higher than 0.25hartree, excluded H_2O^+ and Ps as the main dissociative channel. Experimentally, only PsH (Schrader *et al.*, 1992) has been reported.

1.4.4 Elastic Scattering

When annihilation is an unlikely channel, σ_t is equivalent to σ_{el} below the first inelastic threshold. For the noble gases, the occurrence of the so-called Wigner cusp for σ_{el} at the Ps formation threshold, E_{Ps} , has been investigated in various experiments. The Wigner cusp is an anomaly occurring in the immediate vicinity of the threshold energy of an inelastic channel. The appearance and magnitude of this feature is explained in terms of the strong competition between the two-reaction channels and flux conservation. Campeanu *et al.* (1987) found a pronounced cusp feature in the σ_{el} of He from a careful partitioning of available experimental total cross-section data.

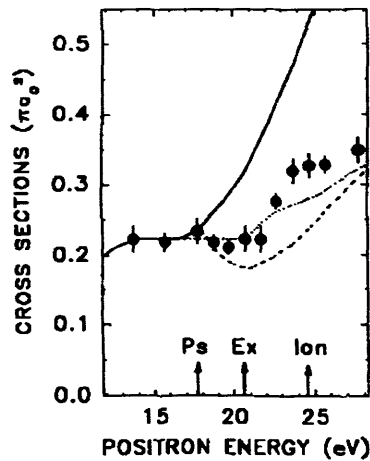


Figure 1.13. Positron-He scattering: • $\sigma_{el} + \sigma_{ex} + \sigma_i$ (Coleman *et al.*, 1992); full curve, σ_t (Stein *et al.*, 1978); broken curve, $\sigma_{el} + \sigma_{ex}$ deduced by Campeanu *et al.* (1987); dotted curve, $0.224|a_0|^2 + \sigma_{ex} + \sigma_i$ (Varracchio, 1990; Knudsen *et al.*, 1990).

(Figure taken from Coleman *et al.*, 1992).

However, later experiments did not support the existence of this structure. Among these later experiments, Coleman *et al.* (1992) determined σ_{el} indirectly for the same target by taking the difference of σ_t and σ_{Ps} near the Ps threshold (fig. 1.13). Analogously, Moxom *et al.* (1993) performed detailed measurements of the total ionisation cross-sections for He, Ar and H₂, which were subtracted from the available σ_t to obtain the sum of the elastic and excitation cross-sections, $\sigma_{el} + \sigma_{ex}$. The failure to observe an increase in $\sigma_{el} + \sigma_{ex}$ at the threshold means that there is a minor contribution to σ_{Ps} from the s-wave function near E_{Ps} . This is in agreement with the near-threshold measurements of Moxom *et al.* (1994) and the Kohn variational calculation of Van

Reeth and Humberston (1997) in the Ore gap (i.e. between the Ps and ionisation threshold). Figure 1.14 shows the results of Moxom *et al.* (1994), which were obtained using R-matrix and threshold theories (Moxom *et al.*, 1994 and references therein). These results suggest that for He the coupling between the incident elastic and nonelastic channels is the weakest and no cusp appears, whereas, as Z increases, the corresponding increase of the positron-atom interaction should result in a significant feature, most prominent in the case of Xe.

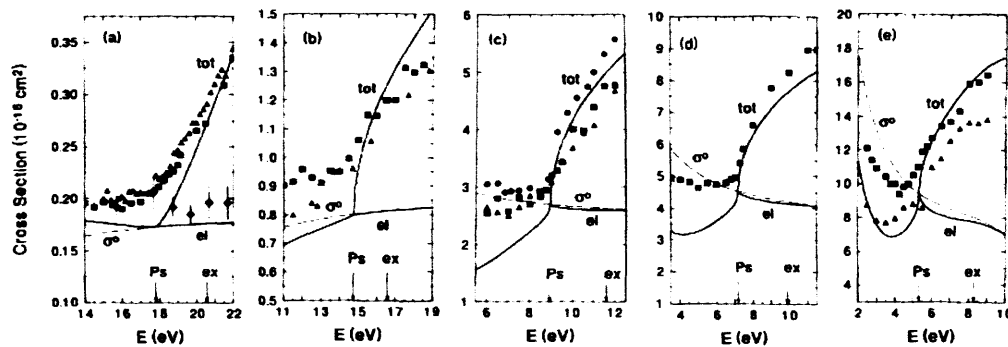


Figure 1.14. Total (*tot*) and elastic (*el*) scattering cross-sections for e^+ + (noble gas atom) collisions near the Ps-formation threshold (P_s) as a function of the positron energy E . The broken curves represent σ^0 , which is the part of the total (or elastic) cross-section at the threshold that is uncoupled from the non elastic channel. The solid curves give the prediction for σ_{tot} and σ_{el} . Below threshold, $\sigma_{tot} = \sigma_{el}$. (Figure taken from Moxom *et al.*, 1994).

A more sensitive and direct method of studying elastic scattering is through measurement of the differential cross-section (DCS). Diffraction like structures are identified below the E_{P_s} in the relative DCS for Ne, Ar, Kr and Xe, which disappear as the incident positron energy increases (Smith *et al.*, 1990; Dou *et al.*, 1992; Kauppila *et al.*, 1996), possibly related to the absorption effect of the Ps formation channel. Recently, several absolute DCS measurements have been performed by the San Diego group using the trap-based beam (see §1.3). Among them, the results of the DCS for positron-xenon elastic scattering at 2eV (Marler *et al.*, 2006) are shown in figure 1.15. An overall agreement between the data and theoretical predictions can be observed. Since the backscattered particles are retransmitted to the detector, the measured DCS

are folded around 90° by summing θ and $180^\circ - \theta$ angles. These results have similar magnitude to the electron data at $\sim 65^\circ$ (Register *et al.*, 1986).

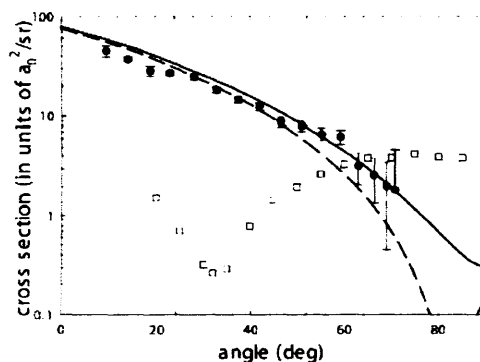


Figure 1.15. Elastic differential cross-section for e^+ - Xe scattering at an incident energy of 2eV: (\bullet) Marler *et al.* (2006); (- -) the theoretical prediction from the calculations carried out within the framework of the Dirac equation with no fitted parameters (see Marler *et al.*, 2006); (-) the theoretical prediction folded about 90° ; (\square) electron data (Register *et al.*, 1986). (Figure taken from Marler *et al.*, 2006).

1.4.5 Molecular Vibrational and Electronic Excitation

The first state-resolved measurements of the integral cross-sections for molecular vibrational and electronic excitations were obtained by Sullivan *et al.* (2001a, 2001b, 2002).

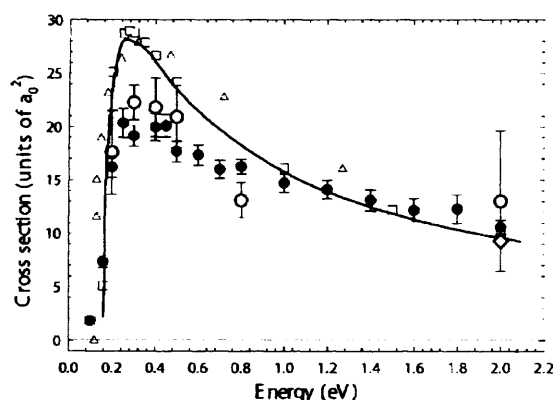


Figure 1.16. Integral electron/positron-impact vibrational excitation of the ν_3 vibrational mode of CF_4 : (\bullet) the positron-impact results and (\circ) the electron-impact results (from Marler and Surko, 2005a)

Marler and Surko (2005a) carried out absolute measurements for the excitation of the ν_3 vibrational mode in CF_4 by positron impact. Their results, shown in figure 1.16, are the largest experimental values for vibrational excitations. The near-threshold cross-section is similar to the corresponding near-threshold cross-section by electron impact (Hayashi, 1987). There is overall a good agreement between the electron impact data of Marler and Surko (2005a) and the predictions by the Born dipole model (Mann and Linder, 1992).

Figure 1.17 shows the sum of the cross-sections for $4s(J=1)$ excited states of Ar: $3p^5(^2P_{3/2})4s$ and $3p^5(^2P_{1/2})4s$ (Sullivan *et al.*, 2001b). A comparison is made with the LS-coupling calculation of Parcell *et al.* (2000), showing similar magnitude only at around 17eV.

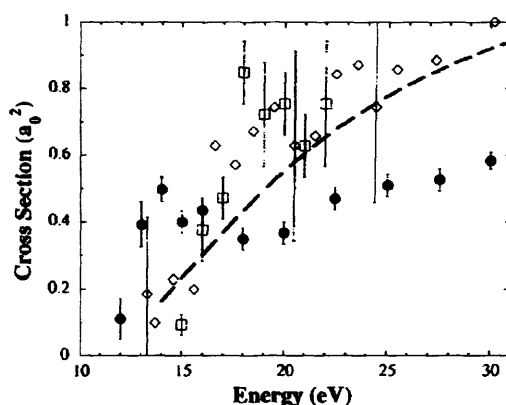


Figure 1.17. Absolute integral cross-sections for the excitation of the $3p^5(^2P_{3/2})4s$ and $3p^5(^2P_{1/2})4s$ atomic states of Ar from the threshold to 30eV. Cross-sections by positron impact: (●) Sullivan *et al.* (2001b). (□) Coleman *et al.* (1982). (◇) Mori and Sueoka (1994) scaled by 0.6. (—) Parcell *et al.* (2000). (Figure taken from Sullivan *et al.*, 2001b).

Moreover, a structure is evident in the experimental data (Sullivan *et al.*, 2001b) near the excitation thresholds. This structure was not observed in earlier works (Coleman *et al.*, 1982; Mori and Sueoka, 1994) or the theory (Parcell *et al.*, 2000). The magnitude of the cross-section predicted by Parcell *et al.* (2000) is similar to that of Sullivan *et al.* (2001b) at around 17eV, but it is around 50% higher at 30eV.

On comparing the electronic excitation of the $a^1\Pi$ state of N_2 with the $A^1\Pi$ state of its isoelectronic partner, CO, Marler and Surko (2005b) observed in both distinctive structures just above their excitation thresholds (Fig. 1.18). This feature, in the case of

CO, are not reproduced by theory and do not appear in measurements for electron impact. The origin of these structures is presently unclear.

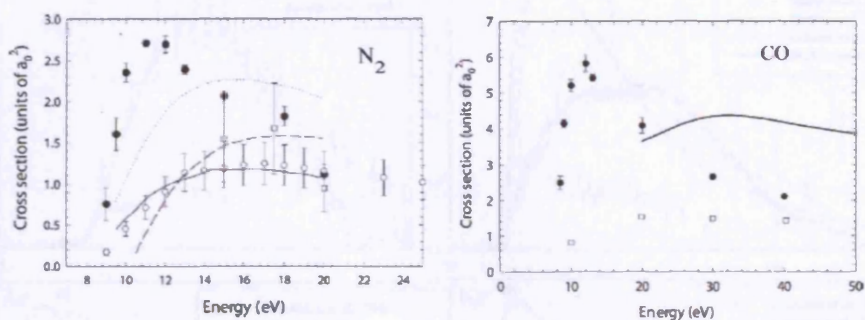


Figure 1.18. On the left, integral cross sections in N_2 for the excitation of the $a^1\Pi$ state by (\bullet) positrons (Marler and Surko, 2005b) and (\circ , \square) electrons (Campbell *et al.*, 2001; Mason and Newell, 1987). The theoretical predictions for positron impact are from Chaudhuri *et al.* (2004). On the right, integral cross sections for the excitation of the $A^1\Pi$ state in CO by (\bullet) positron and (\circ) electron impact (Ajello, 1971). Also shown is the theoretical calculation of the $A^1\Pi$ state in CO by electrons (Lee *et al.*, 1996).

1.4.6 Ps Formation Cross-Sections

Prior to direct measurements, Ps formation cross-sections, σ_{Ps} , were estimated from lifetime spectra of e^+ in gases (Charlton *et al.*, 1979) or by subtracting extrapolated values of σ_{el} from σ_t , for energies below E_{ex} (Griffith and Heyland, 1978). Ps formation has now been experimentally studied by observing a variety of signatures:

a) The simultaneous emission of 3γ -rays (ortho-Ps) in coincidence (e.g. Charlton *et al.*, 1983b). This gives an unambiguous signal of Ps formation, but the method requires no loss of ortho-Ps, e.g. due to quenching on the gas cell or variation in the detection efficiency, as the ortho-Ps moves out of the detection region. These problems seem to have affected the measurements performed by Charlton *et al.* (1983b), except at the lowest energies (Charlton and Laricchia, 1990). Some molecules were studied with this method by Griffith (1983).

b) Loss of the positron in the final state (all Ps) (Fornari *et al.*, 1983; Diana *et al.*, 1986; Overton *et al.*, 1993; Marler *et al.*, 2005). By assuming annihilation to be a negligible process, this method relies on the collection of all the scattered particles and ascribes the loss entirely to Ps formation.

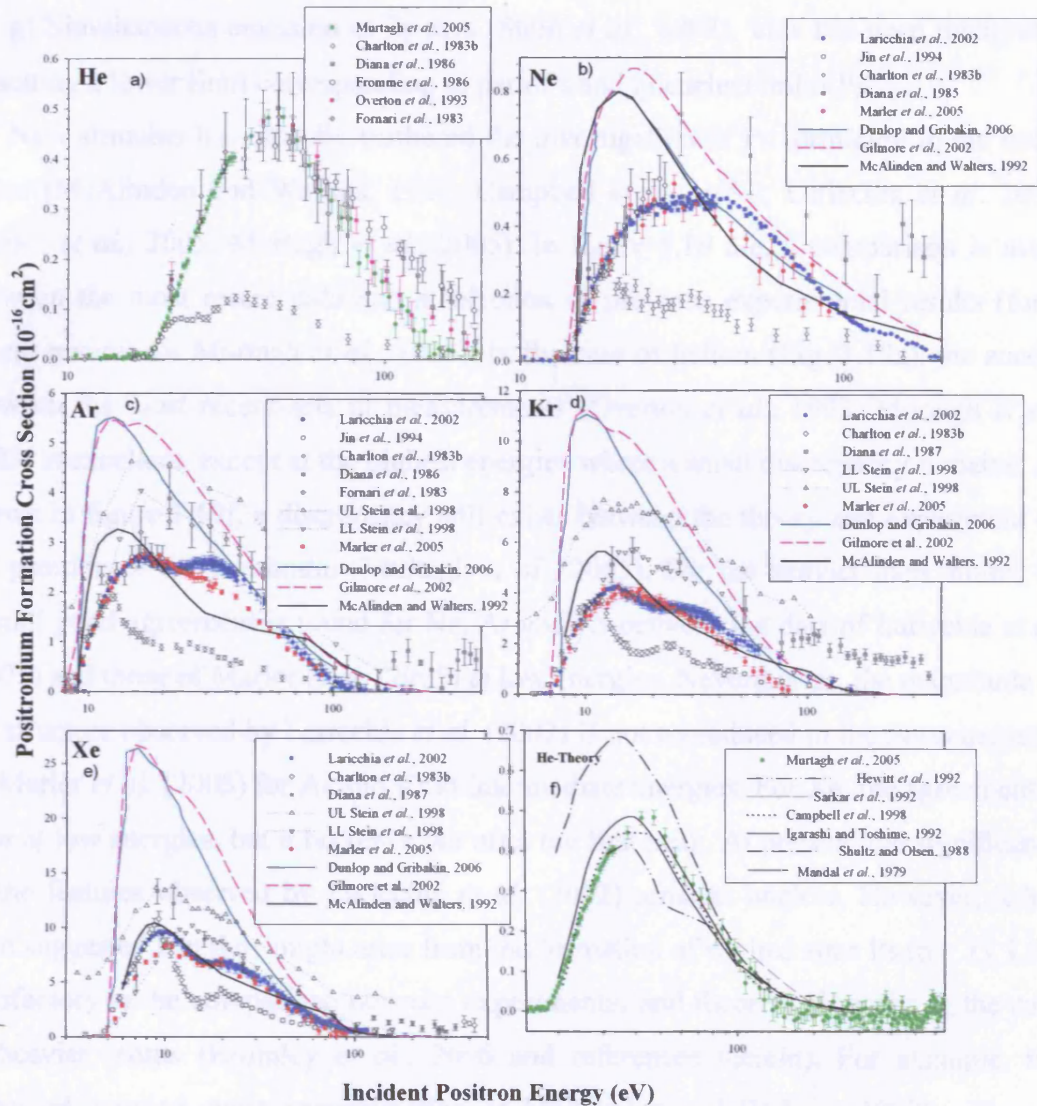


Figure 1.19. Positronium formation cross-sections for He, Ne, Ar, Kr and Xe as a function of incident positron energy.

c) Measurement of all ions and of e^+ - ion coincidences (all Ps). Once again by assuming negligible annihilation, ions not accompanied by a positron in the final state are attributed to Ps formation (Fromme *et al.*, 1986; Laricchia *et al.*, 2002).

d) Direct detection of ortho-Ps (e.g. Laricchia *et al.*, 1987; Finch *et al.*, 1996; Falke *et al.*, 1995, 1997).

e) Detection of the 5.1eV Lyman- α photon from (2P-1S) transition of Ps in delayed coincidence with an annihilation photon (Ps*) (Laricchia *et al.*, 1985). No cross-sections were derived because of unknown efficiencies.

f) Ion production below the ionisation threshold (Moxom *et al.*, 1999).

g) Simultaneous emission of 2γ -rays (Stein *et al.*, 1998). This has been interpreted as setting a lower limit corresponding to para-Ps and quenched ortho-Ps.

New stimulus has recently furthered the investigation of Ps formation in the noble gases (McAlinden and Walters, 1994; Campbell *et al.*, 1998; Laricchia *et al.* 2002; Marler *et al.*, 2005; Murtagh *et al.*, 2005). In figure 1.19 a-e, a comparison is made between the most recent data and a selection of previous experimental results (for a recent review see Murtagh *et al.*, 2006). In the case of helium (Fig. 1.19a), the accord between the most recent sets of measurements (Overton *et al.*, 1993; Murtagh *et al.*, 2005) is excellent, except at the highest energies where a small discrepancy remains. As shown in figure 1.19f, a discrepancy still exists between the theory and experiment on the position of the maximum (Murtagh *et al.*, 2005). For the heavier inert atoms, an overall good agreement is found for Ne, Ar and Kr between the data of Laricchia *et al.* (2002) and those of Marler *et al.* (2005) at low energies. Nevertheless, the magnitude of the structure observed by Laricchia *et al.* (2002) is not reproduced in the measurements by Marler *et al.* (2005) for Ar and Kr at intermediate energies. For Xe, the agreement is poor at low energies, but it becomes fair after the first peak. At present, the significance of the features observed by Laricchia *et al.* (2002) remains unclear. However, it has been suggested that they might arise from the formation of excited state Ps ($n > 1$). Less satisfactory is the comparison between experimental and theoretical results in the case of heavier atoms (Bromley *et al.*, 2006 and references therein). For example, the truncated coupled-static approximation of McAlinden and Walters (1992), although only inclusive of the ground state Ps, reproduces the magnitude of the Ps formation cross-sections well, as shown in Fig. 19 b-e. Gilmore *et al.* (2004) performed calculations within the distorted-wave Born approximation, which includes capture from excited states and the 1st ns^2 -subshell. As Fig 19 b-e shows, their results do not agree well in magnitude with the experimental results, but best reflect the shape. The results of a recent many-body perturbation theory by Dunlop and Gribakin (2006), inclusive of the ground and first ns -subshell, diverge considerably from those of the experiment overestimating by a factor of ~ 2 the magnitude of the peaks (Fig. 19 b-e). However, a good agreement is seen between the experimental data and these calculations at high energies.

A recent study of the San Diego group (Marler and Surko, 2005b) reported Ps formation cross-sections for three diatomic molecules: N₂, CO and O₂. A good

agreement is found between the Ps formation cross-sections for the two isoelectronic targets of N₂ and CO. In the case of O₂, the positronium formation is in agreement with previous data of Griffith (1983) from the Ps formation threshold, E_{Ps} , up to the ionisation energy, I , as shown in figure 1.20. Above I , the determinations from Griffith (1983) undercut the cross-section of Marler and Surko (2005b). A distinct peak is identified in the near-threshold Ps formation cross-section of O₂, which is similar, but smaller in magnitude, to that presented in the total ionisation cross-section by Laricchia *et al.* (1993). In that work, the presence of the dip around 11eV was attributed to channel coupling with the excitation of the Schumann-Runge continuum (dissociation of molecular oxygen) having a threshold just above that of Ps formation. In fact, the peak of this excitation channel (Katayama *et al.*, 1987) rises sharply at the threshold but decreases as the ionisation channel opens and coincides with the structure in the data of Marler and Surko (2005b) and Laricchia *et al.* (1993).

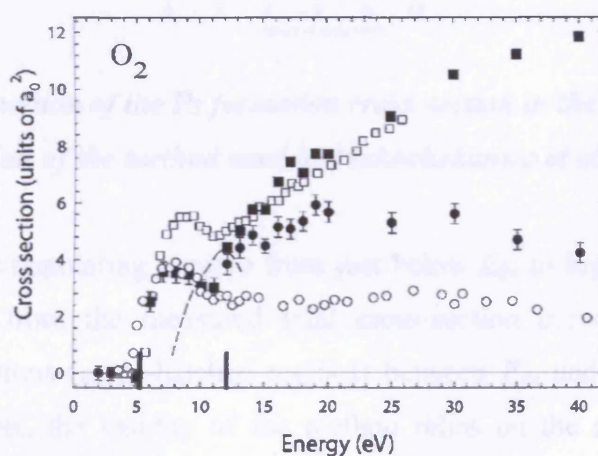


Figure 1.20. Measurements of Marler and Surko (2005b) of the integral cross-sections for O₂: (●) positronium formation and (■) total ionisation cross-section. Also shown for comparison are the experimental results for (□) the total ionisation cross-section from Laricchia *et al.* (1993), and (○) the positronium formation from Griffith (1983). Vertical bars mark the positions of the Ps formation and direct ionisation thresholds. The experimental cross-section for the excitation to the Schumann-Runge continuum from Katayama *et al.* (1987) is also shown as the dashed line.

In the case of higher order polyatomic molecules, simple targets such as CH_4 and CO_2 (e.g. Bluhme, 1999a; Murtagh *et al.*, 2006) have been investigated. For water molecules, only Sueoka *et al.* (1987) inferred indirectly an estimate for the Ps formation cross-section. They found a value of only $(0.3 \pm 0.2) \cdot 10^{-16} \text{cm}^2$ at 2eV above the threshold. A similar value was obtained in an improved experiment performed by Makochekanwa *et al.* (2006). The method employed in both cases is illustrated in figure 1.21.

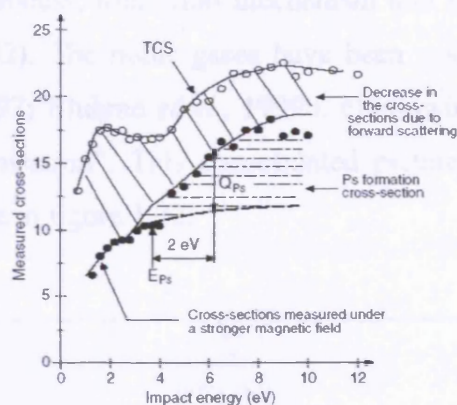


Figure 1.21. Estimation of the Ps formation cross-section in the case of C_3H_8 . An illustration of the method used by Makochekanwa *et al.* (2006).

It consists first in extrapolating a curve from just below E_{Ps} to higher energies. Then, this is subtracted from the measured total cross-section curve to derive the Ps formation cross-sections (cross-hatched regions) between E_{Ps} and the first excitation energy, E_{ex} . However, the validity of the method relies on the assumption that the elastic scattering cross-section varies smoothly through the Ps formation threshold and that neither Wigner cusps (see §1.4.4) nor resonances appear above this energy. The total cross-section was measured in the presence of a strong magnetic field (23G in Sueoka *et al.* (1987) and 31G in Makochekanwa *et al.* (2006)) allowing the detection also of positrons scattered with large angles in the collision cell. This rendered the increase in the total cross-section at E_{Ps} more evident. Makochekanwa *et al.* (2006) also determined the ratios between σ_{Ps} and σ_t , which are indicative of certain patterns in atoms and molecules: for rare gases the ratio is large, for alkanes the ratio decreases with carbon valence number, for fluoroalkanes the ratio is lower than in alkanes and for polar molecules the ratio is very low (less than 7%). In the case of water σ_{Ps}/σ_t is only 2.5%. The observed suppression of Ps formation was attributed in Sueoka *et al.* (1987),

as in Goldanskii (1968), to the large dipole moment of the water molecule. This might cause the electron density around the positron to approach that of metals, within which Ps formation is forbidden (Kanazawa *et al.*, 1965).

1.4.7 Integral and Differential Ionisation Cross-Sections

Comparisons of single ionisation cross section from e^+ impact with those obtained for equivelocity e^- , proton (p^+) and antiproton (p^-) impact have provided insights into the dynamics of the collision process, ionisation mechanism and open reaction channels (Knudsen and Reading, 1992). The noble gases have been studied thoroughly in the past (e.g. Paludan *et al.*, 1997; Bluhme *et al.*, 1999b, c) allowing the development of the “standard picture of ionisation”. This consolidated picture of ionisation is well represented by the case of He in figure 1.22.

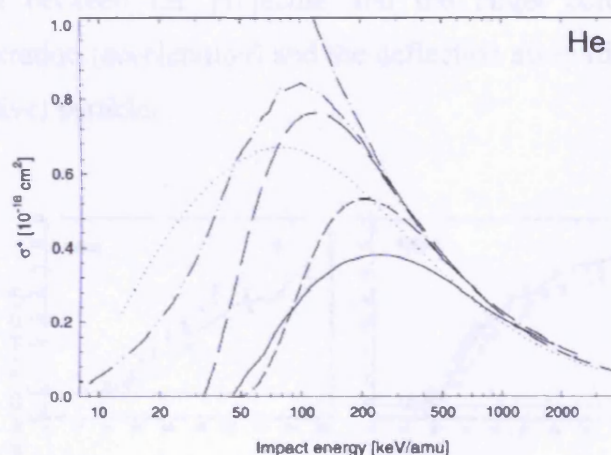


Figure 1.22. Single ionisation cross-section with equivelocity (e^\pm, p^\pm) projectiles on He. Positron impact: (—) σ_i^+ by Moxom *et al.* (1995), (---) σ_i^+ by Jacobsen *et al.* (1995) and Moxom *et al.* (1996). Electron impact: (—) σ_i^+ by Krishnakumar and Srivastava (1988). Proton impact: (- · -) σ_i^+ and (- · -) σ_i^+ by Shah and Gilbody (1985) and Shah *et al.* (1989). Antiproton impact: (·····) σ_i^+ by Andersen *et al.* (1990) and Hvelplund *et al.* (1994). (Figure taken from Knudsen and Reading, 1992).

At high velocities ($v_p \gg v_e$, where v_p is the projectile velocity and v_e is the target electron velocity), the ionisation cross-section displays a similar energy dependence for all four projectiles in accordance to the first Born approximation. At intermediate

velocities, the heavier projectiles have higher σ_i^+ as the threshold is approached, due to a mass/kinetic energy effect, and the positively charged particle has larger (direct and total) ionisation cross-sections than its antiparticle (charge effect). This latter effect is attributed to the target polarisation during the initial stage of the collision. At the lowest velocities $\sigma_i^+(e^+, p^+) < \sigma_i^+(e^-, p^-)$ because of the competition between ionisation and electron capture in the case of positive projectiles. In the case of heavier projectiles, the direct ionisation cross-section is also, in part, suppressed because of binding/antibinding effects. These effects arise from the passage of the projectile through the electron cloud. Intuitively, the passage of a positive/negative particle causes an increase/decrease of the central positive charge and, in turn, the target e^- experiences more/less binding from the central charge. Moreover, the same trend seems also to be due to a trajectory effect especially for light projectiles. This is attributed to the Coulomb interaction between the projectile and the target core nucleus, which determines the deceleration (acceleration) and the deflection away (deflection forward) of the positive (negative) particle.

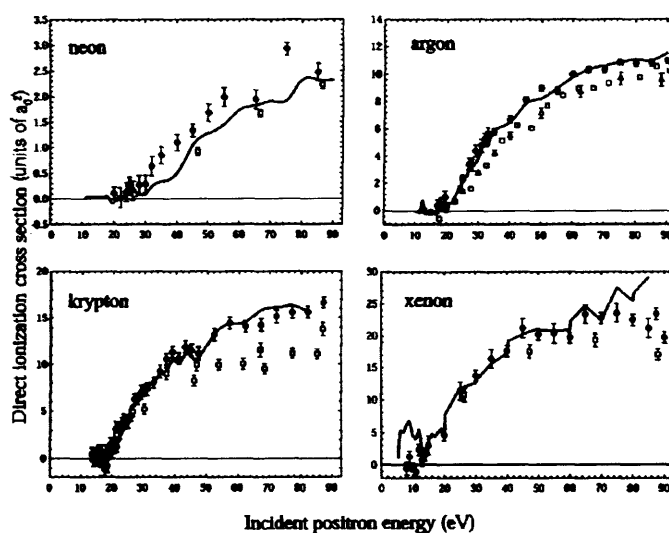


Figure 1.23. Direct ionisation cross-sections as a function of positron energy for Ne, Ar, Kr, and Xe. (o) Marler et al. (2005). These data are compared with two other determinations of these cross-sections: (□) the direct ionisation measurements from Moxom et al. (1996) and Kara et al. (1997); and (—) using the total ionisation from Laricchia et al. (2002) minus the measurements for the positronium formation of Marler et al. (2005). Also shown for comparison in Ar are (Δ) the experimental data from Jacobsen et al. (1995). (Figure taken from Marler et al., 2005).

In ionisation studies by positron impact, well-established ion-atom collision techniques have mainly been adopted (e.g. Andersen *et al.*, 1987). The first fully resolved ionisation measurements was reported by Fromme *et al.* (1986), who employed time-correlation techniques to measure He⁺ ions and scattered positrons in coincidence. Marler *et al.* (2005) presented new absolute measurements of σ_i^+ for Ne, Ar, Kr and Xe using a new technique based on a magnetic trap (§1.3). In figure 1.23, these latest results are compared to the two sets of data of Moxom *et al.* (1996) and Kara *et al.* (1997), which were determined from cross-section measurements in a crossed-beam geometry by establishing the coincidence between the ionised target and the scattered positron. The agreement between the two sets of cross-sections is good, but the data of Marler *et al.* (2005) are generally higher than the other two curves.

An extensive data library is also available for σ_i^+ for positrons scattered from various targets: H (e.g. Spicher *et al.*, 1990; Hofmann *et al.*, 1997), H₂ (Moxom *et al.*, 1993, 1995), and a number of other diatomic and polyatomic molecules (e.g., Moxom *et al.*, 2000). For example, the recent determination of the total ionisation cross-section of O₂ by Marler and Surko (2005b) shows (figure 1.20 in §1.4.6) a good agreement above the ionisation threshold with the results of Laricchia *et al.* (1993), but a serious discrepancy is seen below this threshold. These new results exhibit a feature analogous to that presented by the Ps formation cross-section (§1.4.6) near the Ps formation threshold.

More challenging investigations are differential ionisation measurements, which allow investigations of the temporal and spatial evolution of many mutually interacting particles under the influence of “fundamental” forces (a few-body problem). In addition, these experiments provide a more solid basis for a comparison with theoretical models (e.g. McCurdy *et al.* 2004). Selected experimental works, which have been carried out over last decade, are briefly reviewed here.

Measurements of singly differential cross-section, $d\sigma_i^+/d\Omega$, for singly ionised Ar and, $d\sigma_i^{2+}/d\Omega$, for doubly ionised Ar, and Kr were performed by Finch *et al.* (1996) and Falke *et al.* (1997), respectively. The following differential studies from positron scattering were initially motivated by the quest of the electron capture to the continuum (ECC) cusp in the electron energy spectrum as in the case of positive ion impact. The ECC process might be considered as a special case of ionisation, where the energy and

angular distributions of emitted electrons are strongly influenced by the long-range Coulomb interaction between the scattered projectile and the ionised electron and their relative velocity is close to zero. Hence, ECC can be interpreted as a continuation of the electron capture into high-lying bound states (Rydberg states) of the projectile across the ionisation threshold (Macek, 1970; Rudd and Macek, 1972). In the case of ion impact, most of the experimental investigations of ECC were carried out by measuring the electron cusp peak at the matching velocity ($v_p \sim v_e$ where v_p is the velocity of the ion and v_e that of the target electron) in the doubly differential cross-sections of gaseous targets (e.g. Crooks and Rudd, 1970, Rodbro and Andersen 1979, Knudsen *et al.*, 1986) and of thin foils (Harrison and Lucas, 1970). This post-collision interaction effect is also reflected in the momentum distributions/spectra of the two collision partners (the scattered projectile and the recoil target ion) but it is much smaller than for the electron due to the large mass differences (Vajnai *et al.*, 1995; An *et al.*, 2001; for a review see Ullrich *et al.* 1997). For the same reason, the ECC electrons usually have a narrow angular distribution around the direction of the incident beam and only recently have they been observed at large scattering angles (Sarkadi *et al.* 1998). Two-centre electron emission treatments (Fainstein *et al.*, 1991) are required in order to explain the magnitude and shape of the cusp peak in electronic spectra, i.e. the emitted electron is considered to be influenced by the superposition of the electric fields of the residual target core and of the projectile.

In the case of positron impact, since a positron has the same mass as an electron, ECC events were expected to be distributed over a larger angular range than for heavier ions (Schultz and Reinhold, 1990) and with the outgoing positron and electron sharing approximately equally the remaining kinetic energy ($E_+/2$). As a consequence, the ECC process, also referred as Ps formation in the continuum, would be characterised by the emission of electrons with a distribution of kinetic energies peaked at:

$$E_- = \frac{E_+ - I}{2} = \frac{E_r}{2}, \quad (1.5)$$

where E_+ represents the positron impact energy and I is the ionisation energy.

Different theoretical predictions have emerged concerning the prominence of the ECC cusp structure in the doubly and triply differential cross-sections (Brauner and Briggs, 1986; Mandal *et al.*, 1986; Brauner *et al.*, 1989; Schultz and Reinhold, 1990; Sil *et al.*, 1991; Bandyopadhyay *et al.*, 1994; Sparrow and Olson, 1994; Brauner and Briggs, 1991). Brauner and Briggs (1986, 1989) were the first to identify the ECC feature in the triply differential cross-section (TDCS) for fast positrons in collision with atomic hydrogen employing the first Born approximation to the T-matrix for the transition (the probability with which a given momentum state is reached) but including the final-state Coulomb interaction between the projectile and the electron. The initial state is described by the product of the bound target wave function and a plane wave for the projectile, while the final state is given by the product of a Coulomb function representing the motion of the positron relative to the electron and a plane wave for the motion of the unbound Ps relative to the nucleus. The emergence of similar structures was found in the triply differential cross-section for outgoing particles scattered at all angles. This is typified by the TDCS for 1keV positron impact with electrons emitted in the beam direction, as shown in figure 1.24.

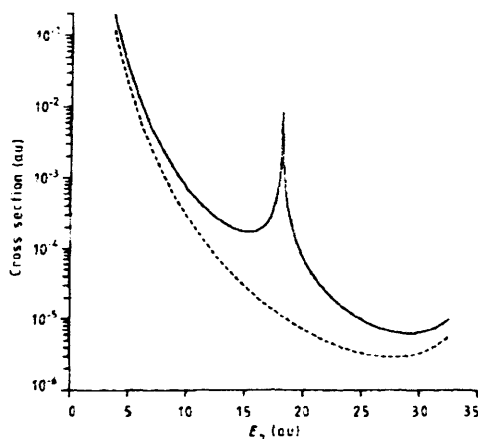


Figure 1.24. *The triply differential cross-section for the ejection of electrons in the beam direction ($\theta_a = \theta_b = 0^\circ$) from the ionisation of atomic hydrogen by 1keV positron impact as a function of the electron ejection energy E_b . The broken curve is for an electron-positron plane wave as the final state; the full curve is for a Coulomb wave as the final state. (Figure taken from Brauner and Briggs, 1986)*

Among the calculations of the doubly differential cross-section, $d^2\sigma_i^+/dEd\Omega$, Bandyopadhyay *et al.* (1994) used asymptotically correct final state wave functions

(Brauner *et al.*, 1989) for 100eV e^+ -H collisions in the 2 - 180° angular region. They found a sharp cusp at 42eV for different ejection angles. Figure 1.25 displays their results along with the corresponding spectra obtained using the CTMC method (Schultz and Reinhold, 1990) that show a ridge-like structure. Schultz and Reinhold (1990) attributed the ridge to the large angular deviation of the light projectile, as mentioned earlier.

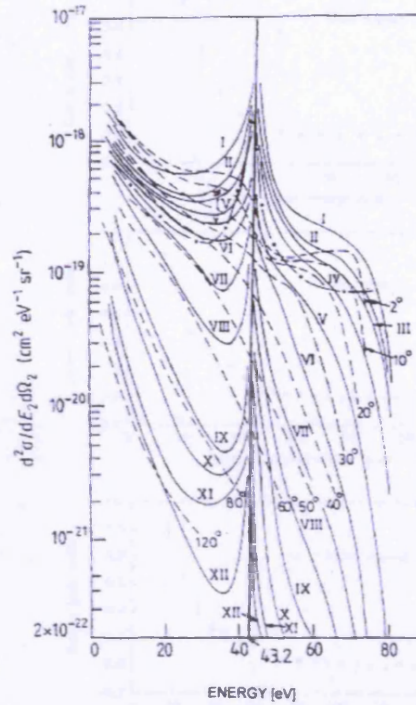


Figure 1.25. Comparison of the DDCS of ejected electrons from 100eV e^+ -H collision determined by (-) a quantum mechanical (Bandyopadhyay *et al.*, 1994) and (- -) a CTMC calculation (Schultz and Reinhold, 1990). The curves marked I to XII represent all angles from 0° to 180°. (Figure taken from Bandyopadhyay *et al.*, 1994).

Various measurements of the doubly differential cross-section (Moxom *et al.*, 1992; Kövér *et al.*, 1993, 1994, 1998) followed these theoretical investigations. Moxom *et al.* (1992) obtained the first $d^2\sigma_i^+/dEd\Omega$ for e^+ impact ionisation of Ar measuring the energy distribution of ejected electrons around 0° for three impact energies: 50eV, 100eV and 150eV. In that work, two different approaches were utilised to measure the electron energies: a time-of-flight technique (TOF) and a retarding electric field method (RFA). The findings of Moxom *et al.* (1992) (Fig. 1.26) showed that the occurrence of

low-energy electrons is most likely and that the electron energy distribution falls steadily to zero as $E_r/2$ is approached. However, small bumps were observed at 40 and 60eV for impact energies of 100 and 150eV, respectively. These are close to the values of energies where ECC is expected; the e^- energy spectra could only suggest that the ECC contribution in $d^2\sigma_i^+/dEd\Omega$ for a light projectile is small.

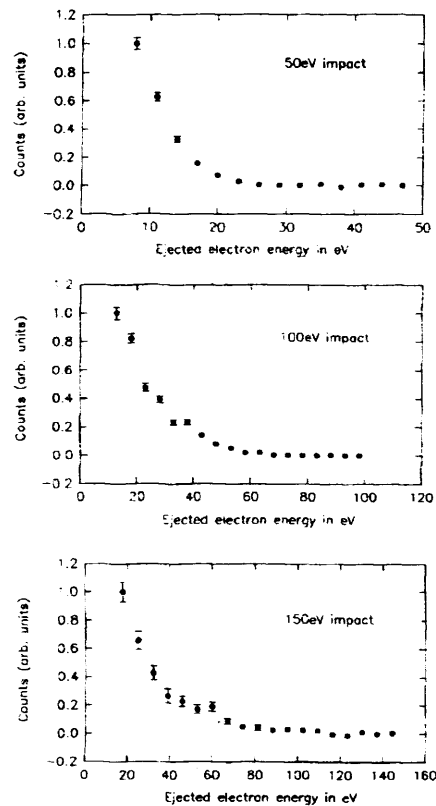


Figure 1.26. Ejected e^- energy spectra deduced from time-of-flights at various e^+ impact energies. (Figure taken from Moxom *et al.*, 1992).

This result was opposite to that obtained with quantum mechanical determinations (e.g. Bandyopadhyay *et al.*, 1994), but in line with the CTMC of Schultz and Reinhold (1990). Subsequently, more difficult measurements of the energy spectra were performed employing an electrostatic system (Kövér *et al.* 1993, 1994, 1997). This was done at great expense to the positron intensity; therefore only targets with high ionisation cross-section were initially investigated (e.g. Ar). Kövér *et al.* (1993) determined the energy distributions for electrons and positrons scattered close to 0° in coincidence with the remnant ion at impact energies of 100, 150 and 250eV. The energy analysis of the scattered projectile was done by a parallel plate analyser (PPA).

Figure 1.27 shows that the e^+/e^- spectra are very similar. For positron impact, no structure appears that could be associated to ECC. This observation was in accordance with the result of Moxom *et al.* (1992).

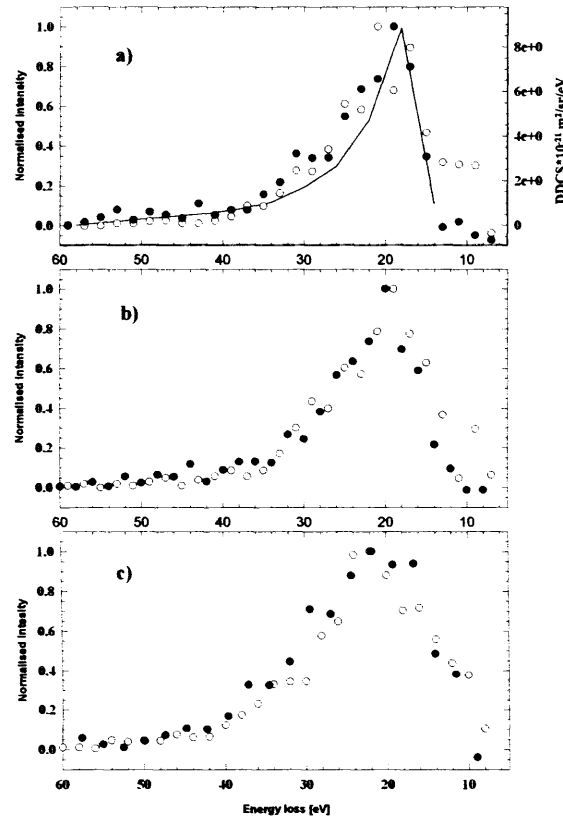


Figure 1.27. Energy distribution for electrons (o) and positrons (●) scattered close to 0° at impact energies of a) 100, b) 150 and c) 250 eV (Kövéř *et al.*, 1993). The line represents the results of CTMC calculations (Sparrow and Olson, 1994).

$d^2\sigma_i^+/dEd\Omega$ for single ionisation of Ar have been reported for non-zero scattering angles by Kövéř *et al.* (1994) and Schmitt *et al.* (1994) at 100 eV incident energy and by Kövéř *et al.* (1997) at 60 eV. Specifically, the data of Kövéř *et al.* (1994) for 100 eV electron impact at 30° and at 45° are displayed in figure 1.28a and b, respectively. Corresponding data for positron impact are shown in figure 1.29a and b. The method consisted of measuring the scattered e^+ /ejected e^- in coincidence with the remnant Ar^+ ions. The energy analysis was performed by using retarding field analysers. In the case of electron collisions, normalisation was performed with the data of DuBois and Rudd (1978) at high energies. Similar features are recognised at both angles: a prevalence of emitted electrons in the low- and high-energy range, which are associated with liberated

electrons and scattered electron projectiles, respectively; although, a clear distinction between the scattered projectile and emitted electron was not possible because of their indistinguishability. Moreover, the probability that electrons are emitted with the same energy of the scattered projectiles is low as can be inferred by Fig.1.28.

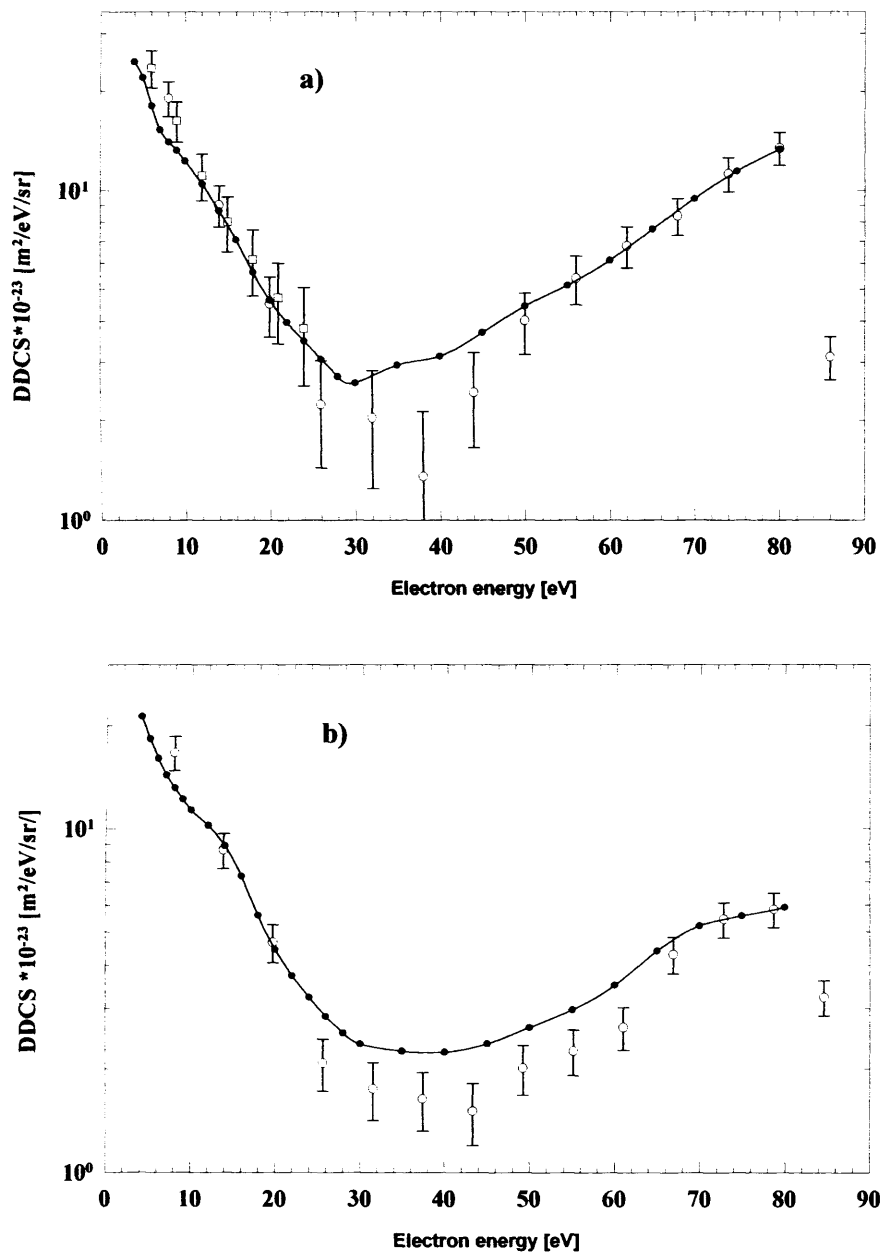


Figure 1.28. Doubly differential cross-sections (DDCS) for the single ionisation cross-section of Ar gas by impact of 100eV electrons.

The solid circles on the eye-guide line are from Dubois and Rudd (1978),

whilst the open circles are Kővér et al. (1994) a) 30°, b) 45°.

For positron impact (Fig. 1.29), data are shown along with the calculations of Sparrow and Olson (1994). These computations are in good accord with the experimental ejected e^- distribution, but exceed the scattered e^+ data at higher energies. e^- and e^+ spectra

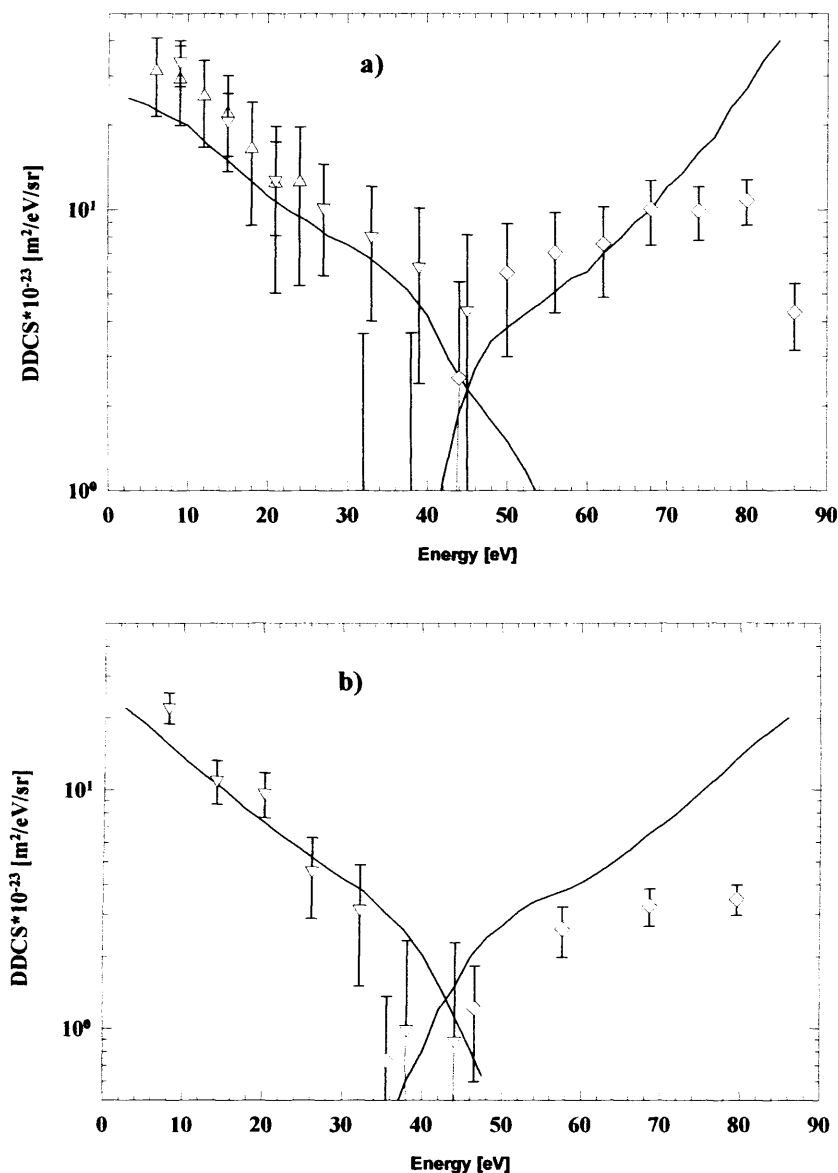


Figure 1.29. Doubly differential cross-sections (DDCS) for the single ionisation cross-section of Ar gas by impact of 100eV positrons.

(\diamond) Scattered positrons; (Δ , ∇) ejected electrons (Kövéř et al., 1994); solid line, calculation of Sparrow and Olson (1994) a) 30°, b) 45°.

could be distinguished unambiguously and exhibit a similar trend: the projectile is scattered at the high energies and the ionised electron is emitted with lower energies.

Again, no evident structure appeared in the ejected electron energy spectra arising from ECC. Kövér *et al.* (1997) remeasured the energy distributions of positrons scattered at 30° employing a parallel plate analyser to analyse the scattered positron energies. The experimental values led to the same conclusions.

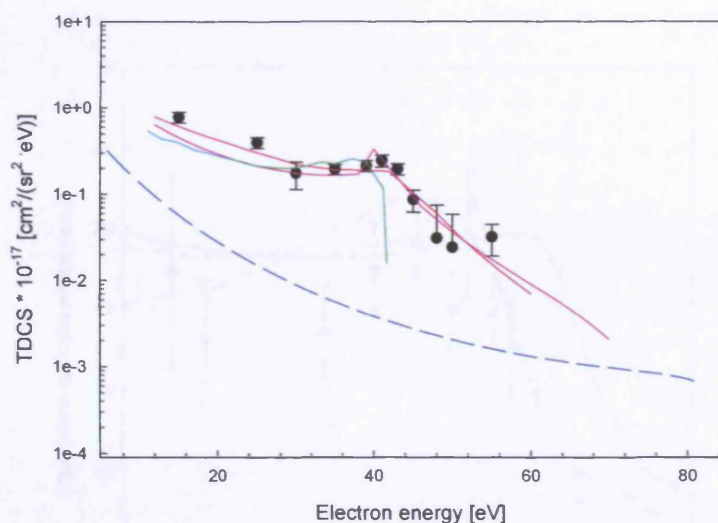


Figure 1.30. *The triply-differential electron spectrum in $e^+(100\text{eV}) + \text{H}_2 \rightarrow e^+(\theta=0^\circ) + e^-(\theta=0^\circ, E) + \text{H}_2^+$; • the experimental work of Kövér and Laricchia (1998); the pink curve and red curve, theory of Berakdar (1998) and Fiol *et al.* (2001) folded with the experimental resolutions, respectively. The green curve is the CTMC by Fiol and Olson (2002). Dashed curve in blue is the First Born Approximation.*

The first experimental observation of ECC for positron impact has been reported by Kövér and Laricchia (1998) in the TDCS, $d^3\sigma_i^+/d\Omega d\Omega_e dE$, around zero degrees for the ionisation of H_2 by 100eV positron impact, namely, $e^+(100\text{eV}) + \text{H}_2 \rightarrow e^+(\theta=0^\circ) + e^-(\theta=0^\circ, E) + \text{H}_2^+$. For this purpose, the coincidence between scattered e^+ and ejected e^- into the same forward direction was set. As shown in figure 1.30, a small broad peak was observed close to 42eV ($E_p/2$) in the ejected-electron energy-spectrum, which was attributed to ECC, in agreement with the calculations of Berakdar (1998). His theory adopts a perturbative quantum-mechanical approach and uses a wave function for the final state, which was used previously for ion atom collision (Garibotti and Miraglia, 1980). Fiol *et al.* (2001) presented a full quantum-mechanical treatment, i.e. treating all interactions (projectile-target, projectile-electron, electron-target) in the final state on

equal balance, and, at the same time, accounting for the three body dynamics. Their computations follow closely the experimental values. It should be pointed out that the classical trajectory Monte Carlo (CTMC) values (Fiol and Olson, 2002) show a distinctive discrepancy with previous theoretical determinations and no consistent description of the experimental data.

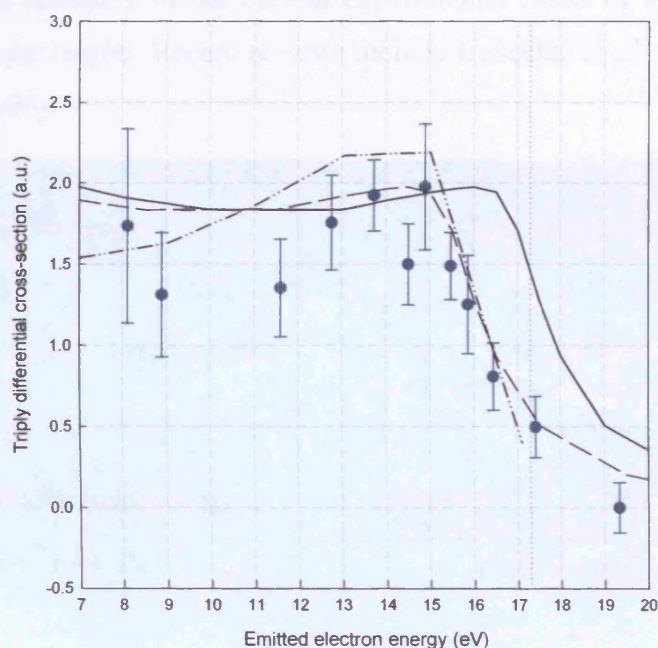


Figure 1.31. The triply differential ionisation cross-section for 50eV positrons incident on H_2 (Kövéř *et al.*, 2001). Full line: theory (Fiol *et al.*, 2001). Dashed Line: theory shifted backwards by 1.6eV. Dashed dot-dot: CTMC (Fiol and Olson, 2002).

Following this investigation, the TDCS study was extended to the lower positron incident energy of 50eV for the same collisional system (Kövéř *et al.*, 2001). In the electron spectrum shown in figure 1.31 a significant shift of almost 2.5eV from $E_r/2=17.3$ eV towards lower energies is observed in the electron TDCS distribution. The discrepancy between the experimental data and the theory of Fiol *et al.* (2001) is 1.6eV. These calculations are convoluted with the angular and energy resolutions of the experimental system but did not include the structure of the target. Fiol and Olson (2002) carried out the Classical Trajectory Monte Carlo calculations at this impact energy, which are in better agreement with the experimental data. A strong correlation between the momenta of the positron and the recoil-ion was also observed (Fiol and Olson, 2002). Another feature, which was observed both in Kövéř and Laricchia (1998)

and in Kövér *et al.* (2001), is the asymmetry around the maximum, which might be related to the increasing three-body fragmentation interaction at lower incident energies (Berakdar, 1998).

1.5 Positronium Interaction with Atoms and Molecules

Table 1.3 shows a summary of the current experimental status of Ps collisions with atomic and molecular targets. Recent reviews include Laricchia *et al.* (2003, 2004) and Armitage *et al.* (2006).

Interaction	Experimental Status
Total scattering cross-section $Ps + A \rightarrow all$	Direct measurements for He, Ar, H ₂ , O ₂ and H ₂ O. Some indirect (N ₂ and Xe).
Ps elastic scattering $Ps + A \rightarrow Ps + A$	Coleman <i>et al.</i> (1994), Nagashima <i>et al.</i> (1998), Skalsey <i>et al.</i> (1998), limited energy range
Ps ionisation $Ps + A \rightarrow e^+ + e^- + A$	Armitage <i>et al.</i> (2002, 2006) and Leslie (2005)
Target ionisation $Ps + A \rightarrow e^+ + e^- + A^+$ $\rightarrow Ps + e^- + A^+$	Armitage <i>et al.</i> (2006)

Table 1.3. Status on experimental collision studies with Ps.

The beam utilised at UCL is formed by neutralising a monoenergetic e^+ beam in a gaseous target via charge exchange (Laricchia *et al.*, 1987; Laricchia and Zafar, 1992; Leslie *et al.*, 2002). The Ps energy, to a first approximation, is given by $E_{Ps} = E_+ - (I - 6.8eV/n^2)$, where I is the target ionisation energy and $6.8eV/n^2$ is the Ps binding energy in a state of principal quantum number n , and is tuneable via the incident positron energy E_+ .

The theoretical prediction that the Ps formed by charge transfer in e^+ -atom/molecule collisions emerges mainly in the forward direction (e.g. Mandal *et al.*, 1979; Brown and Humberston, 1985) motivated the first experimental investigations of $d\sigma_{Ps}/d\Omega$. These investigations were initially made at small forward angles and later at larger scattering angles (e.g. Finch *et al.*, 1996; Falke *et al.*, 1997). Laricchia *et al.* (1987) found that the fraction of e^+ scattered by He and emitted as Ps within 6° was approximately 4%.

The following discussion on Ps scattering is limited to the case of Ps fragmentation as this is of some relevance to the work presented in this thesis.

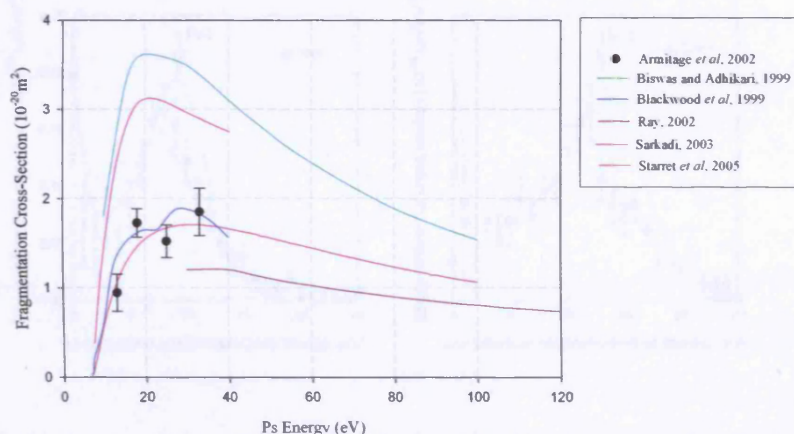


Figure 1.32. Experimentally and theoretically determined cross-section for the fragmentation of Ps in collision with He atoms.

Armitage *et al.* (2002) measured the absolute fragmentation cross-section for the Ps-He collision system at intermediate energies using a time of flight detection system. The findings of Armitage *et al.* (2002), shown in figure 1.32, concord with a coupled state calculation (Blackwood *et al.*, 1999) and the more recent data of Starrett *et al.* (2005), who employed the target elastic impulse approximation (IA). The three-dimensional, three-body version of the classical trajectory Monte Carlo (CTMC) by Sarkadi (2003) overestimates by a factor of ~ 2 the experimental data. Biswas and Adhikari (1999) computations within the Born approximation are also around a factor of two higher than the measurements, whereas the Coulomb Born approximation employed by Ray (2002) underestimates the experimental determinations by $\sim 40\%$.

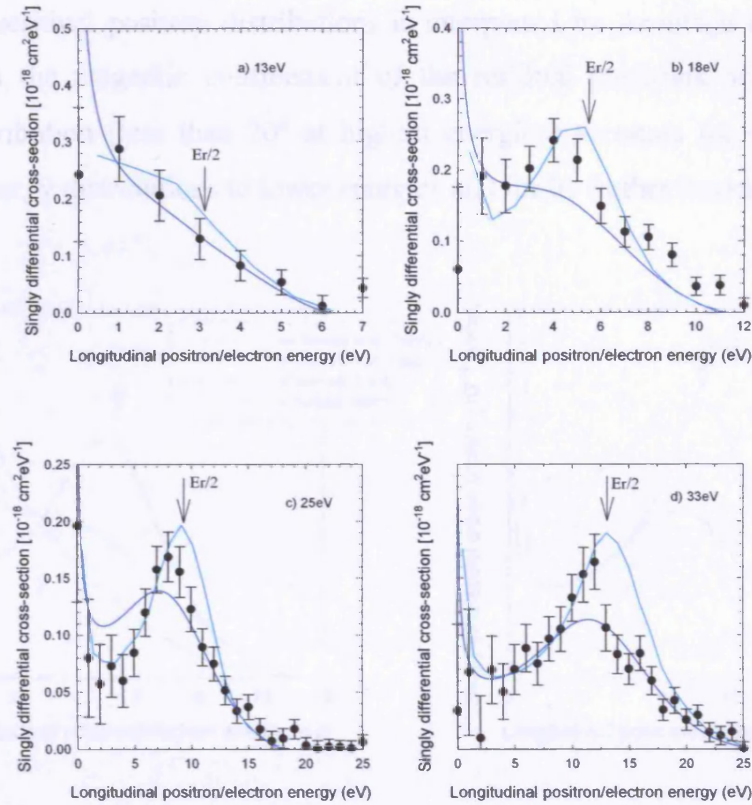


Figure 1.33. Cross-sections, differential in longitudinal energy, for $Ps(1s)+He(1^1S)$ collisions for $E_{Ps} = 13, 18, 25,$ and 33 eV. The experimental data (full circles) of Armitage *et al.* (2002) are shown alongside the blue theoretical curves calculated by Starrett *et al.* (2005). The vertical dotted line shows the expected peak position $E_r/2$. The cyan curves are the CTMC computations by Sarkadi (2003).

In figure 1.33, the measured longitudinal energy spreads for the residual positrons from the fragmentation of Ps (Armitage *et al.*, 2002) are displayed together with the recent computations of Starrett *et al.* (2005) and the CTMC calculations (Sarkadi, 2003). The distributions, both experimental and theoretical, present a peak just below half of the residual energy $E_r/2$ (where $E_r = E_{Ps} - 6.8\text{eV}$), which becomes more pronounced as the Ps energy increases. The peak structure implies that the residual particles, positron and electron, travel in the forward direction with the same velocity, which might indicate the occurrence of the electron loss to the continuum (ELC) (Crooks and Rudd, 1970). The CTMC computations reproduce fairly well only the shape of the measured longitudinal energy spectra, whereas a good agreement exists both in shape and in magnitude with the theoretical values of Starrett *et al.* (2005). The

shift in the residual positron distributions is interpreted by Armitage *et al.* (2002) as arising from the magnetic confinement of the residual positrons, where any finite angular distribution (less than 20° at highest energies) accounts for the shift of the measured energy distributions to lower energies and for its further broadening.

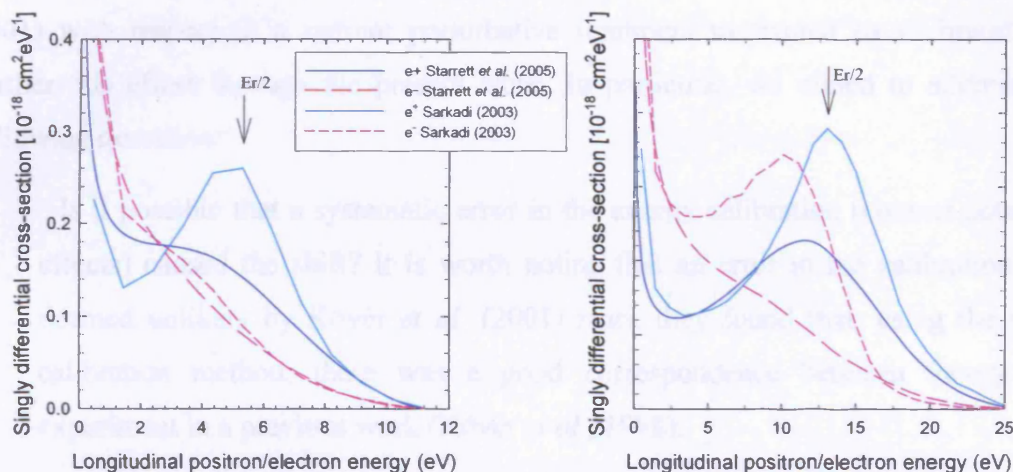


Figure 1.34. Calculations of the longitudinal energy distributions of e^+ (solid line) and e^- (dashed line) ejected in Ps-He collisions for 18eV (left) and 33eV (right) Ps scattering from He atoms by Sarkadi (2003) and Starrett *et al.* (2005).

Figure 1.34 shows the results of Starrett *et al.* (2005) for the longitudinal energy distribution of both the residual electrons and positrons for Ps energies of 18eV and 33eV along with the corresponding determinations of Sarkadi (2003). In the work of Sarkadi (2003), the energy distributions of the residual electrons show a less pronounced peak, which is shifted with respect to the peak in the positron spectra, to lower energies. The discrepancy in the two distributions is tentatively given in terms of the polarisation of the incident Ps, which causes the e^+ to be repelled, whilst the e^- is attracted by the screened Coulomb field of the target. The singly differential cross-section for electrons by Starrett *et al.* (2005) develops a maximum much slower than the correspondent distribution for e^+ as in Sarkadi (2003), but without showing an enhancement at $E_p/2$. In this case, the asymmetry between the energy spectra for positron and electron is explained through some coherent combination of free e^- and e^+ scattering.

1.6 Motivation of the Present Work

Differential ionisation studies by positron impact are intrinsically important because they can provide new insights in the understanding of three-body correlated dynamics, which is still an outstanding problem in physics. However, experimental knowledge is very limited. The discovery of an energy shift in the TDCS of H_2 at 50eV (Kövér *et al.*, 2001) with respect to a current perturbative treatment motivated us to investigate further this effect through the present work. In particular, we aimed to address the following questions:

- i) Is it possible that a systematic error in the energy calibration (contact potential effects) caused the shift? It is worth noting that an error in the calibration was deemed unlikely by Kövér *et al.* (2001) since they found that, using the same calibration method, there was a good correspondence between theory and experiment in a previous work (Kövér *et al.*, 1998).
- ii) As Kövér *et al.* (2001) had conjectured, if the energy shift was genuine, could it be attributed to a doubly-inelastic process, e.g. ionisation simultaneous to vibrational excitation/dissociation of the residual ion?

For these reasons, an absolute energy calibration, new TDCSs for ejected electrons of simple molecular and atomic targets and a TDCS for scattered positrons on H_2 (Arcidiacono *et al.*, 2005a) have been performed for positron impact ionisation. The results of these studies are presented in chapter 3.

The small review presented on previous ionisation works has highlighted discrepancies amongst the experimental and also theoretical results even for the relatively simple case of the noble gases. The water molecule is a much more difficult target to treat theoretically than the noble gases and requires the aid of experiment. In this respect, the important role of the positron in understanding molecular structure and dynamics has recently been pointed out (e.g. Karwasz, 2005). Besides this fundamental aspect, there is urgency in acquiring detailed differential and total ionisation data for the scattering of water with positrons to know, for example, the energy deposited in living matter (simulated by water) during radiotherapy and medical imaging (e.g. PET) (e.g. Champion and Le Loirec, 2006 and §5.1). However, while extensive work has been done on electron-water interactions (e.g. Karwasz *et al.*, 2001; Itikawa and Mason, 2005), the experimental work for positron impact on water molecules was, prior to this

work, confined to σ_i . In addition, the result of a very low value for the Ps formation at 2eV above the threshold (Sueoka *et al.*, 1987) left an open question on possible channel-coupling effects (Laricchia *et al.*, 1993) or the role of the large dipole moment of the water molecule (Kanazawa *et al.*, 1965) in suppressing Ps. All these reasons motivated the extensive ionisation measurements that have been performed with a time-of-flight detection system for positrons in collision with water vapour. As part of a more complete characterisation of the ionisation process of water, $d^2\sigma_i^+/dE_+d\Omega_+$ (DDCS) has also been determined. The presence of a long-range dipole interaction that might influence significantly the DDCS was an additional incentive for these measurements. These investigations are described in chapter 5.

In chapter 6, final conclusions on the work carried out in this thesis are presented together with an outlook in the field.

Chapter 2

Experimental Apparatus for Differential Studies of Positron Impact Ionisation

2.1 Overview

In this chapter, the experimental apparatus and techniques employed in the study of doubly and triply differential ionisation cross-sections of gaseous targets, H₂ and H₂O, are outlined.

The experimental set-up, whose general layout is shown schematically in figure 2.1, was initially designed by Kövér *et al.* (1993, 1994) and, prior to the work described in this thesis, further developed by Finch (1996) where a detailed description of the system can be found. This set-up makes use of a crossed-beam geometry and can be divided into two distinct sections: the source side, which provides a beam of monoenergetic positrons, and the experimental side, which houses the interaction region and the detectors.

The source side comprises a radioisotope of sodium (²²Na) as the source of the fast β^+ particles. These are thermalised using a set of annealed W meshes (moderator) and accelerated to the required energy by applying to the moderator an adjustable positive bias with respect to the chamber ground. The moderated positrons are thus transported and focused by electrostatic fields from the moderator to the target through the electrostatic optics lens system (Kövér *et al.*, 1993, 1994) drawn in figure 2.1. Fast particles and γ -rays emanating from the source are removed from the beam by a deflector, which shifts the beam axis and prevents a line-of-sight between the source and the detectors.

The experimentation side comprises a gas nozzle/capillary array, an ion extractor, a tandem parallel plate analyser (PPA) and associated detectors. The PPA allows the energy analysis of either scattered positrons or electrons ejected by ionisation travelling in the forward direction around $\sim 0^\circ$. A time-of-flight technique was utilised in order to achieve an improved signal-to-background level, to provide a check on the energy of the scattered particles and to perform charge-to-mass analysis of the residual ions.

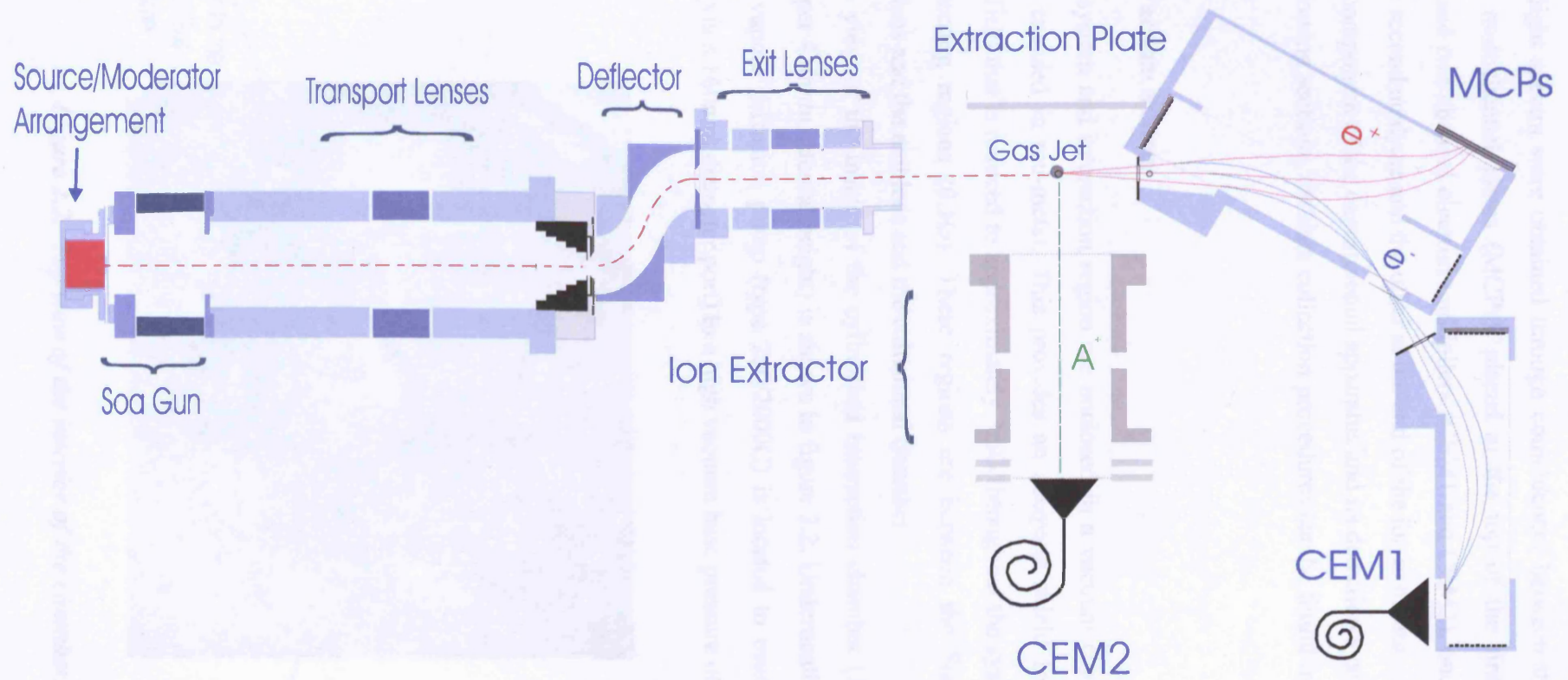


Figure 2.1. Schematic of the experimental arrangement.

Time-of-flight spectra were obtained through coincidences between the two or three detectors: multichannel plates (MCPs), placed at the top of the first parallel plate analyser, and two channel electron multipliers (CEM1 and CEM2), one situated at the end of the second analyser and the other at the end of the ion extractor.

Each component of the experimental apparatus and its detection system is described in the following sections, the data collection procedures can be found in chapters 3 and 5.

2.2 The Vacuum System

The lens system and interaction region are enclosed in a vacuum chamber, which is internally encased in mu-metal. This provides an adequate shield from the Earth's magnetic field that is reduced to approximately 3mG throughout the system, apart from two connecting regions (0.1G). These regions are between the Soa gun and the transport lens and the exit lens and the collisional chamber.

A top view of the inside of the cylindrical interaction chamber (365mm internal diameter per 450mm internal height) is shown in figure 2.2. Underneath this region, an Edwards vapour diffusion pump (type 250/2000C) is located to evacuate the entire chamber (via a 160mm diameter port) to a high vacuum base pressure of $\approx 10^{-6}$ torr.



Figure 2.2. Top view of the interior of the chamber.

The pump is backed by a rotary vane pump (Edwards ED250), which is used to evacuate the system from atmospheric levels to a pressure of $\approx 10^{-2}$ torr.

The system base pressure was measured using an ionisation gauge mounted on one side of the interaction chamber. A pirani gauge monitored the pressure in the backing line between the diffusion and the rotary pump. If the level on this gauge rose above $\approx 10^{-1}$ torr (e.g. due to the malfunction of the backing pump) a system protection device would be triggered. This would cut the power to all the high voltages, the diffusion pump as well as close the magnetic valve between the diffusion and the rotary pump. This isolates the system and prevents backstreaming. This trip mechanism would also be activated if there was a failure in the flow of cooling water to the diffusion pump.

2.3 Positron Beam Production

2.3.1 β^+ Source and Moderator

In the case of most long-term experiments, ^{22}Na is the commonest employed positron source, having a half-life of 2.6 years. The decay scheme of this radioisotope is shown in figure 2.3.

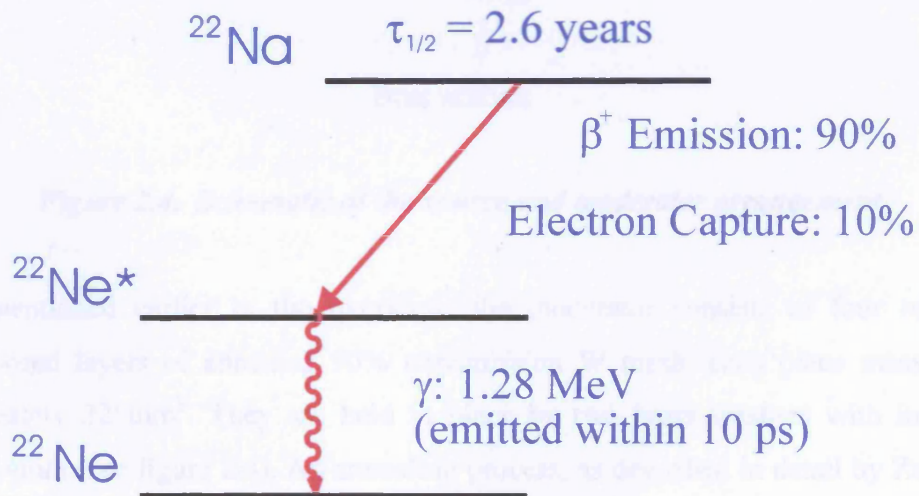


Figure 2.3. The decay scheme and branching ratio of ^{22}Na .

The activity of the ^{22}Na radioactive source, supplied by Dupont PLC/Ltd Amersham International, was initially 13.7mCi when starting the series of measurements discussed in this thesis, decaying to 6.15mCi by the end of the study.

The isotope is deposited within a capsule on a 3mm diameter spot on a W alloy disc (12.7mm diameter x 9.7mm thickness) and sealed with a 13 μ m Ti window. The capsule is fixed onto a piece of studding at the end of a brass plug using a 0.5mm thread. The construction of the source holder assures that there is a minimum distance between the source and the moderator to maximize the flux of fast β^+ particles incident on the moderator. PTFE washers provide electrical isolation between the source-moderator and between the moderator-earth grid. The assembly for the holder of the ^{22}Na source and the W moderator is shown in figure 2.4.

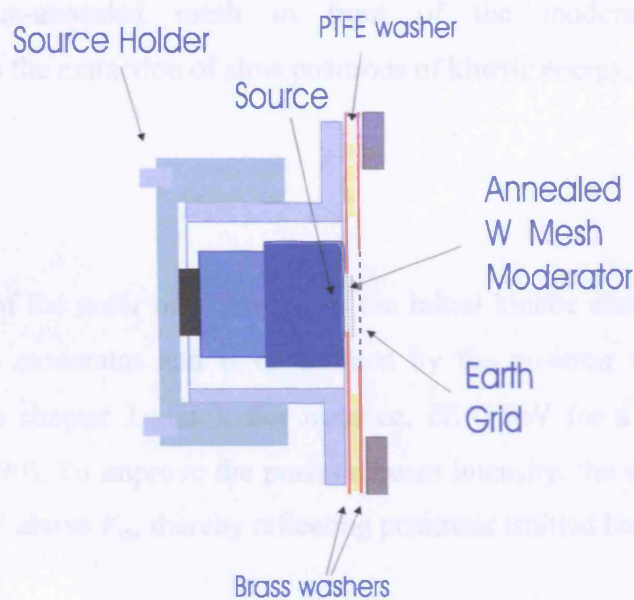


Figure 2.4. Schematic of the source and moderator arrangement.

As mentioned earlier in the overview, the moderator consists of four or five superimposed layers of annealed 90% transmission W mesh, each piece measuring approximately 225mm². They are held in place by two brass washers with internal diameter 4mm (see figure 2.4). An annealing process, as described in detail by Zafar *et al.* (1988 and 1989), was carried out to ensure an optimum yield of slow positrons. This procedure involves heating the meshes resistively in a W foil oven in a vacuum of $\sim 5 \cdot 10^{-2}$ torr, mainly to relax their lattice structure and, in part, to remove contaminants such as adsorbed oxygen and water from the surface. Initially, a constant low current is passed through the foils until the pressure, at first rising largely because of water evaporation from the meshes and oven, nearly returns to the base pressure level. A

gradual heating of the W foil to higher temperatures follows. This results in a pressure increase as further contaminants are removed. To avoid evaporating contaminants from the electrode assembly, the heating is done in bursts of approximately 5sec. This also guarantees that the pressure does not increase above 10^{-1} torr, preventing the occurrence of electrical breakdown. Annealing is concluded when the meshes can be “flashed” at a temperature of approximately 2000°C without an appreciable pressure increase. Once cooled down, the W recrystallises into a more regular structure, that is, with fewer defects, which would act as positron traps. Finally, it is assembled in the moderator holder in air and placed in the experimental system as quickly as possible.

Earthing an un-annealed mesh in front of the moderator held at a potential V_m leads to the extraction of slow positrons of kinetic energy, E_+ , given by:

$$E_+ = eV_m + \delta E, \quad (2.1)$$

where δE , usually of the order of a few eV, is the initial kinetic energy with which a positron leaves the moderator and is determined by the positron work function as discussed further in chapter 1 and 3. For instance, $\delta E=2.8\text{eV}$ for a clean W surface (Jacobsen *et al.*, 1990). To improve the positron beam intensity, the source was biased to approximately 9V above V_m , thereby reflecting positrons emitted backwards.

2.4 Positron Beam Transport

The electron optics (Fig. 2.1) incorporates a modified Soa gun (Canter, 1986) for the extraction of the positron beam and standard beam transport and deflection devices such as double and triple cylinder lenses (Harting and Read, 1976). These lenses are all characterised by cylindrical symmetry. The performance of the beam transport has been simulated by Kövér *et al.* (1992) and Finch (1996). In Appendix I, a detailed description of the beam transport arrangement is given.

2.5 Tandem Parallel Plate Analyser and Detection System

2.5.1 Analyser

A sketch of the tandem parallel plate analyser (PPA) is presented in figure 2.5. This has been developed by Kövér and Laricchia (2001) to study the energy and angular distribution of ejected electrons or scattered positrons from positron-atom/molecule ionising collisions. The main advantage of the present instrument is its time focusing, i.e. particles entering the analyser at different angles arrive at the same time at the detector placed at the end the second stage of the PPA. This feature is useful for increasing signal-to-background levels at low energies.

The PPA consists of two identical aluminium parallelepipeds arranged such that the angle between the two base plates is 120° . Base- and back- plates are separated by a distance $h=18\text{mm}$. By varying the voltage, V_{ppa} , applied to the backplate, the energy of particles (electrons or positrons) entering at 0° ($\pm 5^\circ$) after the collision can be determined by detection using a single channel-electron-multiplier (CEM1) with a wide diameter aperture (10mm). The transverse angular spread is $\pm 15^\circ$. The remaining collision partner (scattered positron or emitted electron), having opposite charge, would be deflected to the top of the first stage and detected by an assembly of microchannel plates.

Two analysers used in series (tandem analyser) reduce the spurious background count due to secondary electrons. In fact, the parabolic deflection of particles with the correct energy in a tandem analyser results in filtering out most of the unwanted secondary electrons. Secondary electrons are generated by positrons of the incorrect energy scattering within the analyser. The grid on the first backplate prevents electrons, mainly escaping from the MCPs, entering the second stage of the PPA. To reduce the emission of secondary electrons from metal surfaces and to provide equipotential surfaces, these are coated with graphite. On each stage of the PPA, 10 guard electrodes (Cu stripes), connected by a resistor divider chain, are used to maintain a uniform electric field.

The focal length of a single PPA (Green and Proca, 1970a; 1970b; Proca, 1973a; Proca, 1973b; Bachmann *et al.*, 1982) consists of three parts: the distance travelled by the particle in a field-free region from the interaction region to the slit on the baseplate; the particle trajectory in the supposed uniform field between the plates to the earth

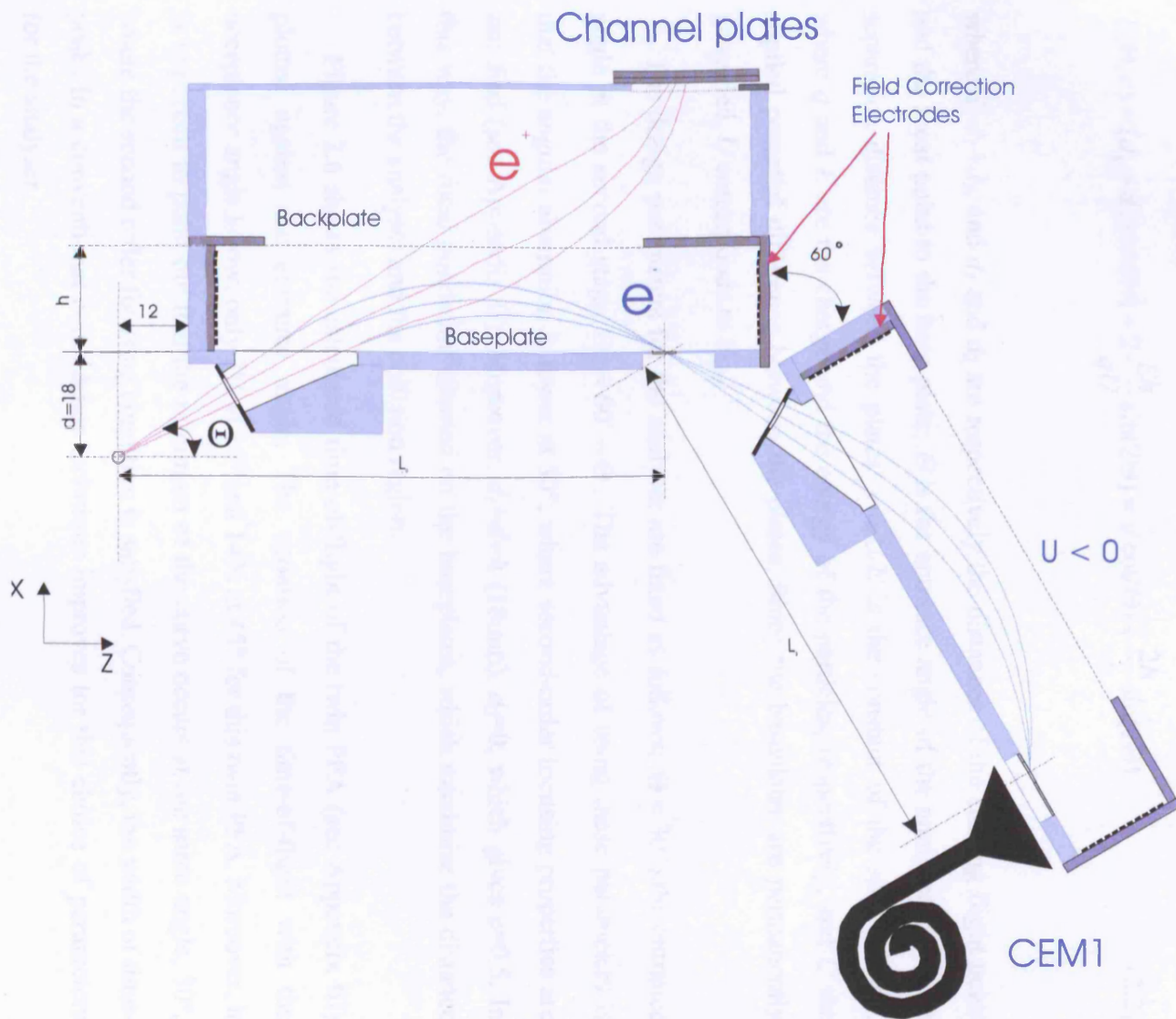


Figure 2.5. Schematic diagram of the cross-section of the Parallel Plate Analyser, to scale (Kövér and Laricchia, 2001).

plate, and the particle flight-path to the focus in a straight line.

It has been shown (Kövéér and Laricchia, 2001) that the total focal length along the axis z (see Fig. 2.5) is given by:

$$L(\Theta, c) = (d_1 + d_2) \cot(\Theta) + 2 \frac{Eh}{qU} \sin(2\Theta) = d \cot(\Theta) + \frac{2h}{c} \sin(2\Theta), \quad (2.2)$$

where $d=d_1+d_2$, and d_1 and d_2 are respectively the distances of the starting flight point and the focal point to the base plate; Θ is the entrance angle of the analyser and h the separation distance between the plates. $c=qU/E$ is the constant of the spectrometer, where q and E are the charge and the energy of the particles, respectively, and U the applied potential difference between the plates. Since the baseplates are permanently grounded, U corresponds to V_{ppa} .

The design parameters for the analyser are fixed as follows: $\Theta = 30^\circ$, the entrance angle at the second stage $\Theta_2 = 60^\circ - \Theta$. The advantage of using these parameters is that the angular aberration is lower at 30° , where second-order focusing properties are satisfied (see Appendix II). Moreover, $d_1=d=h$ (18mm), $d_2=0$, which gives $c=0.5$. In this way, the focal points are situated on the baseplates, which maximise the distance between the analyser and the collision region.

Figure 2.6 shows the calculated time-of-flight of the twin PPA (see Appendix III) plotted against the entrance angle. The variation of the time-of-flight with the acceptance angle is low: only 3% at 15° and 14% at 45° for this twin PPA. Moreover, it is important to point out that the minimum of the curve occurs at the same angle, 30° , where the second order focusing condition is satisfied. Consequently, the width of time-peaks in a conventional coincidence technique improves for this choice of parameters for the analyser.

To account for the effect of the finite source size (diameter 4mm), the entrance aperture (8mm) and exit slit (5mm) on the intensity and time distribution, further effort has been made by performing a model calculation (Kövéér and Laricchia, 2001). This has shown that the energy dispersion of this analyser is improved in comparison to the previously adopted analyser (Finch, 1996).

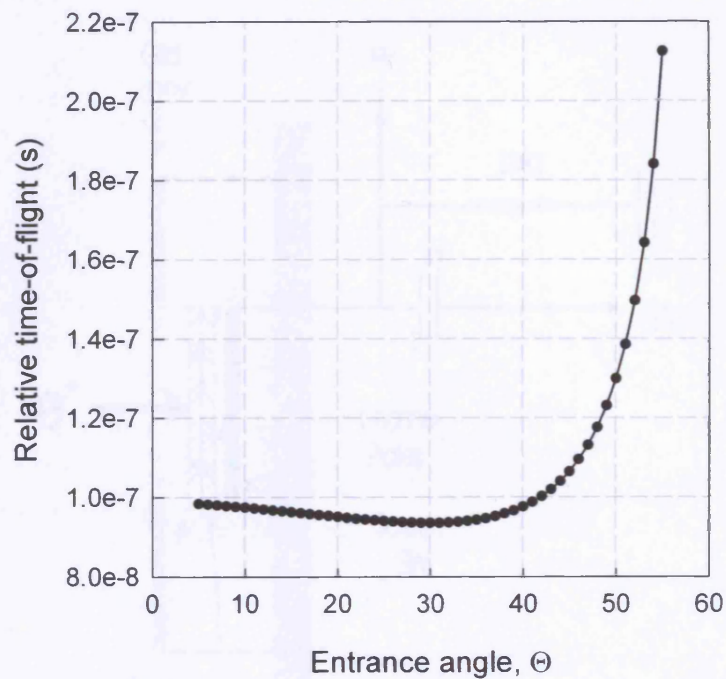


Figure 2.6. Distribution of the calculated time-of-flight as a function of the entrance angle for the PPA (Kövér and Laricchia, 2001).

2.5.2 Multichannel Plate Detector

Figure 2.7 is an enlarged schematic of the MCP detector in front of which a 90% transmission W grid (G) is held. This detector consists of two “channel-plates” (discs of glass tubes, each with an internal diameter of $25\mu\text{m}$ and set at an angle of 51°). The MCPs (Photonics G12-27 DT/13/A) are impedance matched and placed in a chevron configuration in order to optimise the gain and reduce ionic feedback. G is not only used to define better the end of the flight path, but also to increase the MCP gain. In fact, typically G is held at approximately -100V with respect to the potential on the front of the first plate in order to reflect any secondary electrons released from its surface towards the MCP and improve its detection efficiency. To detect positrons, the front of the first MCP and the back of the second MCP were held at -300V and $+2.8\text{kV}$, respectively. Behind this second MCP, the charge created by the electron avalanche is collected by a small potential difference ($+200\text{V}$) between the Cu screen and the back of the MCP. These pulses were then decoupled from the DC voltage by a 1nF capacitor. This provided the signal.

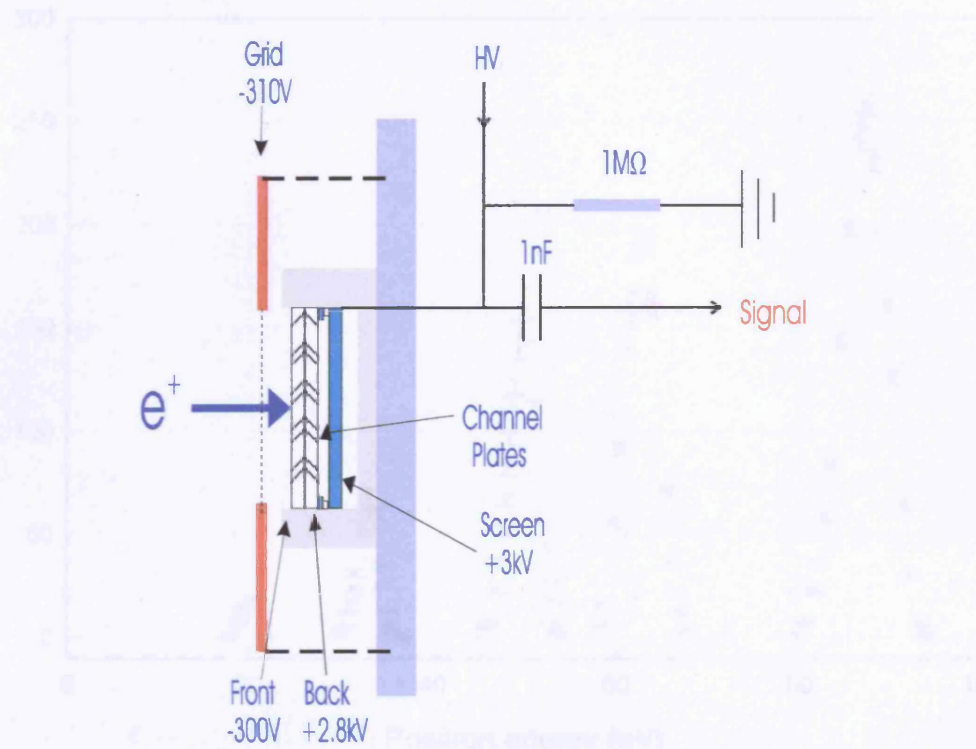


Figure 2.7. A section of the MCPs arrangement.

2.5.3 Channeltron (CEM1)

CEM1 (model X919BL supplied by Philips Ltd), shown in figure 2.5, was employed to detect positrons or electrons whose energy corresponds to the so-called pass-energy of the analyser. This energy is fixed by the constant of the spectrometer (see §2.5.1) as $E=qV_{ppd}/c$. CEM1 was also used to measure the direct beam and thus to find the optimum electrostatic lens voltages for the beam transport. If not possible during a measurement, the intensity of the beam was monitored before and after each measurement.

2.5.4 Energy Resolution of Parallel Plate Analyser

The energy resolution of the analyser has been determined experimentally by measuring the Full-Width-at-Half-Maximum (FWHM) of the peak energy profile of incident positrons at different impact energies, E_0 . Six collected spectra are displayed in figure 2.8 for values of E_0 ranging from 20 to 86eV.

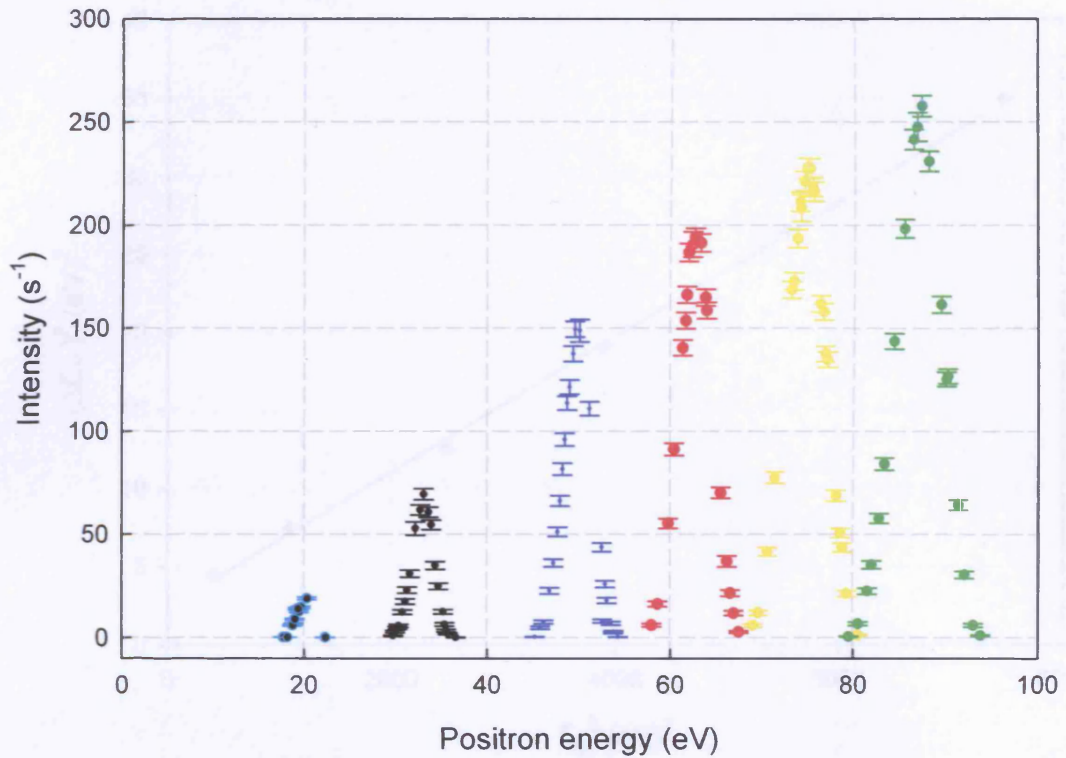


Figure 2.8. Measured beam energy profiles for 20, 33, 50, 62, 74, 86 eV impact energies.

The total energy resolution of the PPA, ΔE_T , is taken as the square root of the quadratic sum of the resolution of the positron incident beam, ΔE_+ , and that of the analyser, ΔE :

$$\Delta E_T = \sqrt{(\Delta E)^2 + (\Delta E_+)^2}. \quad (2.3)$$

Using the relative energy resolution of the PPA, $C = \Delta E / E_0$, equation (2.3) can be rewritten as

$$(\Delta E_T)^2 = C^2 E_0^2 + (\Delta E_+)^2. \quad (2.4)$$

Figure 2.9 shows a plot of $(\Delta E_T)^2$ versus E_0^2 .

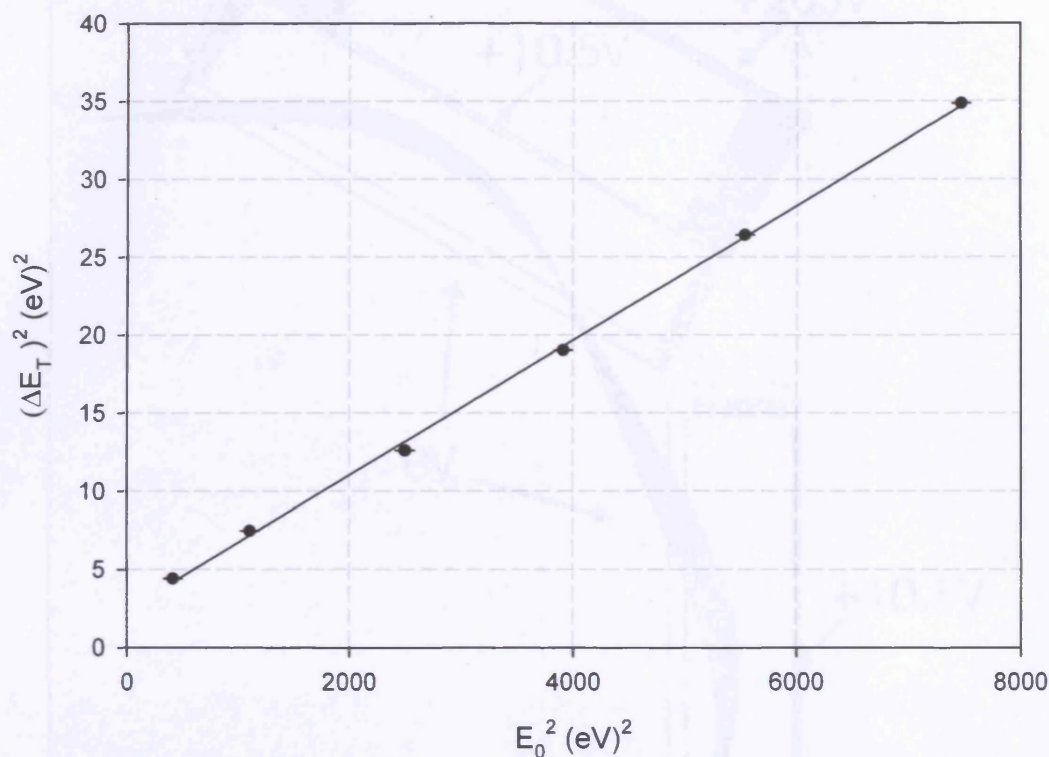


Figure 2.9. The total parallel plate analyser resolution, $(\Delta E_T)^2$, measured as a function of the positron beam energy, E_0^2 .

Figure 2.10 Simulation of the 15eV⁺ trajectories through the PPA

The linear fit yields a value for the energy resolution of the PPA $C = \Delta E/E_0 = (6.56 \pm 0.05)\%$, which is consistent to the previous value of 7.5% both estimated and measured, by Kövér and Laricchia (2001). The inferred intrinsic energy width of the positron beam is $\Delta E_+ = (1.5 \pm 0.1)eV$.

2.5.5 A Computer Simulation of $e^- - e^+$ Flight Times

Various simulations have been performed using an ion optics program (Simion 6, 7) to aid in setting up the experiment. For example, figure 2.10 shows the trajectories for 15eV scattered positrons during the reaction $e^+ (50eV) + H_2 \rightarrow e^- (\theta \sim 0^\circ) + e^+ (\theta \sim 0^\circ; E_+) + H_2^+$ and the corresponding potential setting of the PPA. When produced within the line of sight of the PPA entrance slit, these positrons are successfully extracted and detected.

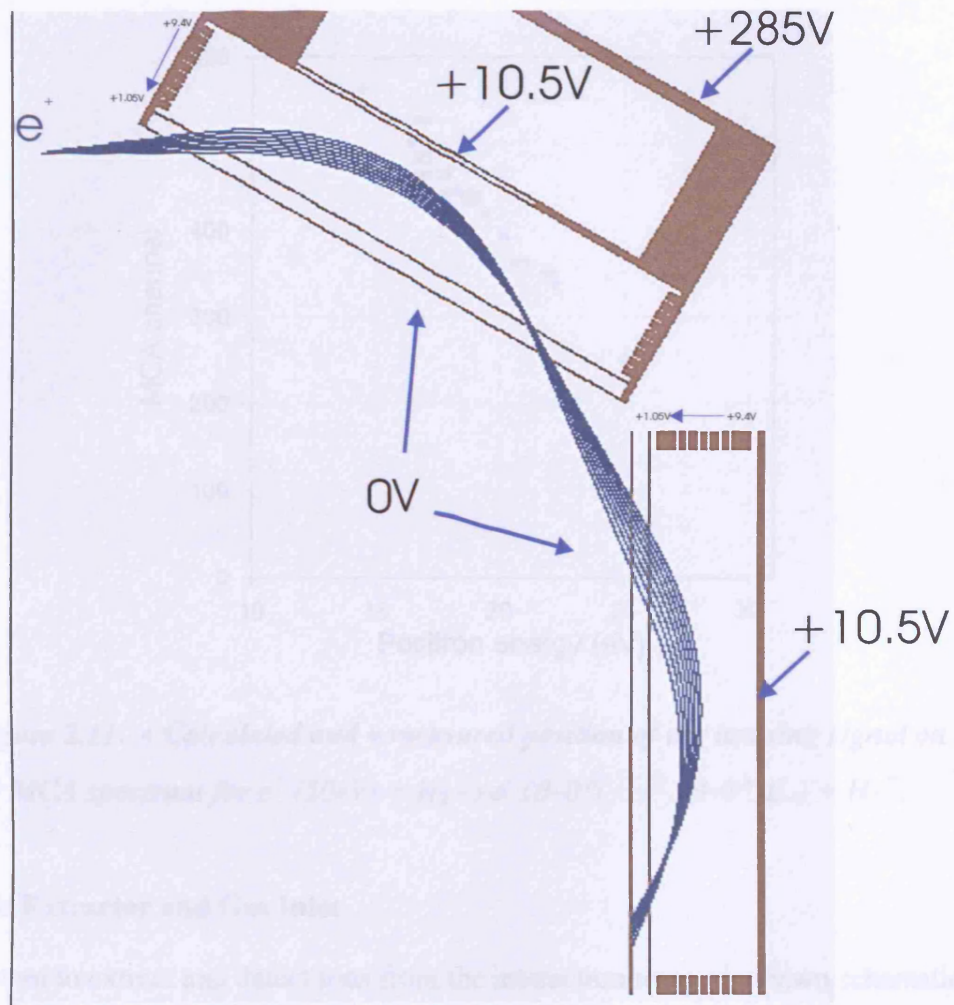


Figure 2.10. Simulation of the $15e^+$ trajectories through the PPA after ionisation from $50e^+$ impact on H_2 . The voltages to the guard electrodes decrease in step of 1V.

Moreover, for each pass-energy the flight time difference between the $e^- - e^+$ has been calculated. As shown in figure 2.11, the agreement between the measured and the calculated position of the ionisation signal has been found to be fair at all positron energies.

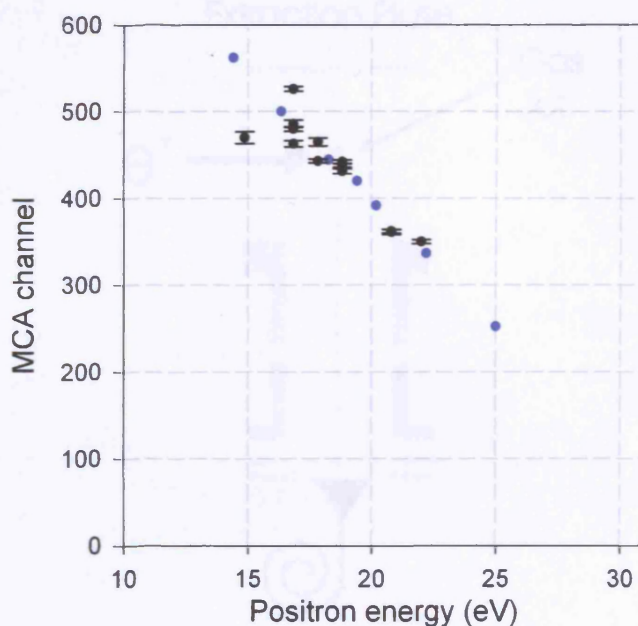


Figure 2.11. • Calculated and • measured position of the ionising signal on the MCA spectrum for $e^+ (50\text{eV}) + \text{H}_2 \rightarrow e^- (\theta \sim 0^\circ) + e^+ (\theta \sim 0^\circ, E_+) + \text{H}_2^+$.

2.6 Ion Extractor and Gas Inlet

The system to extract and detect ions from the interaction region is drawn schematically in figure 2.12. The ion extractor was employed only for the doubly differential cross-section measurements (§5.3) and for the absolute energy calibration of the positron beam (§3.2). In these cases, a parallel electric field is established by applying suitable potentials (typically $\pm 65\text{V}$) to the plate electrodes (50mm x 30mm and 20mm apart) across the interaction region. The extraction of positive ions is enabled within the limits of a 10mm diameter aperture of the negative plate. This hole is covered with 95% transmission Cu mesh to help maintain a uniform electric field between the electrodes. Ions are focused onto the centre of the electrode array (20mm cylindrical lens, 10mm internal diameter; and held at -130V) and accelerated by a 95% transmission Cu grid held at -2600V before hitting the cone of a channel electron multiplier detector (CEM2, type Philips X951BL) at -2500V. As explained in §2.5.2, the grid caused secondary electrons to be reflected back towards the cone of the channeltron. The back of CEM2 was held at -500V. Once again signal pulses are decoupled from the high DC voltage by means of a 1nF capacitor.

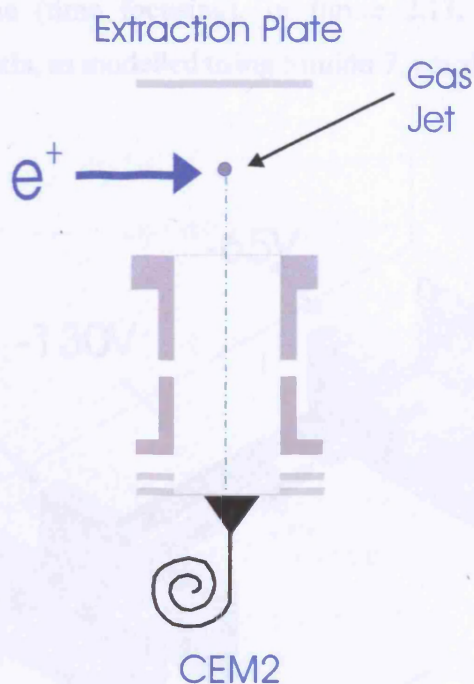


Figure 2.12. Schematic of the extraction and ion detection systems, not to scale.

A multi-capillary array was used to provide a well-defined gas beam with sufficient width to overlap with the positron beam (Steckelmacher *et al.*, 1978; Steckelmacher, 1986). Each capillary was 4mm long with an internal diameter of 4 μ m. A nozzle was preferred for the water differential study, as will be discussed in chapter 4. In both cases, the distance from the end of the gas inlet and the axis of positron beam was 7.5mm. A homemade pressure controller allowed for the fine adjustment of the target gas flow by opening/closing a leak valve with feedback. The pressure of the sample gases above the nozzle was measured using an MKS 127-AA baratron heated capacitance manometer.

The ion yield was measured as a function of the driving pressure and found to be linear over the pressure range used, which was typically around 6torr.

Computer simulations of ion trajectories for singly ionised ions produced from the (dissociative and non-dissociative) ionisation of water have been performed. The method, which is described in §4.7, allowed the estimation of the ion extraction efficiency of the H^+ fragments. Results were found to be in good accord with simulations performed by Beale (2007) using the ion optics program CPO. The simulations also showed that the employed voltage setting achieves the minimum in

time spread of flight-time (time focusing). In figure 2.13, trajectories for H_2O^+ , departing from the beam axis, as modelled using Simion 7, are shown.

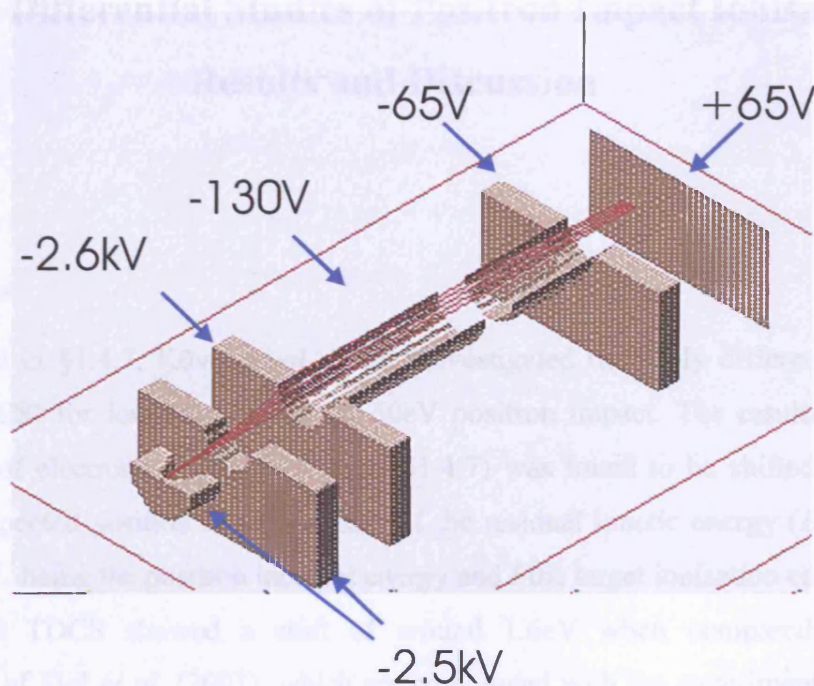


Figure 2.13. Simulation of $0.03\text{eV } H_2O^+$ trajectories through the ion extractor.

2.7 Summary

In this chapter, the experimental set-up used throughout the present work has been described. This includes a discussion of the source and moderator configuration, the vacuum system, the positron beam transport and the detection systems for e^\pm and ions. Moreover, the energy resolution of the analyser and the time-of-flights of positrons and electrons into the analyser, as obtained using a simulation program, have been presented.

Chapter 3

Triply Differential Studies of Positron Impact Ionisation: Results and Discussion

3.1 Overview

As discussed in §1.4.7, Kövér *et al.* (2001) investigated the triply differential cross-section (TDCS) for ionisation of H_2 by 50eV positron impact. The resulting energy distribution of electrons emitted at 0° (see §1.4.7) was found to be shifted by 2.5eV below its expected position of around half of the residual kinetic energy ($E_r/2$, where $E_r = E_+ - I$, E_+ being the positron incident energy and I the target ionisation energy). The experimental TDCS showed a shift of around 1.6eV when compared with the calculations of Fiol *et al.* (2001), which are convoluted with the experimental angular and energy resolutions. Kövér *et al.* (2001) cited among the possible causes of the shift a systematic error or an actual physical effect that occurs simultaneous to ionisation, e.g. vibrational excitation or molecular dissociation of the target. The aim of this work (Arcidiacono *et al.*, 2005a) has been to distinguish between these two conjectures and shed further light on the origin of the effect. Firstly, in order to quantify possible contact potential effects, the beam energy has been calibrated absolutely through the identification of the threshold for positronium formation, E_{Ps} . Secondly, significant contributions from molecular degrees of freedom have been probed by using D_2 and He at the same excess energy of 34.6eV as in Kövér *et al.* (2001). Deuterium has been employed to check the charge-to-mass ratio of the residual target ion and thus investigate possible dissociation, and helium has been used as an example of a target without rotational and vibrational molecular excitations. Finally, to test conclusively the significance of the energy shift, the energy distribution of the positrons scattered from H_2 has also been obtained for the first time (TDCS(e^+)). This has confirmed that the phenomenon is genuine and revealed the occurrence of asymmetries in the energy shared between the two light outgoing particles (electron and positron) after the ionising collision.

In the following sections, details of these experiments and final results are presented for each study and compared with the earlier measurements and theoretical calculations where available.

3.2 Absolute Energy Calibration

The maximum intrinsic energy spread δE of the positron beam in equation 2.1 is mainly dictated by φ_+ , which is the negative positron work function of the moderator surface. Most positrons are thermalised before being re-emitted, and if they reach the surface, they may scatter from contaminants; thus, their kinetic energy can have any value between zero and $e|\varphi_+|$. Additionally, contact potential effects can affect the measured beam energy, E_+ , whose value arises from the cumulative effects of the positron work function and contact potentials.

Since low positron beam intensities prevent conventional absolute energy calibration methods (such as electrons from autoionising or Auger processes), Kövér *et al.* (2001) had employed a relative energy calibration involving scanning the potential on the backplate, V_{ppa} , to determine the energy distribution of the particles passing through the PPA for each voltage applied to the moderator, V_m . In this way, the peak energy is determined for an assigned V_m , as well as the slope of the calibration curve, $V_{ppa}/V_m = c$, where c is the PPA constant (see §2.5.1). For positrons, Kövér *et al.* (2001) found $V_{ppa} = 0.517 (\pm 0.003) \cdot (V_m + 2.22 (\pm 0.01)V)$. Thus, the impact energy of the positron beam was taken as $E_+ = eV_m + 2.2eV$, which means that positrons emerge from the moderator with an initial kinetic energy of 2.2eV. As explained in Kövér *et al.* (2001), this value was found to be consistent with the positron work function $|\varphi_+|$ measured in other experiments in similar non-ultra-high-vacuum-conditions (Zafar *et al.*, 1988; Moxom *et al.*, 1994; Ashley *et al.*, 1996). Furthermore, this value was also found to be in accord with an absolute determination of $2.4 (\pm 0.1)eV$ by a time-of-flight method (Kara, 1999). However, it was not possible to exclude completely a systematic error due to contact potential effects in the present system.

As a consequence of this, a new energy calibration method has been adopted (Arcidiacono *et al.*, 2005a) to allow the determination of the sum of the positron work function and contact potential of the moderator, $e|\varphi_+| + C$. The method consisted of measuring the positronium formation threshold in helium. This has been preferred to,

for example, the ionisation threshold because of the difficulty of distinguishing ions produced by direct ionisation near the threshold from those arising from Ps formation (Ashley *et al.*, 1996). For the energy calibration measurements, the V_m range was chosen in order to establish an incident positron energy that is between the positronium formation threshold in He, E_{Ps} (17.8eV), and the ionisation energy, I (24.6eV).

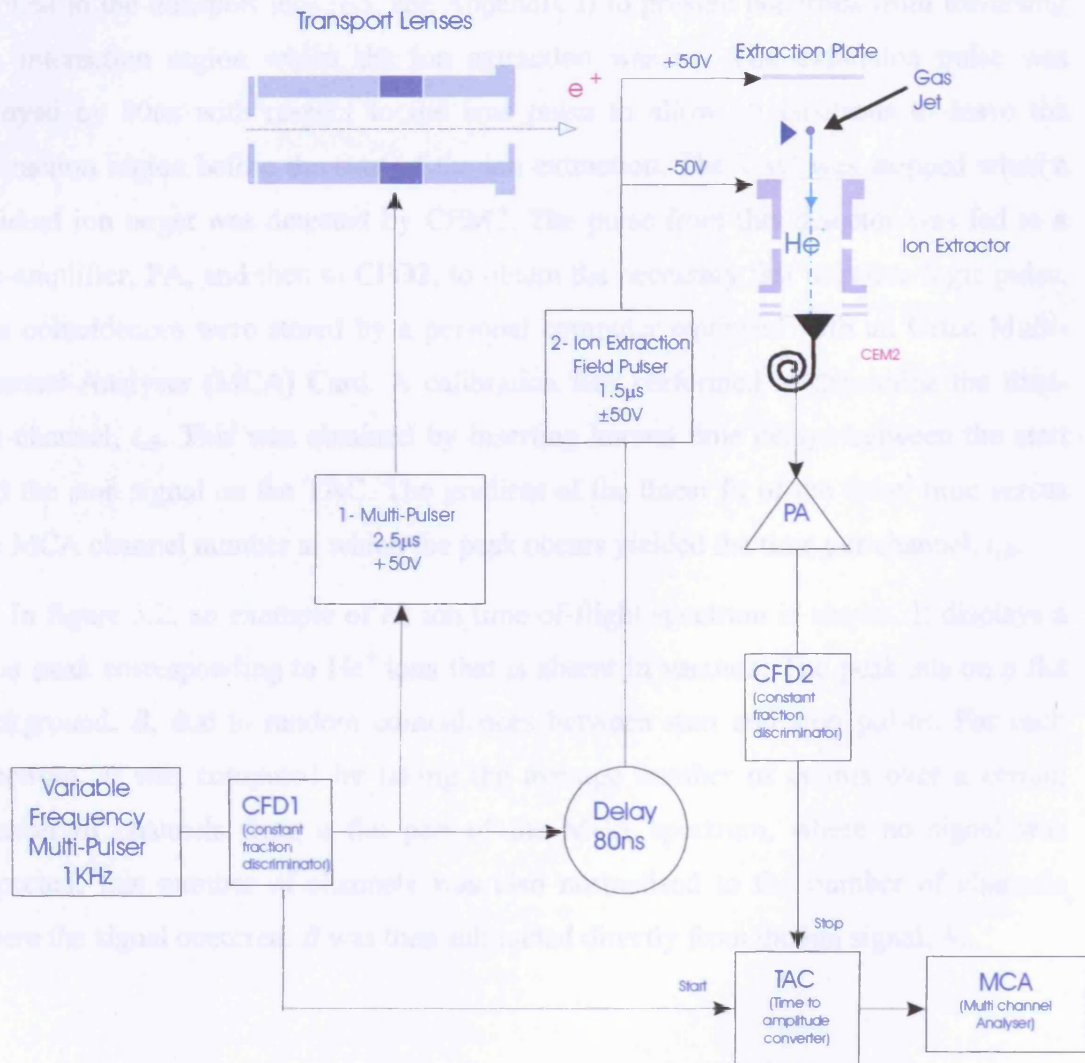


Figure 3.1. A schematic diagram of the electronics and data collection system employed for the absolute energy calibration.

As illustrated in figure 3.1, the ion extraction system was randomly triggered by a homemade variable frequency multi-pulser generator operating at ~1kHz. Its output

was fed into a Constant-Fraction Discriminator (CFD1, Ortec 584) and converted into a fast negative logic pulse. This CFD timing output was used as a start for a Time-to-Amplitude Converter (TAC, Ortec 567). The positive output from CFD1 was used to trigger a second multi-pulser (Carroll&Meynell Ltd), which provided pulses ($\pm 50\text{V}$ high and $1.5\mu\text{s}$ long) to the extraction plates. The same output was also used to feed a third homemade pulser, which generated a pulse ($+50\text{V}$ high and $2.5\mu\text{s}$ long). This was applied to the transport lens (E5, see Appendix I) to prevent positrons from traversing the interaction region whilst the ion extraction was on. The extraction pulse was delayed by 80ns with respect to the lens pulse to allow all positrons to leave the interaction region before the start of the ion extraction. The TAC was stopped when a residual ion target was detected by CEM2. The pulse from this detector was fed to a pre-amplifier, PA, and then to CFD2, to obtain the necessary fast negative logic pulse. The coincidences were stored by a personal computer equipped with an Ortec Multi-Channel-Analyser (MCA) Card. A calibration was performed to determine the time-per-channel, t_{ch} . This was obtained by inserting known time delays between the start and the stop signal on the TAC. The gradient of the linear fit of the delay time versus the MCA channel number at which the peak occurs yielded the time per channel, t_{ch} .

In figure 3.2, an example of an ion time-of-flight spectrum is shown. It displays a clear peak corresponding to He^+ ions that is absent in vacuum. The peak sits on a flat background, B , due to random coincidences between start and stop pulses. For each spectrum, B was computed by taking the average number of counts over a certain number of channels from a flat part of the MCA spectrum, where no signal was expected; this number of channels was also normalised to the number of channels where the signal occurred. B was then subtracted directly from the ion signal, N_i .

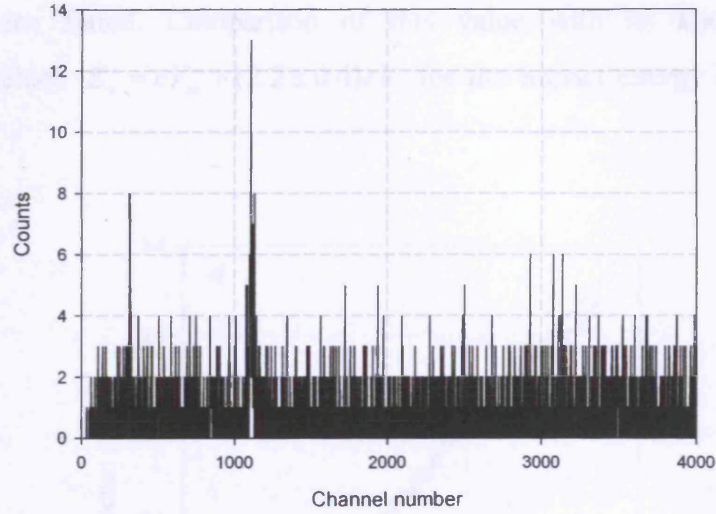


Figure 3.2. A raw ion spectrum obtained for the absolute energy calibration of the positron beam. It was obtained with He for incident e^+ of 19.54eV (run-time ~3 days).

The positronium formation cross-section, $\sigma_{Ps}(E_+)$, is directly proportional to the measured ion yield, $Y_{Ps}(E_+)$, which is defined as:

$$Y_{Ps}(E_+) = \frac{1}{p} \cdot \left[\frac{(N_i(E_+) - B)}{N_+(E_+)} \right], \quad (3.1)$$

where N_i represents the total number of ions with gas; B represents the flat background in the gas spectrum; N_+ is the positron beam intensity and p is the driving pressure of the gas target (see §2.6).

In the course of these measurements, the intensity of the direct beam through the PPA was around $40e^+ \cdot s^{-1}$ and did not vary by more than 10%. The total run time was around two months.

Figure 3.3a shows the energy dependence of the positronium formation cross-section for positrons colliding with He near the threshold, as measured by Moxom *et al.* (1994). By imposing the near-threshold slope of Moxom *et al.* (1994) data, $\sigma_{Ps} = 2.7 \cdot 10^{-2} \cdot (E')^{1.21} \cdot 10^{-16} \text{ cm}^2$ with $E' = E_+ - E_{Ps}$, the fit to the measured ion yield versus moderator voltage has been obtained (Fig. 3.3b). By extrapolating the fitting

curve to a zero ion yield, the inferred position of the onset of Ps formation, $(15.6 \pm 0.4)eV$, has been found. Comparison of this value with its known threshold, $E_{Ps}=17.8eV$, yielded $E_+ = eV_m + (2.2 \pm 0.4)eV$ for the impact energy of the positron beam.

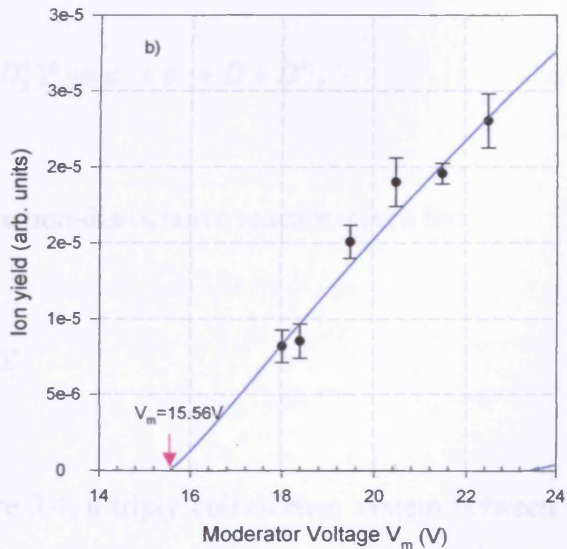
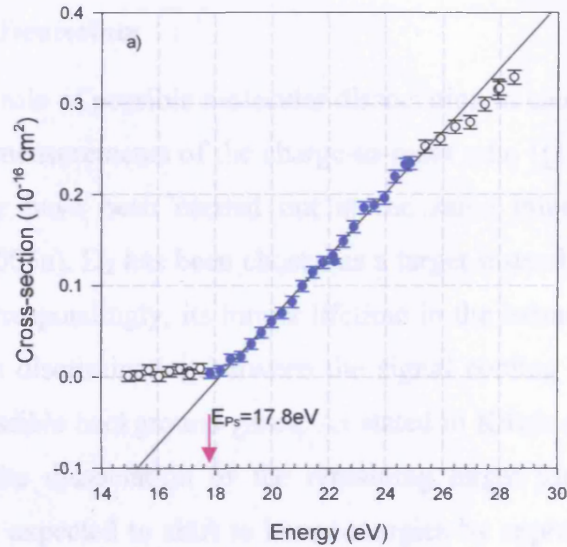


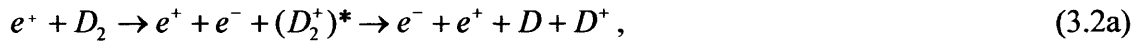
Figure 3.3. a) Positronium formation cross-section, σ_{Ps} , near the threshold (Moxom et al., 1994) and a least square fit to the cross-section.

b) Measurements of the ion yield close to the threshold for positronium formation in helium (Arcidiacono et al., 2005a). The solid line corresponds to the fit to the results of Moxom et al. (1994).

Within experimental uncertainties, this value for E_+ agrees with the previous determination (Kövéér *et al.*, 2001), which means that contact potential effects are not significant. Consequently, the possibility that the energy shift in the TDCS(e^-) is due to a systematic underestimation of the energy has been ruled out.

3.3 TDCS(e^-) for Deuterium

To study the possible role of possible molecular dissociation in causing the energy shift (Kövéér *et al.*, 2001), measurements of the charge-to-mass ratio (Q/M) of the deuterium ion in the final state have been carried out at the same impact energy of 50eV (Arcidiacono *et al.*, 2005a). D_2 has been chosen as a target instead of H_2 because of its heavier mass and, correspondingly, its longer lifetime in the extraction region, as well as the greater ease in discriminating between the signal coming from the target and those arising from possible background gases. As stated in Kövéér *et al.* (2001), if ECC is accompanied by the dissociation of the remaining target ion, D_2^+ , the electron distribution would be expected to shift to lower energies by approximately half of the dissociation energy ($E_d/2$, where $E_d=2.65\text{eV}$) in accordance with the reaction:



and competing with the non-dissociative reaction given by:



As shown in figure 3.4, a triply coincidence system between the ejected electron, the remnant ion and the scattered positron was set-up for this study. This allowed the determination of the Q/M of the final state ion (D_2^+ or D^+) associated with the e^- and e^+ .

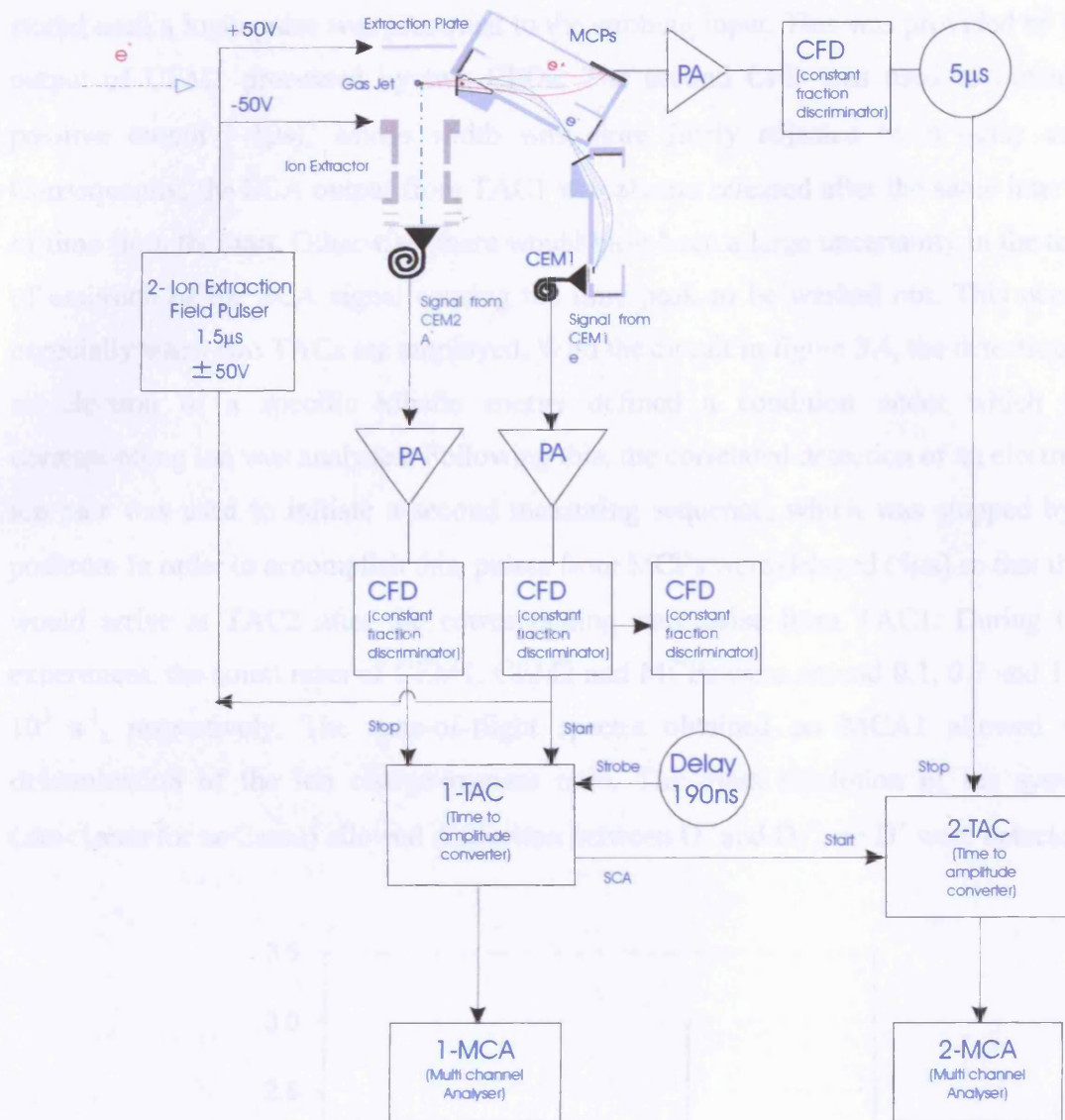


Figure 3.4. A schematic diagram of the ion detection sequence and timing electronics employed for the study of the TDCS(e^-) from positron impact ionisation

upon D_2 : $e^+ (50\text{eV}) + D_2 \rightarrow e^+ (\theta=0^\circ) + e^- (\theta=0^\circ, E.) + D_2^+$ or
 $e^+ (50\text{eV}) + D_2 \rightarrow e^+ + e^- + (D_2^+)^* \rightarrow e^+ (\theta=0^\circ) + e^- (\theta=0^\circ, E.) + D + D^+$.

The voltage pulses (1.5µs; ±50V) applied to the capacitor plates on either side of the gas nozzle allow the extraction of the ions from the scattering region. The extraction was triggered upon detection of an electron of a given energy by CEM1. Pulses from CEM1 and CEM2 were processed by the CFDs and used as the start and stop signals respectively for TAC1. This was operated in a strobe mode, in which the output was

stored until a logic pulse was presented to the strobing input. This was provided by the output of CEM1 processed by two CFDs. The second CFD was used to obtain a positive output ($\sim 1\mu\text{s}$), whose width was more finely adjusted by a delay unit. Consequently, the SCA output from TAC1 was always released after the same interval of time from the start. Otherwise, there would have been a large uncertainty in the time of emission of the SCA signal causing the time peak to be washed out. This occurs especially when two TACs are employed. With the circuit in figure 3.4, the detection of an electron of a specific kinetic energy defined a condition under which the corresponding ion was analysed. Following this, the correlated detection of an electron-ion pair was used to initiate a second measuring sequence, which was stopped by a positron. In order to accomplish this, pulses from MCPs were delayed ($5\mu\text{s}$) so that they would arrive at TAC2 after the corresponding start pulse from TAC1. During this experiment, the count rates of CEM1, CEM2 and MCPs were around 0.1 , 0.7 and 10^2 - 10^3 s^{-1} , respectively. The time-of-flight spectra obtained on MCA1 allowed the determination of the ion charge-to-mass ratio. The mass resolution of the system ($\Delta m < 1 \text{ amu}$ for $m = 2 \text{ amu}$) allowed distinction between D^+ and D_2^+ , no D^+ were detected.

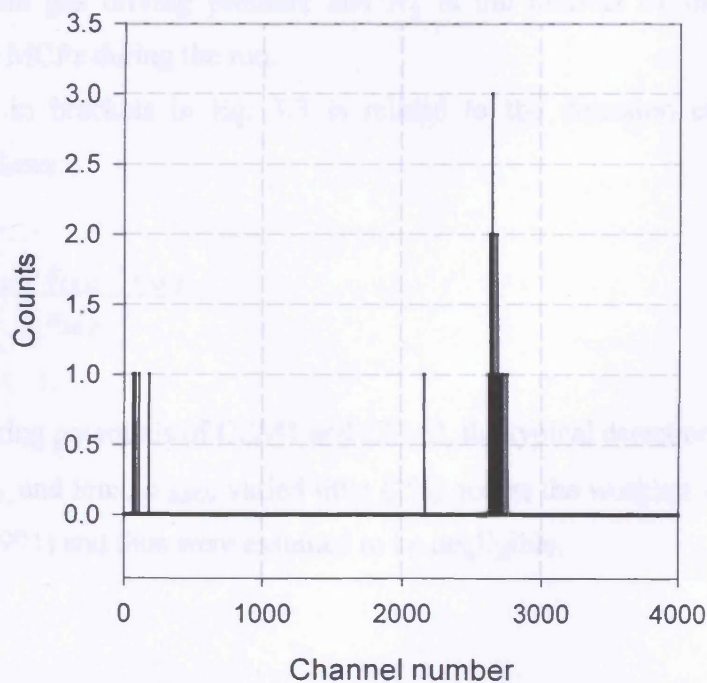


Figure 3.5. A coincidence spectrum between $e^- - \text{D}_2^+$ as obtained with the PPA set to detect 24.4eV electron (run time = 325,641s).

Figure 3.5 shows the product ion mass spectrum obtained by the collision of 50eV positrons with deuterium with the PPA set to detect 24.4eV electron. The low counting rate in TDCS studies for positron impact ensures that dead-time of the electronics does not cause relevant distortion in coincidence spectra.

As before (§3.2), the random background was determined in each gas spectrum. Also, to take fully into account possible background underneath the ionisation signal, C_G , the measurements were repeated in vacuum yielding, C_V .

The relative triply differential ionisation cross-section is determined from the D_2^+ yield as follows:

$$\frac{d^3\sigma_i^+}{d\Omega_-d\Omega_+dE_-} \propto Y_i = \frac{1}{E_-p} \cdot \left[\frac{(C_G - C_V)}{N_+} \right], \quad (3.3)$$

where C_G and C_V represent the number of electron-positron-ion coincidences recorded in gas and vacuum, respectively; $E_- = eV_{ppd}/c$ (see §2.5.1) is the energy of the electron transmitted by the spectrometer and corrects for the transport efficiency of the PPA (see §2.5.4); p is the gas driving pressure and N_+ is the number of incident positrons detected by the MCPs during the run.

The term in brackets in Eq. 3.3 is related to the detection efficiency of the detectors as follows:

$$\frac{C_G - C_V}{N_+} \propto \frac{\varepsilon_{CEM1} \cdot \varepsilon_{CEM2} \cdot \varepsilon_{MCP}}{\varepsilon_{MCP}}. \quad (3.4)$$

At the working potentials of CEM1 and CEM2, the typical detection efficiencies for electrons, ε_{CEM1} , and ions, ε_{CEM2} , varied little (2%) across the working voltages (Philips Components, 1991) and thus were assumed to be negligible.

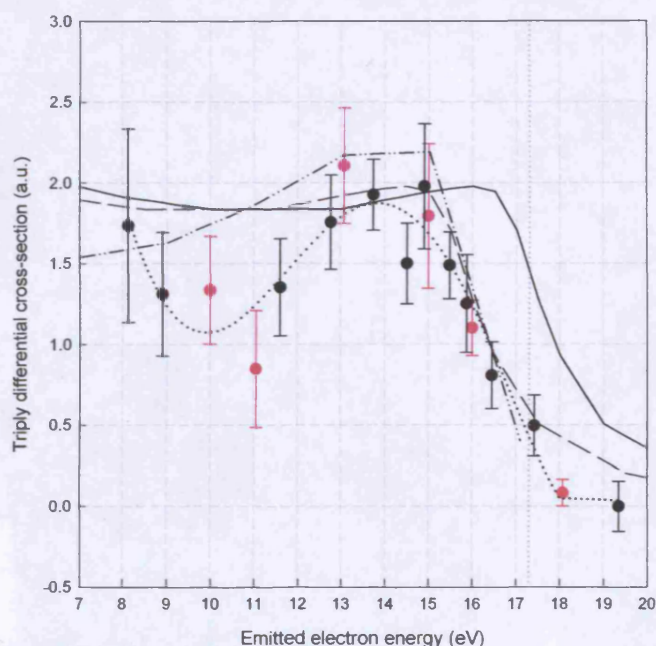


Figure 3.6. The triply differential ionisation cross-section for 50 eV positron incident on \bullet D_2 (Arcidiacono *et al.*, 2005a) \bullet H_2 (Kövér *et al.*, 2001). Full line: theory (Fiol *et al.*, 2001), 3C. Dashed line: theory shifted backwards by 1.6 eV. Dashed dot-dot: CTMC (Fiol and Olson, 2002). Dot line: eye guide representing a polynomial fit.

Following Kövér *et al.* (2001), the relative triply differential cross-section measured for D_2 has been converted to an absolute scale by normalisation to the theoretical results of Fiol *et al.* (2001). The results are shown in figure 3.6 along with the previous data of Kövér *et al.* (2001), the CTMC calculations of Fiol and Olson (2002) and the quantum mechanical prediction of Fiol *et al.* (2001). These theories have been discussed previously in §1.4.7.

The most distinctive feature of the comparison between both sets of experimental data is their agreement and, once again, their displacement from the theory of Fiol *et al.* (2001) towards lower energies: the theory peaks at 16.5 eV, while the experimental results rise to a maximum at around 15 eV.

The fact that no D^+ has been observed during the measurements is not a conclusive proof that dissociative ionisation simultaneous to ionisation does not occur, as the extraction may not be as efficient in collecting energetic atomic fragments. However, the observation that the energy dependence of the triply coincident D_2^+ signal in figure

3.6 is the same as that earlier observed (Kövér *et al.*, 2001) does exclude dissociative ionisation from being responsible for the energy shift in the electron energy distribution.

3.4. TDCS(e^-) for Helium and TDCS(e^+) for Molecular Hydrogen

3.4.1 The Electronics

The electronic units employed to process the signals in these determinations are schematically indicated in figure 3.7 and they comprise a TAC, an MCA and associated pulse shaping circuitry.

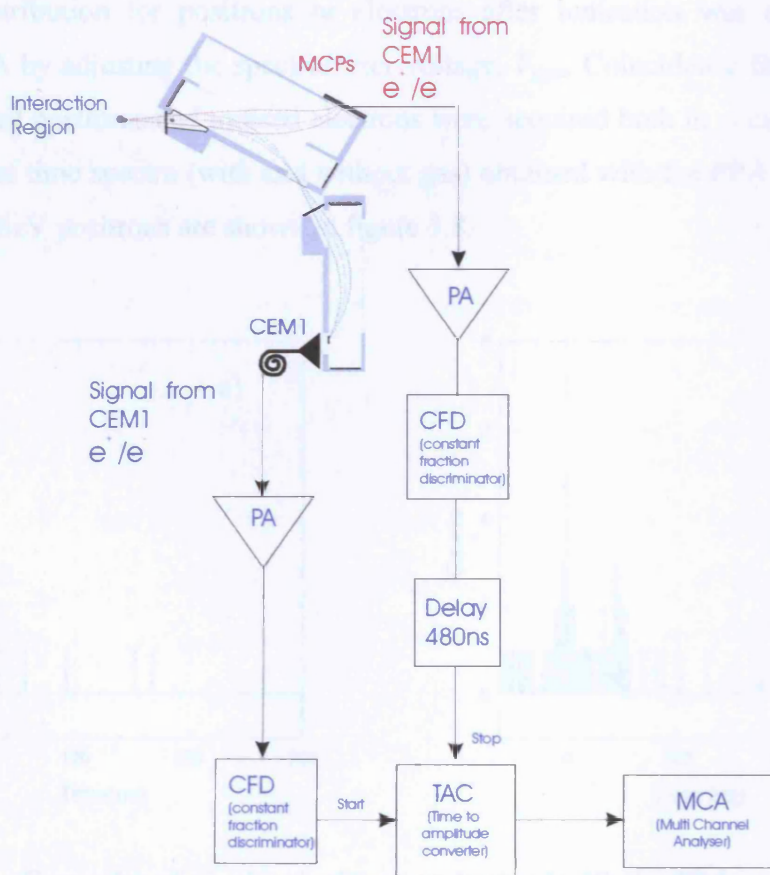
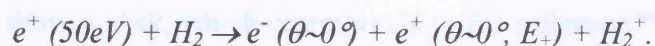
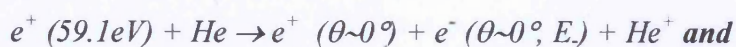


Figure 3.7. A schematic illustration of the delayed coincidence timing circuit used to measure the $e^+ - e^-$ coincidences from the following reactions:



The timing sequence was initiated by a positron (or an electron), arriving at CEM1. This pulse, after being amplified by a pre-amplifier, was fed into CFD1. The timing output from CFD1 started a TAC (Ortec 567). The corresponding remnant partner (electron or positron) was detected by the MCPs. This signal was delayed by 480ns and fed to the stop of the TAC. As a result of the high-count rate of the MCPs, an inverted timing sequence was adopted to reduce the probability of pulses from CEM1 arriving during the TAC dead time. The positron-electron coincidences were collected and stored event-by-event by a PC-based MCA.

3.4.2 Experimental Method

The energy distribution for positrons or electrons after ionisation was ascertained through the PPA by adjusting the spectrometer voltage, V_{ppa} . Coincidence time spectra between scattered positrons and ionised electrons were acquired both in vacuum and in gas. Examples of time spectra (with and without gas) obtained with the PPA set for the detection of 20.8eV positrons are shown in figure 3.8.

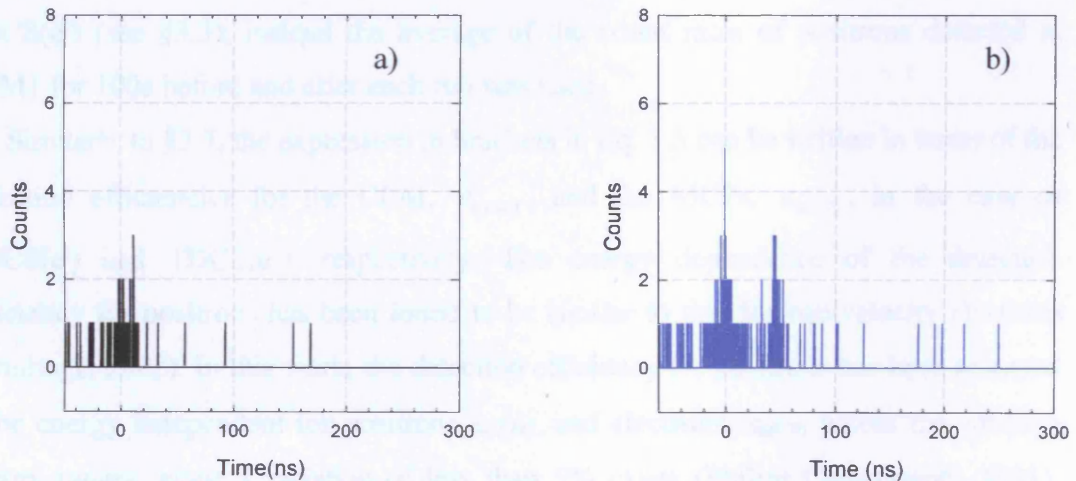


Figure 3.8. Examples of $e^+ - e^-$ coincidences obtained with the PPA set to detect 20.8eV positrons. (a) Raw spectrum acquired in 2 days in vacuum. (b) Sum of raw spectra with gas, H_2 , for a total run-time of 5 days.

Both these spectra show a peak, which corresponds to the reference “time zero”. This peak arises from positron-gamma coincidences due to the annihilation of positrons at a

detector (Kövér and Laricchia, 1998). In gas spectra (Fig 3.8b), an additional signal occurred at a time, $t \sim 45\text{ns}$, in this case, corresponding to the e^-e^+ time-of-flight difference, $\Delta t = |t_- - t_+|$ (see e.g. §2.5.5). In addition, a flat background can be observed in gas-on and gas-off spectra (Fig. 3.8a and b). This is due to random coincidences between CEM1 and the MCPs.

The relative triply differential cross-section for ionisation of He and H₂ can be expressed in terms of experimentally determined parameters as:

$$\frac{d^3\sigma_i^+}{d\Omega_- d\Omega_+ dE_{+/-}} \propto \frac{1}{E_{+/-} p} \cdot \left[\frac{(C_G - C_V)}{N_+} \right], \quad (3.5)$$

where C_G and C_V represent the time-normalised number of the measured electron-positron coincidences in gas and vacuum, respectively; p is the driving pressure of the He or H₂ targets, and $E_{+/-}$ is the energy for the scattered positron or ejected electron, respectively (see §2.5.1). During the measurements of the positron energy distribution, TDCS(e^+), the direct beam, N_+ , could not be measured simultaneously as for the TDCS(e^-) (see §3.3), instead the average of the count rates of positrons detected at CEM1 for 100s before and after each run was used.

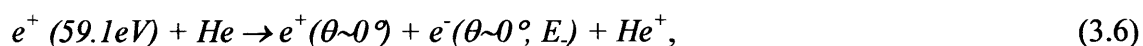
Similarly to §3.3, the expression in brackets in Eq. 3.5 can be written in terms of the detection efficiencies for the CEM, ε_{CEM1} , and the MCPs, ε_{MCPs} , in the case of TDCS(e^-) and TDCS(e^+), respectively. The energy dependence of the detection efficiency for positrons has been found to be similar to that for equivelocity electrons (Armitage, 2002). In this work, the detection efficiency for positrons has been assumed to be energy independent for positrons ε_{CEM1} , and electrons, ε_{MCPs} across the working energy ranges, since a variation of less than 5% exists (Philips Components, 1991). Therefore no correction was introduced in Eq. 3.5.

The number of voltage values of V_{ppa} was chosen as a compromise between avoiding too lengthy acquisition times and achieving a detailed spectrum with good statistics. In the case of the TDCS(e^-) measurements for He (§3.4.3), the total run time was around 1 month. The count rate at CEM1 was approximately 0.07s^{-1} and the count rate at the MCPs was of the order of 10^2s^{-1} .

For the TDCS(e^+) study (§3.4.4), the overall measuring time was around 10^5 s at each positron energy in the (15–24)eV region. The intensity of the incident positron beam was found to be constant (to within 2%), throughout the course of these measurements. The count rate at CEM1 was around 0.03s^{-1} and the count rate at the MCPs was of the order of 10^2s^{-1} , as measured sequentially at each pass-energy (§2.5.3). The uncertainty associated with the results for the TDCS(e^+) comprises both statistical errors and a fluctuation of the gas pressure (typically $\sim 1\%$).

3.4.3 TDCS(e^-) for Helium

The following reaction has been investigated:



as an example of an atomic target for which no energy loss through molecular excitations occurs (Arcidiacono *et al.*, 2005a).

The triply differential cross-section, TDCS(e^-), for He has been studied for a positron impact energy of 59.1eV in order to have the same residual kinetic energy of 34.3eV as in the case of H_2 . Experimental data have been normalised to the theoretical values calculated by Fiol *et al.* (2001) for comparison.

Figure 3.9 displays the results for He along with the previous results (Kövéér *et al.*, 2001 and §3.3) and theories (Fiol *et al.*, 2001; Fiol and Olson 2002). Again, the most striking aspect of these data is the similarity of energy dependence to that for H_2 and the shift towards lower energies when compared with the theory of Fiol *et al.* (2001).

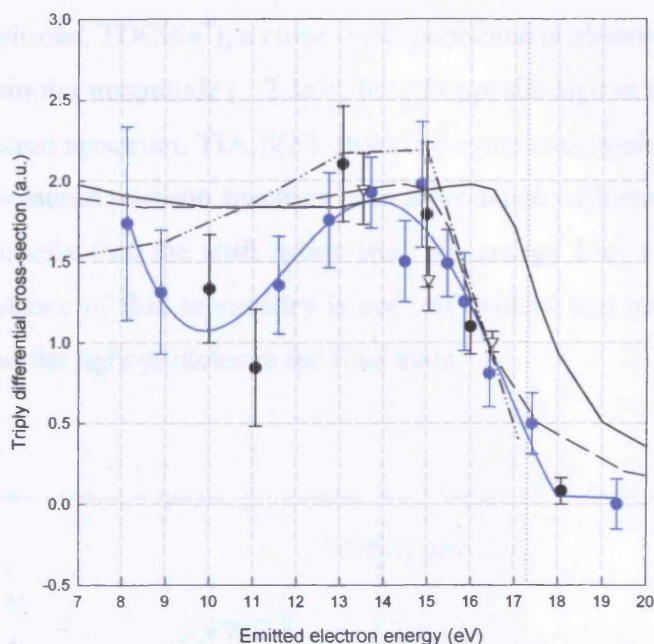


Figure 3.9. The triply differential ionisation cross-section for \bullet 50eV positron incident on H_2 (Kövér *et al.*, 2001); \bullet 50eV positrons incident on D_2 (Arcidiacono *et al.*, 2005a); ∇ 59.1eV positrons incident on He (Arcidiacono *et al.*, 2005a). Full line: theory (Fiol *et al.*, 2001), 3C. Dashed Line: theory shifted backwards by 1.6eV. Dashed dot-dot: CTMC (Fiol and Olson, 2002). Blue line: eye guide.

Summarising, the present results for He indicate as unlikely the possibility that the shift arises from an energy loss through molecular excitation simultaneous to ionisation.

3.4.4 Positron Energy Spectrum for H_2 : TDCS(e^+)

The energy shift observed in the TDCS(e^-) (Kövér *et al.*, 2001) was confirmed by an absolute energy calibration (§3.2). The analysis of the residual ion (§3.3) and the study with He (§3.4.3) imply that the energy balance should be provided by the energy spectrum of the scattered positron. This has been investigated by measuring it explicitly in the reaction: $e^+ (50\text{eV}) + H_2 \rightarrow e^- (\theta \sim 0^\circ) + e^+ (\theta \sim 0^\circ, E_+) + H_2^+$. The scattered positron spectrum for 50eV positron impact on H_2 is presented in figure 3.10. The positron spectrum has been normalised to the maximum of the electron data.

On comparing the energy distributions of the ejected electrons, $\text{TDCS}(e^-)$, and that of the scattered positrons, $\text{TDCS}(e^+)$, a close correspondence is observed: the $\text{TDCS}(e^+)$ exhibits a shift of similar magnitude ($\sim 2.5\text{eV}$) but of opposite sign in comparison to the corresponding electron spectrum, $\text{TDCS}(e^-)$, from the equal energy-sharing value, $E_r/2$. The fact that the measured positron spectrum is in accordance with energy conservation excludes the hypothesis that the shift arises from an energy loss to the target. The reason for the existence of this asymmetry is not self-evident and might be related to the low velocities of the light particles in the final state.

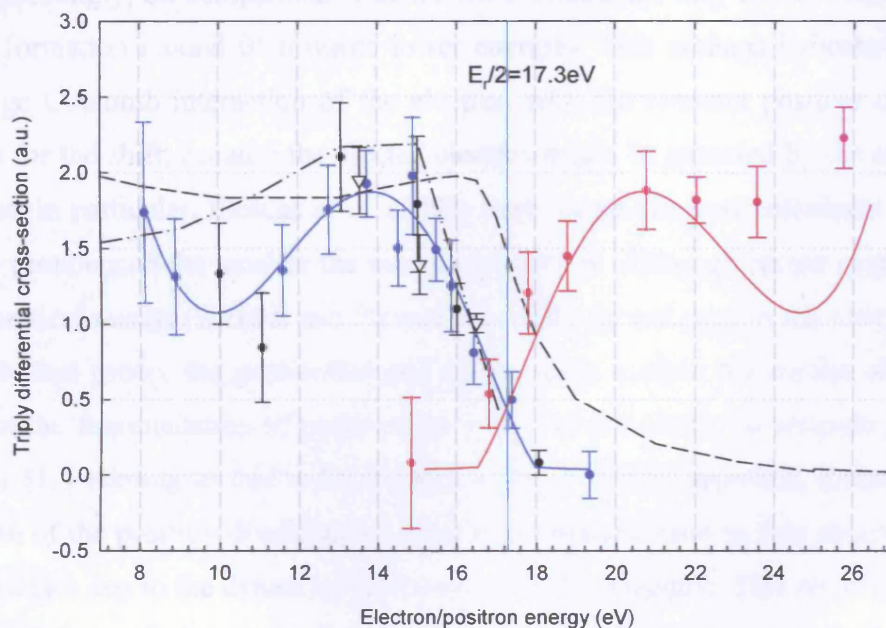


Figure 3.10. Experimental and theoretical results for the triply-differential ionisation cross-sections for ● the scattered positron spectrum for H_2 for 50eV incident positrons (Arcidiacono et al., 2005a); ● the ejected electron spectrum for H_2 for 50eV incident positrons (Kövér et al., 2001); ● the ejected electron spectrum for D_2^+ (Arcidiacono et al., 2005a); ▽ the electron spectrum for 59.1eV positrons incident on He (Arcidiacono et al., 2005a). Dashed line is the theory folded with the experimental resolutions (Fiol et al., 2001). Dash-dot line is the CTMC calculation (Fiol and Olson, 2002). The blue and red solid lines are guides to the eye only.

Since Ps formation is very competitive at the low energy investigated, it has been suggested (Walters, 2005) that the Ps formation channel might strongly influence the shape of the positron and electron energy distributions by absorbing events around $E_r/2$. Alternatively, it is proposed that the smaller energy sharing between the departing particles could arise from a stronger post-collisional interaction between the e^\pm and the receding ion target at this impact energy than at the higher energy of 100eV. This suggestion has been used in a recent study by the Belfast group (Shah *et al.*, 2003). They performed measurements with 10 and 20 keV H^+ incident on H_2 and He resulting in electrons ejected with velocities comparable with those of the present study ($\sim 2 \cdot 10^6$ m/s). Interestingly, on comparison with CTMC calculations, they found a similar shift in ECC formation around 0° towards lower energies. This perhaps indicates that the long-range Coulomb interaction of the electron with the remnant positive target ion accounts for the shift, because the ejected electron might be attracted by the remaining ion target. In particular, Illescas *et al.* (2002) have found this post collisional effect to be more pronounced the smaller the nuclear velocity is. Although recent experimental and theoretical results (Sarkadi and Barrachina, 2005) do not support the interpretation of the Belfast group, the post-collisional effect might explain the results of Sarkadi (2003) in the fragmentation of positronium in Ps–He collisions. To reiterate the main points in §1.5 relating to this work, Sarkadi, using a CTMC approach, found that the maximum of the positron distribution in the fragmentation cross-section should drift to lower energies due to the dynamical polarisation of the projectile. This result displays a good agreement with the shape of the measured longitudinal energy distribution of the positron of Armitage *et al.* (2002). Moreover, Sarkadi (2003) determined the longitudinal energy distribution of the residual electrons by employing the same method and found to be shifted with respect to the peak in the positron spectra. Although this prediction still awaits experimental confirmation, it can be hypothesised that if the effect is significant in the fragmentation of Ps with the target left in a neutral state, then in the ionisation of H_2 with the target left in an ion state, the phenomenon would be expected to be even more manifest.

In conclusion, at present, the energy-shift effect observed by Kövér *et al.* (2001) and Arcidiacono *et al.* (2005a) is genuine and not due to doubly inelastic processes. However, it still has no clear explanation and no consistent description by quantum-mechanical theoretical treatments. Since the process is a potentially important few-body

effect, it might be a suitable testing ground for recently developed *ab initio* approaches. These might shed some light into its exact origin.

3.5 Summary

Several systematic investigations have been carried out to complement the work of Kövér *et al.* (2001) and resolve the main uncertainties of that study. Firstly, an absolute energy calibration has been outlined (§3.2), which has been used to check for a possible underestimation of contact potential contribution in Kövér *et al.* (2001). Good agreement has been found with the previous result. Secondly, results for the TDCS(e^-) for D_2 as in Kövér *et al.* (2001) have been presented (§3.3), which ruled out that occurrence of molecular dissociation together with ionisation could determine the shift. The following work on the TDCS(e^-) for He indicated as unlikely that molecular excitations were involved. Finally, the distribution of kinetic energies of positrons scattered in the forward direction from a H_2 target by 50eV positron impact have been measured. This conclusively confirmed the existence of an asymmetric energy sharing between e^- and e^+ around $E_r/2$.

Two possible hypotheses of the observed asymmetry have been reported. One suggestion is the dominance of the Ps formation channel over ionisation at the low e^+ impact energy of this study (Walters, 2005). The other is the presence of a long-range Coulomb interaction between the residual ion target with the e^+ and the e^- after ionisation. Hence, whilst the e^- is pulled back towards, the e^+ is pushed forward by the recoiling ion. This is an extension of the explanation which Shah *et al.* (2003) offered for the case of proton impact.

Chapter 4

Experimental Apparatus for Measuring Integral Cross Section for Positron Impact Ionisation of H₂O

4.1 Overview

The experimental apparatus used to study the ionisation of water vapour by positron impact with and without Ps formation is outlined in this chapter. A schematic diagram of the layout is given in figure 4.1. The basic system, which employed a crossed-beam geometry, has previously been described by Ashley (1996) and Kara (1999). The modifications made in order to carry out the measurements on water vapour are detailed.

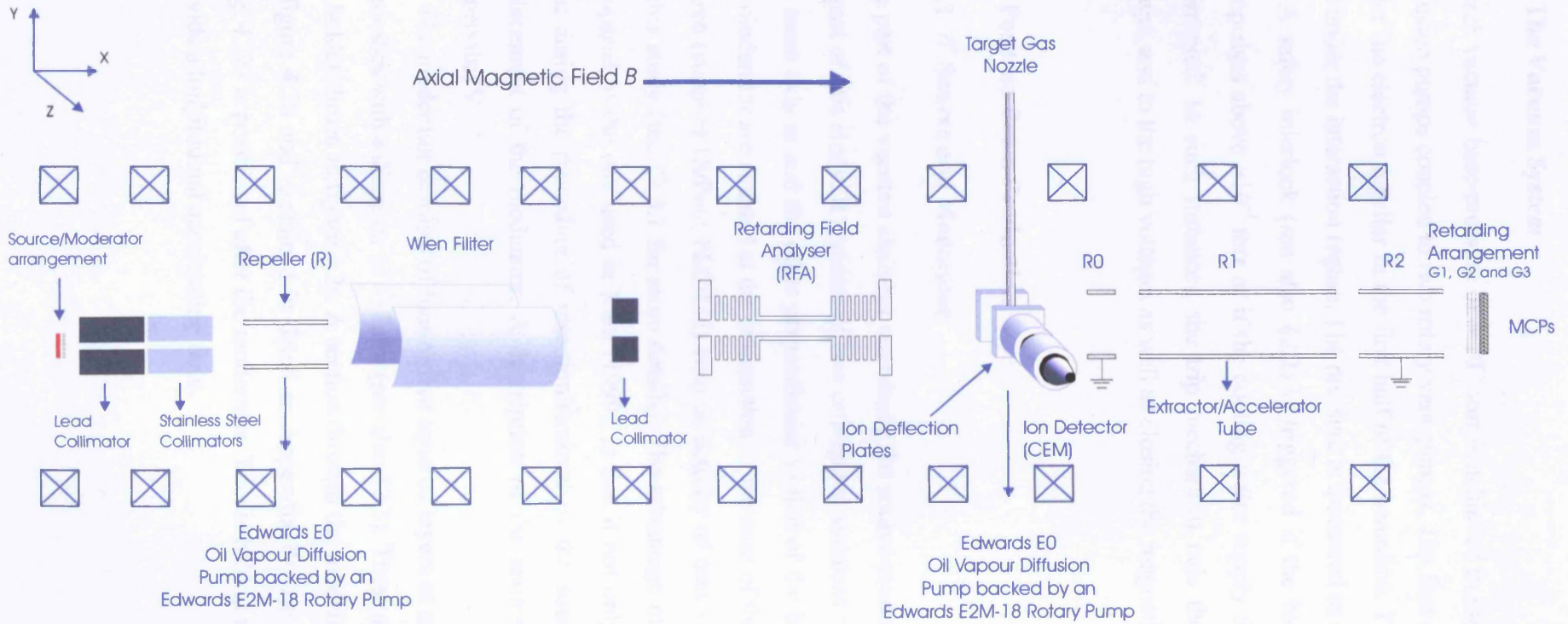
As for the electrostatic apparatus described in §2.3, the slow positron beam is produced by moderating the fast β^+ particles from a ²²Na source by a set of annealed W meshes, accelerating the slow particles to the desired energy and by guiding them using a magnetic field.

Most secondary electrons originating from the source-moderator assembly are removed from the positron beam by a repeller tube. A Wien filter separates the beam from the background of residual fast particles and γ -rays. This filter is followed by a retarding field analyser.

In the interaction region, the positron beam intersects a jet of the target gas emerging from a graphite nozzle. The region of beam overlap is positioned between the two parallel plates used for the extraction of ions. These are focused onto the cone of a channeltron detector by a two-element electrostatic lens system as in §2.6.

On leaving the interaction chamber, scattered and unscattered positrons are accelerated by a cylindrical electrode towards a detector at the end of the beam line. Further retarding elements are employed to bias off completely or partially the positron beam.

The various parts of the system are discussed in the following sections and include the source and moderator assembly, the ion extractor, and the various components of the beamline. Data collection procedures for water vapour studies can be found in chapter 5.



102

In order from left to right:
 1 Lead Collimator; 10mm diameter per 65mm long
 2 Stainless Steel Collimators; 15mm diameter per 15mm long
 1 Lead Collimator; 10mm diameter

 Helmholtz Coil

Figure 4.1. Schematic overview of the experimental set-up.

4.2 The Vacuum System

A high vacuum base-pressure of $\approx 10^{-6}$ torr is achieved in the system by means of two diffusion pumps coupled to two rotary vane pumps. The first diffusion pump is situated under the electron repeller in the first half of the beamline. The second one is situated, just under the interaction region. The pressure is measured as described in §4.6.

A safety interlock (see also §2.2) is triggered if the backing pressure for either pump rises above $\approx 10^{-1}$ torr or if the cooling water supply for the diffusion pumps is interrupted. In such instances, the trip mechanism cuts the power to the diffusion pumps, and to the high voltages as well as closing the magnetic valves.

4.3 Positron Beam Production

4.3.1 β^+ Source and Moderator

The part of the vacuum chamber containing the source-moderator has been redesigned as part of this study. It consists of two orthogonal stainless steel housings, one having the same axis as and the other perpendicular to that of the beam-line. The source and the moderator are situated at the intersection of the axes of these cylinders. A new ²²Na source (supplier DuPont PLC/Ltd) with an activity of 6mCi was used over the course of this study (see §2.3.1 for more details). The advantage of the new arrangement, as compared to the one used in Kara (1999), is that it not only minimises the exposure time during the procedure of insertion/removal of the source, but also allows easy replacement of the moderator. A description of the source holder can be found in Appendix IV.

The moderator consists of four or five squared layers of annealed 90% transmission W meshes with a diameter of ~ 18 mm (see also §2.3). These are maintained in place via the holder shown in figure 4.2a. A section through the moderator arrangement is shown in figure 4.2b and explained in detail in Appendix IV. An earthed un-annealed grid (Fig. 4.2b) is positioned after the moderator. This is held at a positive potential, V_m , to provide a longitudinal accelerating field.

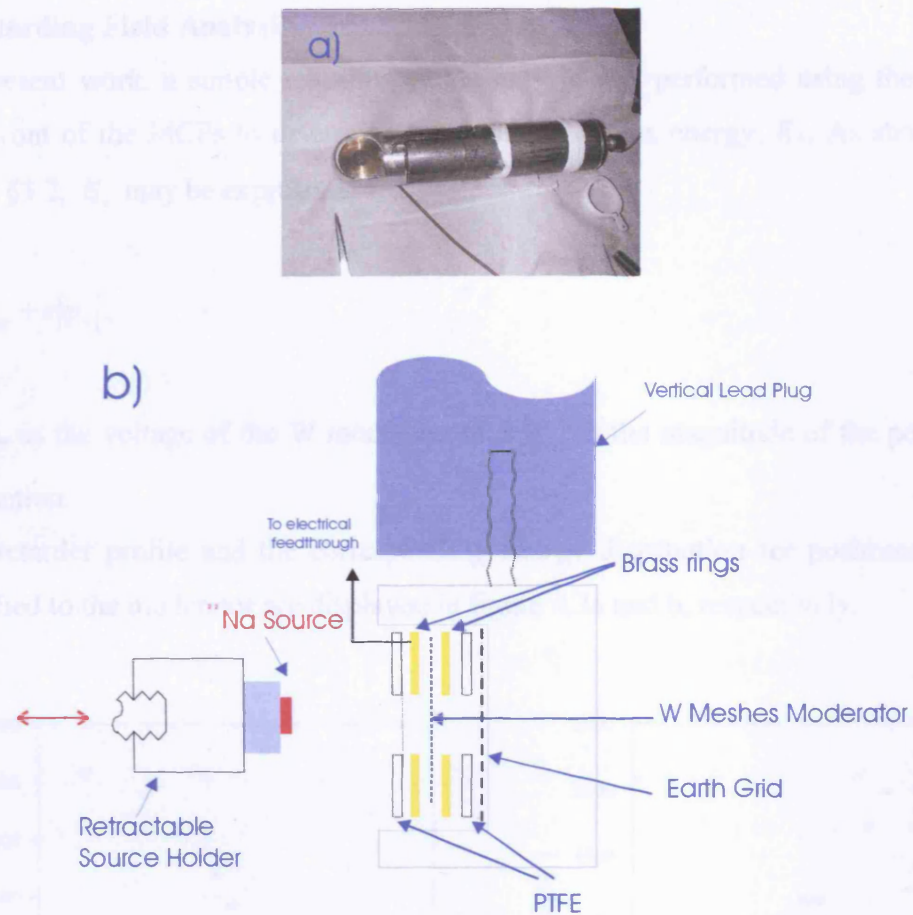


Figure 4.2. a) Picture of the moderator holder and Pb plug.

b) Section through the source-moderator arrangement (not to scale).

In this respect, before substituting the source-moderator assembly, several tests were performed using a dummy-source to ensure that the moderator and the earthed grid would be positioned normally to the beam axis and to test for possible difficulties. The correct alignment between the moderator and the source was marked at the top of the Pb plug and the top flange for subsequent operation.

4.3.2 Retarding Field Analysis

In the present work, a simple retarding field analysis was performed using the grids (G₂) in front of the MCPs to determine the positron kinetic energy, E_+ . As shown in §2.3 and §3.2, E_+ may be expressed:

$$E_+ = eV_m + e|\phi_+|, \quad (4.1)$$

where V_m is the voltage of the W moderator and $|\phi_+|$ is the magnitude of the positron work function.

The retarder profile and the corresponding energy distribution for positrons with 10V applied to the moderator are displayed in figure 4.3a and b, respectively.

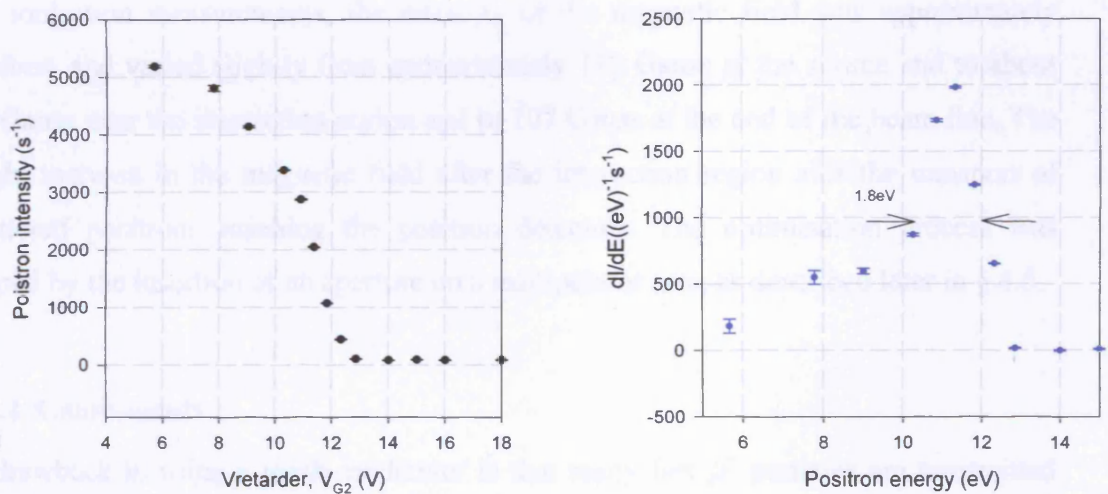


Figure 4.3. a) A retarding field profile with $V_m=10V$ and b) the corresponding e^+ beam energy distribution.

In figure 4.3b, the distribution of positron energies has a full width-at-half maximum (FWHM) of $\sim 1.8\text{eV}$, which includes the intrinsic energy spread of the beam from the moderator and that arising from the angular distribution of positron velocities. A low energy tail of the beam profile can be observed. This may originate from the spiralling of positrons in the magnetic field and/or inelastic scattering on the surface of the moderator. The positron impact energy is generally defined by the position of the peak of the beam profile.

4.4 Positron Beam Transport and Detection System

4.4.1 Magnetic Guidance

As shown in figure 4.1, the positron beam is magnetically confined to the beam axis (x) by means of thirteen Helmholtz coils distributed along the entire length of the apparatus. The pitch angle, α , of the positron trajectories is defined as the angle between the direction of the applied magnetic field and the emission vector of the particle. As the particle moves from a region of magnetic field B_1 to one of field intensity B_2 , the pitch angle changes from α_1 to α_2 according to:

$$\sin \alpha_2 = \sqrt{(B_2 / B_1)} \cdot \sin \alpha_1, \quad (4.2)$$

provided that the magnetic field strength varies slowly (Kruit and Read, 1983). During the ionisation measurements, the intensity of the magnetic field was approximately uniform and varied slightly from approximately 110 Gauss at the source end to about 80 Gauss near the interaction region and to 107 Gauss at the end of the beam line. The slight increase in the magnetic field after the interaction region aids the transport of scattered positrons reaching the positron detectors. The optimisation process was helped by the insertion of an aperture on a manipulator arm, as described later in § 4.5.

4.4.2 Components

A drawback in using a mesh moderator is that many fast β^+ particles are transmitted into the transported beam. The use of collimators (two stainless steel plugs and one lead plug), shown previously in figure 4.1, partially accomplishes the removal of fast particles, γ -rays and secondary electrons. These secondary electrons are released when fast particles strike the surrounding surfaces in the vacuum chamber.

A cylindrical electrode, R , repels secondary electrons. R was typically held at a voltage of $\sim -100\text{V}$ (Fig. 4.4).



Figure 4.4. Top-view of the repeller into the vacuum chamber.

This element is followed by a widely used trochoidal velocity selector (e.g. Mills, 1980), also named Wien filter, which is shown schematically in figure 4.5.

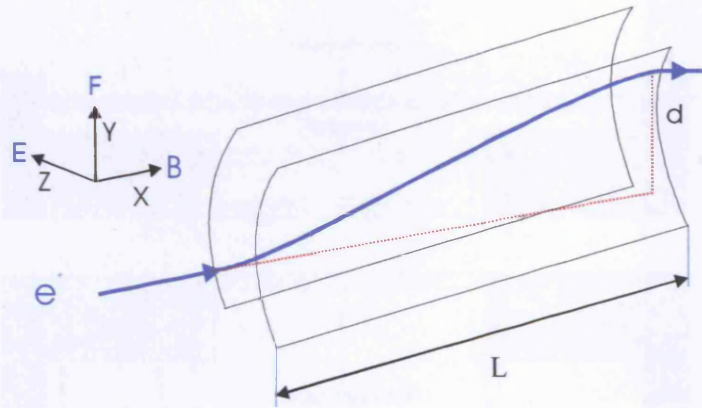


Figure 4.5. Schematic of a Wien Filter.

This separates the moderated positron beam from the flux of residual fast particles and γ -rays emanating from the source by deflection off axis (x). The filter is composed of a pair of parallel curved copper plates flared at the ends (Hutchins *et al.*, 1986) in order to prevent spatial distortion of the beam spot and to minimise fringe effects. The combination of an orthogonal electric field, E , and magnetic field, B , generated by the Helmholtz coils, results in the displacement of charged particles with velocity v by an amount d given by:

$$d = \frac{|\vec{E} \wedge \vec{B}|}{B^2} \left(\frac{L}{v_x} \right), \quad (4.3)$$

where L is the length of the plates and v_x the initial velocity of the particle along B . Since the deflection of the beam is proportional to v_x^{-1} and therefore to $E_+^{-1/2}$, the plates were held at equal and opposite voltages of approximately $2\sqrt{V_m}$ in magnitude. Consequently, during the measurements, the positron beam moved in a region of zero potential and acquired no additional kinetic energy during the traversal of the plates.

A lead collimator (10mm internal diameter) placed at the exit of the velocity selector allows only the passage of positrons with selected velocities and provides a shield from γ -rays originating from β^+ annihilating along their path.

A cylindrical retarding field analyser (RFA), positioned coaxially with the positron beam, follows the lead collimator. In this work, the RFA was only used to bias off the incident positron beam during background measurements (§5.2). The RFA is illustrated schematically in figure 4.6.

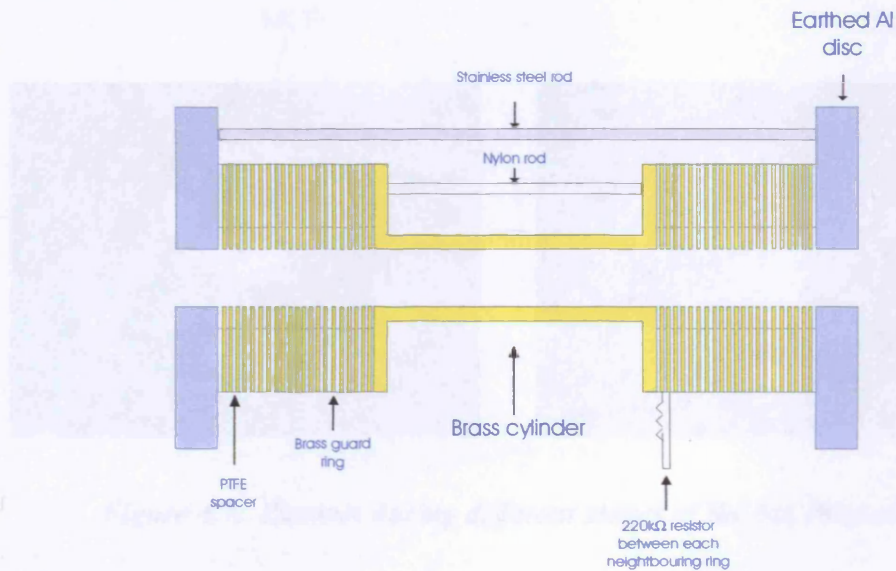


Figure 4.6. Schematic diagram of the cylindrical retarding field analyser (Ashley, 1996).

The length of the RFA ensures that the application of a voltage to its inner cylinder produces a constant potential at its centre, equal to the applied voltage, decreasing to zero at either end of the RFA due to a sequence of brass rings, interlayered with PTFE spacers, and connected by 220k Ω resistors (total resistance 11.4M Ω). The main purpose of this arrangement is to prevent divergent electric fields at the extremities of the RFA and to avoid problems typically associated with analyser grids (such as attenuation and emission of secondary electrons).

Immediately after the RFA, the beam enters the interaction chamber. Major details about the chamber, the target gas supply and the ion extraction system can be found in the following sections (§4.5-4.6).

In the remaining section of the apparatus, there are three cylindrical electrodes to accelerate/decelerate the scattered and unscattered positrons leaving the interaction chamber. The first, R_0 , and the second, R_1 , electrodes are grounded to prevent the potential on R_2 , $-530V$, from disturbing the field at the interaction region.

At the end of the flight path, a multi-channel plate array (MCPs, model no. G25-25DT/13 from Philips) is situated to detect both scattered and unscattered positrons. For further details about its configuration, see §2.5.2. Figure 4.7 shows two stages during the assembly of the detector.

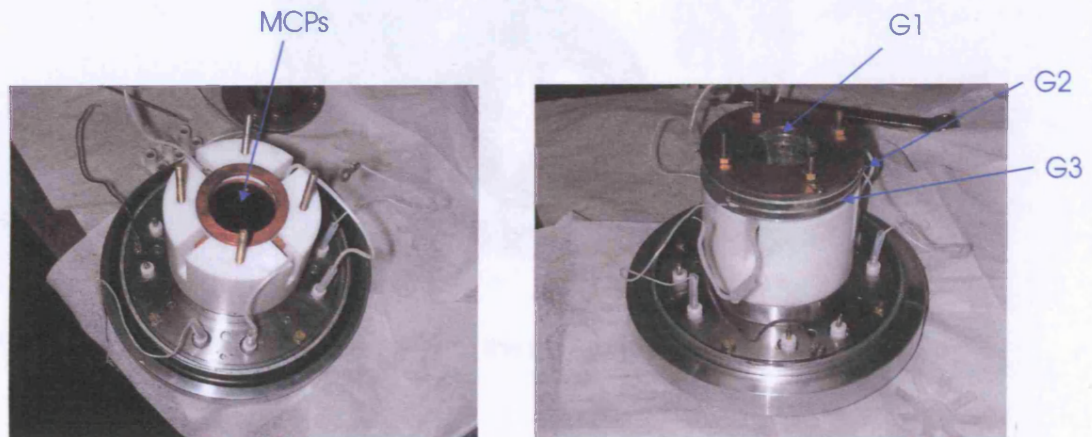


Figure 4.7. Pictures during different stages of the MCPs assembly.

As illustrated in figure 4.1, a retarding assembly is situated in front of the MCPs. This consists of 90% transmission W grids mounted onto separate Al rings (Fig. 4.7, on the right). The first grid, G_1 , is permanently grounded in order to avoid possible perturbation from the detector electrostatic field (Ashley, 1996). Secondary electrons that are produced from positron impact on this grid cannot travel back towards the interaction region because of the negative potential on R_2 . The two following grids, G_2 , are connected together and grounded, except during measurements of the beam background and of the ion background. The value of the retarding potential set for each of these background measurements is discussed fully in §5.2. The last grid, G_3 , is held at approximately $-100V$ with respect to the potential on the front of the MCPs in order to repel back any secondary electron released from its surface. The pulses obtained

from the MCP screen (see §2.5.2) feed into the external electronics, which are described in the following chapter.

4.5 Interaction Region

Figure 4.8 displays a top-view of the interaction region where the positron beam intersects the target gas jet, which emerges from the nozzle entering the top flange centrally.

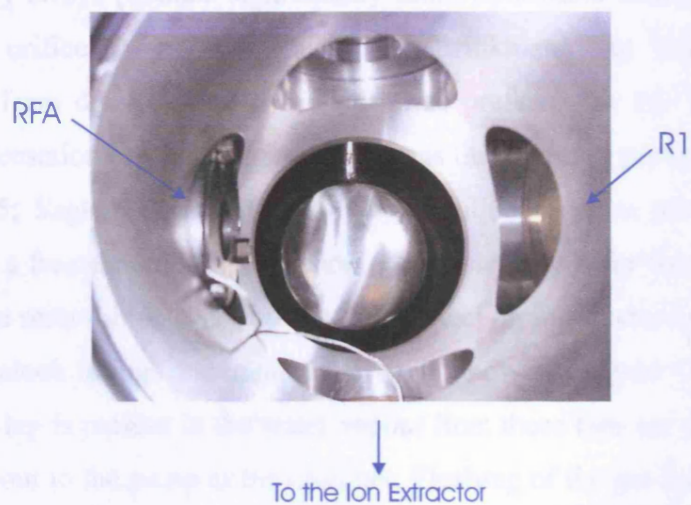


Figure 4.8. Top-view of the scattering region before coating with graphite.

This interaction chamber is made from a machined Al block (152mm³ in volume) and is entirely coated with graphite in order to reduce the emission of secondary electrons.

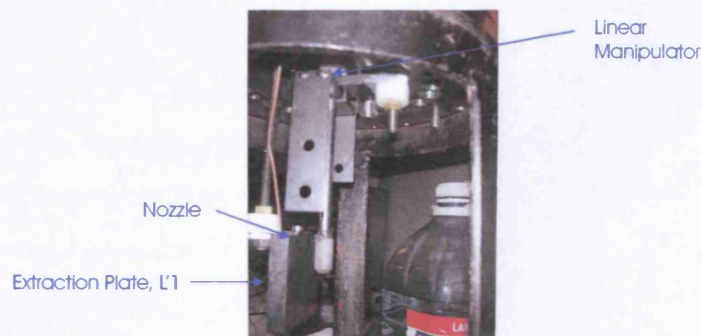


Figure 4.9. Aperture on a linear manipulator employed during the beam alignment.

The alignment of the beam with respect to the gas jet can be performed by using an aperture on a linear manipulator arm (figure 4.9). One 6.5mm diameter aperture positioned 30mm before the scattering region can be inserted by manually guiding the manipulator arm to locate the beam. As this aperture might restrict the maximum angle at which particles can scatter and still be detected, it is removed before the start of each run.

4.6 System for Purification of Water and Target Gas Jet

Although capillary arrays produce significantly more collimated beams than a single tube or a walled orifice (Angel and Giles, 1972; Brinkmann and Trajmar, 1981), a graphite nozzle (1mm diameter, 10mm length) was preferred in this study to avoid problems of condensation of water vapour on the gas outlet. As in previous works (e.g. Rudd *et al.*, 1985; Saglam and Aktekin, 1990), distilled water is purified from the residual gases by a freeze-pump-thaw method. The system built for the purification of water consists of a reservoir of water on a stainless steel piping interconnected with the appropriate Swagelock fittings and manual valves, as shown in Figure 4.10. Either side of the reservoir a tap is present in the water vapour line; these taps are used to halt the flow of water vapour to the pump or the chamber. Flushing of the gas line is performed by a backing pump (Edwards E2M-18) and the pressure is monitored by a pirani gauge. The magnetic valve feedback allows the adjustment of the gas flow, which is read by a capacitance manometer. A manual valve (not shown in the figure) allows the vacuum chamber to be isolated from this gas line from water vapour.

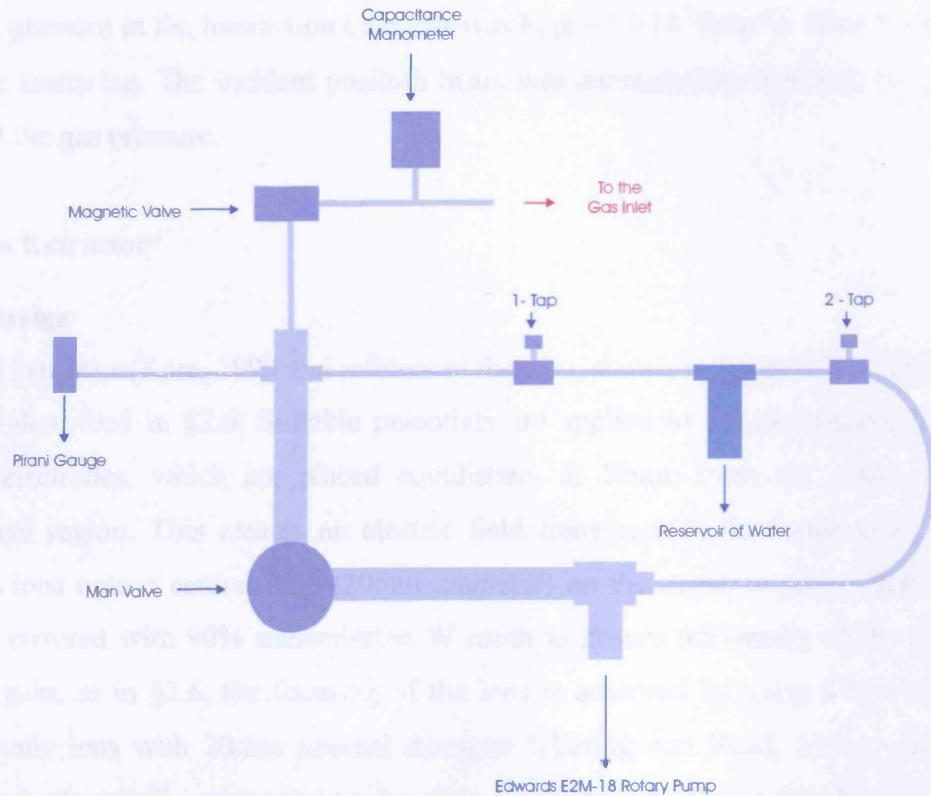


Figure 4.10. System employed for the water purification.

The purification procedure occurs as follows. Firstly, the water in the reservoir is frozen by liquid nitrogen while air (mainly N_2 and O_2) and other gases are pumped away for ~ 20 min (tap 2 and manual valve open). Afterwards, the pump is valved off and the water warmed up to drive out any remaining dissolved gas. This operation is repeated twice. Finally, the purity of the water vapour is checked through time-of-flight mass-spectroscopy (TOF-MS) as described in §5.2.1.

The sample gases were introduced into the middle of the interaction region through a needle valve (for the test measurements with Ar) or through a leak valve (for the measurements of H_2O). The manual valve, preceding the vacuum chamber, was kept fully open during the measurements and closed during its evacuation. The driving pressure could be measured using an MKS 127A baratron capacitance manometer (calibrated to measure pressures in the range 0-10 torr). During each run, this was monitored and its output was recorded on a PC every 30 s. Moreover, before and after each measurement, the driving pressure could also be checked by an ionisation gauge (AIG17P, Caburn), which was connected to one arm on one side of the interaction chamber.

The pressure in the interaction chamber was kept $\sim 1.1 \cdot 10^{-5}$ mbar in order to prevent multiple scattering. The incident positron beam was attenuated by less than 1% at this value of the gas pressure.

4.7 Ion Extractor

4.7.1 Design

The ion extractor (Kara, 1999 and references therein), shown in figure 4.1, is similar to the one described in §2.6. Suitable potentials are applied to the two parallel square 30mm electrodes, which are placed equidistant, at 10mm from the centre of the collisional region. This creates an electric field transverse to the beam axis, which deflects ions onto a central hole (20mm diameter) on the negative plate. This latter plate is covered with 90% transmission W mesh to ensure uniformity of the electric field. Again, as in §2.6, the focusing of the ions is achieved by using a two-element electrostatic lens with 20mm internal diameter (Harting and Read, 1976). The first element is electrically connected to the plate electrode (L1, 40mm length) of the ion extractor. The advantage of the second element (L2, 35mm length) is that ions entering with widely divergent trajectories are focused onto the active area of the detector (see §4.7.2). The detector is a channel electron multiplier (CEM, Philips type X951BL). Its axis is slightly offset from the extraction cylinder axis by ~ 1.5 mm in order to ensure that the ions hit the cone and release secondary electrons with high efficiency: otherwise, a loss of ion signal would occur. The lenses and the detector are housed inside an earthed Al cylinder to shield the detector from pick-up.

Typically, in this work the front cone of the CEM was held at $-3,000$ V and the back of the CEM was held at $+100$ V. A 95% transmission Cu grid, in front of the CEM was held at $-3,150$ V. For further details about the CEM, see §2.5.3 and §2.6.

4.7.2 Simulated Performance of the Ion Extractor

Figure 4.11 shows the results of a simulation performed using Simion 7. This demonstrates the focusing properties of the ion extractor for H₂O⁺ ions created within the line-of-sight of its aperture at the working voltages (Setting IV in table 4.1). For simplicity, only ions originating along the axis of the e⁺ beam in steps of 1mm are shown.

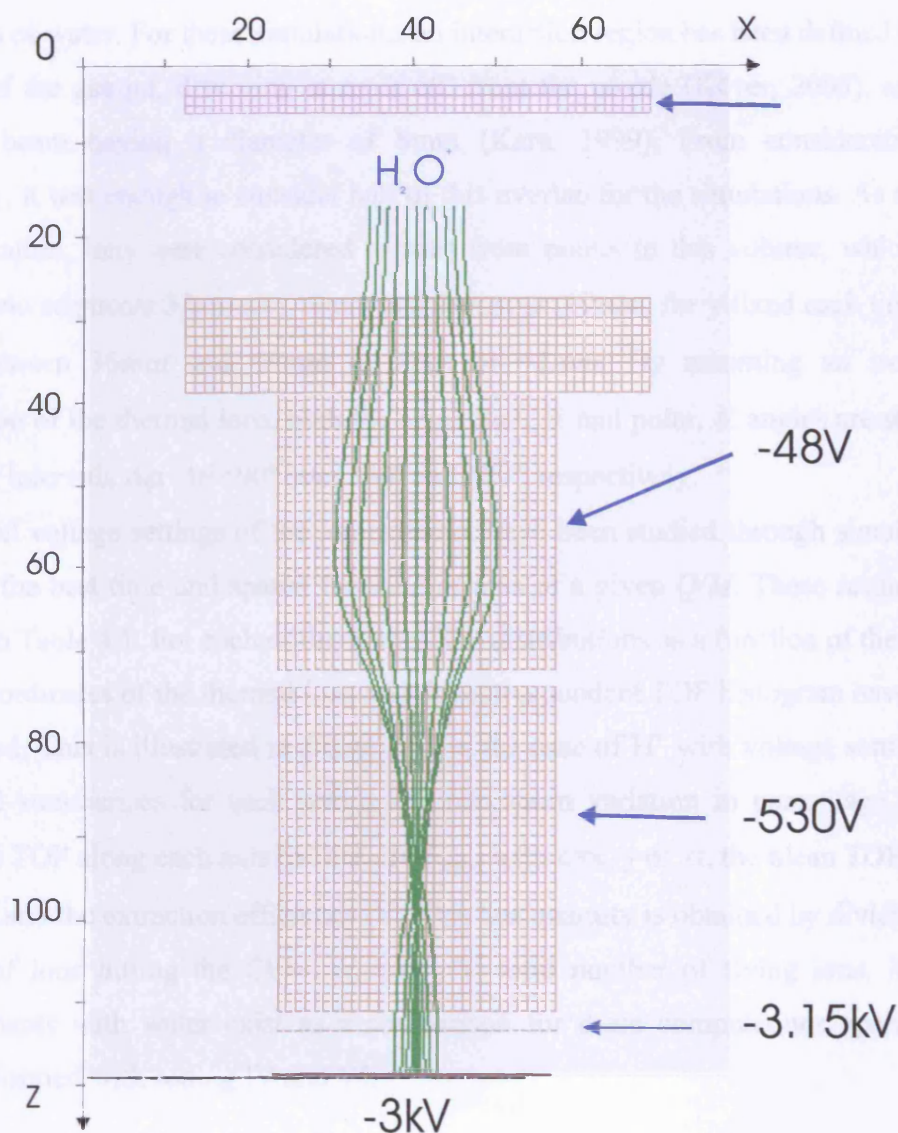


Figure 4.11. Simulation of the ion trajectories of H_2O^+ through the ion extractor (Setting IV). The dimensions on the x and y axes are expressed in mm.

More detailed simulations have been carried out to determine the relative ion extraction efficiency for the ion fragment (H^+). These simulations and the accompanying analysis are described in this subsection and in the following one, §4.7.3. Another feature that has been investigated is the ion time-of-flight (TOF), which is the time taken for an ion to travel from its formation point in the interaction region to the channeltron. The TOF depends upon various factors: the ion charge-to-mass ratio (Q/M), its initial velocity and the magnitude of the potential applied to the ion-extractor. Simulations of the ion flight trajectories have also aided the experiment by predicting the TOF for various ion products in the dissociative and non-dissociative

ionisation of water. For these simulations, an interaction region has been defined by the overlap of the gas jet, diverging at most 60° from the nozzle (Kövér, 2005), and the positron beam having a diameter of 8mm (Kara, 1999). From consideration of symmetry, it was enough to consider half of this overlap for the simulations. As a good approximation, ions were considered to start from points in this volume, which was divided into segments $33\text{mm} \leq x \leq 40\text{mm}$ and $11\text{mm} \leq z \leq 19\text{mm}$, for y fixed each time at a value between 36mm and 44mm in steps of ~1mm. By assuming an isotropic distribution of the thermal ions, both the azimuthal, φ , and polar, θ , angles are stepped in regular intervals $\Delta\varphi, \Delta\theta < 90^\circ$ over 360° and 180° , respectively.

Several voltage settings of the ion extractor have been studied through simulations to obtain the best time and spatial focusing of ions of a given Q/M . These settings are detailed in Table 4.1. For each of them, the TOF distributions as a function of the initial spatial coordinates of the thermal ions and the correspondent TOF histogram have been determined. This is illustrated in figure 4.12 in the case of H⁺ with voltage setting IV. Table 4.2 summarises for each setting the maximum variation in percentage of the simulated TOF along each axis ($\Delta\text{TOF}_c / \text{TOF}_{\text{MAX}c}$, with $c=x, y$ or z), the mean TOF value ($\langle\text{TOF}\rangle$) and the extraction efficiency (ε). This last quantity is obtained by dividing the number of ions hitting the CEM, N , over the total number of flying ions, N_0 . No measurements with water exist as a comparison for these computations apart from those performed with setting IV and VI.

<i>Settings</i>	$V_{L'1}$	V_{L1}	V_{L2}	V_G
<i>I</i>	+150	-150	-530	-3,150
<i>II</i>	+100	-100	-530	-3,150
<i>III</i>	+50	-50	-530	-3,150
<i>IV</i>	+17.2	-48	-530	-3,150
<i>V</i>	+100	-100	-200	-2,700
<i>VI</i>	+1	-1	-530	-3,150

Table 4.1. Voltage settings employed for the ion extractor. The units are in Volts.

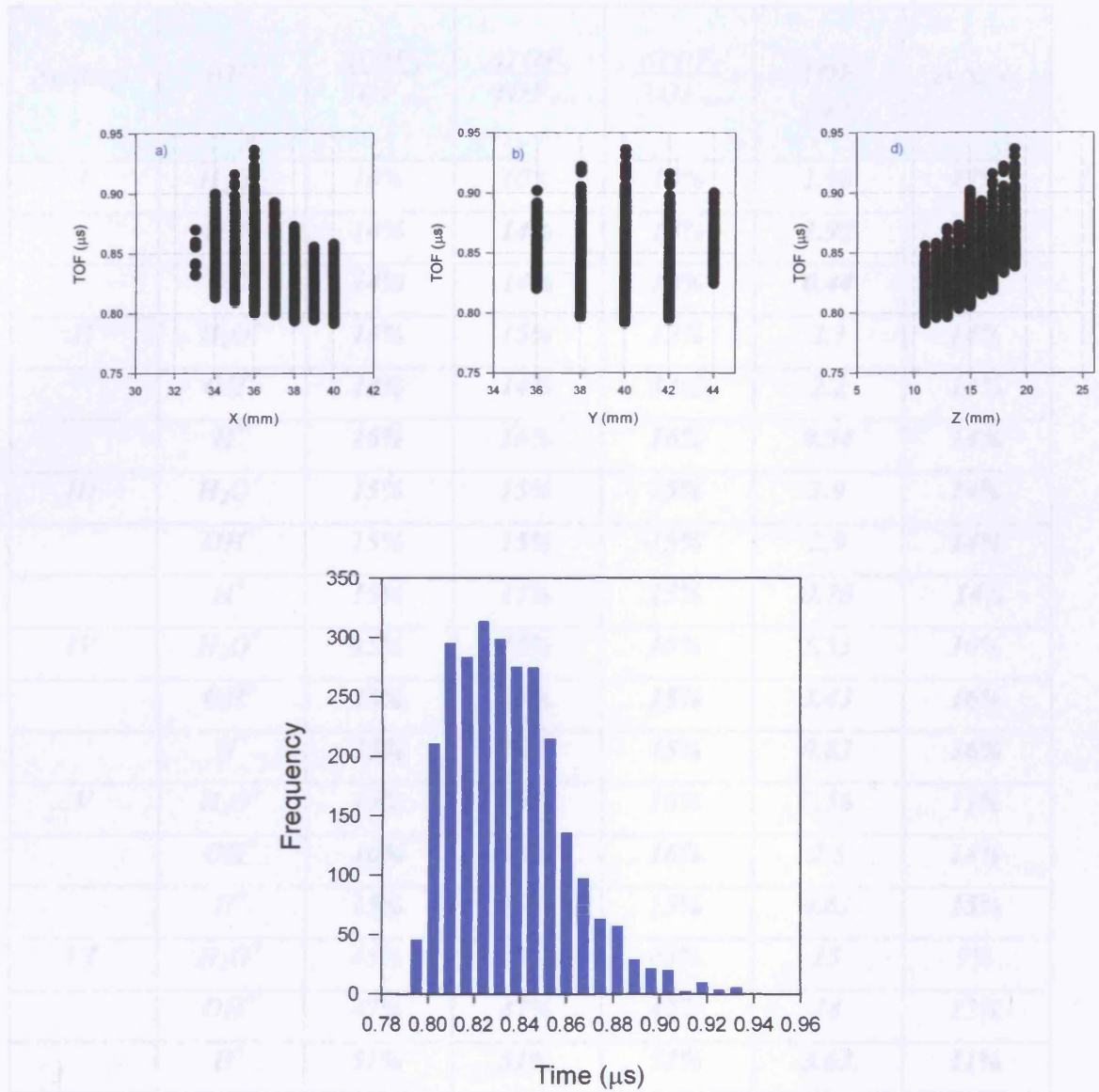


Figure 4.12. a) TOF dependence along x , b) TOF dependence along y , c) TOF dependence along z , d) TOF histogram for thermal H^+ relative to voltage setting IV.

TOF and H^+ ions have been measured in this channel.

In figure 4.12, it can be observed that the maximum variation in the TOF occurs with the distance from the start of the overlap, i.e., for $x = 40$. However, at the edge of the region of overlap ($31 < x < 34$) the relative H^+ ionisation decreases due to the asymmetric overlap. Figure 4.12(d) illustrates a symmetrical TOF distribution with respect to the axis $x = 40$ position (from $y = 40$) due to the cylindrical geometry of the overlap. Figure 4.12(c) shows that the ions that start flying closer to the positive plate ($11.5 < z < 13$) arrive earlier than the ions created by the proximity of the negative plate.

Settings	ION	$\frac{\Delta TOF_x}{TOF_{MAX}}$	$\frac{\Delta TOF_y}{TOF_{MAX}}$	$\frac{\Delta TOF_z}{TOF_{MAX}}$	$\langle TOF \rangle$ (μs)	$\epsilon = N/N_0$
I	H_2O^+	10%	10%	10%	1.98	17%
	OH^+	14%	14%	14%	1.92	15%
	H^+	14%	14%	14%	0.44	14%
II	H_2O^+	15%	15%	15%	2.3	14%
	OH^+	14%	14%	14%	2.2	14%
	H^+	16%	16%	16%	0.54	14%
III	H_2O^+	15%	15%	15%	2.9	14%
	OH^+	15%	15%	15%	2.9	14%
	H^+	15%	15%	15%	0.70	14%
IV	H_2O^+	15%	15%	15%	3.53	16%
	OH^+	15%	15%	15%	3.43	16%
	H^+	15%	15%	15%	0.83	16%
V	H_2O^+	16%	16%	16%	2.56	11%
	OH^+	16%	16%	16%	2.5	14%
	H^+	15%	15%	15%	0.62	15%
VI	H_2O^+	45%	45%	45%	15	9%
	OH^+	47%	47%	47%	14	12%
	H^+	51%	51%	51%	3.63	11%

Table 4.2. The maximum variation of TOF along each axis ($\Delta TOF_c / TOF_{MAXc}$ with $c=x, y$ or z), the mean TOF value ($\langle TOF \rangle$) and extraction efficiencies (ϵ) for H_2O^+ and H^+ . All ions have been considered to have thermal energies.

In figure 4.12a, it can be observed that the maximum variation in the TOF increases with the distance from the axis of the extractor, i.e., for $36 \leq x < 40$. However, at the edge of the region of overlap $33 \leq x < 35$ the relative ΔTOF_x diminishes because of the asymmetric overlap. Figure 4.12b illustrates a symmetrical TOF distribution with respect to the axis of the positron beam ($y=40$) due to the symmetrical geometry of the overlap. Figure 4.12c shows that the ions that start flying close to the positive plate ($11 \leq z < 15$) arrive earlier than the ions created in the proximity of the negative plate

($15 < z \leq 18$) because of the enhanced acceleration experienced along their path between the extraction plates.

The most recurrent TOF and overall spread in the TOF could be inferred from histograms such as that in figure 4.12d. To consider the non-uniform target density, a gaussian distribution (Brinkmann and Trajmar, 1981) has been considered, which introduced in the histogram a variation in the TOF frequency of less than 10% and therefore was neglected.

As can be inferred from Table 4.2, the best time focusing is obtained at higher extraction voltages. The extraction efficiency tends to decrease at low extractor voltages but only by a few percent. None of these settings allows a resolving power large enough to distinguish OH⁺ from H₂O⁺. The voltage settings used in this work (Setting IV) allowed a good time and spatial focusing, whilst minimising pick-up noise on the signal line from the pulsed extraction voltages.

4.7.3 Extraction Efficiency

The partial cross-section for the production of H⁺ from the ionising dissociation of water (§5.2.1) has to be corrected for the extraction efficiency of the system, because unlike the parent ions, H₂O⁺, which have mostly thermal energies, the lightest fragment ions, H⁺, have energies ranging from thermal to some eVs. These high kinetic energy fragments are collected less efficiently than the thermal ones (Maerk and Dunn, 1985). The probability of extracting thermal H⁺ ions, ε , has been investigated from simulations with Simion 7 in the previous sub-section (§4.7.2). However, ε has also been determined for H⁺ as a function of energy from thermal to 7eV. Figure 4.13 shows the probability of extracting fragments, H⁺, of a certain kinetic energy, K , with the working potentials (Setting IV). This probability has been convoluted with the kinetic energy distribution for protons dissociating from water (Fig. 4.14, Cordaro *et al.*, 1986), to find the probability of extracting H⁺ with a given K (Figure 4.15).

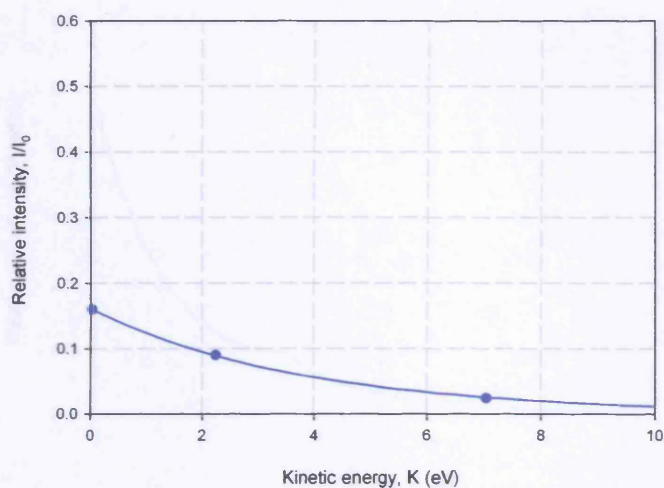


Figure 4.13. Probability of extracting fragments, H^+ , of a certain kinetic energy, K , with the present ion extractor and working potentials (Setting IV).

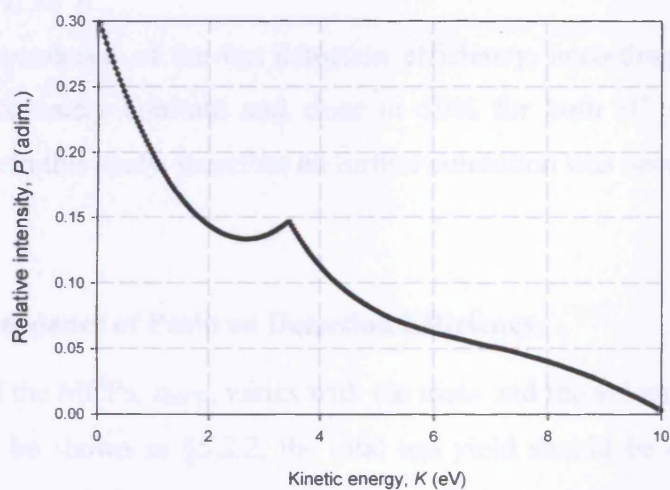


Figure 4.14. Kinetic energy distribution for proton dissociation from water (Cordaro et al., 1986).

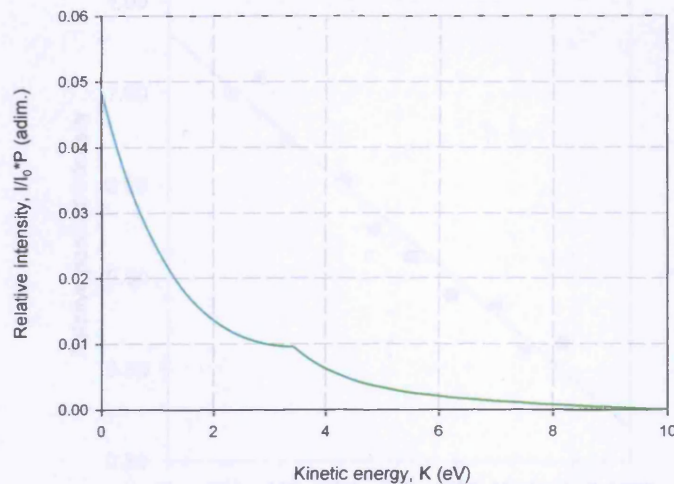


Figure 4.15. Probability of extracting ions of a certain kinetic energy, K .

The area underneath this last curve (Fig. 4.15) represents the overall extraction efficiency ($\sim 8.5\%$) for H^+ .

The mass dependence of the ion detection efficiency, according to Fields *et al.* (1977), is approximately constant and close to 50% for both H^+ and H_2O^+ at the working voltages in this study, therefore no further correction was necessary.

4.8 Energy Dependence of Positron Detection Efficiency

The efficiency of the MCPs, ϵ_{MCP} , varies with the mass and the velocity of the incident particle. As will be shown in §5.2.2, the total ion yield should be corrected for the energy dependence of the positron detection efficiency, ϵ_{MCP} , which has been determined as follows. The potential difference across the plates, namely front and back, was fixed throughout this study in order to keep the secondary electron gain constant. Initially 15eV positrons are accelerated by $-250V$ applied to the front. The velocity of the positrons incident upon the MCPs was then varied by changing the potential on the front of the detector, V_F (range from 202 to 1220V), and keeping V_m constant. The number of incident positrons was measured for 10 seconds.

Figure 4.16 shows a linear fit of the relative intensity of incident positrons versus the impact energy.

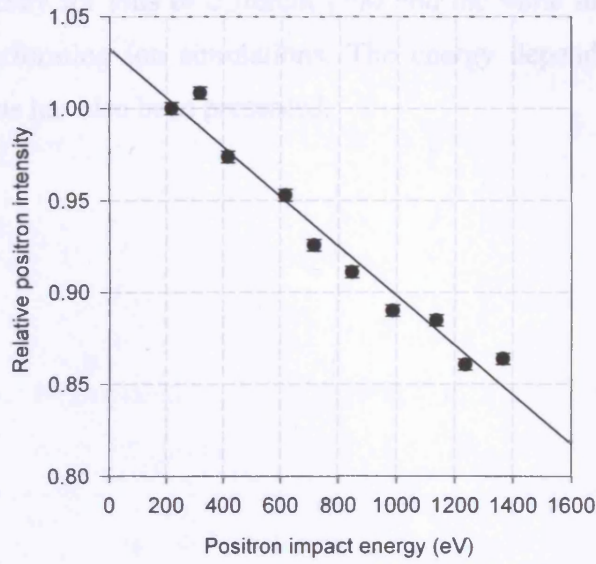


Figure 4.16. The energy dependence of the positron detection efficiency.

The energy dependence of the relative positron detection efficiency, ε_{MCP} , was determined as follows:

$$\varepsilon_{MCP}(E) = (1.033(\pm 0.008) - 0.00013(\pm 1 \cdot 10^{-5}) \cdot E), \quad (4.4)$$

where the positron impact energy on the plate is $E = eV_i = e(V_m + |V_F|)$.

As the incident energy increases across the working energy range, the MCP efficiency decreases with a maximum variation of $\approx 13\%$.

Finally, the number of positrons detected by the MCPs, N_+ , was corrected for this factor in Eq. 5.7 according to:

$$N_+^{true} = N_+ / \varepsilon_{MCP}(E). \quad (4.5)$$

4.9 Summary

In this chapter, the main components of the experimental system used throughout the measurement of the integral cross sections for positron impact ionisation of H₂O have been described. This includes the discussion of the source and moderator configuration, the vacuum system, the positron beam transport, the positron and ion detection system.

The extraction efficiency for ions of different Q/M and the same initial velocities has been obtained by performing ion simulations. The energy dependence of the MCP efficiency for positrons has also been presented.

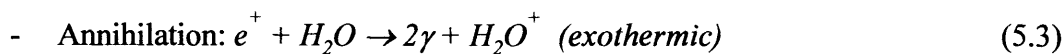
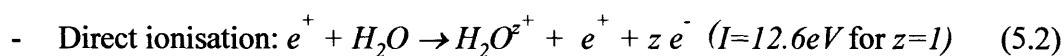
Chapter 5

Positron Impact Ionisation of Water Molecules

5.1 Overview

Water has a particular significance among polyatomic molecules. It is the third most abundant molecule in the Universe (e.g. Bernath, 2002); it is the principal molecule in comets and is present in the atmospheres of Venus, Mars, giant planets and even in the solar atmosphere (Wallace *et al.*, 1995). Water is the most important greenhouse gas (Taylor, 2002). From a biological point of view, water is the principal component of living cells. Hence, it becomes clear why understanding the complex interactions involved when a water molecule is ionised by electron (ionisation) or positron (ionisation or capture process) impact is important and represents a great challenge for various domains of science (e.g. see the recent review by Itikawa and Mason, 2005).

The main non-dissociative ionisation channels for positron-water collision are expressed by the following reactions:



where threshold energies are indicated between brackets.

The total single ionisation cross-section (§1.4.7) for e^+ incident on an atom/molecule is given by:

$$\sigma_i^+ = \sigma_{Ps} + \sigma_i^+ + \sum HO, \quad (5.4)$$

where σ_{Ps} is the Ps formation cross-section, σ_i^+ is the direct single ionisation cross-section ($z=1$ in formula 5.2) and $\sum HO$ is the sum over all higher order processes contributing to ionisation (e.g. multiple ionisation, annihilation) (e.g. Rapp *et al.*, 1965; Laricchia and Moxom, 1993). The total ionisation cross-section for the creation of H_2O^+ stems mostly from Ps formation (5.1) and direct ionisation (5.2) since $\sum HO$ is considered to be relatively small. In particular, annihilation is considered to give generally a negligible contribution to the total ionisation cross-section (Van Reeth *et al.*, 2005). The σ_{Ps} can be extracted from the relation (5.4) by measuring σ_i^+ and σ_i^+ , independently. This has been proved to be a useful and widely employed technique (e.g. Laricchia *et al.*, 2002 and references therein).

An extensive study has been carried out to determine for the first time both integral and differential single ionisation cross-sections for the interaction of positrons with the water molecule. The (dissociative and non-dissociative) ionisation cross-sections (σ_D^+ , σ_i^+ and σ_i^+) have been measured from the threshold up to around 1keV (Pešić *et al.*, 2004, Arcidiacono *et al.*, 2005b, 2007). Moreover, using the technique afore mentioned, σ_{Ps} has also been extracted (Murtagh *et al.*, 2006; Arcidiacono *et al.* 2007). Prior to investigating the positron impact ionisation of water, measurements of σ_i^+ and σ_i^+ for Ar were performed to ensure the correct performance of the system. Measurements of σ_i^+ have been carried out using two techniques: DC and pulsed extraction. In both cases, an electric field was applied across the interaction region and positron-ion coincidences were recorded. The σ_i^+ has only been determined using the DC extraction method. To investigate further the ionisation of water by positron impact, the energy spectra of positrons scattered in the forward direction $\sim 0^\circ$ (see §2.5) following ionisation in $e^+(100\text{eV})\text{-H}_2\text{O}$ collisions have been measured in a coincidence experiment (Arcidiacono *et al.*, 2006). Branching ratios for $\text{OH}^+/\text{H}_2\text{O}^+$ and $\text{H}^+/\text{H}_2\text{O}^+$ have also been determined.

In the following sections, the techniques used to collect data for the integral and doubly differential ionisation cross-sections are described. Final results are presented and compared with other data where available.

5.2 Integral Ionisation Cross-Sections

5.2.1 Direct Ionisation Cross-Section: Methods

Two operating modes were applied to determine the single direct ionisation cross-section: a pulsed (e.g. Fromme *et al.*, 1986; Knudsen *et al.*, 1990) and a continuous ion extraction (e.g. Laricchia *et al.*, 1993). Both approaches are based upon the extraction and detection of the ion in time correlation with the scattered projectile. This allows higher signal-to-background levels than in the single counting method and also allows identification of the final state ion.

Pulsed extraction

A schematic illustration of the timing electronics and the ion detection sequence employed with pulsed extraction is displayed in figure 5.1. The ion extraction was triggered by the detection of a positron at the end of the beamline. A weak electrostatic field ($\pm 50\text{V/m}$ at the plates) pointing away from the ion detector was permanently applied across the interaction region to avoid lingering of ions. This, while perturbing the incident positron beam negligibly, reduced effectively the ion lifetime, τ , and the contribution to the gross signal due to random coincidences. The positron signal, as obtained by the MCPs, was amplified by a preamplifier, PA, and passed through the constant-fraction discriminator, CFD2 (Ortec 584). The resulting pulse was inverted and widened using a pulse stretcher to obtain a positive square pulse, $1.5\mu\text{s}$ in width. For the test measurement with Ar, the pulse was stretched to $4\mu\text{s}$ to account for the larger mass of argon and thus its longer lifetime in the interaction region. The output of the stretcher initiated an ion extraction pulser that served to apply voltage pulses ($V_{L1}=+17\text{V}$ and $V_{L1}=-48\text{V}$, see also §4.7.2) to the two extraction electrodes.

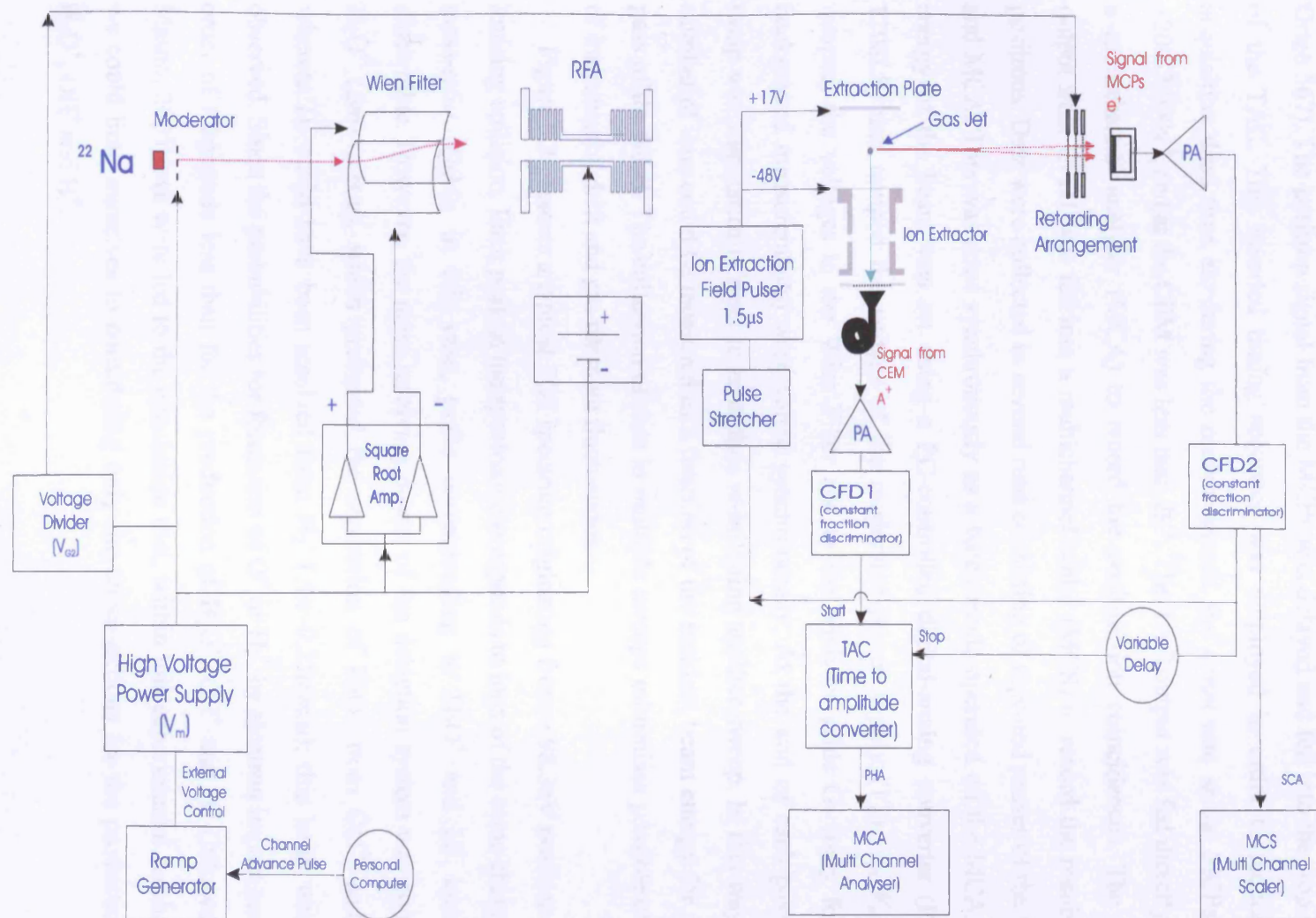


Figure 5.1. Schematic diagram illustrating the timing electronics for the direct ionisation cross-section measurements.

The signal from the ion detector was fed to a PA and then into a CFD1 (Ortec 584). This was connected to the start input of a time-to-amplitude converter (TAC, model Ortec 567). The positron signal from the MCPs was delayed and fed into the stop input of the TAC. This inverted timing sequence was employed in order to reduce the acquisition dead time as, during the measurements, the count rate at the MCPs was $\sim 200\text{--}7,000\text{s}^{-1}$, and at the CEM was less than 2s^{-1} . The TAC output was fed directly into a multichannel analyser (MCA) to record the positron-ion coincidences. The SCA output from CFD1 was fed into a multichannel scaler (MCS) to record the number of positrons. Data were collected in several runs consisting of repeated passes of the MCS and MCA. This was done synchronously as a batch mode operated on the MCA. The energy of the beam was set using a PC-controlled digital-analog converter (PMD-1208LS) that ramped the voltage of the moderator power supply (V_m). As V_m was ramped, the voltages to the Wien Filter and to the analyser grids G_2 (only for the background measurements) were varied synchronously. At the end of each pass, the ramp was automatically reset to zero, thus re-initiating another sweep. In this way, the number of ions could be measured as a function of the incident beam energy for every pass of the MCS. The collection of data in multiple sweeps minimises possible effects of instrumental drift and gas pressure fluctuations.

Figure 5.2 presents a typical TOF spectrum originating from a 98.3eV positron- H_2O ionising collision. Each peak in the spectrum corresponds to ions of the same charge-to-mass-ratio (Q/M); in this case, peaks corresponding to H_2O^+ and H^+ ions are discernible. However, the mass resolving power of the detection system was poor for H_2O^+ ($\Delta m \sim 4\text{a.m.u}$), which prevented the separation of H_2O^+ from OH^+ , and O^+ , whereas H^+ could have been resolved from H_2^+ ($\Delta m \sim 0.25\text{a.m.u}$); this latter was not observed. Since the probabilities for formation of O^+ or H_2^+ by electron impact are two orders of magnitude less than for the production of H_2O^+ , OH^+ and H^+ (Itikawa and Mason, 2005), we were led to the conclusion that, within this experimental resolution, we could limit ourselves to considering only the cross-sections for the production of H_2O^+ , OH^+ and H^+ .

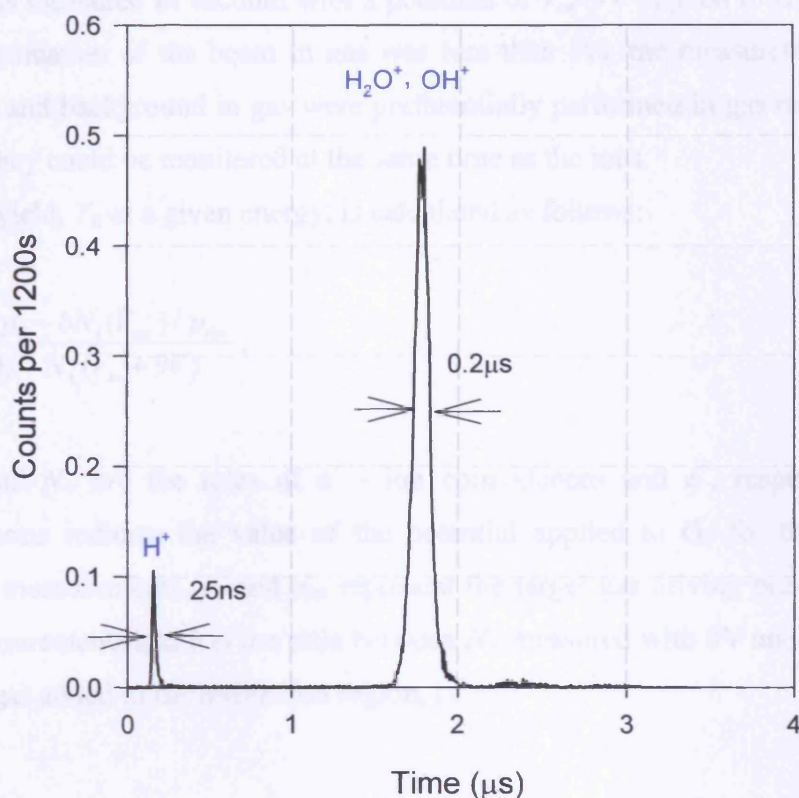


Figure 5.2. Time-of-flight spectrum of ions produced in water due to impact of 98.3eV positrons.

The background contribution to the ionisation signal originates from ions created during Ps formation or ionisation by the remaining fast particles in the beam. This was measured by employing a retarder (G_2 , see §4.4.2) to prevent detection of positrons that have lost energy via ionisation (as in Kara *et al.*, 1997). Hence, the retarding potential V_{ret} applied to G_2 was given by:

$$eV_{ret} = \alpha eV_m - I + \delta E, \quad (5.5)$$

where $1/\alpha$ is the energy resolution of the analyser grids, I is the ionisation energy and δE is the maximum energy spread of the beam (see §2.3).

The value for α was measured to be $1.009 (\pm 0.001)$. Hence, to bias-off the positron beam, the voltage that it was necessary to apply to G_2 (cut-off voltage) was approximately $V_m + 2V$ at low energies ($\approx 10eV$), and $V_m + 9V$ at high energies ($\approx 1keV$).

The beam background consisted mainly of fast particles passing through the Wien filter and was measured in vacuum with a potential of V_m+9V applied to G_2 . However, since the attenuation of the beam in gas was less than 1%, the measurements of the beam signal and background in gas were preferentially performed in gas rather than in vacuum as they could be monitored at the same time as the ions.

The ion yield, Y_i , at a given energy, is calculated as follows:

$$Y_i = \frac{N_i(0)/p_0 - bN_i(V_{ret})/p_{ret}}{N_+(0) - N_+(V_m + 9V)}, \quad (5.6)$$

where N_i and N_+ are the rates of e^+ - ion coincidences and e^+ , respectively; the bracketed terms indicate the value of the potential applied to G_2 for the signal or background measurements. p_0 and p_{ret} represent the target gas driving pressure during the two measurements and b is the ratio between N_+ measured with 0V and V_{ret} applied to G_2 , with gas added to the interaction region, i.e.

$$b = \frac{N_+(0)}{N_+(V_{ret})}. \quad (5.7)$$

This term corrects for the underestimation of the measured background due to the decreased frequency with which the ion extraction is triggered.

To reduce the effects of possible drifts, the gross signal and background passes were alternated by switching the potential applied to G_2 between 0V and V_{ret} . The first MCS measurement was usually repeated after each pass to allow capacitance effects to dissipate (~1min). At the beginning and end of each run, the incident positron beam intensity, N_+ , was also measured in vacuum as a function of the incident energy using the MCS.

The measured ion yield depends on the detection efficiency of the CEM, ε_{CEM} , as $Y_i \propto \varepsilon_{CEM} \sigma_i^+$. However, the detection efficiencies relative to H_2O^+ , OH^+ and H^+ ions are constant across the energies investigated (Fields *et al.*, 1977) and thus no further correction is required in Eq. 5.6.

A plot of the variation of the positron beam intensity with energy during a gas run is shown in figure 5.3. The curve varies smoothly up to 100eV but a significant drop in

the positron count rate of up to 40% can be observed at the highest energy. Although it was not possible to improve substantially the e^+ beam transport at these energies, the ion yields measured with different beam tuning were found to be consistent.

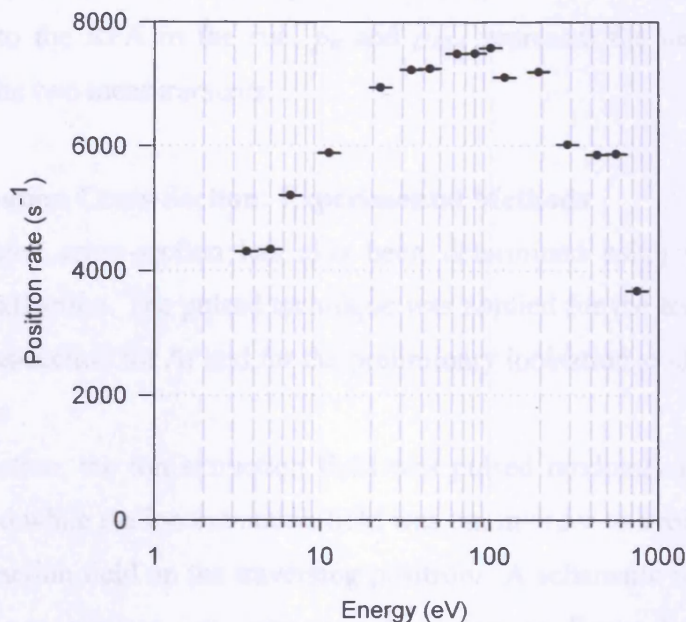


Figure 5.3. Energy dependence of the e^+ beam intensity during a gas run.

Continuous extraction

For continuous extraction, ions are collected by applying a sufficiently low DC voltage to the plates such that perturbations on the positron trajectories are negligible across the energy range studied. Two different voltages ($\pm 0.5V$ and $\pm 1V$) have been used in order to check for possible systematic effects. Ion-positron time-reversed coincidences were also recorded in this extraction mode. The electronics used were identical to figure 5.1, apart from the removal of the induced extraction system upon positron detection. One of the benefits of DC extraction is that residual ions are continuously pulled out from the collision region, and, as a result, random coincidences are separated from the true signal. This means that a random coincidence will occur on a flat region of the spectrum, whereas the signal will appear in the ionisation peak.

The background, which arises mostly from fast particle contributions, was measured by biasing off the beam by applying $V_{RFA} = V_m + 9V$ to the retarding field analyser. The yield may be expressed as follows:

$$Y_i = \frac{N_i(0)/p_0 - N_i(V_m + 9V)/p_{RFA}}{N_+(0) - N_+(V_m + 9V)}, \quad (5.8)$$

where N_i and N_+ are the same as in equation (5.6); the bracketed values indicate the voltage applied to the RFA in the run; p_0 and p_{RFA} represent the target gas driving pressure during the two measurements.

5.2.2 Total Ionisation Cross-Section: Experimental Methods

The total ionisation cross-section has also been determined using two techniques: pulsed and DC extraction. The pulsed technique was applied for the test measurements of ionisation cross-section for Ar and for the preliminary ionisation studies of H₂O.

Pulsed extraction

For pulsed extraction, the ion extraction field was pulsed randomly and the positron beam was stopped while the ion extraction field was on, in order to avoid the perturbing effect of the extraction field on the traversing positrons. A schematic illustration of the beam chopping and random ion extraction is shown in figure 5.4. A schematic representation of the pulses applied to the ion extractor and the Wien filter is shown in figure 5.5.

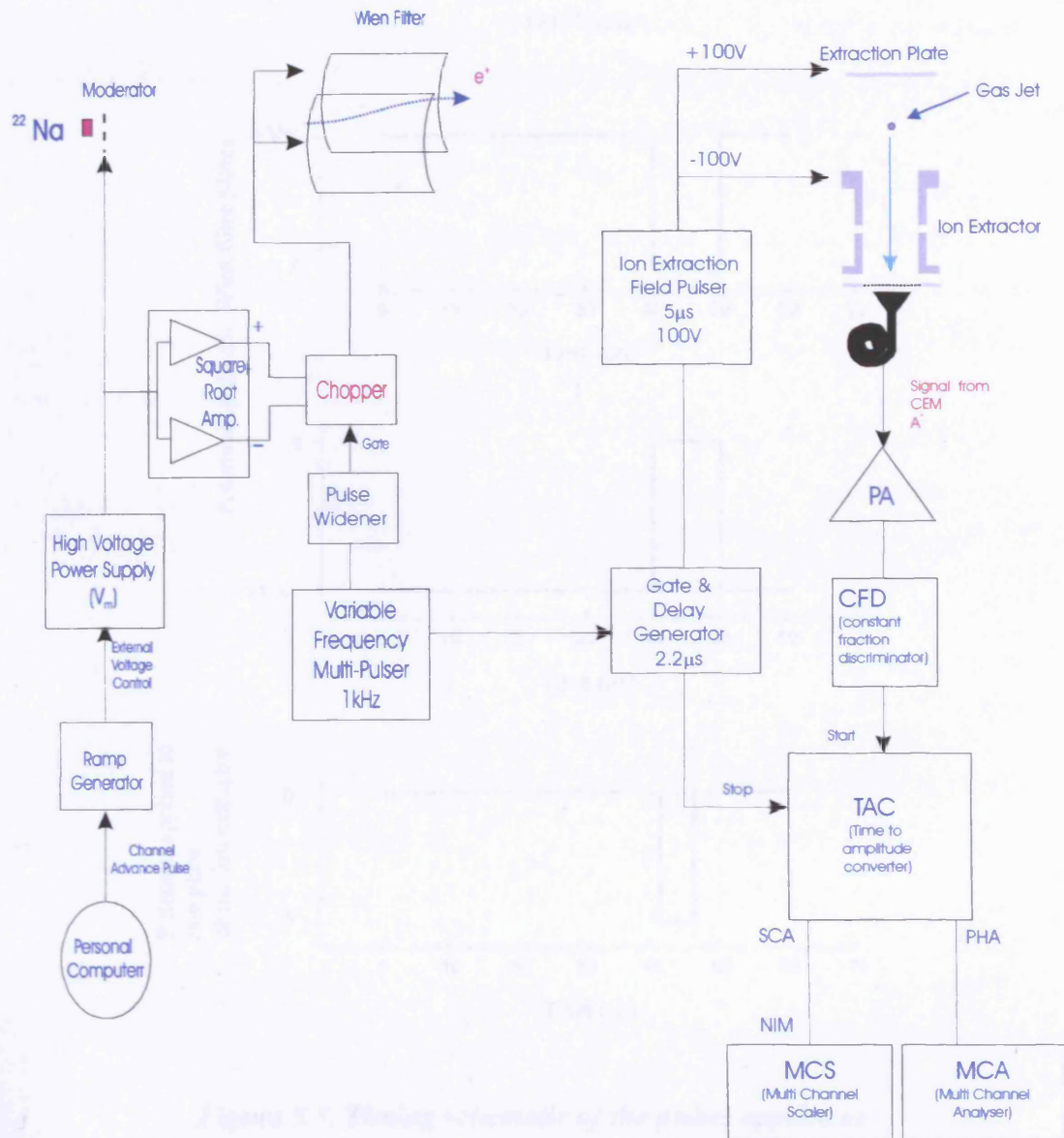


Figure 5.4. Schematic illustration of the random ion extraction circuit employed for the measurement of the total ionisation cross-section of water vapour.

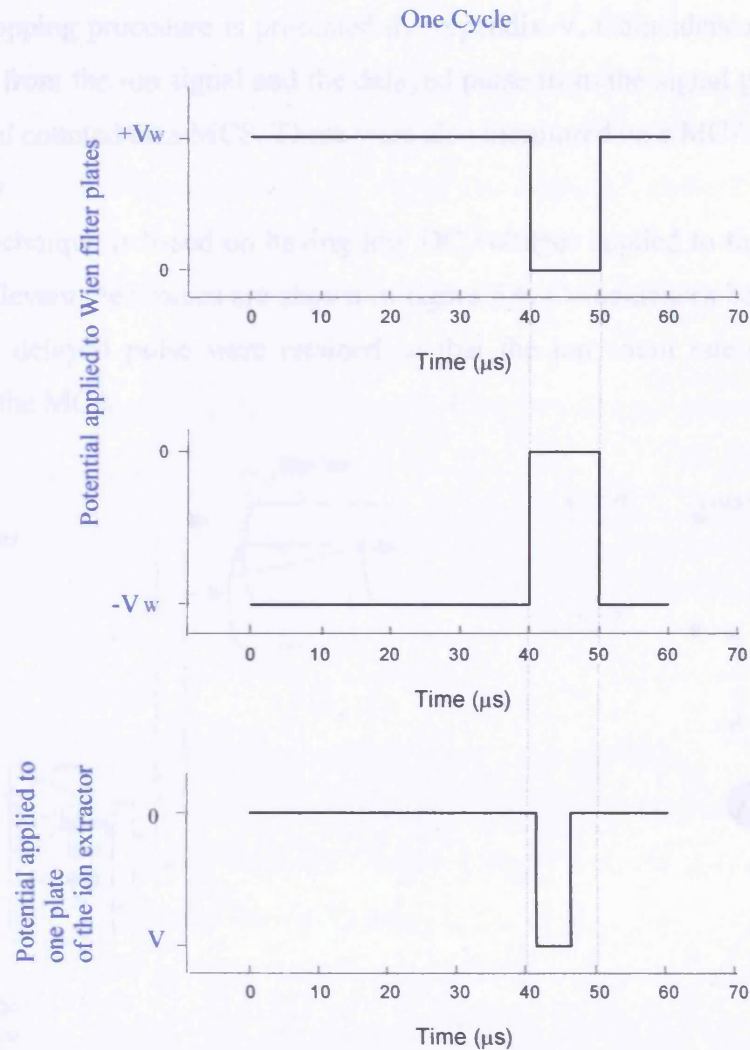


Figure 5.5. Timing schematic of the pulses applied to the ion extractor and Wien filter.

The entire timing sequence was driven by a homemade variable-frequency signal generator (1kHz), whose TTL output was delayed and stretched to $5\mu\text{s}$ using a gate & delay generator (Ortec 416A). The pulse was fed from here into another pulser that supplied the positive and negative pulses needed for the ion extraction ($5\mu\text{s}$; $\pm 100\text{V}$). The signal generator also fed a pulse widener, which was used to stretch the incoming pulse to $10\mu\text{s}$ in width. This pulse was then presented to the blocking input of an electronic device, hereafter referred to as the chopper, which acts as a switch that, in response to the blocking pulse, earths the two plates of the Wien filter stopping the passage of positrons. A $1\mu\text{s}$ delay between the pulses to the chopper and the extractor ensured that all positrons had passed the interaction region prior the ion extraction. A

test of the chopping procedure is presented in Appendix V. Coincidences between the timing output from the ion signal and the delayed pulse from the signal generator were established and counted on a MCS. These were also monitored on a MCA.

DC extraction

The second technique is based on having low DC voltages applied to the plates, as in §5.2.1. The relevant electronics are shown in figure 5.6. Coincidences between the ion signal and its delayed pulse were retained so that the ion count rate could also be monitored by the MCA.

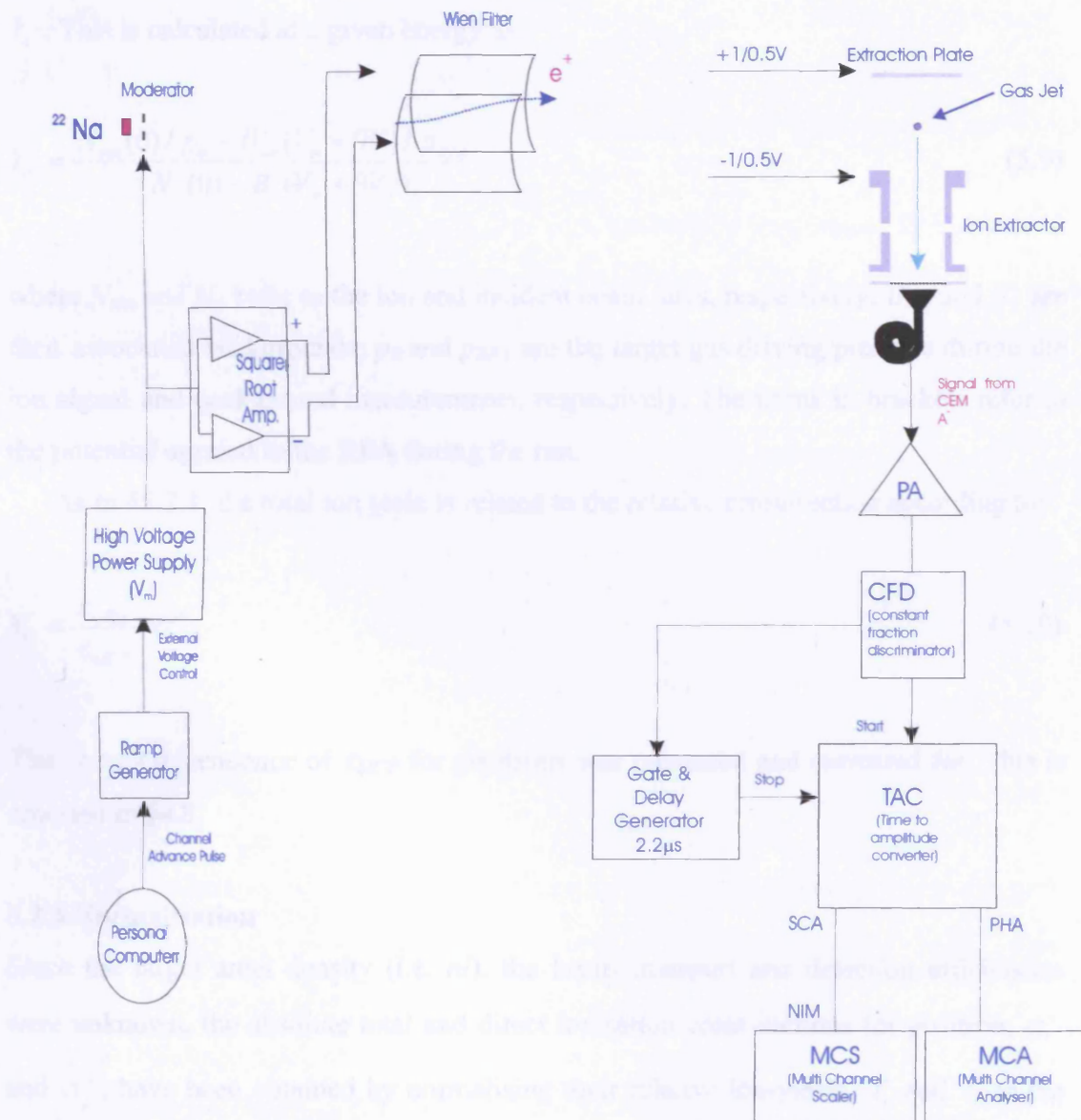


Figure 5.6. A schematic illustration of the continuous ion extraction circuit employed for the measurement of the total ionisation cross-section of water vapour.

Similarly to the procedure described in §5.2.1, in both the pulsed and DC techniques for measuring total ionisation, V_m was ramped. For each value of V_m the rate of events, $N_{ion}(V_m)$, was acquired simultaneously by a MCS and a MCA.

The fast particle contribution to the ion signal was measured, as described in §5.2.1, by biasing-off the e^+ beam using the RFA ($V_{RFA}=V_m+9V$). Before and after each run, the number of positrons was recorded by the MCS for both $V_{RFA}=0$ and V_m+9V for each value of V_m .

The total ionisation cross-section, σ_i^+ , is directly proportional to the total ion yield, Y_i . This is calculated at a given energy as:

$$Y_i = \frac{N_{ion}(0)/p_0 - B_{ion}(V_m + 9V)/p_{RFA}}{(N_+(0) - B_+(V_m + 9V))}, \quad (5.9)$$

where N_{ion} and N_+ refer to the ion and incident beam rates, respectively; B_{ion} and B_+ are their associated backgrounds; p_0 and p_{RFA} are the target gas driving pressure during the ion signal and background measurements, respectively. The terms in brackets refer to the potential applied to the RFA during the run.

As in §5.2.1, the total ion yield is related to the relative cross-section according to:

$$Y_i \propto \frac{\varepsilon_{CEM}}{\varepsilon_{MCP}} \cdot \sigma_i^+. \quad (5.10)$$

The energy dependence of ε_{MCP} for positrons was measured and corrected for. This is reported in §4.8.

5.2.3 Normalisation

Since the target areal density (i.e. nl), the beam transport and detection efficiencies were unknown, the absolute total and direct ionisation cross-sections for positron, σ_i^+ and σ_d^+ , have been obtained by normalising their relative ion-yields, Y_i and Y_d to the ionisation cross-sections for electron impact, $\sigma_i^+(e^-)$, at high energies, as was done for the noble gases (Laricchia *et al.*, 2002). The normalisation method relies on the fact that, as expressed by the first Born approximation, at sufficiently high impact energies

the cross-sections for both projectiles merge. In fact, the energy region where the normalisation is performed is where the ionisation cross-sections for the two projectiles display a similar energy dependence (Van Reeth *et al.*, 2002). To allow a direct comparison with the present data, $\sigma_i^+(e^-)$ has been taken as the sum of the partial ionisation cross-sections for H_2O^+ and OH^+ for electron impact. These are known with an accuracy of 6 % and 7 %, respectively (Itikawa and Mason, 2005).

For electron-water collisions, the main process contributing to the total ionisation cross-section is single ionisation, with double-ionisation processes contributing negligibly. For example, O^{++} contributes less than 0.1% at 1kV (Itikawa and Mason, 2005). No doubly ionised atoms/molecules were observed in the present work, which indicates that higher order processes for positron impact are negligible as in the electron case.

Firstly, to normalise the positron-impact data, a weighted least square fit to a plot of the electron-data versus energy was performed above 600eV. The fitting curve obtained is given by the polynomial $f^-(E) = [10^{-17} + 5 \cdot 10^{-14}/E - 5 \cdot 10^{-12}/E^2] \cdot 10^{-16} \text{ cm}^2$, where the energy is expressed in eV. Subsequently, the yields for positron-impact have been normalised to the electron data by fitting respectively $\sigma_i^+(e^+)$ and $\sigma_i^+(e^+)$:-

$$\sigma_{i,j}^+(e^+) = C^{i,j} f^-, \quad (5.11)$$

where C^i and C^j are the corresponding normalisation factors.

In this work, the region suitable for normalisation has been determined to be above 600eV for the total ionisation cross-section. However, the direct ionisation cross-section has been normalised above 420eV to include a larger number of points and reduce the uncertainty in the fitting procedure. It is noted that the two cross-sections, $\sigma_i^+(e^+)$ and $\sigma_j^+(e^+)$, present slightly different slopes at high energies, which might arise from the poor transport of the positron beam at these energies.

In the following figures, the experimental uncertainties comprise those arising from the background subtraction (~15%), counting statistics (~20%) and the normalisation (3% for C^i and 1% for C^j).

5.2.4 Test of the System with Argon

Initial experimentation was carried out with argon to check the measured cross sections against previously published values. This allows sources of systematic errors in the experiment to be identified and eliminated.

Figure 5.7 shows the single ionisation cross-section, which was obtained using the pulsed extraction method, in comparison to the data by Moxom *et al.* (1996). A fair agreement exists, within the experimental error bars, between the two sets of data.

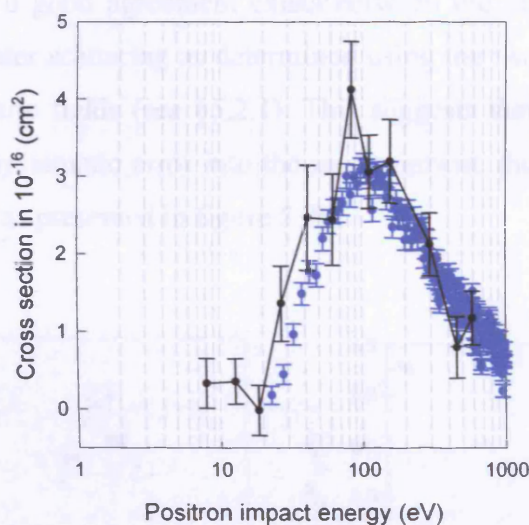


Figure 5.7. Direct ionisation cross-section for e^+ - Ar collision: ● Present results; ● Moxom *et al.* (1996).

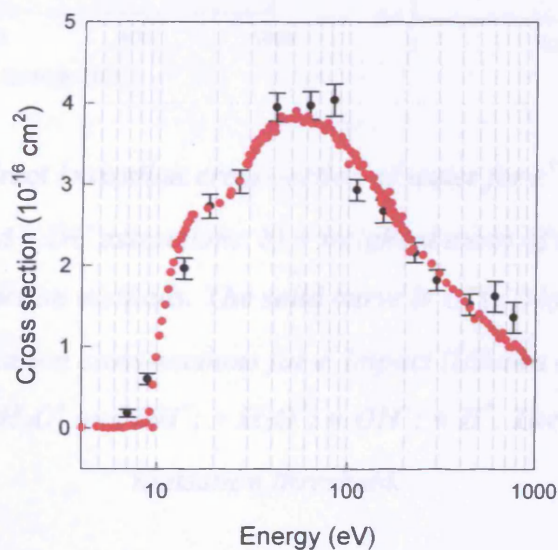


Figure 5.8. Total ionisation cross-section for e^+ - Ar collision: ● Present results; ● Laricchia *et al.* (2002).

In figure 5.8, the total ionisation cross-section is presented. This has been obtained by taking the weighted mean of the values obtained using both the pulsed and DC extraction techniques. As can be seen, a satisfactory agreement between this and the data of Laricchia *et al.* (2002) is found demonstrating the reliable performance of the present system.

5.2.5 Direct and Total Ionisation Cross-Sections of Water: Preliminary Results

Figure 5.9a shows that a good agreement exists between the direct ionisation cross-sections for positron–water scattering as determined using the two extraction methods: the pulsed and DC electric fields (see §5.2.1). This suggests that neither technique is introducing significant systematic error into the measurement, therefore, the data have been combined together as presented in figure 5.9b.

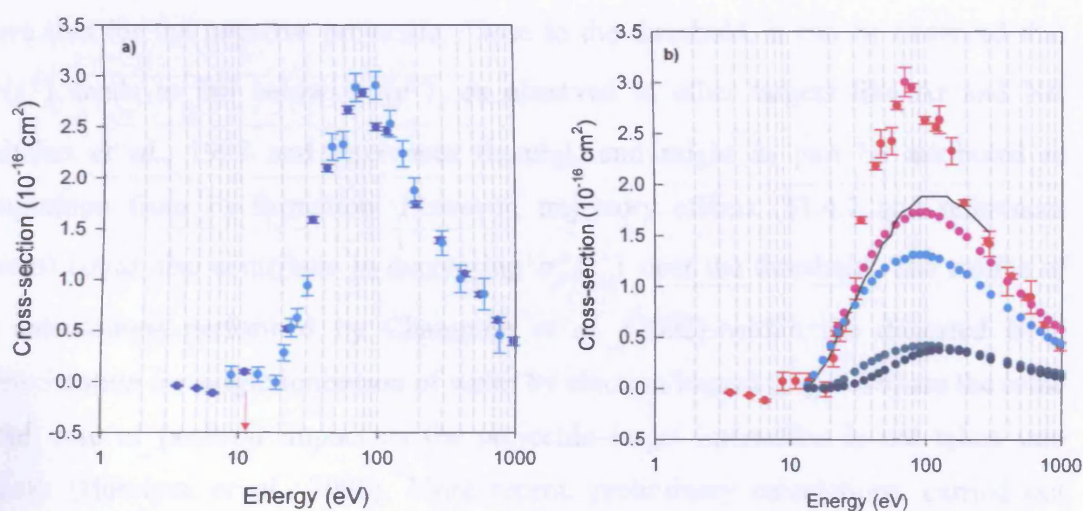


Figure 5.9. Direct ionisation cross-section of water for e^+ impact, $\sigma_i^+(e^+)$:

- a) using ● pulsed and ● DC extraction; b) ● weighted mean of the values obtained using the two extraction methods. The solid curve is $\sigma_i^+(e^-)$ by Champion *et al.* (2002). Partial ionisation cross-sections for e^- impact (Itikawa and Mason, 2005): ● $\sigma_i^+(e^-)$ inclusive of H_2O^+ and OH^+ ; ● H_2O^+ ; ● OH^+ ; ● H^+ . The arrow indicates the ionisation threshold.

As explained in §5.2.2, within the present mass resolution of the system, the measured cross-section is inclusive of both H_2O^+ and OH^+ ions. Corresponding partial

cross-sections for the production of H_2O^+ , OH^+ and H^+ by electron impact are also illustrated in figure 5.9b for comparison. The cross-section for positrons rises from the ionisation threshold up to a peak value of $(3.0 \pm 0.1) \cdot 10^{-16} \text{cm}^2$ at around 70eV. Above this value, $\sigma_i^+(e^+)$ decreases smoothly to join with the electron values. The findings show that the ionisation cross-section for positrons is higher than that for electrons by a factor of two around the maximum. This feature has already been encountered for the noble gases (Paludan *et al.*, 1997) where it has been attributed to the effect of the target polarisation, which tends to attract the target electrons towards the positively charged projectile and away from negatively charged projectile. In the case of the water molecule, because of its permanent electric dipole moment, it may be conjectured that the positron projectile is attracted preferentially by the water negative pole, i.e. oxygen, while the electron projectile by hydrogen. The higher electron densities near oxygen rather than hydrogen could thus favour the ionisation process for the positive projectile above that for the negative projectile. Close to the threshold, it can be observed that $\sigma_i^+(e^+)$ tends to fall below $\sigma_i^+(e^-)$, as observed in other targets like Ar and Ne, (Paludan *et al.*, 1997 and references therein), and might in part be attributed to competition from Ps formation. However, trajectory effects (§1.4.7 and references therein) could also contribute in decreasing $\sigma_i^+(e^+)$ near the threshold. The results of the calculations performed by Champion *et al.* (2002) within the distorted Born approximation for single ionisation of water by electron impact (Fig. 5.9b) are the same in the case of positron impact as the projectile–target interaction is not taken into account (Hervieux *et al.*, 2006). More recent, preliminary calculations, carried out using a Coulomb wave for describing the scattered positron, the ejected electron and the electron-positron interaction and including exchange for electron scattering, have shown nearly undistinguishable differences between the results for electron and positron impact (Champion, 2006).

The partial cross-section for H^+ production from the ionising dissociation of water, $\sigma_D^+(e^+)$, is shown in figure 5.10a.

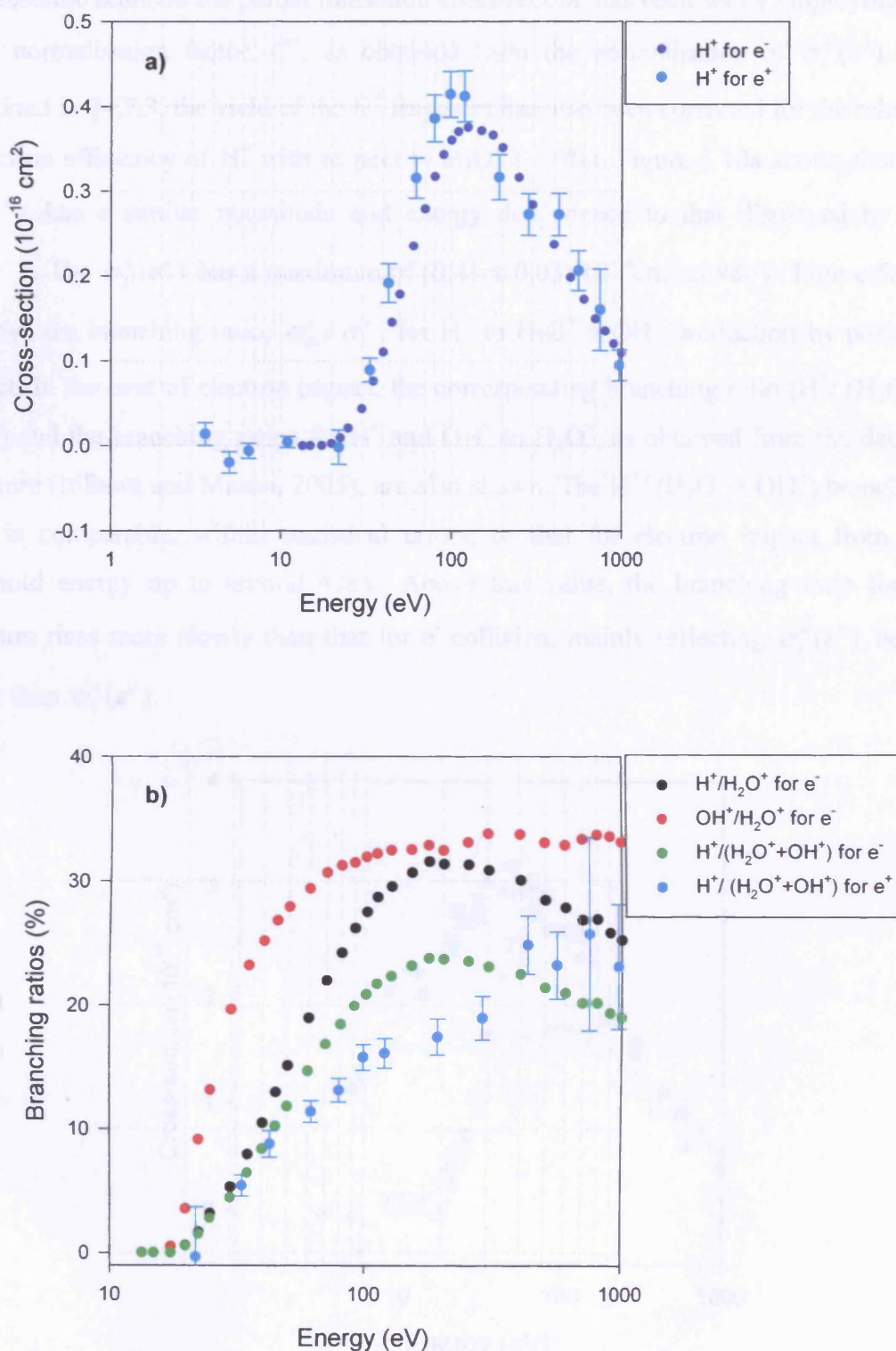


Figure 5.10. a) Partial ionisation cross section for H^+ in the dissociation of water: \bullet present results, $\sigma_D^+(e^+)$; \bullet electron impact, $\sigma_D^+(e^-)$ (Itikawa and Mason, 2005); **b)** the branching ratio $H^+/(H_2O^++OH^+)$ for \bullet electron and \bullet positron impact. Other branching ratios in the e^- case are shown (see label).

The absolute scale on the partial ionisation cross-section has been set by employing the same normalisation factor, C^+ , as obtained from the normalisation of $\sigma_i^+(e^+)$. As explained in §4.7.3, the yield of the H^+ fragment has also been corrected for the relative extraction efficiency of H^+ with respect to H_2O^+ (~39%). Figure 5.10a shows that the $\sigma_D^+(e^+)$ has a similar magnitude and energy dependence to that displayed by the $\sigma_D^+(e^-)$. The $\sigma_D^+(e^+)$ has a maximum of $(0.41 \pm 0.03) \cdot 10^{-16} \text{ cm}^2$ at 98eV. Figure 5.10b displays the branching ratio, σ_D^+ / σ_i^+ , for H^+ to $H_2O^+ + OH^+$ production by positron impact. In the case of electron impact, the corresponding branching ratio ($H^+ / (H_2O^+ + OH^+)$) and the branching ratios for H^+ and OH^+ to H_2O^+ , as obtained from the data in literature (Itikawa and Mason, 2005), are also shown. The $H^+ / (H_2O^+ + OH^+)$ branching ratio is comparable, within statistical errors, to that for electron impact from the threshold energy up to around 43eV. Above this value, the branching ratio for e^+ collision rises more slowly than that for e^- collision, mainly reflecting $\sigma_i^+(e^+)$ being larger than $\sigma_i^+(e^-)$.

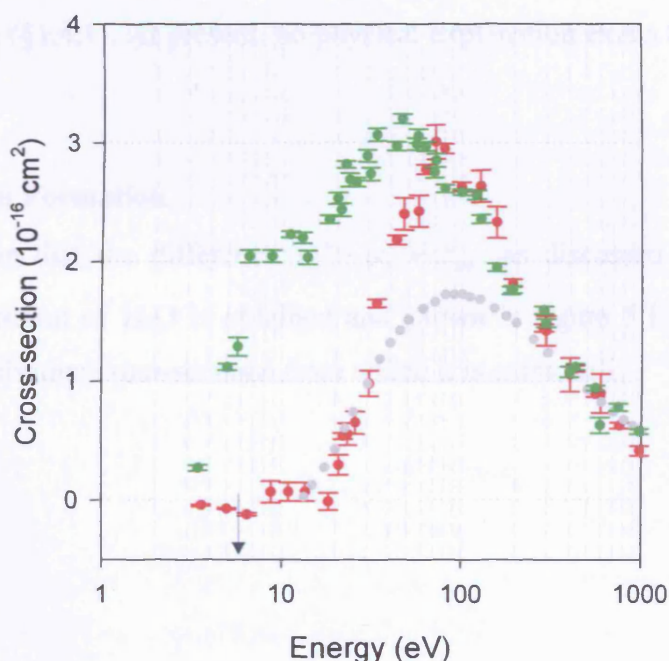


Figure 5.11. ● Total ionisation cross-section for $e^+ - H_2O$ collisions; ● direct ionisation cross-section for $e^+ - H_2O$ collisions; ● direct ionisation cross-section for $e^- - H_2O$ collisions (Itikawa and Mason, 2005). The arrow shows the Ps formation threshold.

The total ionisation cross-section for $\text{H}_2\text{O} - e^+$ collision is displayed in figure 5.11. Non-zero values can be observed below the Ps formation threshold shown by the arrow. The $\sigma_i^+(e^+)$ curve rises sharply with increasing energy reaching a small shoulder between 6.8 and 15eV. This feature is followed by another increase of the $\sigma_i^+(e^+)$ until a broad maximum, $\sim 3.2 \cdot 10^{-16} \text{cm}^2$, is reached between 33-62eV, where both positronium formation and direct ionisation are open. Then, $\sigma_i^+(e^+)$ drops as the collision energy increases to reach a small plateau between 79-119eV (just hinted at in the $\sigma_i^+(e^+)$), which is accompanied by a monotonic decrease of the curve up to the highest energies to follow the $\sigma_i^+(e^-)$. The origin of the signals below the Ps threshold has not yet been identified and further investigations are necessary, primarily to rule out a possible miscalibration in the beam energy, possible contributions from fast particles or residual gases. Within the context of positron bound states with molecules (see §1.4.3), it is noted that, e.g. molecular vibrations or virtual Ps have been proposed to lead to large annihilation values near inelastic thresholds (§1.4.5). It is also noted that a small and narrow structure at around 3.5eV was recently reported by Zecca *et al.* (2006) in the total cross-section (§1.4.1). At present, no physical explanation exists for this structure either.

5.2.6 Positronium Formation

On the assumption that the difference $\sigma_i^+ - \sigma_i^- = \sigma_{Ps}$, as discussed in §5.1, the Ps formation cross-section of H_2O is obtained and shown in figure 5.12 along with the direct and total ionisation cross-sections from which it is extracted.

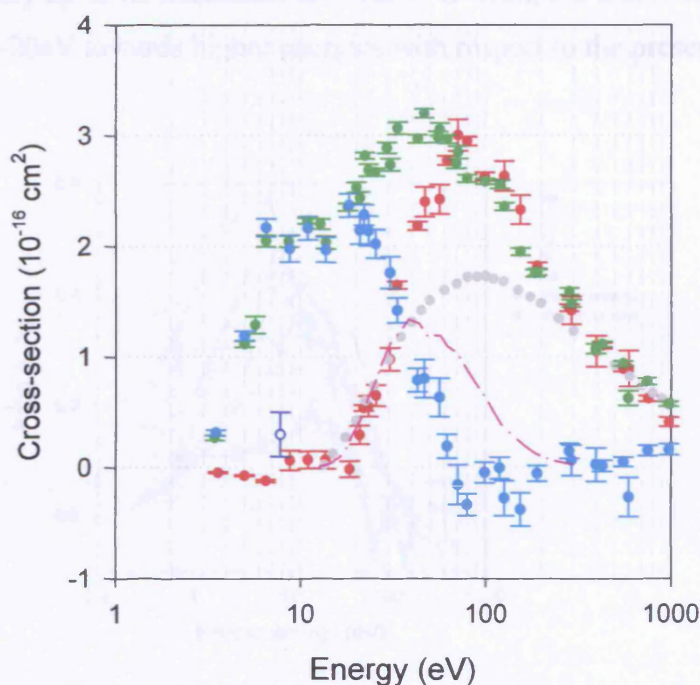


Figure 5.12. Positronium formation cross-section for $e^+ - \text{H}_2\text{O}$ collisions:

- present results; ○ $\sigma_{\text{Ps}}(E_{\text{Ps}}+2\text{eV})$ by Sueoka *et al.* (1987); dash-dot pink curve is the CDW-FS theory for $\sigma_{\text{Ps}(1\text{s}+2\text{s})}$ formation (Hervieux *et al.*, 2006). ● $\sigma_i^+(e^+)$; ● $\sigma_i'(e^+)$;
- direct ionisation cross-section for $\text{H}_2\text{O} - e^-$ collision (Itikawa and Mason, 2005).

The Ps formation cross-section reaches a broad maximum between 6 and 20 eV with a magnitude of $\sim 2.4 \cdot 10^{-16} \text{ cm}^2$. The Ps signal approaches zero at around 60 eV, significantly below that for the inert atoms. A slight over-subtraction occurs above this energy up to around 190 eV, while an under-subtraction takes place mainly at high energies. These inaccuracies may be attributable to the direct ionisation data (see §5.2.5). As can be observed in Fig. 5.12, the previous estimate by Sueoka *et al.* (1987) for σ_{Ps} at 2 eV above the Ps formation threshold (see §1.4.6) is around seven times smaller than present results. The recent results of the calculation performed within the Continuum Distorted-Wave Final State approximation (CDW-FS, Hervieux *et al.*, 2006) for the positronium formation in the 1s ground and 2s excited states, $\sigma_{\text{Ps}(1\text{s}+2\text{s})}$, are also displayed. The calculation, which accounts for the interaction of the projectile and electron with the residual ion in the final state, yields a cross-section with a very different energy dependence and magnitude to the experimental one, rising very slowly above the Ps formation threshold and following the ionisation cross-section for electron

impact very closely up to its maximum at $\sim 40\text{eV}$. Overall, the theoretical curve seems to be shifted by $\sim 20\text{eV}$ towards higher energies with respect to the present experimental data.

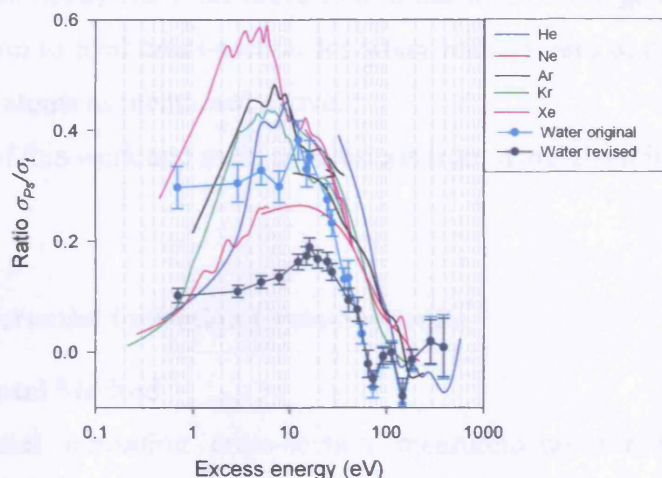


Figure 5.13. Ratio between the Ps formation and total cross-section, σ_{Ps}/σ_t , versus excess energy ($E_+ - E_{th}$) • water (σ_{Ps} by Arcidiacono *et al.*, 2005b, 2007) and σ_t by Sueoka *et al.*, 1987); • water (σ_{Ps} by Arcidiacono *et al.*, 2005b, 2007) and σ_t by Kimura *et al.*, 2000); for the noble gases see legend.

In figure 5.13 the ratios, σ_{Ps}/σ_t , between the present Ps formation cross-section and the total cross-section, σ_t , by Sueoka *et al.* (1987) and the revised σ_t data of Kimura *et al.* (2000) are shown. The maximum of σ_{Ps}/σ_t is $\sim 38\%$ for the Sueoka data (1987), whereas this maximum decreases to $\sim 19\%$ if the forward scattering corrected data are used. It is interesting to compare these ratios for water to those for the noble gases. In helium, the maximum value of σ_{Ps}/σ_t is $\sim 45\%$ using the data of Murtagh *et al.* (2005) for σ_{Ps} and combining those of Kauppila *et al.* (1981) and Stein *et al.* (1978) for σ_t . The maxima of σ_{Ps}/σ_t for argon (σ_{Ps} by Laricchia *et al.*, 2002 and σ_t by Kauppila *et al.*, 1981) and krypton (σ_{Ps} by Laricchia *et al.*, 2002 and σ_t by Dababneh *et al.*, 1980 and 1982) have similar maximum values to that of helium, i.e. 48 % and 43%, respectively. The major contribution from Ps formation, among the noble gases, occurs in xenon (σ_{Ps} by Laricchia *et al.*, 2002 and σ_t by Dababneh *et al.*, 1980 and 1982) with a maximum of 59%, whereas the minimum occurs in neon (σ_{Ps} by Laricchia *et al.*, 2002 and σ_t by Stein *et al.*, 1978 and Kauppila *et al.*, 1981) with a maximum of 26%. Hence, the Ps formation probability from water tends to be lower than in the noble gases except

possibly for Ne. Moreover, it is observed that Xe presents a very large onset for σ_{Ps}/σ_t , compared to that for the other inert atoms. A comparable low energy value is found if the original results of Sueoka *et al.* (1987) are used. However, for the revised water data (Kimura *et al.* 2000), the value is reduced to that of all noble gases but Xe. Finally, the Ps contribution to total cross-section for water reaches zero at much lower energy than for the inert atoms as mentioned above.

A summary of this work and main conclusions from it are given in §5.4.

5.3 Doubly Differential Ionisation Cross-Sections

5.3.1 Experimental Method

Doubly differential ionisation cross-section measurements for water have been conducted with the electrostatic beam apparatus described in chapter 2 after a few modifications (§2.5.6). Figure 5.14 shows a schematic diagram of the electronics employed.

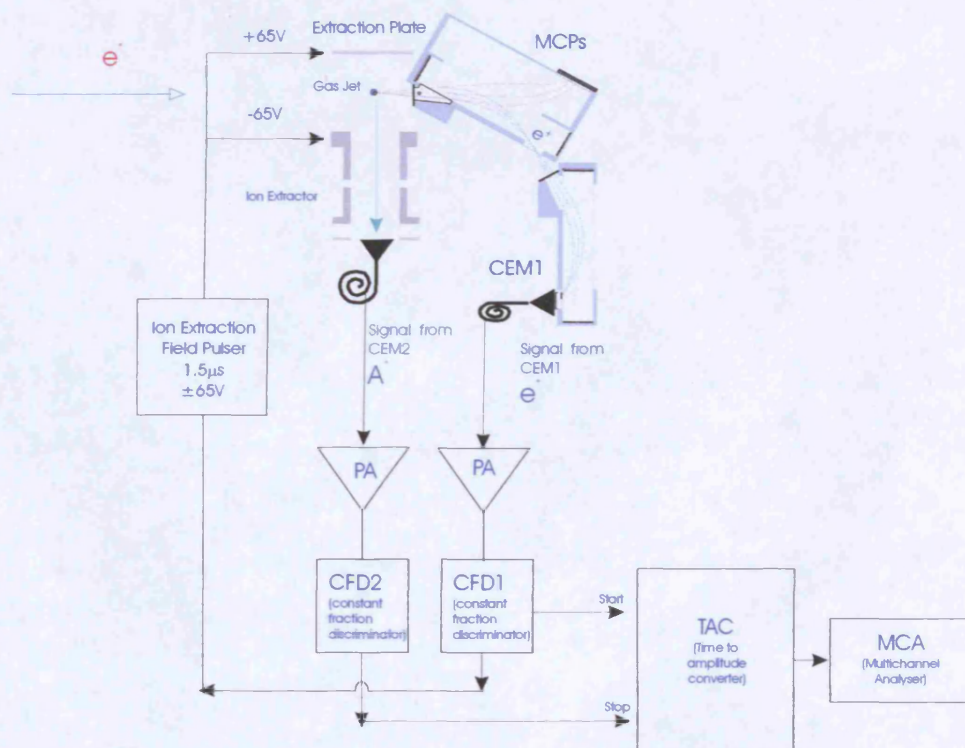


Figure 5.14. A schematic diagram of the electronics and data collection employed for the doubly differential cross-section.

Coincidences between the residual target ion and the energy-analysed scattered positron were monitored. Positrons exiting the interaction region at 0° and of a given energy, E_+ , were detected by a single channel-electron-multiplier (CEM1) after passing through the tandem parallel plate analyser (as described in §2.5). The amplified signal from the positron detection was fed into CFD1 (Ortec 584), which in turn started a TAC (Ortec 567). Ions were detected by a second channeltron (CEM2) at the end of the ion extractor. After amplification, the ion signal was processed by CFD2 and fed into the stop input of the TAC. The ion extraction field between the two parallel plates was established by pulses of $\pm 65\text{V}$ and $1.5\mu\text{s}$ wide as supplied by a multipulser (Carroll&Meynell Ltd). These were applied upon the detection of a positron. Positron-ion coincidences were again collected by a PC-based MCA.

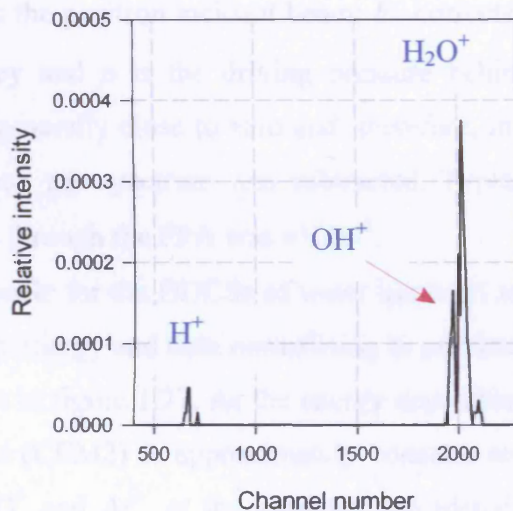
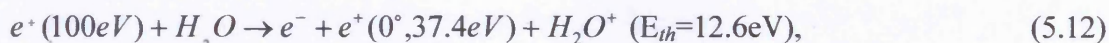
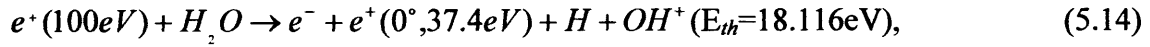


Figure 5.15. Time-of-flight spectrum of charged water ions for a scattered positron energy of 37.4eV

Ions of the appropriate charge-to-mass ratio could be identified on the MCA by their TOF. The coincidence signals yielded well-resolved peaks for different residual ions (H^+ , OH^+ and H_2O^+) as illustrated by the spectrum in figure 5.15. These peaks arise from the following reactions:





where threshold energies are indicated between brackets.

Similarly to the case of the triply differential cross-section (e.g. §3.3), to convert the measured coincidence signal to a quantity directly proportional to the DDCS, the following procedure was used. The areas under the peaks in the TOF spectra were integrated after subtracting the random background to determine the yield:

$$Y_{DDCS} \propto \frac{C - B}{pN_+E_+}, \quad (5.15)$$

where C and B are the total number of positron-ion coincidences in gas and vacuum, respectively; N_+ is the positron incident beam; E_+ corrects for variation of the analyzer transport efficiency and p is the driving pressure behind the water vapour nozzle. However, B was generally close to zero and, therefore, in most cases only the random background in each gas spectrum was subtracted. Typical value for the intensity of incident positrons through the PPA was $\approx 100\text{s}^{-1}$.

The absolute scale for the DDCSs of water has been set by measuring yields for Ar at the same impact energy and then normalising to previous data of Kövér *et al.* (1993), which were shown in figure 1.27. As the energy dependence of the detection efficiency of the channeltron (CEM2) is approximately constant and close to 50% for all ions, including H^+ , H_2O^+ and Ar^+ , at the energies considered in this study (Fields *et al.*, 1977), no further correction were required in the normalisation.

5.3.2 Results and Discussion

The absolute doubly differential ionisation cross-sections at 0° for the non-dissociative and dissociative reactions for 100eV positron collision energy are presented in figure 5.16.

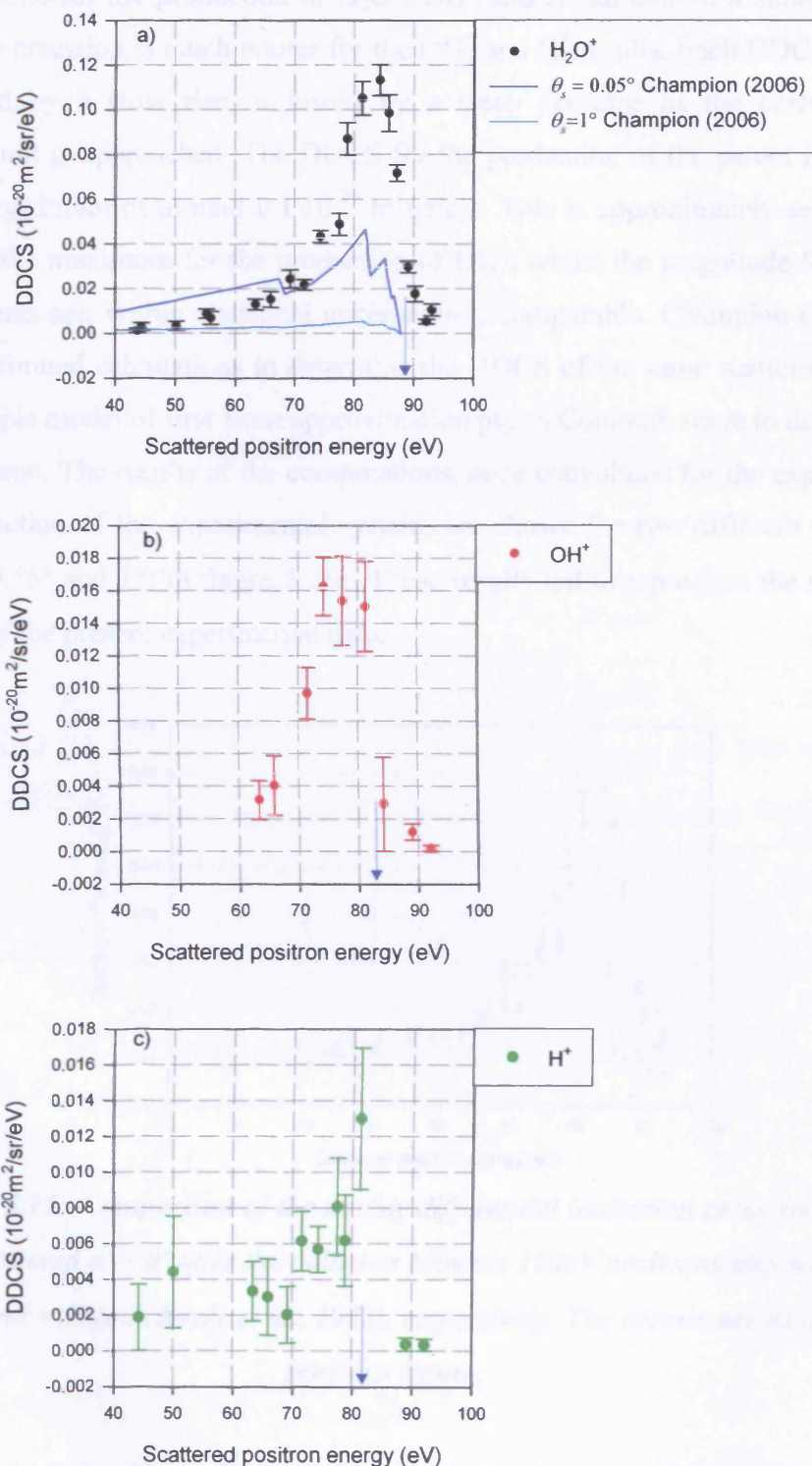


Figure 5.16. Doubly differential ionisation cross-sections at 0° for $e^+(100\text{eV}) - \text{H}_2\text{O}$ collisions resulting in the production of the following ions: $\bullet \text{H}_2\text{O}^+$; $\bullet \text{OH}^+$; $\bullet \text{H}^+$. The curves represent the theory (Champion, 2006). The arrows indicate the corresponding ionisation limit ($E_+ - E_{th}$).

The DDCCSs for the production of H_2O^+ , OH^+ and H^+ all exhibit a similar pattern although the precision is much poorer for the OH^+ and H^+ results. Each DDCCS curve is characterised by a slow rise, followed by a steep decrease as the corresponding ionisation limit is approached. The DDCCS for the production of the parent ion, H_2O^+ , presents a maximum of around $0.1 \cdot 10^{-20} \text{ m}^2/\text{sr}/\text{eV}$. This is approximately seven times higher than the maximum for the production of OH^+ , whilst the magnitude for H^+ and OH^+ fragments are, within statistical uncertainties, comparable. Champion (2006) has recently performed calculations to determine the DDCCS of the same scattering system within a simple model of first Born approximation plus a Coulomb wave to describe the ejected electron. The results of the computations, once convoluted for the experimental energy resolution of the experimental system, are shown for two different scattering angles, θ_s (0.55° and 1°) in figure 5.16a. These results fail to reproduce the shape and magnitude of the present experimental data.

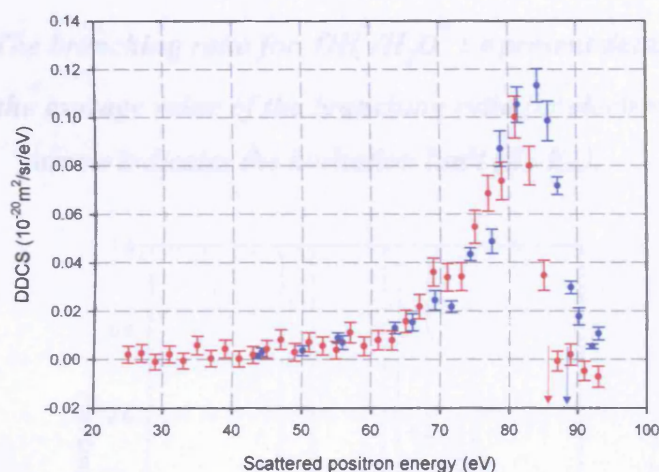


Figure 5.17. Comparison of the doubly differential ionisation cross-section for positrons scattered at $\sim 0^\circ$ after the collision between 100eV positrons and $\bullet \text{H}_2\text{O}$ (this work) and $\bullet \text{Argon}$ (Kövrer *et al.*, 1993), respectively. The arrows are as in the previous figure.

In figure 5.17, the shape of the DDCCS for H_2O (Arcidiacono *et al.*, 2006), is seen to be similar to that observed for Ar (Kövrer *et al.*, 1993) whilst its magnitude is higher. In fact, the ratio between the area of each DDCCS to its corresponding σ_i^+ at 100eV has been calculated and that for H_2O has been found to be approximately 1.5 higher than for Ar, indicating a higher probability for forward inelastic scattering of the projectile at

an acceptance polar angle of $\pm 5^\circ$. These findings could assist in the development of accurate predictions concerning energy deposition by positrons in tissues and organs during e.g. PET.

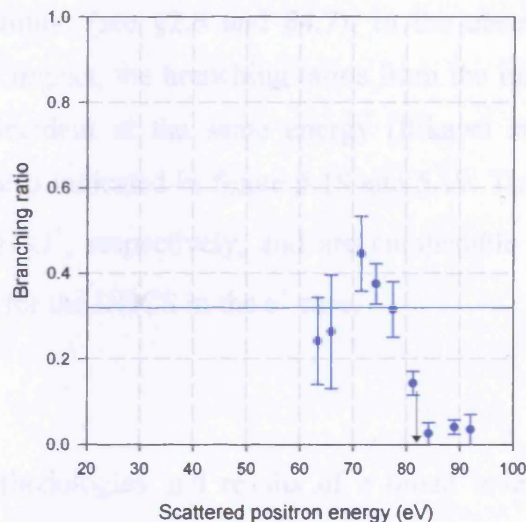


Figure 5.18. The branching ratio for $\text{OH}^+/\text{H}_2\text{O}^+$: • present data. The horizontal line represents the average value of the branching ratio for electron impact. The arrow indicates the ionisation limit ($E_+ - E_{th}$).

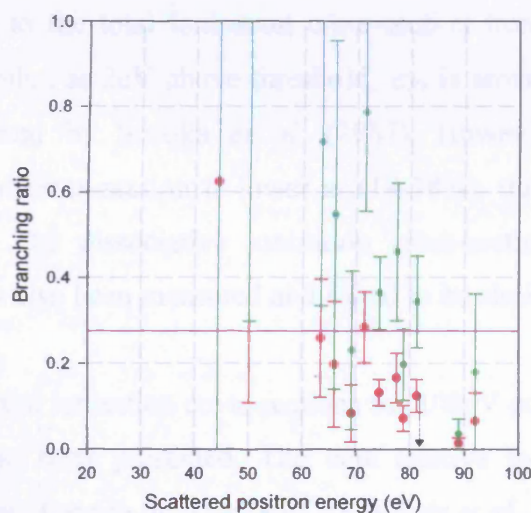


Figure 5.19. The branching ratio for $\text{H}^+/\text{H}_2\text{O}^+$: • present data corrected and • uncorrected for the extraction efficiency. The horizontal line and the arrow as in the previous figure.

In figures 5.18 and 5.19, the branching ratios corresponding to $\text{OH}^+/\text{H}_2\text{O}^+$ and $\text{H}^+/\text{H}_2\text{O}^+$ are shown. In this study, the ratio for $\text{H}^+/\text{H}_2\text{O}^+$ has been corrected for the relative probability ($\sim 36\%$) of extracting the H^+ fragments from the interaction region in the electrostatic beamline (see §2.6 and §4.7). In the absence of corresponding DDCS data for electron impact, the branching ratios from the integral ionisation cross sections for electrons incident at the same energy (Itikawa and Mason, 2003 and references therein) are also indicated in figure 5.18 and 5.19. These are 32% and 27% for $\text{OH}^+/\text{H}_2\text{O}^+$ and $\text{H}^+/\text{H}_2\text{O}^+$, respectively, and are comparable to the corresponding branching ratio maxima for the DDCS in the e^+ case.

5.4 Summary

In this chapter, the methodologies and results of a broad investigation of positron-induced ionisation of water have been presented. To date, we are unaware of any previous corresponding data.

It is found that the ionisation probability for positron collisions is larger than for electron by up to a factor of 2 and that, contrary to earlier conjectures (Sueoka *et al.*, 1987; Makochekanwa *et al.*, 2006), Ps formation is non-negligible, making an important contribution to the total ionisation cross-section from the threshold up to around 40eV. In particular, at 2eV above threshold, σ_{Ps} is around seven times higher than the value estimated by Sueoka *et al.* (1987). However, the Ps formation contribution to the total cross-section is lower at (19-38%), than for the inert atoms (except possibly Ne). The dissociative ionisation cross-section for production of hydrogen fragments has also been measured and found to be similar to that for electron impact.

The doubly differential ionisation cross-sections for 100eV positrons colliding with water vapour have also been presented. The data relative to the non-dissociative ionisation show a similar shape to the DDCS of Ar (Kövéér *et al.*, 1993). On comparing the integral and differential ionisation for these two targets, it is found that the forward emission of the scattered projectile is higher in water than in Ar, possibly due to the presence of the long-range dipole interaction in the former case as in the case of elastic scattering. The doubly differential cross-section for the production of OH^+ and H^+ ions in the dissociative ionisation show a similar pattern to that of the parent ion. Their maxima are similar within statistical uncertainties but are a factor of 7 less than that of

H_2O^+ . Finally, the branching ratios of the DDCS for $\text{OH}^+/\text{H}_2\text{O}^+$ and $\text{H}^+/\text{H}_2\text{O}^+$ have also been obtained. No corresponding DDCS for electron impact was found in the literature for comparison. These results for DDCSs in dissociative and non-dissociative ionisation represent a sensitive test for theoretical models and useful for the description of the distribution of energy deposits during the slowing down of positrons in living matter through Monte Carlo simulations (Champion and Le Loirec, 2006).

The differences and similarities between the various results raise some interesting questions, especially on the different behaviour between positron- and electron-impact ionisation of water molecule. Some of these questions concern:

- 1) the role of the permanent electric dipole moment in determining the differences in the single ionisation cross-section for positron and electron impact.
- 2) The similarity of the dissociative ionisation cross-sections for positron and electron impact. However, the present result is very sensitive to the estimated value of the extraction efficiency of H^+ . In this respect, it would be useful to determine the extraction efficiency for H^+ with another method (see §6.2).
- 3) The non-zero signals observed in the total ionisation cross-section below the Ps formation threshold. A more careful investigation near the threshold, which allows a better discrimination of background signals (e.g. Moxom *et al.*, 1994; Szluinska and Laricchia, 2004; Szluinska *et al.*, 2005), would be required to establish their origin.
- 4) The unexplained appearance of a small shoulder/plateau in the total ionisation cross-section between 79-119eV.
- 5) The total discord between experiment and the only available theory (Hervieux *et al.*, 2006), which would modify significantly the results of Monte Carlo work of Champion and Le Loirec (2006).
- 6) The role of the permanent dipole moment in explaining the greater forward inelastic scattering of positrons from H_2O , as highlighted from the comparison with Ar.

These should provide a stimulus for future theoretical and experimental work.

Chapter 6

Conclusions and Suggestions for the Future Work

6.1 Summary and Conclusions

The work reported in this thesis has been concerned with positron-induced ionisation phenomena. Firstly, an extensive study has been carried out into an outstanding problem that appeared in the ionisation of molecular hydrogen by 50eV positron impact. This was represented by an energy shift of $\sim 1.6\text{eV}$ between the theoretical and measured energy spectrum of ejected electrons in the triply-differential cross-section (TDCS), $d^3\sigma_i^+ / dE_- d\Omega_- d\Omega_+$, reported by Kövér *et al.* (2001). In order to understand this discrepancy, an absolute energy calibration, two new TDCSs for ejected electrons plus one for scattered positrons have been measured using an electrostatic apparatus. An asymmetric share of the residual kinetic energy between the ejected electron and the scattered positron is unambiguously confirmed by the results of this study. The precise physical origin of this asymmetry however remains presently unclear.

Secondly, absolute total and direct ionisation cross-sections have been measured for the first time for positron impact on water molecules for collisional energies in the range from threshold to $\sim 1\text{keV}$. This has been done by employing a magnetically guided beamline, which has been set-up for this purpose. The present results for the direct ionisation cross section are up to a factor of two higher than corresponding values for electrons, whilst those for the dissociative ionisation cross-section, $\sigma_D^+(H^+)$, are similar to that for electron impact. Non-zero values appear below the Ps threshold in the total ionisation cross-section, which, as discussed in §5.2.5, must be considered preliminary. The positronium formation cross-section, σ_{Ps} , has been extracted by taking the difference between σ_i^+ and σ_i^+ . The preliminary data show that there is a significant contribution to the ionisation channel unlike what had been inferred by previous works (Sueoka *et al.*, 1987; Makochekanwa *et al.*, 2006). The contribution to the total cross-section however is lower than in the noble gases, except perhaps Ne.

Moreover, the experimental results for σ_{Ps} are inconsistent with a recent theoretical determination (Hervieux, 2006), which has been used to describe the energy depositions in living matter during, e.g. PET (Champion and Le Loirec, 2006 and §6.2)

Following modifications of the experimental arrangement of the electrostatic apparatus, first measurements of doubly differential ionisation cross-sections (DDCS), $d^2\sigma_i^+ / dE_+ d\Omega_+$, at around zero degrees for 100eV positron impact on water have been reported. The pattern of the DDCS for H_2O^+ is similar to the one measured for Ar^+ (Kövéér *et al.*, 1993). The comparison with this latter target reveals a greater degree of forward inelastic scattering of the projectile by approximately a factor of 1.5, possibly due to the presence of a long-range dipole interaction in water. The simple model proposed by Champion (2006) is not able to reproduce the present findings. The DDCS for the dissociative ionisation with the production of H^+ and OH^+ fragments have also been obtained. Corresponding peak values are found to be comparable and a factor of 7 less than in the DDCS for non-dissociative ionisation. Further studies are planned.

6.2 Outlook and Future Work

As stated in chapter 3, considering the discrepancy between the experimental TDCSSs (Kövéér *et al.*, 2001; Arcidiacono *et al.*, 2005a) and the results of the theory (Fiol *et al.*, 2001), an *ab initio* calculation would seem necessary to progress in understanding of the dynamics of positron induced ionisation in simple systems, such as H_2 , D_2 and He . Experimentally, a new apparatus is planned at UCL (Laricchia, 2006) for this type of studies using a reaction microscope (Ullrich *et al.*, 2003).

Further work is required to finalise the integral ionisation cross-sections for water vapour and to explain the non-zero signals that have been observed in the total ionisation cross section below Ps formation. The widespread interest in this molecular target confirms the necessity for a detailed experimental work (Champion, 2006). Moreover, to improve the time-of-flight resolution of the system, a longer drift tube or better pulsing units could be employed. This would aid in resolving the various water fragments emerging from dissociative ionisation upon positron collision. It may be worthwhile to measure the extraction efficiency of the system for this target. Indeed, a possible uncertainty in the present data remains the determination of the ion extraction efficiency correction that could be overcome by repeating the measurements using the

same apparatus and a beam of electrons and compare with the values in the literature. Finally, it would be interesting to investigate other polar molecules, such as NH_3 , SO_2 and H_2S .

In future investigations, and in line with current trends, it would be of interest to study biomolecules and the angular and energy distribution of low energy electrons in positron-induced ionisation of water. This latter is highly relevant because of the genotoxic effect (e.g. single and double strand break in DNA) of ionising radiation in cells that is not only due to the impact of the primary radiation but also induced by secondary species (e.g. in cancer treatment methods). The most abundant among these secondary radiation species are free secondary electrons with energies between 1-20eV (e.g. Boudaiffa *et al.*, 2000). Knowledge of the cross-section differential with respect to the energy and/or angle of the secondary electrons would help to quantify the extent of the tissue and DNA damage, e.g. through Monte Carlo tracks simulations (Champion and Le Loirec, 2006).

APPENDIX I

Positron Beam Transport in the Electrostatic Beam

A description of the design and operational characteristics of the lens arrangement, which provides the electrostatic fields used to focus a beam of positrons, follows.

Figures 1 a) and b) show the employed double and triple cylinder lenses respectively. These are two of the most common lens geometries in electron/ion optics (Harting and Read, 1976).

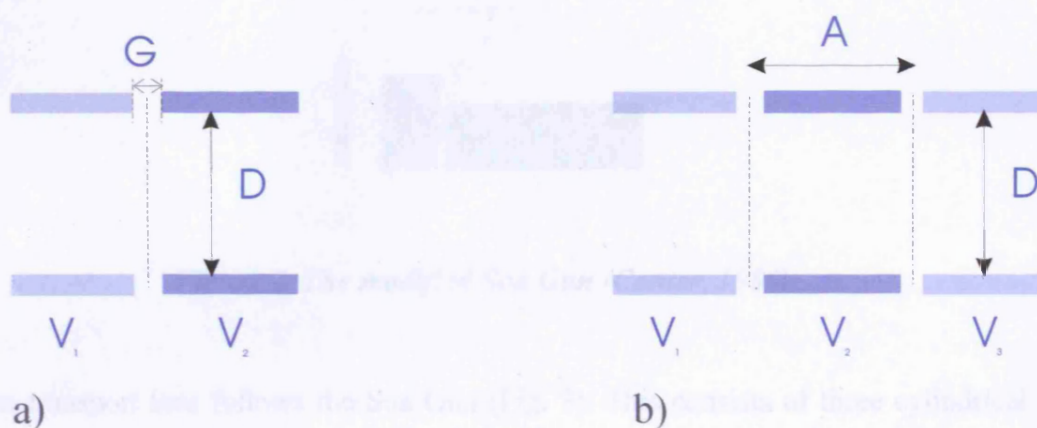


Figure 1. a) A double element cylindrical lens; b) a triple element cylindrical lens.

The double element cylindrical lens consists in two cylindrical electrodes with a diameter D held at voltages V_1 and V_2 and separated by a gap G . Its resulting effect is the focusing of the traversing particles and a change in their energy. The focal lengths of this lens depend on the ratio V_2/V_1 . With respect to this kind of lens, the triple element cylindrical lens, shown in figure 1 b), has the advantage of changing the acceleration ratio of the flying charged particles without varying their image position. Practically, it works as a zoom lens characterized by the ratios G/D and A/D , where A is the distance between the midpoints of the gaps between the inner and outer cylinders along the cylinder axis. The focusing properties of a triple element lens depend on the voltage ratios V_3/V_1 and V_2/V_1 .

To focus the quasi-monoenergetic positrons once emitted from the moderator and accelerated by the grid, a modified Soa Gun (Canter, 1986) is employed. This lens system, shown in figure 2, is essentially constituted by three electrodes: E1, E2 and E3, having internal diameters 10, 19 and 35mm, respectively. The first two lenses, E1 and

E2, are held at the same potential and separated by a distance 2.5mm, while the last one, E3, with a separation distance of 0.5mm from E2, is held independently at a certain voltage.



Figure 2. The modified Soa Gun (Canter, 1986).

The transport lens follows the Soa Gun (Fig. 3). This consists of three cylindrical elements: E4, E5 and E6 ($A/D=1$, $G/D=0.1$, with $D=30\text{mm}$). Electrodes E4 and E6 are always held at the ground potential of the chamber; hence the lens assembly works as an Einzel lens. This means that there is no change in the beam energy, but only a focusing effect. The potential applied to the mid-electrode, E5, is varied according to the energy of the beam. Two apertures with 6mm of internal diameter, located at each end of the transport lens, provide a reduction in the angular spread of the beam.

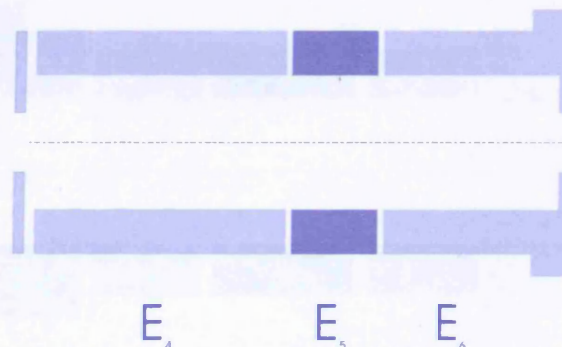


Figure 3. Schematic of the transport lens.

The double cylindrical condenser, E7 and E8, illustrated in figure 4, is employed as a deflector. This separates the monoenergetic positron beam from the high energy β^+ particles and γ radiation. The working principle of this deflector is to apply the same negative potential to E7 and E8 in order to deflect the positron beam upwards by 20mm and then parallel to its original trajectory towards the interaction region.

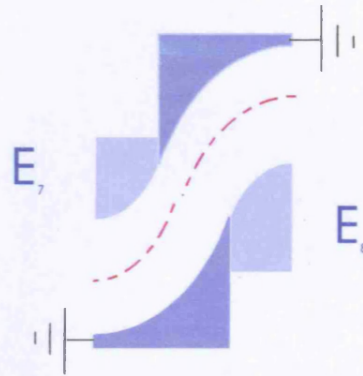


Figure 4. Schematic of the deflector.

Finally, the exit lens in figure 5 is a combination of an aperture E9, with an internal diameter of 6mm, an electrode E10, usually grounded, and a three element lens system (E11, E12 and E13, with $A/D=1$, $G/D=0.1$, $D=20$ mm). This last is used to provide a final focusing of the beam before entering the interaction region. The potential at which E12 is kept depended on the energy of the beam.

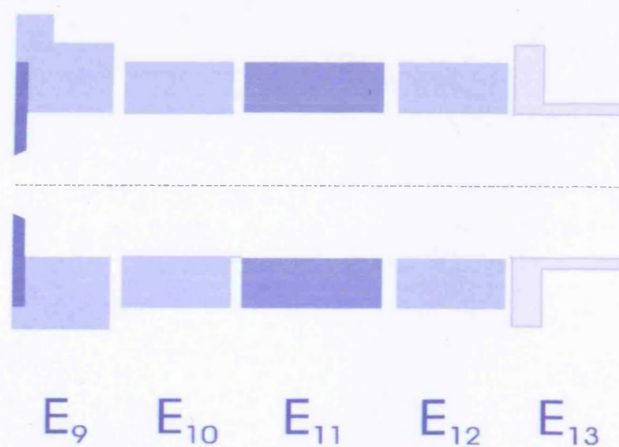


Figure 5. Schematic of the exit lens.

The diameter of the positron beam at the centre of the collision chamber is estimated to be less than 4mm.

APPENDIX II

Second Order Focusing in a Parallel Plate Analyser

Using a Taylor expansion for L in terms of the angle variation $\Delta\Theta$:

$$L = L_0 + \sum_{i=1}^{\infty} \frac{1}{i!} \frac{\partial^i L}{\partial \Theta^i} (\Delta\Theta)^i, \quad (1)$$

which explicitly is:

$$L - L_0 = \frac{\partial L}{\partial \Theta} (\Delta\Theta) + \frac{1}{2} \frac{\partial^2 L}{\partial \Theta^2} (\Delta\Theta)^2 + \frac{1}{6} \frac{\partial^3 L}{\partial \Theta^3} (\Delta\Theta)^3 + \text{higher order terms.} \quad (2)$$

This can be re-written as:

$$\Delta L = \frac{2h}{c} \left[\frac{2(\Delta\Theta)^2 \cos 3\Theta}{\sin \Theta} - \frac{2}{3} \left(\frac{3 \sin 3\Theta + \cos 3\Theta \cos \Theta}{\sin^2 \Theta} \right) (\Delta\Theta)^3 \right] + \text{HO.} \quad (3)$$

By setting the first and second order partial derivatives to zero:

$$\frac{\partial L}{\partial \Theta} = 0 \quad \text{and} \quad \frac{\partial^2 L}{\partial \Theta^2} = 0, \quad (4)$$

It is found that the condition is satisfied when $\Theta=30^\circ$ and $\frac{h}{cd} = 2$.

APPENDIX III

Time-of-Flight in the Tandem Parallel Plate Analyser

The time-of-flight of a particle from the starting point to the focal point in the first PPA is:

$$T(\Theta, c) = \frac{L(\Theta, c)}{v_z} = \frac{d \cot(\Theta) + (2/c)d \sin(2\Theta)}{\sqrt{2E/m} \cos(\Theta)} = \frac{d}{\sqrt{2E/m}} \left(\frac{1}{\sin(\Theta)} + \frac{4}{c} \sin(\Theta) \right), \quad (1)$$

where v_z is the velocity of the particle along the z axis and m is the mass of the focused particles.

For the present design parameters (see §2.5.1), the starting point of the particle trajectory of the second stage is on the baseplate of the first analyser. Hence, the focal length of the second analyser is:

$$L_2(\Theta, c) = \left[d - (L_1(\Theta, c) - L_0) \sin(60^\circ) \right] \cot(\Theta_2) + \frac{2h}{c} \sin(2\Theta_2), \quad (2)$$

where L_0 is the focal length in the first analyser, with $\Theta = 30^\circ$, $c=0.5$.

The corresponding time of flight in the second stage of the PPA is:

$$T_2(\Theta, c) = \frac{L_2(\Theta, c)}{v_{2z}} = \frac{d}{\sqrt{2E/m}} \left(\frac{1 - (L_1(\Theta, c) - L_0) \sin(60^\circ) / d}{\sin(\Theta_2)} + \frac{4}{c} \sin(\Theta_2) \right). \quad (3)$$

The total time of flight of the twin analyser is:

$$T = T(\Theta) + T(\Theta_2). \quad (4)$$

APPENDIX IV

Source holder

Figure 1 shows a schematic layout of the source arrangement: the source capsule is mounted via a M3 rod to an Al plug, which is externally isolated from the ground by a cylindrical PTFE block. In turn, the PTFE is attached to a linear motion manipulator. This enables the source to be withdrawn from the moderator, thus allowing the safe removal of the central lead plug on which the moderator is mounted.

Moderator holder

The W mesh moderator is held between two brass washers (10mm internal diameter) fixed on an Al plug. These washers are electrically isolated from the moderator by a set of PTFE washers. Holes are tapped around the edge of these washers so that they may be fixed in place with 3 PTFE screws. A PTFE cylinder surrounds the moderator assembly into the Al plug hole. The lead plug ensures that the moderator meshes are vertically located in front of the radioactive source and provides shielding from the source radiation. Electrical contact to the moderator is achieved by a wire soldered to one of the brass washers reaching a feedthrough on the top flange of the vertical housing.

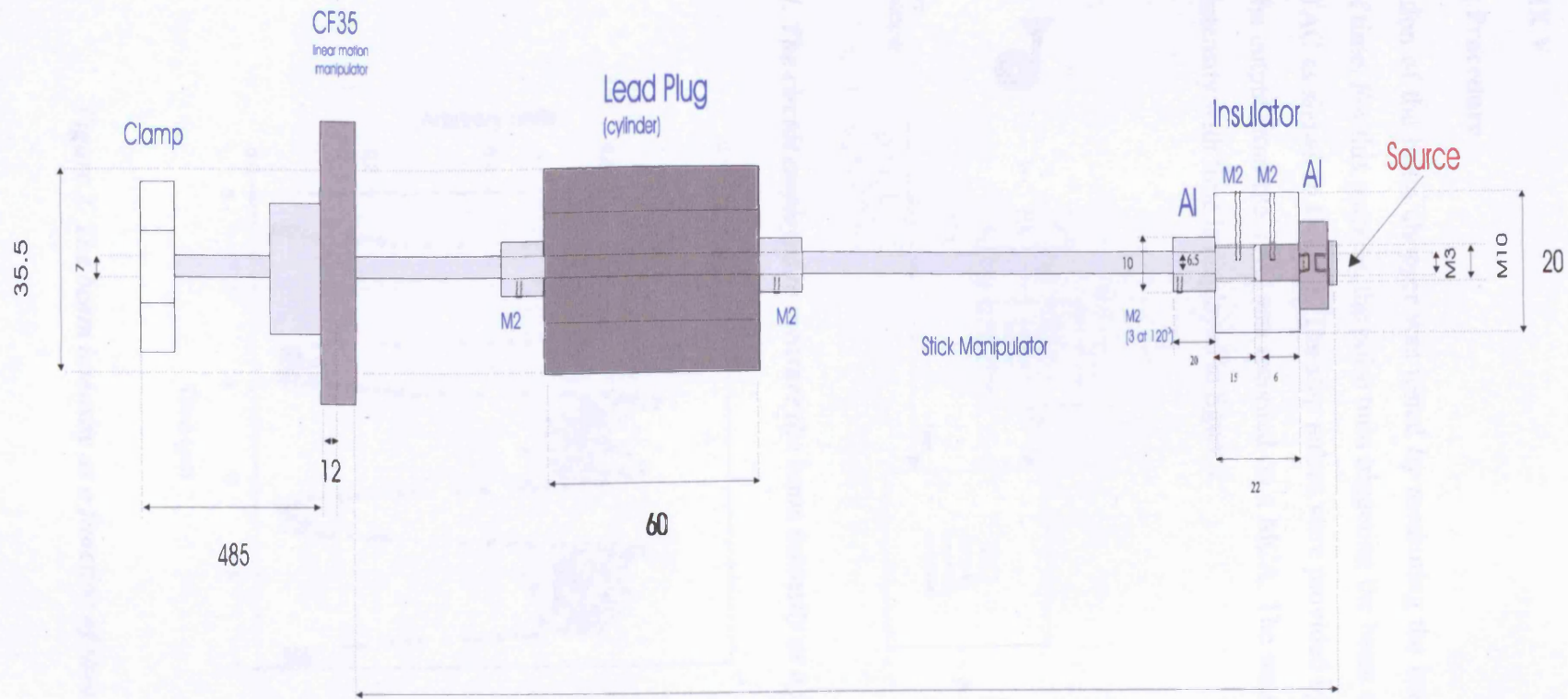


Figure 1. Section through the source holder designed for the experiment. The dimensions are indicated in mm (not drawn to scale).

APPENDIX V

Chopping Procedure

The operation of the beam chopper was tested by measuring the beam intensity as a function of time. For this purpose, the pulse train triggering the beam chopper was used to start a TAC as shown in figure 1. The stop pulses were provided by the ion detector (CEM). The output from the TAC was recorded on a MCA. The resulting variation of the beam intensity with time is displayed in figure 2.

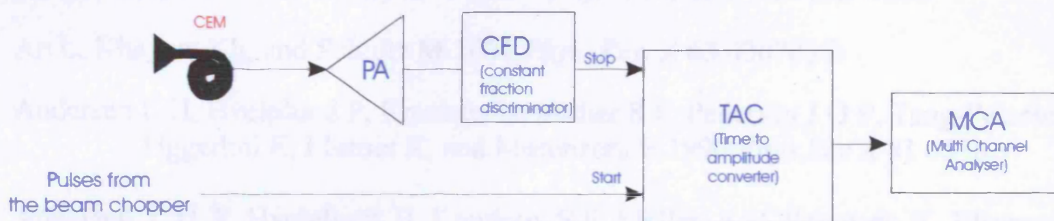


Figure 1. The circuit employed to measure the beam intensity as a function of time.

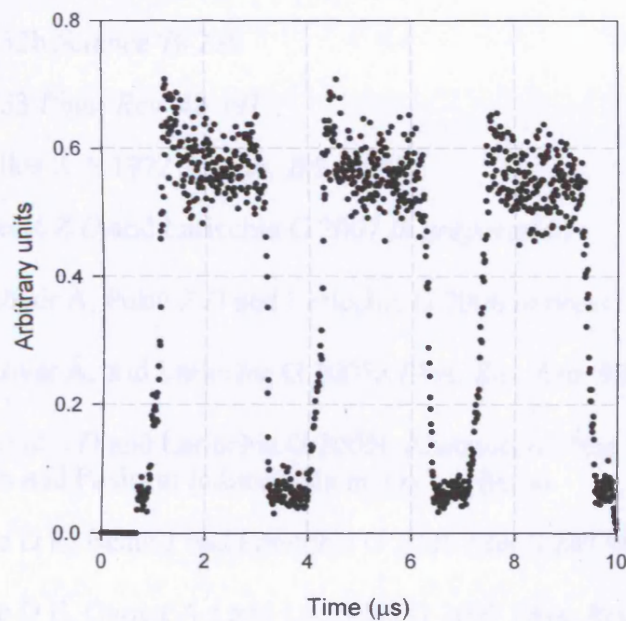


Figure 2. The beam intensity as a function of time.

References

- Adachi S, Chiba M, Hirose T, Nagayama S, Nakamitsu Y, Sato T and Yamada T 1990 *Phys. Rev. Lett.* **65** 2634–2637
- Adkins G S 2005 *Phys. Rev. A* **72** 032501
- Adkins G S and McGovern N, Fell R N, Sapirstein J 2003 *Phys. Rev. A* **68** 032512-1
- Adkins G S Salahuddin A A and Schalm K E 1992 *Phys. Rev. A* **45** 7774-7781
- Ajello D J 1971 *J. Chem. Phys.* **55** 3158
- Al-Ramadhan A H and Gidley D W 1994 *Phys. Rev. Lett.* **72** 1632–1635
- An L, Khayyat Kh, and Schultz M 2001 *Phys. Rev. A* **63** 030703@
- Andersen L H, Hvelplund P, Knudsen H, Moller S P, Pedersen J O P, Tang-Petersen S, Uggerhoj E, Elsener K, and Morenzoni E 1990 *Phys Rev A* **41** 6536
- Andersen L H, P. Hvelplund, H. Knudsen, S.P. Møller, A.H. Sørensen, K. Elsener, E-G. Rensfelt, E. Uggerhøj 1987 *Phys. Rev. A* **36** 3612
- Anderson C D 1932a *Phys. Rev.* **41** 405
- Anderson C D 1932b *Science* **76** 238
- Anderson C D 1933 *Phys. Rev.* **43** 491
- Angel G C and Giles R A 1972 *J. Phys. B* **5** 80-89
- Arcidiacono C, Pešić Z D and Laricchia G 2007 *in preparation*
- Arcidiacono C, Kövér Á, Pešić Z D and Laricchia G 2006 *in press*
- Arcidiacono C, Kövér Á, and Laricchia G 2005a *Phys. Rev. Lett.* **95**, 223202
- Arcidiacono C, Pešić Z D and Laricchia G 2005b Abstracts on “the EPIC meeting Electron and Positron Induced Chemistry”, Viterbo
- Armitage S, Leslie D E, Beale J and Laricchia G 2006 *Nim B* **247** 98-104
- Armitage S, Leslie D E, Garner A J and Laricchia G 2002 *Phys. Rev. Lett.* **89** 173402-1
- Ashley P 1996 *Ph.D. Thesis* University of London
- Ashley P, Moxom J and Laricchia G 1996 *Phys. Rev. Lett.* **77** 1250
- Bachmann P, Eberlein A and Bruch R 1982 *J. Phys. E* **15** 207
- Bandyopadhyay A, Roy K, Mandal P and Sil N C 1994 *J. Phys. B* **27** 4337

- Barnes L D, Young J A, and Surko C M 2006 *Phys. Rev. A* **74** 012706
- Beale J, Armitage S and Laricchia G 2006 *J. Phys. B* **39** 1337–1344
- Beale 2007 *in preparation*
- Bellotti E, Corti M, Fiorini E, Liguori C, Pullia A, Sarracino A, Sverzellati P and Zanotti L 1983 *Phys Lett B* **124** 435–438
- Berakdar J 1998 *Phys. Rev. Lett.* **81** 1393
- Bernath P F 2002 *Phys. Chem.* **4** 1501
- Biswas P K and Adhikari S D 1999 *Phys. Rev. A* **59** 363 - 370
- Blackett P M S and Occhialini G P S 1933 *Proc. Roc. Soc. A* **139** 699
- Blackwood J E, McAlinden M T, and H R J 2002 *J. Phys. B* **35** 2661
- Blackwood Jennifer E, Campbell C P, McAlinden Mary T, Walters H R J 1999 *Phys. Rev. A* **60** 4454–4460
- Bluhme H, Frandsen N P, Jacobsen F M, Knudsen H, Merrison J P, Mitchell R, Paludan K and Poulsen M R 1999a *J. Phys. B* **32** 5825
- Bluhme H, Knudsen H, Merrison J P and Nielsen K A 1999b *J. Phys. B* **32** 5835–5842
- Bluhme H, Knudsen H, Merrison J P and Nielsen K A 1999c *J. Phys. B* **32** 5237–5245
- Boudaiffa B, Cloutier P, Hunting D, Huels M, Sanche L 2000 *Nature* **287** 1658
- Bransden B H 1969 "Case Studies in Atomic Collisions" eds. McDaniel and McDowell (North Holland) 161
- Braunert M and Briggs J S 1991 *J. Phys. E* **24** 2227-2236
- Brauner M, Briggs J S, and H. Klar 1989 *J. Phys. B* **22** 2265
- Brauner M and Briggs J S 1986 *J. Phys. B* **19** L325-L330
- Bressanini D, Mella M and Morosi G 1998 *J. Chem. Phys.* **109** 1716-1720
- Brinkmann R T and Trajmar S 1981 *J. Phys. E* **14** 245-255
- Bromley M W J, Lima M A P and Laricchia G 2006 *Phys. Scr.* **74** C37–C45
- Brown B L and Leventhal M 1987 *Astrophys. J.* 637-642
- Brown C J and Humberston J W 1985 *J. Phys. B* **18** L401-L406
- Campbell L, Brunger M J, Nolan A M, Kelly L J, Wedding A B, Harrison J, Teubner J P O, Cartwright D C, and McLaughlin B 2001 *J. Phys. B* **34** 1185

- Campbell C P, McAlinden M T, Kernoghanand A A, Walters H R J 1998 *Nim B* **143** 41
- Campeanu R I, Fromme D, Kruse G, McEachran R P, Parcell L A, Raith W, Sinapius G and Stauffer A D 1987 *J. Phys. B* **20** 3557-3570
- Canter K F, Lippel P H, Crane W S and Mills A P Jr 1986 *Positron Studies of Solids. Surfaces and Atom* ed. A P Mills Jr, W S Crane and K F Canter (Singapore: World Scientific) p 199
- Canter K F, Coleman P G, Griffith T C and Heyland G R 1972 *J. Phys. B* **5** L167-L169
- Cassidy D B, Deng S H M, Greaves R G, Maruo T, Nishiyama N, Snyder J B, Tanaka H K M and Mills A P Jr 2005 *Phys. Rev. Lett.* **95** 95006
- Champion C 2006 *Private communication*
- Champion C and Le Loirec C 2006 *Phys. Med. Biol.* **51** 1707-1723
- Champion C, Hanssen J and Hervieux P A 2002 *J. Chem. Phys.* **117** 197
- Chang T Li, Q Wang Y and Li Y 1985 "*Positron Annihilation*" eds. P C Jain R M Singru, and K P Gopinathan (Singapore: World Scientific) p212
- Chang T Li Q, Wang Y and Li Y 1982 "*Positron Annihilation*" eds. P Coleman, S C Sharman and L M Diana (North Holland: Amsterdam) p 32
- Charlton M and Humberston J W 2001 in "*Positron Physics*" Cambridge University Press
- Charlton M. and G. Laricchia 1990 *J. Phys. B* **23** 1045
- Charlton M 1990 *Physica Scripta* **42** 164-172
- Charlton M, Griffith T C, Heyland G R and Wright G L 1983a *J. Phys. B* **16** 323-341
- Charlton M, Clark G, Griffith T C and Heyland G R 1983b *J. Phys. B* **16** L465
- Charlton M, Griffith T C, Heyland G R and Lines K S 1979 *J. Phys. B* **12** L633
- Chaudhuri P, Varella M T Do N, de Carvalho C R C and Lima M A P 2004 *Phys. Rev. A* **69** 042703
- Coleman P G 2006 *Appl. Surf. Sci.* **252** 3372-3374
- Coleman P G, Raynber S, Jacobsen F M, Charlton M and West R N 1994 *J Phys B* **27** 981
- Coleman P G, Johnston K A, Cox A M G, Goodyear A and Charlton M 1992 *J. Phys. B* **25** L585-L588
- Coleman P G, Hutton J T, Cook D R, and Chandler C A 1982 *Can. J. Phys.* **60** 584

- Cordaro R B, Hsieh K C and McIntyre Jr L C 1986 *J. Phys. B* **19** 1863-1872
- Costello D G, Groce D E, Herring D F and McGowan J W 1972 *Can. J. Phys.* **50** 23
- Crooks G B and Rudd M E 1970 *Phys. Rev. Lett.* **25** 1599-601
- Czernin J and Phelps M E 2002 *Annu. Rev. Med.* **53** 89
- Dababneh M S, Hsieh Y-F, Kauppila W E, Pol V, and Stein T S 1982 *Phys. Rev. A* **26** 1252
- Dababneh M S, Kauppila W E, Downing J P, Laperriere F, Pol V, Smart J H and Stein T S 1980 *Phys. Rev. A* **22** 1872
- Dahl D A 1995 and 2000 SIMION 3D Version 6 and 7 Idaho National Engineering Laboratory, Idaho Falls, Idaho 83415
- Deuring A, Floeder K, Fromme D, Raith W, Schwab, Sinapius G, Zitzewitz P W, Krug J 1983 *J. Phys. B* **16** 1633
- Deutsch M 1951 *Phys. Rev.* **82** 455-456
- Diana L M, Coleman P G, Brooks D L, Chaplin R L 1987 in: J.W. Humberston, E.A.G. Armour (Eds.), *Atomic Physics with Positron*, Plenum, New York p. 55
- Diana L. M, Coleman P G, Brooks D L, Pendleton P K, Norman D M 1986 *Phys. Rev. A* **34** 2731-2737
- Dirac P A M 1930a *Proceedings of the Royal Society A* **126** 360
- Dirac P A M 1930b *Proc. Camb. Phil. Soc.* **26** 361
- Dou L, Kauppila W E, Kwan C K, and Stein T S 1992 *Phys. Rev. Lett.* **68** 2913-2916
- DuBois and Rudd 1978 *Phys. Rev. A* **17** 843-848
- Dunlop L J M and Gribakin G F 2006 *Nim B* **247** 61-67
- Fainstein P D, Ponce V H, and Rivarola R D 1991 *J. Phys. B* **24** 3091
- Falke T, Raith W, and Weber M 1995 *Phys. Rev. Lett.* **75** 3418-3421
- Falke T, T Brandt, O Köhl, W Raith and Weber M 1997 *J. Phys. B* **30** 3247-3256
- Fields S A, Burch J L, and Oran W A 1977 *Rev. Sci. Instrum.* **48** 1076
- Finch 1996 *PhD Thesis*, University of London
- Finch R M, Kövér Á, Charlton M and Laricchia G 1996 *J. Phys. B* **29** L667
- Fiol J and Olson R E 2002 *J. Phys. B* **35** 1173
- Fiol J, Rodríguez V D, Barrachina R O 2001 *J. Phys. B* **34** 933-944

- Fleischer Frank, Degreif Kai, Gwinner Gerald, Lestinsky Michael, Liechtenstein Vitality, Plenge Florian, and Schwalm Dirk 2006 *Phys. Rev. Lett.* **96** 063401
- Fornari L. S., L. M. Diana and P. G. Coleman 1983 *Phys. Rev. Lett.* **51** 2276
- Fromme D, Kruse G, Raith W and Sinapius G 1986 *Phys. Rev. Lett.* **57** 3031-3034
- Fulton T and Martin P C 1954 *Phys. Rev.* **95** 811
- Garibotti C R and Miraglia J E 1980 *Phys. Rev. A* **21** 572 - 580
- Garrett W R 1980 *J. Chem. Phys.* **73** 5721
- Gianturco F A, T. Mukherjee, and A. Occhigrossi 2001 *Phys. Rev. A* **64** 0327151
- Gianturco F A, Paoletti P, Rodriguez-Ruiz J A 1996 *J. Phys. D* **36** 51
- Gilbert S J, L. D. Barnes, J. P. Sullivan, and C. M. Surko 2002 *Phys. Rev. Lett.* **88** 43201
- Gilbert S J, Barnes L D, Greaves L G and Surko C M 1997 *Appl. Phys. Lett.* **70** 1944
- Gilmore S, Jennifer E Blackwood, Walters H R J 2004 *Nim B* **221** 129-133
- Goldanskii V I 1968 *At. Energ. Rea.* **6** 3-148
- Green T S and Proca G A 1970a *Rev. Sci. Instrum.* **41** 1778
- Green T S and Proca G A 1970b *Rev. Sci. Instrum.* **41** 1409
- Gribakin G F and Gill P M W 2004 *Nim B* **221** 30
- Gribakin G F 2000 *Phys. Rev. A* **61** 22720
- Griffith T C 1983 *Positron Scattering in Gases* ed J W Humberston and M R C McDowell (New York: Plenum) 53-63
- Griffith T C and Heyland G R 1978 *Phys. Rep.* **39** 169-177
- Gullikson E M and Mills A P Jr 1986 *Phys. Rev. Lett.* **57** 376
- Harrison K G and Lucas M 1970 *Phys. Rev. Lett. A* **33** 149
- Harting E and Read F H 1976 *Electrostatic Lenses*, Amsterdam ed. Elsevier
- Hayashi M 1987 in *Swarm Studies and Inelastic Electron-Molecule Collisions* edited by L C P *et al.* Springer, Berlin pp. A148
- Hervieux P-A, Fojon O A, Champion C, Rivarola R D and Hanssen J 2006 *J. Phys. B* **39** 409-419
- Hewitt R N, Noble C J and Bransden B H 1992 *J. Phys. B* **25** 557

- Heyland G R, Charlton M, Griffith T C and Wright G L 1982 *Can. J. Phys.* **60** 503
- Hoffman K R, Dababneh M S, Hsieh Y F, Kauppila W E, Pol V, Smart J H, and Stein T S 1982 *Phys. Rev. A* **25** 1393–1403
- Hutchins S M, Coleman P G, Stone R J and West R N 1986 *J. Phys. E* **19** 282
- Hvelplund P, Knudsen H, Mikkelsen U, Morenzoni E, Moller S P, Uggerhoj E and Worm T 1994 *J. Phys. B* **27** 925
- Igarashi A and Toshima N 1992 *Phys. Lett. A* **164** 70
- Illescas C, Pons B and Riera A 2002 *Phys. Rev. A* **65** 030703(R)
- Itikawa Y and Mason N 2005 *J. Phys. Chem. Ref. Data* **3** 1
- Iwata K, Gribakin G F, Greaves R G, Kutz C, and Surko C M 2000 *ibid.* **61** 022719
- Iwata K, Greaves R G, Murphy T J, Tinkle M D, and Surko C M 1995 *Phys. Rev. A* **51** 473–487
- Jacobsen F M, Frandsen N P, Knudsen H, Mikkelsen U and Schrader D M 1995 *J. Phys. B* **28** 4691
- Jacobsen F M, Charlton M, Chevallier J, Deutch B I, Laricchia G, and Poulsen M R 1990 *J. App. Phys.* **67** 575
- Jin B, Miyamoto S, Sueoka O and Hamada A 1994 *At. Collision Res. Japan* **20** 9
- Kanazawa H, Ohtsuki Y H and Yanagawa S 1965 *Phys. Rev.* **138** A1155 - A1157
- Kara V 1999 *Ph.D. Thesis*, University of London
- Kara V, Paludan K, Moxom J, Ashley P and Laricchia G 1997 *J. Phys. B.* **30** 3933
- Karwasz G P, Pliszka D, Brusa R S 2006 *Nim B* **247** 6874 1
- Karwasz G P 2005 *Eur. Phys. J. D* **35** 267
- Karwasz G P, Brusa R S, Karwasz G P, Zecca Antonio 2001 *Rivista del Nuovo Cimento* **24**
- Katayama Y, Sueoka O, and Mori S 1987 *J. Phys. B* **20** 1645
- Kauppila W E, Edwards J J, Miller E G, Stein T S and Surdutovich E 2006 *Nim B* **247** 117-122
- Kauppila W E, Miller E G, Mohamed H F M, Pipinos K, Stein T S and Surdutovich E 2004 *Phys. Rev. Lett.* **93** 113401
- Kauppila W E, Kwan C K, Przybyla D, Smith S J, Stein T S 1996 *Can. J. Phys.* **74** 474

- Kauppila W E and Stein T S 1990 *Adv. At. Mol. Phys.* **26** 1
- Kauppila W E, Stein T S, Smart J H, Dababneh M S, Ho Y H, Downing J P and Pol V 1981 *Phys. Rev. A* **24** 725
- Khriplovic I B and Yelkhovskiy A B 1990 *Phys. Lett. B* **246** 520-522
- Kimura M, Sueoka O, Hamada A and Itikawa Y 2000 *Adv. Chem. Phys.* **111** 537
- Klemperer O 1934 *Proceedings of the Cambridge Philosophical Society* **30** 347
- Knudsen H and Reading J F 1992 *Phys. Rep.* **212** 107
- Knudsen H, Brun-Nielsen L, Charlton M and Poulsen M R 1990 *J. Phys. B* **23** 3955
- Knudsen H, Andersen L H and Jensen K E 1986 *J. Phys. B* **19** 3341-3351
- Kövér Á 2005 *Private communication*
- Kövér Á, Paludan K and Laricchia G 2001 *J. Phys. B* **34** L219-L222
- Kövér Á and Laricchia G 2001 *Meas. Sci. Technol.* **12** 1875
- Kövér Á and Laricchia G 1998 *Phys. Rev. Lett.* **80** 5309-5312
- Kövér Á, Finch R M, Charlton M and Laricchia G 1997 *J. Phys. B* **30** L507-L512
- Kövér Á, Laricchia G and Charlton M 1994 *J. Phys. B* **27** L2409
- Kövér Á, Laricchia G and Charlton M 1993 *J. Phys. B* **26** L575-L580
- Kövér Á, Laricchia G and Charlton M 1992 *Materials Science Forum* **105-110** 1919-1922
- Krishnakumar E and Srivastava S K 1988 *J. Phys. B* **21** 1055
- Kruit P and Read F H 1983 *J. Phys. E* **16** 313
- Laricchia G 2006 *Private communication*
- Laricchia G, Armitage S, and Leslie D E 2004 *Nim B* **225** 86-85
- Laricchia L, Armitage S, Leslie D E, Szluiska M and Van Reeth P 2003 *Rad. Phys. and Chem.* **68** 21-31
- Laricchia G 2002 in *"The Physics of Electronic and Atomic Collisions"* Rinton Press, New York 329
- Laricchia G, Van Reeth P, Szluiska M and Moxom J 2002 *J. Phys. B* **35** 2525
- Laricchia G and Charlton M 1999 *Phil. Trans. R. Soc. London A* **357** 1259-1277
- Laricchia G and Wilkin C 1997 *Phys. Rev. Lett.* **79** 2241-2244

- Laricchia G and Moxom J 1993 *Phys. Lett. A* **174** 255
- Laricchia G, Moxom J and Charlton M 1993 *Phys. Rev. Lett.* **70** 3229-3230
- Laricchia G and Zafar N 1992 *Solid State Phenom.* **28/29** 347
- Laricchia G, Charlton M, Davies S A, Beling C D and Griffith T C 1987 *J. Phys. B* **20** L99-L105
- Laricchia G, Charlton M, Clark G and Griffith T C 1985 *Phys. Lett.* **109A** 97-100
- Lee M T, Machado A M, Fujimoto M M, Machado L E, and Brescansin L M 1996 *J. Phys. B* **29** 4285
- Leslie D 2005 *PhD Thesis*, University of London
- Leslie D E, Armitage S and Laricchia G 2002 *J Phys B* **35** 4819-4827
- Linder F 1977 *Electronic and Atomic Collisions* ed G Watel (Amsterdam: North-Holland) 51-69
- Macek J 1970 *Phys. Rev. A* **1** 1235-41
- Madansky L and Rasetti F 1950 *Phys. Rev.* **79** 397
- Maerk T D and Dunn G H 1985 *Electron Impact ionization*, Wien, Springer Verlag edited by Maerk, T D and Dunn, G.H.00/1985
- Makochekanwa C, Sueoka O, Kimura M 2006 *Nim B* **247** 79-86
- Mandal P, Guha S, Sil N C 1979 *J. Phys. B* **12** 2913-2924
- Mandal P, Roy K and Sil N C 1986 *Phys. Rev. A* **33** 756-758
- Mann A and Linder F 1992 *J. Phys B.* **25** 545
- Marler J P, Surko C M, McEachran R P and Stauffer A D 2006 *Phys. Rev. A* **73** 064702
- Marler J P and Surko C M 2005a *Phys. Rev. A* **72** 062702
- Marler J P and Surko C M 2005b *Phys. Rev. A* **72** 062713
- Marler J P, Sullivan J P and Surko C M 2005 *Phys. Rev. A* **71** 022701
- Mason N J and Newell W R 1987 *J. Phys. B* **20** 3913
- McAlinden M T and Walters H R J 1994 *Hyp. Int.* **89** 407-418
- McAlinden M T, Walters H R J 1992 *Hyperfine Interact* **73** 65
- McCurdy C W, Baertschy M and Rescigno T N 2004 *J. Phys. B* **37** R137
- Mills A P Jr 1983a in *Positron Solid State Physics* eds. Brandt W and Duspasquier A

(North Holland) p432

- Mills A P 1983b *Phys. Rev. Lett.* **50** 671
- Mills A P Jr 1981 *Phys. Rev. Lett.* **46** 717
- Mills A P 1980 *Appl. Phys.* **22** 273
- Milstein A I and Khirplovich I B 1994 *JETP* **79** 379-383
- Mohorovic S 1934 *Astronomische Nachrichten* **235** 94
- Mori S and Sueoka O 1994 *J. Phys. B* **27** 4349
- Moxom J, Schrader D M, Laricchia G, Xu J, Hulett L D 2000 *Phys. Rev. A* **62** 052708
- Moxom J, Schrader D M, Laricchia G, Xu L and Hulett L D 1999 *Phys. Rev. A* **60** 2940
- Moxom J, Ashley P and Laricchia G 1996 *Can. J. Phys.* **74** 367-372
- Moxom J, Laricchia G and Charlton M 1995 *J. Phys. B* **28** 1331
- Moxom J, Laricchia G, Charlton M, Kövér Á and Meyerhof W E 1994 *Phys. Rev. A* **50** 3129-3133
- Moxom J, Laricchia G and Charlton M 1993 *J. Phys. B* **26** L367-L372
- Moxom J, Laricchia G, Charlton M, Jones G O and Kövér Á 1992 *J. Phys. B* **25** L613-L619
- Muehllehener and Karp 2006 *Phys. Med. Biol.* **51** R117
- Murtagh D J, Arcidiacono C, Pešić Z D and Laricchia G 2006 *Nim B* **247** 92-97
- Murtagh D J, Szluinska M, Moxom J, Van Reeth P and Laricchia G 2005 *J. Phys. B* **38** 3857-3866
- Nagashima y, Hyodo T, Fujiwara K and Ichimura A 1998 *J. Phys. B* **31** 329
- Ore A 1951 *Phys. Rev.* **83** 665
- Ore A and Powell J L 1949 *Phys. Rev.* **75** 1963-1963
- Overton N, Mills R J and Coleman P G 1993 *J. Phys. B.* **26** 3951-3957
- Palathingal J C, Asoka-Kumar P, Lynn K G, Posada Y, Wu X Y 1991 *Phys. Rev. Lett.* **67** 3491-3494
- Paludan K, Laricchia G, Ashley P, Kara V, Moxom J, Bluhme H, Knudsen H, Mikkelsen U, Møller S P, Uggerhøj E and Morenzoni E 1997 *J. Phys. B* **30** L581
- Parcell L A, McEachran R P, and Stauffer A 2000 *Nim B* **171** 113

- Pešić Z D, Arcidiacono C and Laricchia G 2004 Abstract on "the meeting EPIC Electron and Positron Induced Chemistry", Obergurgle, Austria.
- Phelps M E, Hoffman E J, Mullani N A and Te-Pogossian M M 1975 *J. Nucl. Med.* **16** 210
- Proca G A 1973a *Rev. Sci. Instrum.* **44** 1365
- Proca G A 1973b *Rev. Sci. Instrum.* **44** 1376
- Raith W 1998 in "Photonic, Electronic and Atomic Collisions" eds. F Aumayr and H Winter (World Scientific) 341
- Ramsauer C and Kollath R 1929 *Annalen der Physik* (Leipzig) **3** 536
- Ramsauer C 1923 *Annalen der Physik* (Leipzig) **72** 345
- Ramsauer C 1921 *Annalen der Physik* (Leipzig) **64** 513
- Rapp D, Golden E and Briglia D D 1965 *J. Chem. Phys.* **42** 4081
- Ray H 2002 *J. Phys. B* **35** 3365
- Register D F, Vuskovic L and Trajmar S 1986 *J. Phys. B* **19** 1685
- Rodbro M and Andersen F D 1979 *J. Phys. B* **12** 2883-2903
- Ruark A E 1945 *Phys. Rev. Lett.* **68** 278-278
- Rudd M E, Goffe T V, DuBois R D and Toburen L H 1985 *Phys. Rev. A* **31** 492-494
- Rudd M E and Macek J 1972 *Case Stud. At. Phys.* **3** 48-136
- Saglam Z and Aktekin N 1990 *J. Phys. B* **23** 1529-1536
- Sarkadi L and Barrachina R O 2005 *Phys Rev A* **71** 062712
- Sarkadi L 2003 *Phys. Rev. A* **68** 032706-1
- Sarkadi L, Brinkmann U, Báder A, Hippler R, Tökési K, and Gulyás L 1998 *Phys. Rev. A* **58** 296 - 303
- Sarkar N K, Basu M and Ghosh A S 1992 *Phys. Rev. A* **45** 6887
- Schmitt A, Cerny U, Möller H, Raith W, and Weber M 1994 *Phys. Rev. A* **49** R5 - R7
- Schrader D M, Jacobsen F M, Frandsen N P, and Mikkelsen U 1992 *Phys. Rev. Lett.* **69** 000057
- Shultz D R and Reinhold C O 1990 *J. Phys. B* **23** L9-L14
- Schultz D R and Olson R E 1988 *Phys. Rev. A* **38** 1866
- Shah M B, McGrath C, Illescas C, Pons B, Riera A, Luna H, Crothers D S F, O'Rourke S F C and Gilbody H B 2003 *Phys. Rev. A* **67** 010704

- Shah M B, McCallion P and Gilbody H B 1989 *J. Phys. B* **22** 3037
- Shah M B and Gilbody H B 1985 *J. Phys. B* **18** 899
- Sil N C, Roy K and Manda P 1991 *Proc. 17th Int. Conf. on Physics of Electronic and Atomic Collisions* (Brisbane) (Bristol: Hilger) Abstracts p 354
- Skalsey M, Engbrecht J J, Bithell R K, Vallery R S and Gidley D W 1998 *Phys. Rev. Lett.* **80** 3727–3730
- Smith S J, Hyder G M A, Kauppila W E, Kwan C K and Stein T S 1990 *Phys. Rev. Lett.* **64** 1227
- Sparrow R A and Olson R E 1994 *J. Phys. B* **27** 2647-2655
- Spicher G, Olsson B, Raith W, Sinapius G and Sperber W 1990 *Phys. Rev. Lett.* **64** 1019
- Starrett C, McAlinden Mary T, and Walters H R J 2005 *Phys. Rev. A* **72** 012508
- Steckelmacher W 1986 *Rep. Prog. Phys.* **49** 1083
- Steckelmacher W, Strong R and Lucas M W 1978 *J. Phys. D.* **11** 1553
- Stein T S, Harte M, Jiang J, Kauppila W E, Kwan C K, Li H and Zhou S 1998 *Nim B* **143** 68
- Stein T S and Kauppila W E and 1982 *Adv. At. Mol. Phys.* **18** 53
- Stein T S, Kauppila W E, Pol V, Smart J H, and Jesion G 1978 *Phys. Rev. A* **17** 1600-1608
- Sueoka, Kawada M K, Kimura M 2000 *Nim B* **171** 96
- Sueoka O, Mori S and Katayama Y 1987 *J. Phys. B* **20** 3237-3246
- Sueoka O, Mori S and Katayama Y 1986 *J. Phys. B* **19** L373
- Sullivan J P, Gilbert S J, Marler J P, Greaves R G, Buckman S J, and Surko C M 2002 *Phys. Rev. A* **66** 042708
- Sullivan J P, Gilbert S J, and Surko C M 2001a *Phys. Rev. Lett.* **86** 1494–1497
- Sullivan J P, Marler J P, Gilbert S J, Buckman S J and Surko C M 2001b *Phys. Rev. Lett.* **87** 073201
- Surko C M, Gribakin G F and Buckman S J 2005 *J. Phys. B* **38** R57-R126
- Szluinska M, Murtagh D J and Laricchia G 2005 *Nim B* **229** 51-54
- Szluinska M and Laricchia G 2004 *Nim B* **221** 100

- Taylor F W 2002 *Rep. Prog. Phys.* **65** 1
- Teegarden B J, Watanabe K, Jean P, Knödlseeder J, Lonjou V, Roques J P, Skinner G K, von Ballmoos P, Weidenspointner G, Bazzano A, Butt Y M, Decourchelle A, Fabian A C, Goldwurm A, Güdel M, Hannikainen D C, Hartmann D H, Hornstrup A, Lewin W H G, Makishima K, Malzac A, Miller J, Parmar A N, Reynolds S P, Rothschild R E, Schönfelder V, Tomsick J A, and Vink J. 2005 *Astrophys. J.* **A22** part 1 296–300
- Tong B Y 1972 *Phys. Rev. B* **5** 1436
- Townsend J S and Bailey V A 1922 *Philosophical Magazine* **43** 593
- Ullrich J, Moshhammer R, Dorn A, Dorner R, Schmidt L Ph H and Schmidt-Bocking H 2003 *Rep. Prog. Phys.* **66** 1463–1545
- Ullrich J, Moshhammer R, Dorner R, Jagutzki O, Mergel V, Schmidt-Bocking H, and Spilleberger L 1997 *J. Phys. B* **30** 2917
- Vajnai T, Gaus A D, Brand J A, Htwe W, Madison D H, Olson R E, Peacher J L, and Schulz M 1995 *Phys. Rev. Lett.* **74** 3588
- Vallery R S, Zitzewitz P W and Gidley D W 2003 *Phys. Rev. Lett.* **90** 20
- Van Reeth P, Laricchia G and Humberston J W 2005 *Physica Scripta* **71** C9-C13
- Van Reeth P, Szluinska M and Laricchia G 2002 *Nim B* **192** 220
- Van Reeth P and Humberston J W 1997 *J. Phys. B* **30** L95–L100
- Varella M.T. do N, Azevedo D L, Lima M A P 2002 *J. Phys. B* **35** 3531
- Varracchio F 1990 *J. Phys. B* **13** L779
- Wallace L, Bernath P, Livingston W, Hinkle K, Busler J, Guo B, Zhang K 1995 *Science* **268** 1155
- Walters H R J 2005 *Private communication*
- Weil H 1931 *Gruppentheorie und Quantenmechanik* 2nd Ed. p 234
- Yang C N 1950 *Phys. Rev* **77** 242–245
- Zafar N, Chevalier J, Jacobsen F M, Charlton M and Laricchia G 1988 *Appl. Phys. A* **47** 409
- Zafar N, Chevallier J, Laricchia G and Charlton M 1989 *J Phys D* **22** 868-870
- Zecca A, Sanyal D, Chakrabarti M and Brunger M J 2006 *J. Phys. B* **39** 1597–1604
- Zhou S, Li H, Kauppila H W, Kwan C K, and Stein T S 1997 *Phys. Rev. A* **55** 361–368

Zhou S, Parikh S P, Kauppila W E, Kwan C K, Lin D, Surdutovich A, and Stein T S
1994 *Phys. Rev. Lett.* **73** 236–239

APPENDIX VI

Published works

Positronium Formation from CO₂ and H₂O

D. J. Murtagh , C. Arcidiacono, Z. D. Pešić and G. Laricchia 2006

Nucl. Instr. Meth. B **247** 92–97

Energy-sharing asymmetries in ionization by positron impact

C. Arcidiacono, Á. Kövér, and G. Laricchia 2005

Phys. Rev. Lett. **95** 223202

Differential ionization experiments on positron – atom scattering

Á. Kövér, C. Arcidiacono and G. Laricchia 2004

Nucl. Instr. Meth. B **221** 56-59

Energy-Sharing Asymmetries in Ionization by Positron Impact

C. Arcidiacono,¹ Á. Kövér,² and G. Laricchia¹

¹*Department of Physics and Astronomy, University College London, Gower Street, London, WC1E 6BT, United Kingdom*

²*Institute of Nuclear Research of Hungarian Academy of Science (ATOMKI), Debrecen, POB 51, H-4001, Hungary*

(Received 13 May 2005; published 23 November 2005)

The triply differential cross section of molecular hydrogen for ionization by 50 eV positrons has been determined, for the first time, for both the ejected electron in coincidence with the remnant ion and for the scattered projectile. Asymmetries in the energy sharing between the two light particles in the final state are observed, with the electron spectrum being shifted to significantly lower (and the scattered positron to correspondingly higher) energies than expected. A similar shape is observed in the case of the ejected electron spectrum from a helium target at the same excess energy.

DOI: 10.1103/PhysRevLett.95.223202

PACS numbers: 34.85.+x

The correlated dynamics of few interacting particles is a fundamental physics problem that may be exemplified through the process of ionization. Despite the tremendous progress in its theoretical description during the past decade or so (e.g., [1,2]), concomitant experimental investigations remain essential in assessing the accuracy of the various approaches and in guiding further developments. In this respect, particularly sensitive are studies in which there are two or more *light* particles (e.g., an electron and a positron) in the final state and which yield cross sections which are differential in the energy and/or angular distribution of the ejected electron(s) and/or scattered projectile. The most stringent among these is the triply differential cross section (TDCS) in which all the kinematic parameters are determined. A significant body of data has been gained using the ($e, 2e$) method (e.g., [3]) and, more recently, the COLTRIM technique (e.g., [4]), which has been applied to electron, photon, proton, and ion impact. Differential studies with positrons, mainly confined to doubly differential investigations (e.g., [5–7]), remain scarce but are desirable both intrinsically and for comparison with equivelocity electrons or protons to probe the role of the projectile charge or mass on the collision dynamics (e.g., [8,9]). In this Letter, we report experimental TDCS results for positron impact ionization of simple molecular and atomic targets that reveal major discrepancies with current quantum-mechanical treatments and should thus provide new insights into the understanding of three-body correlated dynamics.

Over the past decade, sophisticated distorted wave calculations have been developed based on the 3-Coulomb-wave final-state wave function (3C) of Brauner *et al.* [10] which approximates the strictly inseparable many-body system in terms of pairs of interacting particles. At lower energies, the use of the eikonal approximation for the initial state has been found to improve agreement with experiments (e.g., [11]). While such methods have been successful with a variety of projectiles and over a wide energy range, nonperturbative approaches remain superior at lower energies. Particularly noteworthy in this respect

are the exterior complex scaling (ECS) method (e.g., [2]), which yielded the first accurate TDCS for e^- -H ionization for the case of equal energy-sharing kinematics [12], and close-coupling techniques which have been used for electron and photon collisions with various atoms and ions (e.g., [13]). In the case of integrated cross sections, also for collisions with positrons (e.g., [14,15]) and positronium (e.g., [16]).

A special case of ionization is electron capture, where the ejected electron is captured by the projectile to a bound or low-lying continuum state [17,18]. This latter process, often referred to as electron capture to the continuum (ECC), arises from the dominance of the final-state Coulomb attraction between the scattered projectile and the ionized electron. It is well known in ion-atom ionizing collisions and easily observable in the energy spectrum of electrons ejected around the direction of the scattered ion which, owing to its mass, suffers little deflection through the collision [19]. Positrons, on the other hand, are light and easily deflected. For this reason, the observation of ECC with these projectiles had to await the first kinematically complete experiment where increased sensitivity was achieved by detecting the projectile scattered near 0° in coincidence with the electron ejected in the same direction [20]. In that study, the TDCS was determined for positrons at an incident energy of 100 eV in collision with a H_2 target, namely $e^+(100 \text{ eV}) + H_2 \rightarrow e^+(\theta \sim 0^\circ) + e^-(\theta \sim 0^\circ, E_-) + H_2^+$. The ECC process was manifest by a small peak at half of the residual kinetic energy ($E_r/2$ where $E_r = E_i - I$, E_i being the positron incident energy and I the target ionization energy). The results were well described by the calculations [21,22] employing 3C wave functions for the final state. More recently, however, in an experiment at 50 eV incident energy, a significant shift of almost 2.5 eV from $E_r/2 = 17.3$ eV has been observed in the electron TDCS peak towards lower energies [23]. In comparison with the calculations of Fiol *et al.* [22], convoluted with the angular and energy resolutions, the experimental TDCS was shifted by around 1.6 eV. Although in [23], an error in the energy calibration was deemed

unlikely, it could not be entirely excluded and thus the experimental results have remained preliminary until now. Kövér *et al.* [23] had conjectured that, if genuine, a possible cause of this energy shift could be a doubly inelastic process, e.g., ionization simultaneous to vibrational excitation or dissociation of the remnant ion.

Fiol and Olson [24] carried out calculations for impact ionization of H_2 using both the classical trajectory Monte Carlo (CTMC) method and the perturbative quantum-mechanical approach using 3C final-state wave function (CDW) at 50 and 100 eV positron incident energy. They found discrepancies between the results from the two theoretical methods and no consistent description of the experimental data, with CDW giving better agreement at 100 eV while the CTMC model better describes the experiment at 50 eV, where a strong correlation between the momenta of the positron and the recoil ion was noticed.

In this study, (i) we resolve the main uncertainties of the study of Kövér *et al.* [23], by calibrating the absolute energy through the identification of the threshold for positronium formation and by checking the remnant hydrogen ion for possible dissociation; (ii) we determine, for the first time, the energy spectrum of the positrons scattered from molecular hydrogen, and (iii) we measure, also for the first time, the energies of electrons ejected by positron impact ionization of helium at the same excess energy as in the molecular hydrogen study.

The experiment has been carried out at University College London using the apparatus previously described [5,25]. Briefly, positrons are transported through an electrostatic system from the moderator to a crossed gas jet. A ^{22}Na source (activity $\sim 3 \times 10^8$ Bq), in conjunction with an annealed tungsten mesh moderator, provides a positron beam intensity of $\sim 10^3$ s $^{-1}$. The energy distribution of the particles ejected (or scattered) at around 0° has been measured using a single channel electron multiplier (CEM) at the end of a tandem parallel-plate energy analyzer (PPA) [26], as shown in Fig. 1. The particles scattered (or ejected) at the same angle have been detected in delayed coincidence with an assembly of microchannel plates (MCP) fixed within the first stage of the PPA. Time spectra have been recorded both with and without target gas. The overall measuring time at each energy was around 10^5 s. After normalizing the time spectra for the number of positrons incident upon the MCP, the gas pressure, and the possible variation in the detection efficiency, the difference between the normalized gas-on and gas-off spectra has been determined and the total coincidence signal calculated. The absolute energy of the beam has been obtained by determining the positronium formation threshold (E_{Ps}) in He. This has been done by measuring the ion yield versus moderator voltage, V_m , yielding $E_i = eV_m + (2.24 \pm 0.36)$ eV in agreement with the previous determination [23]. During this measurement, the positron beam was stopped while pulses ± 50 V high and 2 μ s long, from

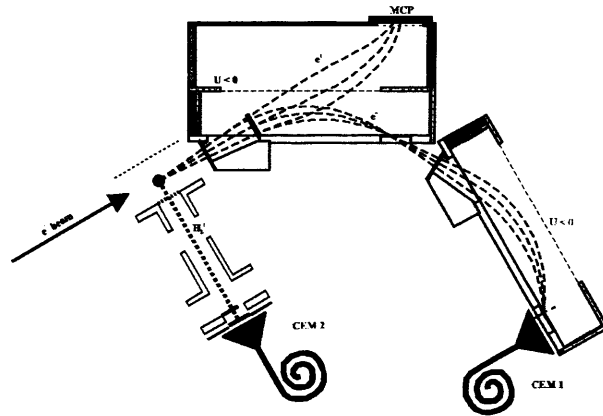


FIG. 1. Schematic diagram of the interaction region comprising the gas jet, the parallel-plate analyzer, and the ion extractor.

a generator operating at ~ 10 kHz, were applied to the ion-extractor plates in Fig. 1.

To investigate the possibility of dissociation, the charge-to-mass ratio (Q/M) of the ion in the final state was measured. For this purpose, a triple coincidence system has been set up between the ejected electron, the remnant ion and the scattered positron. Detection of an electron of a given energy triggered the application of the voltage pulses to the capacitor plates to extract possible ions present in the scattering region. In this measurement, D_2 was used as the target gas to increase the lifetime of the ion in the extraction region and to distinguish it from possible contributions from background gases. The correlated detection of an electron-ion pair has then been used to initiate a second measuring sequence stopped by a positron. From the time-of-flight spectra obtained from the delayed coincidence between CEM1 and CEM2, the ion Q/M has been determined.

In these measurements, no D^+ has been observed but this is not a conclusive proof that dissociative ionization is not responsible for the shift, as the extraction efficiency of the dissociation products may be significantly suppressed by their relatively large speed. However, as shown in Fig. 2(a), the energy dependence of the triply coincident D_2^+ signal has been found to be the same as that observed in [23]. It is this observation that excludes the involvement of dissociative ionization. In the figure, the triply differential electron spectrum for D_2 has been normalized to the theoretical calculation of Fiol *et al.* [22], as it was done in [23]. The most conspicuous feature of the comparison with the theory is the displacement of the experimental distribution towards lower energies: the theory of [22] peaks at 16.5 eV, while both sets of experimental data rise to a maximum at ~ 15 eV. Both theoretical and experimental data decrease with a similar slope above their respective peaks. Also shown in the figure are the CTMC calculations of Fiol and Olson [24]. As mentioned earlier, this approach failed to describe the 100 eV data of Kövér and Laricchia

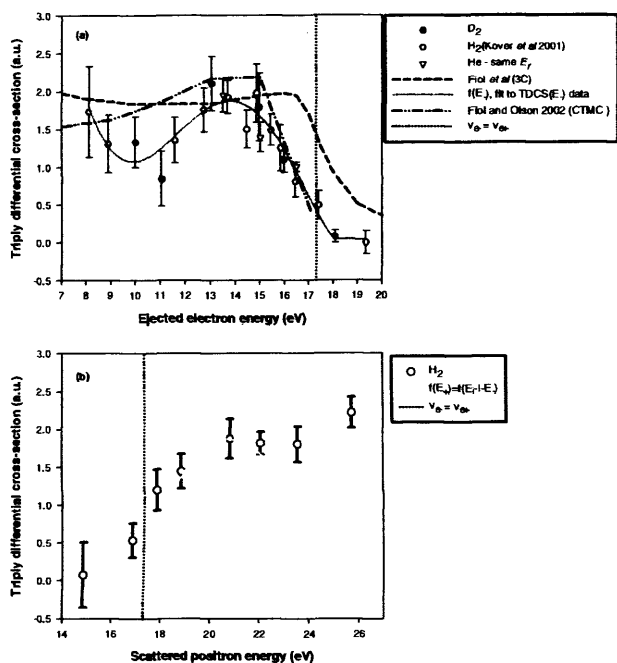


FIG. 2. Experimental and theoretical results for the triply differential ionization cross sections for ejected electrons (a) and scattered positrons (b) in 50 eV positron collision with molecular hydrogen. Data for ejected electrons from helium at the same residual energy are also presented. The gray lines are guides to the eye only.

[20], but it reproduces the main features of the 50 eV data of Kövecz *et al.* [23] and of the present data.

The measured energy spectrum of the scattered positrons is shown in Fig. 2(b). The positron data have been normalized around the maximum to the peak value of the electron data. A close correspondence is observed between the energy distributions of the ejected electrons, TDCS(E_-), and that of scattered positrons, TDCS(E_+), with $E_+ = E_i - E_- - I$, as expected from energy conservation. This establishes that the shift does not arise from an energy loss to the target as, for example, through molecular excitations.

Finally, the TDCS (E_-) obtained by positron impact ionization of helium at the same residual energy, $E_r = 34.6$ eV, can also be seen in Fig. 2(a) to follow the same shape as for hydrogen, implying that the significant parameter for the shift is the final-state kinetic energy.

Recently, a study has been performed with H^+ incident on H_2 and He resulting in electrons being ejected with velocities comparable with those of the present study. At 10 and 20 keV impact energy, the ECC cusp formation around 0° has been found to be shifted below its standard position around the projectile velocity [27]. CTMC calculations by the same authors indicate that the long-range residual interaction of the electron with the remnant target

ion is responsible for the shifts that manifest the pull of the target on the ejected electron.

Although we note that recent experimental and theoretical results [28] do not support the findings of [27], the interpretation of Shah *et al.* [27] might be compatible with the findings by Sarkadi [29], who investigated the fragmentation of positronium (Ps) in Ps-He collision also with the CTMC method and compared the results with the experimental data of Armitage *et al.* [30]. While good agreement has been found with the shape of the measured longitudinal energy distribution of the positron, he has predicted that the maximum of the electron peak should be shifted to lower energies due to the dynamical polarization of the target. While this prediction awaits experimental verification, the effect may reasonably be conjectured to be more pronounced in the case of a charged final state for the target.

Alternatively, it has been suggested that competition from the Ps formation channel might strongly influence the shape of the distributions at the lower energies [31]. Clearly, further work is needed in order to understand the observations.

In conclusion, the triply differential ionization cross section of molecular hydrogen has been determined for both ejected electrons and scattered positrons. Investigations have also been performed with a helium target. An unexpected asymmetry in the energy sharing between the two light particles in the final state has been observed around half of the residual energy: the electron spectrum is shifted to lower energies than predicted by perturbative calculations by around 1.5 eV while the positron distribution exhibits a shift of similar magnitude, but opposite sign from the equal energy-sharing value. From these studies, a significant factor in the shift appears to be the final-state kinetic energy and, in particular, perhaps, the low velocities of the light particles in the final state.

At present, the data have no consistent description by quantum-mechanical theoretical treatments and, in this respect, might be a suitable testing ground for recently developed *ab initio* approaches.

We wish to thank Laszlo Sarkadi and Jonathan Tennyson for helpful comments on this Letter. This work has been supported by the Engineering and Physical Science Research Council UK (Grant No. GR/S16041/01), the Royal Society, the Hungarian Scientific Research Found (OTKA No. T037203), and the European Union (HPRN-CT-2002-00179 EPIC). Akos Kover wishes to thank UCL for the excellent working conditions and hospitality.

-
- [1] J.S. Briggs and V. Schmidt, *J. Phys. B* **33**, R1 (2000).
 - [2] C.W. McCurdy, M. Baertschy, and T.N. Rescigno, *J. Phys. B* **37**, R137 (2004).
 - [3] P. Schlemmer, T. Rosel, K. Jung, and H. Ehrhardt, *Phys. Rev. Lett.* **63**, 252 (1989).

- [4] J. Ullrich, R. Moshhammer, A. Dorn, R. Dorner, L. Schmidt, and H. Schmidt-Bocking, *Rep. Prog. Phys.* **66**, 1463 (2003).
- [5] Á. Kövér, G. Laricchia, and M. Charlton, *J. Phys. B* **27**, 2409 (1994).
- [6] Á. Kövér, R. M. Finch, M. Charlton, and G. Laricchia, *J. Phys. B* **30**, L507 (1997).
- [7] A. C. F. Santos, A. Hasan, and R. D. DuBois, *Phys. Rev. A* **69**, 032706 (2004).
- [8] H. Knudsen and J. F. Reading, *Phys. Rep.* **212**, 107 (1992).
- [9] K. Paludan, G. Laricchia, P. Ashley, V. Kara, J. Moxom, H. Bluhme, H. Knudsen, U. Mikkelsen, S. P. Møller, E. Uggerhøj, and E. Morenzoni, *J. Phys. B* **30**, L581 (1997).
- [10] M. Brauner, J. S. Briggs, and H. Klar, *J. Phys. B* **22**, 2265 (1989).
- [11] S. Jones and D. H. Madison, *Phys. Rev. A* **62**, 042701 (2000).
- [12] M. Baertschy, T. N. Rescigno, and C. W. McCurdy, *Phys. Rev. A* **64**, 022709 (2001).
- [13] I. Bray, D. V. Fursa, A. S. Kheifets, and A. Stelbovics, *J. Phys. B* **35**, R117 (2002).
- [14] H. Wu, I. Bray, D. V. Fursa, and A. T. Stelbovics, *J. Phys. B* **37**, 1165 (2004).
- [15] C. P. Campbell, M. T. McAlinden, A. A. Kernoghan, and H. R. J. Walters, *Nucl. Instrum. Methods Phys. Res., Sect. B* **143**, 41 (1998).
- [16] J. E. Blackwood, M. T. McAlinden, and H. R. J. Walters, *J. Phys. B* **35**, 2661 (2002).
- [17] M. W. Lucas and K. G. Harrison, *J. Phys. B* **5**, L20 (1972).
- [18] M. Rodbro and F. D. Andersen, *J. Phys. B* **12**, 2883 (1979).
- [19] L. Sarkadi, U. Brinkmann, A. Bader, R. Hippler, K. Tökési, and L. Gulyás, *Phys. Rev. A* **58**, 296 (1998).
- [20] Á. Kövér and G. Laricchia, *Phys. Rev. Lett.* **80**, 5309 (1998).
- [21] J. Berakdar, *Phys. Rev. Lett.* **81**, 1393 (1998).
- [22] J. Fiol, V. D. Rodríguez, and R. O. Barrachina, *J. Phys. B* **34**, 933 (2001).
- [23] Á. Kövér, K. Paludan, and G. Laricchia, *J. Phys. B* **34**, L219 (2001).
- [24] J. Fiol and R. E. Olson, *J. Phys. B* **35**, 1173 (2002).
- [25] Á. Kövér, G. Laricchia, and M. Charlton, *J. Phys. B* **26**, L575 (1993).
- [26] Á. Kövér and G. Laricchia, *Meas. Sci. Technol.* **12**, 1875 (2001).
- [27] M. B. Shah, C. McGrath, Clara Illescas, B. Pons, A. Riera, H. Luna, D. S. F. Crothers, S. F. C. O'Rourke, and H. B. Gilbody, *Phys. Rev. A* **67**, 010704(R) (2003).
- [28] L. Sarkadi and R. O. Barrachina (to be published).
- [29] L. Sarkadi, *Phys. Rev. A* **68**, 032706 (2003).
- [30] S. Armitage, D. E. Leslie, A. J. Garner, and G. Laricchia, *Phys. Rev. Lett.* **89**, 173402 (2002).
- [31] H. R. J. Walters (private Communication).